Cranfield University

School of Engineering

Numerical Modelling of Through-Thickness Reinforced Structural Joints

Francesco Bianchi

Ph.D. Thesis

June 2012

Supervisor: Dr. Xiang Zhang

Abstract

The main objective of this research study was to develop numerical models to analyse the mechanical and fracture properties of through-thickness reinforced (TTR) structural joints. The development of numerical tools was mainly based on the finite element (FE) method. A multi-scale approach was used: the bridging characteristics of a single reinforcement was studied at micro-mechanical level by simulating the single-pin response loaded either in mode-I or in mode-II. The force-displacement curve (bridging law) of the pin was used to define the constitutive law of cohesive elements to be used in a FE analysis of the global structure.

This thesis is divided into three main parts: (I) Background, context and methodology, (II) Development for composite joints, and (III) Development for hybrid metal-composite joints. In the first part the objectives of the thesis are identified and a comprehensive literature review of state-of-art through-thickness reinforcement methods and relative modelling techniques has been undertaken to provide a solid background to the reader.

The second part of the thesis deals with TTR composite/composite joints. The multi-scale modelling technique was firstly applied to predict delamination behaviour of mode-I and in mode-II test coupons. The bridging mechanisms of reinforcements and the way these increase the delamination resistance of bonded interfaces was deeply analysed, showing how the bridging characteristics of the reinforcement features affected the delamination behaviour. The modelling technique was then applied to a z-pin reinforced composite T-joint structure. The joint presented a complicated failure mode which involved multiple crack path and mixed-mode delamination, demonstrating the capability of the model of predicting delamination propagation under complex loading states.

The third part of the thesis is focused on hybrid metal/composite joints. Mode-I and mode-II single-pin tests of metal pin reinforcements embedded into a carbon/epoxy laminate were simulated. The model was validated by comparing with experimental tests. Then the effects of the pin geometry on the pin bridging characteristics were analysed. The model revealed that both in mode-I and mode-II small pins perform better than large pins and also that the pin shape plays an important role in the pin failure behaviour. The modelling technique was then applied to simulate a metal-composite double-lap joint loaded in traction. The model showed that to obtain the best performance of the joint an accurate selection of pin geometry, pin arrangement and thickness of the two adherends should be done.

Acknowledgments

Looking with retrospective these three years spent working restlessly on this project I have to admit that I had to face my hard-times and there have been difficulties... moments when I lost the goal. In those moments I found great help in the guidance of my supervisor, Dr Xiang Zhang, who I need to thank deeply.

I want to thank with all my strength my Chiara, without whom I would never get to the end of this. I'd like to thank you for your continuous support that always encouraged me in facing and overcoming difficulties... in all-meaning sense.

I'd like to thank all my friends: housemates, volleyball team-mates and colleagues with whom I had the pleasure of having great time throughout these years, and also my home-friends who made me feel like I never left.

Finally I want to thank my family, for giving me the opportunity of dedicating my-self to my education along a path that started long before this achievement. Thank you for letting me arrive where I managed to get today.

To Chiara

Who has always been there for me...

CONTENTS

LIST OF FIGURES

LIST OF TABLES

ACRONYMS

CFRP	Carbon fibre reinforced plastics
DCB	Double cantilever beam
ENF	End notch flexure
FE	Finite element
FML	Fibre metal laminate
LEFM	Linear elastic fracture mechanics
LSB	Large scale bridging
NDI	Non destructive inspection
SERR	Strain energy release rate
SSB	Small scale bridging
TSL	Traction separation law
TTR	Through-thickness reinforcement
VCCT	Virtual crack closure technique

Part I

Background, context and methodology

CHAPTER 1

INTRODUCTION

1.1 Background

There has been a continuous growth of the use of composite materials in aeronautical structures in the past three decades. Previous aircraft structures were mostly made of aluminium alloys and composites were limited to secondary structures. With growing experience and confidence, the use of these materials, with particular reference to carbon fibre reinforced plastic (CFRP), has been extended to primary structures (e.g. the Airbus A310 and A320). The A310 vertical stabiliser (a primary fin structure) was entirely fabricated in carbon fibre composites with a weight savings of about 400 kg compared with the metallic solution. In the A320 the use of CFRP was also extended to the horizonal stabiliser [1]. In addition, composites were also extensively used for A320 control surfaces and secondary structures, as shown in Fig. 1.1 [2], reaching up to 28% of the total airframe weight.

New generation of aircraft has about 50% of aircraft structures being made of composites; for instance the main wing of the Airbus military cargo A400M, the Airbus A350 and the Boeing B787 fuselage and main wing, all of them are made entirely in CFRP. Another example of the extensive use of CFRP is in Fig. 1.2, which shows a fuselage section of the A350 with skin panels, doublers, joints and stringers entirely made of carbon fibre composites. The use of composite materials allows weight savings and reduction of operation costs, for this reason their use is believed to increase further in the near future. However, their effective application to aircraft structures is strongly limited by the low efficiency and damage tolerance of composite joints.

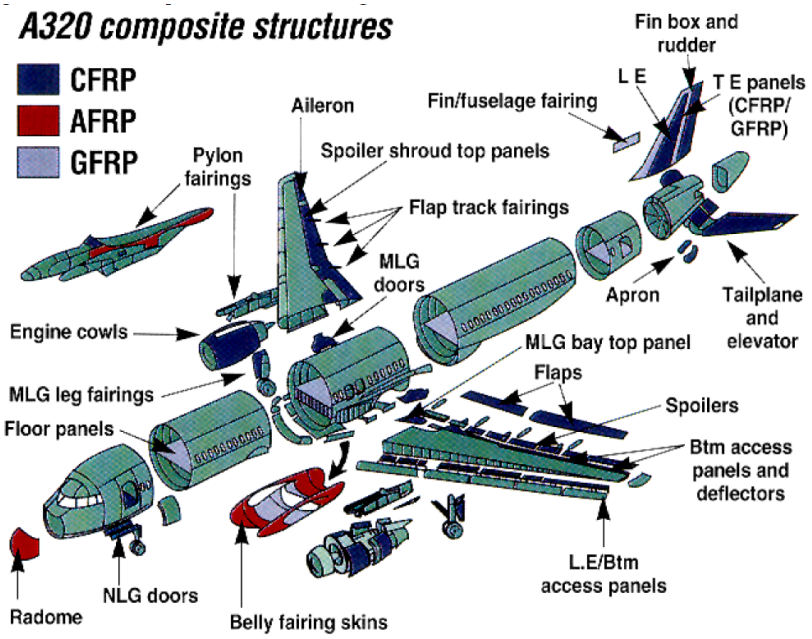

Figure 1.1: Composite material applications on Airbus A320

The current practice is simply using mechanical fastening (e.g. bolting, riveting) or bonding. Mechanically fastened joint brings several issues in composites such as stress concentrations at fastener holes, possible water ingression and possible damage introduced by the drilling process. Due to composite brittle behaviour, stress concentrations cause early failure. The joint needs to be thickened and thus the average stress remains low (inefficient material use). Moreover, the sealing used to avoid water ingression and the rivet weight contributes to increase the total aircraft weight. All these factors decrease the benefits brought by the use of advanced materials, thus making unjustified increase of costs for the composite solution.

An alternative to mechanical fastening is adhesive bonding. The aim of this joining technique is to distribute the load over a larger surface in order to avoid high stress concentration at bearing points. However, the discontinuity of geometry at runouts still causes stress concentrations, inducing delamination/disbond failure under relatively low loads. Moreover, because delamination runs at the interface between plies or at the bondline, the damage is usually not detectable by visual inspection. Nowadays non-destructive inspection (NDI) methods to detect delamination damage on an operating aircraft have not yet been developed. For this reason aircraft manufactures and regulatory authorities consider the damage tolerance capability of bonded joints difficult to assess (i.e. not suitable for primary structures).

The damage tolerance requirements for aircraft primary metallic structures[1]

[1]That is structure whose failure could cause the direct loss of the entire aircraft

are that the presence of any damages or flaws within the material, either caused by manufacturing processes, induced by impact events or ageing, has to be accounted for. These defects (cracks) have to grow safely and remain small enough not to cause a dramatic reduction of static strength before the damage could be detected and action could be taken. Although damage tolerance as we know it today can be considered a relative modern discipline, the importance of flight-safety, when dealing with human lives, was already recognised almost 500 years ago by Loenardo da Vinci. On his notebook, discussing the design of "flying machines" he applied for the first time the concept of fail-safe design:

> *In constructing wings one should make one cord to bear the strain and a looser one in the same position that if one breaks under strain the other is in position to serve the same function.*
>
> *Leonardo da Vinci*

There are two ways to satisfy the damage tolerance requirements: one, as already identified in its rudimental concept by the medieval Italian scientist, is to provide a fail-safe design, where at a partial structural failure load is safely redistributed over the rest of the structure causing the crack to stop (crack arrest) or by backup structures (multiple load path). A second way, alternative to fail-safe design, is to assure a slow and stable crack growth for a period long enough that the crack could be detected and the component replaced (safe crack growth). Such a requirement is difficult to fulfil for a conventional bonded joint: there is no way to arrest a crack when this starts propagating, nor an alternative load path. Moreover, considering the difficulty of damage detection, even improving the toughness of adhesives, which reduces the onset and growth, results being ineffective since there is no way to judge the criticality of the structure and thus to provide the necessary replacement.

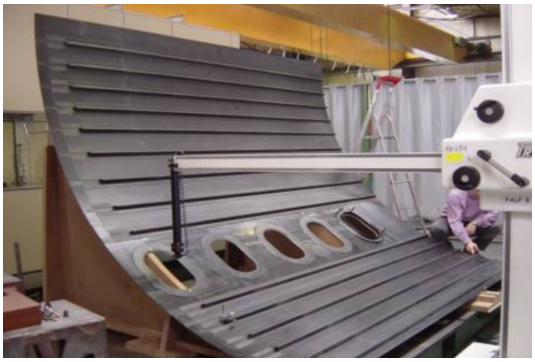

Figure 1.2: A fuselage section of the A350: skin panel, doublers, joints and stringers made of CFRP

Another important aspect is that, due to the load transfer mechanisms of bonded joints based on transverse shear stress, the strength of bonded joints is usually limited by the low interlaminar toughness of composite materials [3]. Several methods have been developed for improving the interlaminar fracture toughness of composites. These techniques can be divided into two main categories: one is based on toughening the material either by using thermoplastic

(such as PEEK) rather than thermoset resins, increasing the improving the interphase bonding between matrix and fibres [4], interleaving thicker layers of resin [5] or adding thermoplastic or rubber particles to the matrix of the composite [6]. The other method uses a certain percentage of reinforcements, either fibres or metallic rods, directed through the thickness. Several through-thickness reinforcement (TTR) techniques have been developed, e.g. stitching [7], z-fibre pinning (or z-pinning) [8, 9], and tufting [9, 10]. Stitching and tufting are effective toughening methods, but they can only be applied to fabric preforms and then resin infused. Z-pinning has attracted larger interest in its application in the aircraft structures, because it is the only through-thickness toughening technique that can be readily applied to composite joints made of prepreg materials [8].

1.2 Through-thickness reinforced composite joints

Through-thickness reinforcements (TTR) can be used to increase effectively interlaminar strength and toughness of the composite laminates. Their effect acts at two levels: increasing the fracture toughness of the adhesive at the bondline and enhancing the interlaminar strength and toughness of laminate itself (i.e. acting at the ply-to-ply interface). They provide crack bridging traction forces when a delamination crack initiates, which oppose the crack propagation. Ultimate strength, energy absorption at failure and fatigue life of composite joints can be largely improved by TTR.

Whereas stitching and tufting involve more complex technologies to be applied, one due to the need of access to both sides of the laminate during the stitching process, the other due to necessity of use of relatively bulky machinery to drive the needle through the laminate, z-pinning has a more attractive ease-of-use. Z-pin reinforcements have been used for the Boeing F18 E/F engine inlet ducts, as depicted in Fig. 1.3a; replacing 4000 titanium fasteners in previous bolted design, a cost savings of $83000 and a reduction of 35 pounds in weight was achieved. Z-pinning has been also used for replacing bolted joints in the Lockheed Martin *Joint strike fighter* (JSF) F-35 (Fig. 1.3b), obtaining a predicted savings of 70% in cost and 10.3 pounds of weight reduction per 1000 fasteners. However, due to the lack of reliable modelling techniques to predict their effect on real structures their application is very small, and limited to military aircraft and the automotive industry [8].

Although the mechanisms which these reinforcements use to enhance the laminate fracture toughness have been largely studied during the past years, only few models exists in the literature, the majority of which still limited to delamination test samples and focused on the mode-I delamination behaviours. The nowadays techniques to measure the interlaminar fracture toughness of

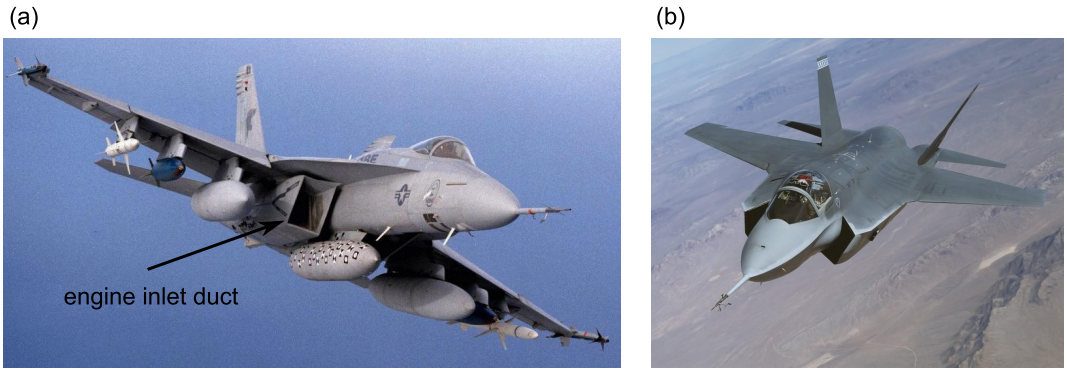

Figure 1.3: Z-pinning applications in aerospace: (a) engine inlet ducts of the F-18 E/F, (b) Lockheed Martin JSF

composite laminates are based on delamination tests samples such as the double cantilever beam (DCB) and the end notch flexure (ENF) tests (full review of these test is given in Chapter 2). These tests give a valuable information in terms of the strain energy release rate (SERR) as a measure laminate delamination resistance. However, the effect of TTR is hardly estimated by these tests. Studying the effect of TTR in enhancing the damage tolerance of real structures will provide a deeper understanding on how these reinforcements have to be designed and will help bringing more confidence on their application.

1.3 Hybrid metal-composite joints

Another aspect to accounted for is that, although the high specific strength and stiffness of CFRP are appealing properties, some drawbacks, such as high impact damage sensitivity and low out of plane properties, make metals to be more suitable for certain applications. Thus, metals and composites need to be joined.

The lack of effective techniques to join composite to metal causes integration difficulty issues. In that lies one of the major limitations of this material application. For this reason, developing new hybrid jointing techniques is a nowadays top-priority challenge. Several studies oriented to combine the features of the two conventional joining techniques (bolting and boding) have been already carried out. Three categories have been identified:

- **Bolted-bonded**: the two conventional techniques are effectively used together in order to decrease the load taken by fasteners and better distribute it over a larger area Fig. 1.4a [11–15].

- **Interleaved**: CFRP plies are progressively substituted by metal sheets forming a transition region of fibre metal laminate (FML). The increased bonded surface reduces the average shear stress, which is the major cause

of delamination. Furthermore, the ply substitution hybridises the laminate properties: shear strength and bearing resistance are increased, making the laminate more compatible with bolting Fig. 1.4b [16–20].

- **Surface structured**: mechanical features are manufactured on the bonding surface of the metal adherend. These surface protrusions are driven into the composite part before the curing process, without the need of any drilling process (expensive and potentially harmful procedure in composite materials). As result the mechanical reinforcements improves the joint performances by suppressing debond cracks onset and propagation Fig. 1.4c [21–24].

The coupling of CFRP and aluminium alloys presents issues related to corrosion sparked off by the C-Al galvanic cell. For this reason the above mentioned technologies are mainly addressed to titanium alloys for high performance, weight saving application, typically demanded by aerospace industry. However, for civil and naval applications, and research scopes these technologies apply also to stainless steel providing high-strength, low-cost joint solution.

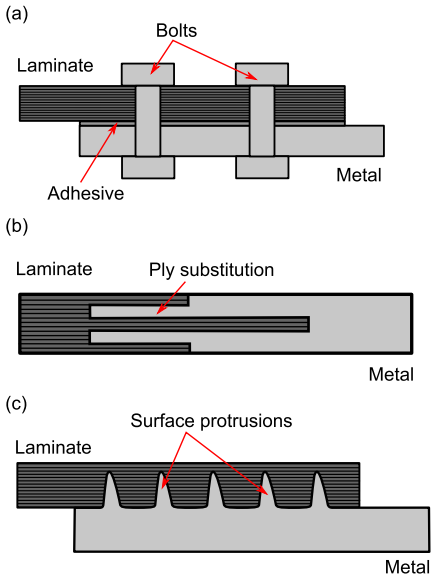

Figure 1.4: Hybrid joint techniques: (a) bolted-bonded, (b) interleaved, (c) surface structured.

Bolted-bonded joints have been studied in the early eighties; initial founding showed that the load transfer mainly involves adhesive, leaving the bolt almost unloaded and thus not contributing to improve the joint efficiency. However, the dormant bolt takes a larger part of the load as soon as a disbonding crack surpasses it, providing a shielding effect to the crack tip and opposing further crack propagation. Fatigue life of bonded joint therefore can be highly improved by such a technique [15]. Nevertheless bolting is typically used for repairing delamination damage in adhesive joints.

The concept of alternating metal and composite plies for creating a new material with tailored properties has been largely investigated for glass-reinforced fibre metal laminates (GLARE). The hybrid material shows better damage tolerance properties, higher corrosion resistance, higher heat resistance and lower weight than pure metal. Compared to plain composite, glare has also a lower impact damage sensitivity and higher bearing strength which lead to higher load transfer capability of bolted joints. However, the technology can be considered mature and it is indeed already in service on the Airbus A380. The application of interleaving for CFRP-Ti joints cannot be considered either

innovative or novel and, thus, it is beyond the purpose of in this thesis.

A very promising technology is the so-called surface structuring. The idea of transferring part of the load by bearing and part by adhesive bonding is very similar to bolted-bonded joints. However, the coupling is realised entirely on uncured laminate: no drilling process is involved, avoiding fibre breakage and water infiltration issues. The z-protrusions do not contribute to the load transfer until a debond crack grows underneath and surpasses the reinforcement structure. From this point on z-protrusions start to bear load, providing a shielding effect to the crack tip and preventing the crack to grow further. Recent studies have demonstrated that this technology can bring significant improvement in terms of joint strength and absorbed energy at failure [21, 25, 26]. However, a substantial lack in the literature of numerical model for predicting strength and behaviour of such a joint has been found: to the author's knowledge the only model of surface structured joint available is a stress based model for determining damage initiation [22–24]. However, the effect of design parameters on joint strength and behaviour has not been well clarified and up to date no valid model for predicting structural properties and failure has been found in the open literature.

As often happens in developing new technologies a very important task is to develop modelling techniques capable of predicting joint strength and failure modes. The certification process involves a massive number of tests, which can be reduced by providing a consistent modelling technique. The concept of supporting experiments with modelling is called building block approach: the certification process starts from coupon level moving towards to sub-component till the entire structure test. The experiments are supported by models and the models are validated step-by-step by the experiments, as represented in Fig. 1.5. This synergic process allows to limit unpleasant surprises in experiments and to develop consistent models useful in aircraft structure design [27].

1.4 Scope, Aim and Objectives

The scope of this research is to develop innovative modelling techniques to predict the structural properties and failure behaviours of through-thickness reinforced composite and hybrid metal-composite joints. This research is aiming to develop reliable models usable for the design of high-efficiency, low cost, composite and hybrid structures, also and to provide a solid basis for increasing the confidence on this technology and therefore promoting their application to aircraft primary structures.

In this project the modelling will involve analyses at different scales in order to characterise structural response of the reinforcements and their failure mechanisms at the smallest scale and then using the bridging forces of the re-

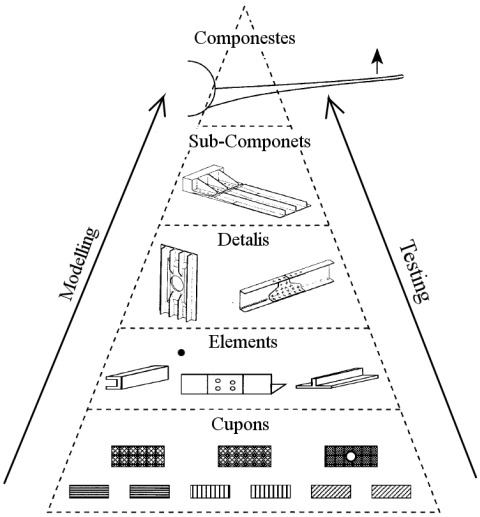

Figure 1.5: The "pyramid" of test in the "building block approach".

inforcements to model the joint response at the structural level. The concept of using different scales to predict mechanical properties of composites is well consolidated [28, 29]. The modelling process will follow the scheme bellow:

1. **Unit-cell model**: to simulate the pullout and shear response of a single-pin specimen. The bridging laws of the pins under elementary load conditions will be predicted. These bridging forces then will be implemented into a structural-level model.

2. **Macro-scale structural model**: to predict the strength and failure behaviour of joints. The model from one side simulated the joint behaviour as a structure, accounting for the bridging effect of TTR that opposes and eventually inhibits delamination/debond cracks. On the other hand the model is useful also to calculate the stresses on the reinforcements and going backwards to the unit cell model it is possible to evaluate the stress state of the reinforcement and its margin to failure.

The research objectives can be summarised as bellow:

- To develop unit-cell single pin model to predict the reinforcement bridging laws under different load conditions and investigate the fracture mechanisms in the reinforcement pullout and shear from the laminate. These models will be validated by experimental tests and will provide a tool for designing reinforcements for tailored needs.

- To study the relative importance of through-thickness reinforcement geometrical parameters in enhancing disbond resistance of composite and hybrid joints.

- To develop macro-scale structural model for predicting the delamination/disbond enhancement of TTR.
- To generate a simplified, computational-time-efficient model suitable for parametric studies of different geometries or different reinforcement configurations.
- To investigate the effects of geometrical parameters on the bridging force capability of single-pins.
- To study the effects of different pin densities and arrangements on the structural response of surface structured joints, with par reference to double lap (DLJ) configuration.
- To investigate the relative importance of through-thickness bridging parameters (e.g. initial stiffness, maximum strength and energy absorption) on the structural response of surface structured joints.

1.5 Workframe

This research work is part of a larger project intended to investigate innovative solutions for hybrid metal/composite joints. The project was named "Bridging the Divide"(BtD) and it has been run in collaboration with EPSRC, Bae Systems and Airbus Germany, which fully funded it.

The project involved three PhD students: two focused on developing and testing novel joining techniques and joint designs and one dedicated to define and validate modelling techniques able to predict the structural properties of these new-design joints. The research work presented in this PhD thesis covers the modelling part of the project. Experimental results presented in the following chapters have only validation purpose and they have been used as a comparison metre to evaluate the accuracy of the modelling technique developed.

In particulary the experimental work on metal pin reinforcements presented in Chap.6 has been carried out by John Butler and the experimental results on hybrid metal/composite joints presented in Chap.7 have been achieved by Adam Joesbury during their PhD research works. References to original works have been indicated specifically when applicable.

1.6 Structure of the Thesis

This thesis is structured in three main parts: firstly an overview of the problem statement is given, the literature review is covered and the modelling

methodology described. This part is communal to the whole thesis and it describe the essence of the work done. Secondly the model is dedicated to z-pin reinforced and hybrid metal-composite joints. The second part of this thesis regards z-pin reinforced joints: the development of unit-cell models to study the effects of z-pin geometrical parameters, the validation of the model for different fracture modes and the application of the model to real T-joint structures. The third part finally focuses on towards hybrid metal-composite surface structured joints: the unit-cell models for mode-I and mode-II bridging forces is specialised for this kind of reinforcements, the model is validated by mechanical tests and the effects of geometrical parameters studied. The model is then validated by DLJ static tensile tests and the effect of metal pin parameters on the response of the joint is studied. A summary of the contents of each chapter is given as follows:

Part I – Background, context and theory

Chapter 1 outlines the background, the necessity of developing modelling tools for through-thickness reinforce composite and hybrid metal-composite joints and the research work objectives.

Chapter 2 provides to the reader an introduction to the necessity of developing new joining techniques. This is followed by a detailed review of through-thickness reinforcement method for strengthening composite joints, their failure mechanisms and existent modelling techniques to predict their behaviours. Review of to-date methods for measuring the fracture toughness of laminates is also given in order to provide the reader the necessary knowledge to interpret results. The knowledge of the these methods is necessary also to understand the need of a tool to correlate the bridging force exerted by a single pin and their global effect on the structure. Finally a review of the cohesive zone modelling (CZM) approach is also given to furnish to the reader the knowledge to understand the model assumptions and their effect on results.

Chapter 3 contains the modelling methodology: a detailed description of the multi-scale approach used is given. The unit-cell single pin model for predicting the bridging forces of pins and the cohesive zone macro-scale model for evaluating the structural properties and fracture of composite structures, are described together with assumptions made and boundary conditions applied. The model is then specialised, adjusting assumptions and boundary condition to each specific case, to predict either composite or hybrid metal-composite structures.

Part II – Model development for composite joints

Chapter 4 validates the model predicting the mode I delamination of z-pinned laminates. Double cantilever beam tests of composite laminates reinforced by z-pins having different diameter and density are analysed.

Chapter 5 deals with the mode II delamination of z-pin reinforced laminates. The model is validated by end notch flexure tests of composite laminates reinforced by z-pins of different diameter and density. The mode II bridging law of z-pins is predicted at the unit-cell single pin scale and than implemented into the macro scale model. A simplified bi-linear law for pin reinforcements is proposed and the effect of such assumptions are analysed.

Chapter 6 shows the analysis of a z-pin reinforced T-joint, demonstrating the validity of the model for complex structures subjected to mixed mode, multiple delamination damage failure. The study shows the potentiality of the model for predicting the structural properties and failure behaviours of z-pin reinforced structures.

Part III – Model development for hybrid metal-composite joints

Chapter 7 presents the validation of the unit-cell single-pin model for pull-out and shear. The validation is done by comparing numerical results with mechanical tests. The design, preparation, mechanical test of the single-pin specimens, as well as the procedure for analysing test data is also presented in this chapter. Few key parameters of the bridging-law generated by the pin are identified and the effects of geometric pin parameters on those bridging characteristics are studied.

Chapter 8 presents a numerical study of a hybrid surface structured DLJ. The model validation is achieved by comparing the numerical results with test data. The effects of bridging law characteristic (which can be controlled by the pin geometry), the pin density and arrangement are analysed in detail.

Chapter 9 is addressed to draw specific conclusions regarding the research work. The accomplishment of thesis objectives is presented and critically analyses, focusing on the potentiality and limits of the model. Some recommendation in how to carry on with the research about hybrid surface structured joints is also addressed.

CHAPTER 2

LITERATURE REVIEW

2.1 Current joining techniques for composite materials

Through-thickness reinforced joints exhibit characteristics of both adhesively bonded and mechanically fastened joints. The load bearing of the reinforcement reduces the strain energy release rate of the incipient delamination crack and increases the interlaminar strength of composite, but also introduces stress concentrations and fibre misalignment which weakens the in-plane laminate properties. Depending on the dimension of the reinforcement the weak point of the laminate might vary from being either interlaminar delamination, adhesive debond or the in-plane failure due to the high stress concentrations introduced by the reinforcement it-self.

Through-thickness reinforced joints, being a cross between adhesively bonded and mechanically fastened joints, will exhibit behaviour and failure modes which can vary from one to the other of the two conventional joining techniques. A deep understanding of the of the failure modes of these is therefore necessary.

2.1.1 Mechanical fastening

A large part of the research on mechanical fastened joints has concerned with the experimental determination of the influence of geometrical factors on the joint behaviour and strength. In order to obtain comparable results and limit the experimental issues in running tests, standardization organizations (e.g. ASTM, NASA and MIL) have developed testing procedures to characterise

composite strength and failure behaviours. Among the others, the most representative are the open-hole tensile [30] and compressive test [31], filled-hole tensile and compressive test [32], and the bearing test configuration [33].

In these standard tests there are reported all the information needed to set up, to run and to gather data of the test under study. A unique way to describe the specimen failure modes is reported in order to facilitate the use and the interpretation of the collected data. According to [33], mechanically fastened joints show five possible failure modes: (a) net-tension, (b) shear-out, (c) bearing, (d) tear-out, (e) cleavage, as shown in Fig. 2.1.

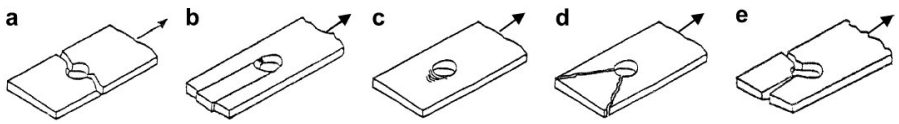

Figure 2.1: Failure modes for bolted joints: (a) Net-tension, (b) Shear-out, (c) Bearing, (d) Tear-out, (e) Cleavage.

Net-tension failure mode is believed to be associated with the tensile lamina strength, shear out and bearing instead are due to shear and compressive lamina strengths. Whilst the first two are usually unstable failure modes, the last one is progressive, thus the joint has a post critic load capability. Tear-out and cleavage are believed to be transition failure modes between the two principal net-tension and shear-out. Several authors have highlighted the importance of width (w), end distance (e), hole diameter (d) and laminate thickness (t) on the joint strength. Therefore the non-dimensional parameters (w/d, e/d, t/d) are often used in studies addressed to characterise the strength and behaviour of suck a joint. However, many authors emphasised the relevance of even of other parameters such as: ply-orientation, lay-up, interlaminar delamination toughness and the clearance between the joining device and the hole [34, 35].

Failure prediction of bolted joints under static loads has been the subject of several researches. Many strength failure theories for composite laminate materials have been proposed, among the others: maximum strength criterion (Jenkins, 1920), maximum strain (Waddoups, 1967), maximum strain energy (Hill, 1948), Hoffmann theory, Tsai-Wu, Tsai-Hill and Hashin [36]. These criteria has been applied to either analytical or numerical models to study the stress concentration at bolt-hole and thus, to predict the joint strength. Analytical methods have the advantage to provide a quicker solution, FE analysis is usually more accurate, but more time costly. Several studies have been carried out on this topic, however, a detailed description of all models and methods used is beyond the purpose of this thesis; nevertheless, a review of these methods can be found in [37].

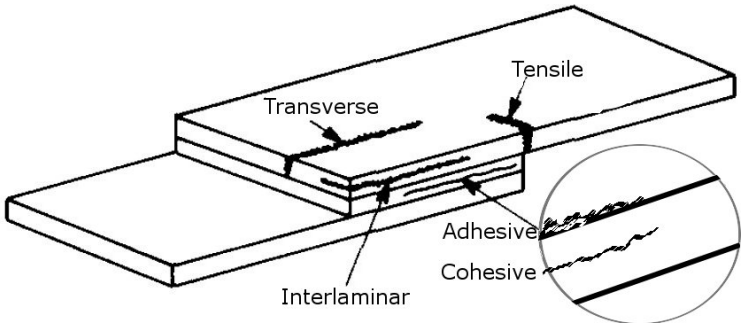

Figure 2.2: Adhesively bonded joint failure modes.

2.1.2 Adhesive bonding

Adhesive joint was developed in order to overcome the issues concerning the low bearing properties of CFRP laminates. The purpose of such joint is to avoid load transferring through concentrated forces by distributing stress over a larger surface. Although this joining technique offers an effective alternative to bearing load transfer, it introduces high out-of-plane shear and peel stresses, which can cause delamination either in the adhesive or interlaminarly between laminate plies. Due to the elasticity of the adherends, stress concentrations arise at bonding runouts. These locations are typically critical for bonded joints: form there, delamination cracks usually initiates and propagates, causing an early failure.

Adhesively bonded joint shows five typical failure modes: cohesive, adhesive, interlaminar, tensile and transverse (Fig. 2.2). The first two occur in the adhesive and the last three in the adherend. Cohesive and adhesive failure modes are due to delamination respectively through the adhesive it-self and at adhesive-adherend interface. However, the latter is believed to be caused by incorrect preparation of bonding surface. Interlaminar, tensile and transverse failure modes involve the adherend failure: the former is related to interlaminar delamination between plies and the other two due to exceeding either the shear or compressive laminate strengths [38].

Adhesive bonded joints can be divided into two categories: co-cured and co-bonded. In co-cured joints, laminate forming and bonding happens together during a same cure process, co-bonding instead uses two distinct cure cycles. The co-cured joints can either be manufactured with or without adhesive. Co-curing is usually preferred because structural performance and reliability are usually better than those of co-bonding [39].

Either classic analytical of finite element methods have been used to predict strength and behaviour of adhesively bonded joints. Analytical methods attempt to develop simplified relationship of the adherend-adhesive interactions in order to calculate the interfacial stresses: shear and peel. However, too sim-

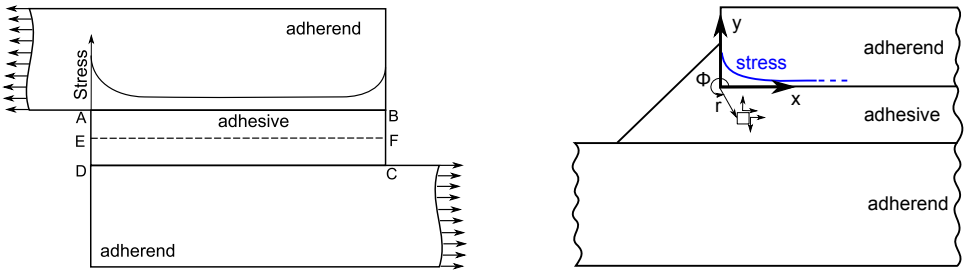

Figure 2.3: (a) Stress concentration points of adhesive bonded joints, (b) generalised stress intensity factor for adhesively bonded joints.

plified hypotheses can alter results. Finite element methods usually reduce the number of simplifying hypothesises, they can be used either with a strength based [39–42], fracture mechanics [43–45] or damage mechanics approaches [46–48]. Sufficiently accurate results can be obtained refining the mesh only in the regions of high stress concentrations. However, due to the material property mismatch, the adhesive layer corners are singularity points of the stress field (considering a perfectly elastic model) as depicted in Fig. 2.3.

The stress values at these locations are mesh sensitive (i.e. the higher the finer the mesh used) thus it cannot be used for strength based failure criteria. One way to solve this problem is to define a characteristic distance from the corner where to evaluate the stress; this stress is compared with the adhesive strength to calculate the critical load [39, 40]. However, the definition of the characteristic distance is arbitrary and generally dependents upon the joint configuration. Another way to tackle the problem is to consider the stress distribution along the centre of the adhesive (i.e. on the segment EF, as depicted in Fig. 2.3a) instead of the adhesive-adherend interface [49]. At these points beyond a certain mesh density, convergence can be achieved. Nevertheless at these points the stress in not maximum and it can be more accurately described as an average stress.

Another way to assess the strength of adhesive joints is using methods based on fracture mechanics. The stress singularities at the corners of the adhesive region is studied without considering an actual stress value, but the severity of the stress field close to it. Linear elastic fracture mechanics (LEFM) is historically the first of these methods. It is based on the definition of stress intensity factor (K) which is the multiplying factor of a predefined stress field having a singular point with a order of magnitude $1/\sqrt{r}$ at the crack tip (where r is the distance from the crack tip). However, whereas this method works well for cracks in isotropic materials, the stress singularities at inhomogeneous interfaces do not generally respect the stress field assumption. Another relatively recent method defines generalised stress intensity factors at the corners of the

adhesive area. This theory assumes the stress field at the bi-material interface corners can be expresses as the summation of several stress function, each one of those converging to the asymptote with a different power exponent[50–52]. The Chauchy's stress tensor at the corner is defined as follows:

$$\sigma_{ij} = \sum_{k=1}^{\infty} \left(K_k H_{ij}^k(\Phi) \xi^{-\lambda_k} \right) \tag{2.1}$$

Where, $H_{ij}^k(\Phi)$ are shape functions the depends on the angle Φ, as depicted in Fig. 2.3b, ξ is a non-dimensional radial distance from the singularity $\xi = r/h$, K_k are the generalised stress intensity factors and λ_k in the order of magnitude stress intensity factor. This latest parameter can be interpreted as a measure of the strength of the singularity. However, the criterium to evaluate the critical generalised stress intensity factor should take into account the severity of the stress singularity, to the contrary the critical stress intensity factor is usually calculated as the algebraic summation of all of them.

Contrarily to other fracture mechanics based, generalised stress intensity factor method does not need of any crack: the joint is assumed to be perfectly bonded. Nevertheless, when a disbond crack starts propagating this method is inapplicable and other techniques oriented to calculate the strain energy release rate (SERR) of the crack (such as the crack extension method virtual crack closure technique (VCCT) [53]) becomes more effective.

The VCCT uses the nodal forces of the element at the crack tip and the opening displacements of the first element on the crack wake to calculate the strain energy released by the system. The SERR is calculated by dividing the energy by the crack increment Δa as follows:

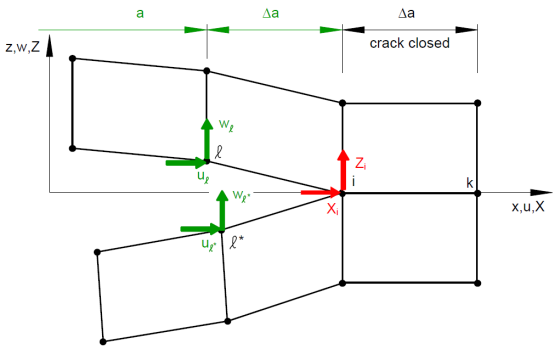

Figure 2.4: Stress concentration points of adhesive bonded joints.

$$G_I = -\frac{1}{2\Delta a} Z_i (w_\ell - w_{\ell^*})$$
$$G_{II} = -\frac{1}{2\Delta a} X_i (u_\ell - u_{\ell^*}) \tag{2.2}$$

Where G_I and G_{II} are the respectively the mode I and mode II SERR, X_i and Z_i the nodal forces and w_ℓ, u_ℓ, w_{ℓ^*} and u_{ℓ^*} are the displacements of the nodes on the crack wake, as depicted in Fig. 2.4. For delamination in laminated composite materials where the failure criterion is highly dependent on the mixed-mode ratio and propagation occurs in the laminate plane, the VCCT has been most widely used for computing energy release rates because fracture mode separation is determined explicitly [54]. However, this method is suitable to evaluate the propagation of

an existent crack only and it becomes reliable after the crack reaches a certain extension. Adhesively bonded joints shows typically an unstable crack propagation, this means that after the crack onset, this propagates rapidly to the complete failure of the joint.

The use of damage mechanics methods attempt to solve the problem of studying incipient delamination cracks: a material damage criterion is used to determine the damage initiation, a damage parameter is defined and used to reduce the material properties and finally a fracture criterion is employed for material failure (i.e. crack propagation). The damage variable can be regarded as measure of the defect density. This variable has also constitutive equations for evolution, written in terms of stress or strain which are used to determine the initiation of cracks [55]. Using this method, damage initiation and propagation can be evaluated at any place, however, for adhesive bonded joints the damage usually follows a foreseeable path.

Delamination/disbond on composite bonded joints can be studied evaluating the damage only at interface elements saving large computational time. This is the concept pursued by cohesive zone modelling (CZM). These interface elements are usually based on traction-separation law (TSL) which is intended to address the three aforementioned requirements of damage mechanics: (1) to provide a damage initiation criterium, based on the stress at the interface, (2) to define a damage parameter, used to decrease the element stiffness, and to furnish a fracture criterium which is met when the damage parameter (D) reaches a critical value (typically $D = 1$). A full review of cohesive zone modelling and its application for composite joints is reported in Sec.2.4

2.2 Through-thickness reinforcements

When designing conventional composite joints, either bolting or bonding show low load transfer efficiency. For the former it is due to low resistance of composite to bearing loads, for the latter it is mainly due to stress concentrations at runouts, which result in delamination of adhesive layer. Adhesive joint strength is also limited by the interlaminar weakness of composites: the load is principally transferred by out-of-plane shear. Thus, increasing the adherend adhesion only is often insufficient; resistance to both adhesive disbond and interlaminar delamination need to be strengthened.

Through-thickness reinforcements enhance the laminate delamination resistance by a mechanism called bridging effect: when a delamination crack reaches the reinforcement, this starts shielding the crack tip by exerting a bridging force which lasts even after the crack propagated several millimetres inside. This bridging effect reduces the crack driving force, opposing further crack propagation and therefore increasing the delamination resistance. This mechanisms

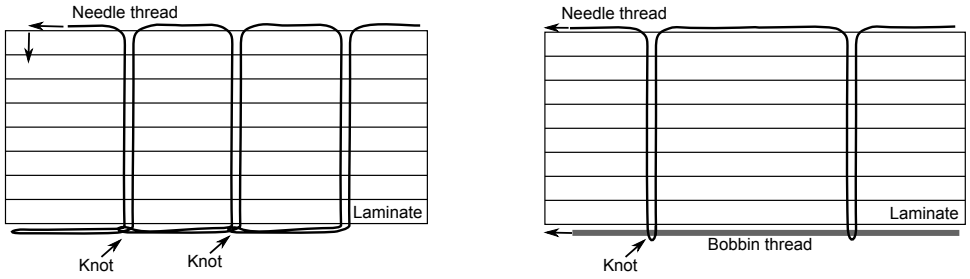

Figure 2.5: Stitching methods: (a) chain stitch, (b) modified lock stitch.

is called large-scale bridging (LSB) [56, 57].

The relationship between the force exerted by reinforcement and the cracked surface separation is called bridging law; the three components along directions of opening, sliding and tearing are usually referred to as mode I, II and III bridging laws. However, considering that for interlaminar delamination or debond mode II and III are both fracture modes under transverse shear stress (in the two perpendicular direction that defines the delamination plane), these are usually treated equally. Mode I bridging is also known as pin pullout and mode II and III as pin shear bridging.

Stitching, tufting and z-pinning are the most common TTR methods. Stitching involves the insertion of a dry thread (either made of carbon, glass or kevlar) into the laminate by a sewing needle. The needle thread is driven through the laminate and interlocked with the bobbin thread (chain stitch, depicted in Fig. 2.5a). Thread interlocking may also be achieved using only one thread, as shown in Fig. 2.5b for the modified lock stitch. The tension of needle and bobbin threads can be adjusted so that the knot forms either internally or on the outer surface (usually this latter case is preferable since it affects the laminate properties the less). Stitching requires special tooling and access to both sides of the laminate. This latter requirement make this technique unsuitable for all those applications with limited access to the backing surface such as wing box.

Stitching technology is more commonly used for preform laminates rather than prepreg due to the high viscosity of the resin. Manufacturing preform laminates ensures higher productivity (the needle can be driven into the laminate with no harm) and lower damage of laminate fibres, which strongly improves the laminate mechanical properties. [58]

Tufting uses a similar insertion technique to stitching, but it is a one-side access process. As for stitching a needle is used to push the yarn through the laminate, but no interlocking is realised on the outer surface; the needle is simply withdrawn leaving a free loop of the yarn. The friction between laminate preform and thread allows the needle to slide away leaving the tuft in position. Tufting can significantly increase the resistance to propagation of

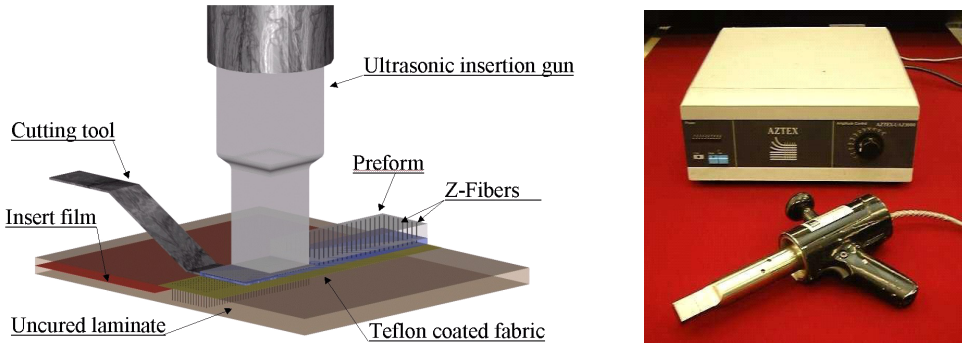

Figure 2.6: (a) Schematic of the z-pin insertion process. (b) Picture of the ultrasonic gun for z-pin insertion.

delamination cracks as well as the compression after impact performance of composite laminates [10], however, the dimension of the resin rich areas and the damage of laminate fibres strongly depends on the dimension of needle, used for the tuft insertion process.

2.2.1 Z-pinning

Z-pinning is a technology used to improve fracture toughness, delamination resistance and impact damage sensitivity of composite laminates, and also to improve ultimate strength and energy absorption of bonded composite joints. This technology involves the use of through the thickness reinforcements (TTR), made either of metal or reinforced plastic, to increase the out-of-plane properties of composite laminates. The insertion is performed on uncured laminates with an ultrasonic gun. Ultrasonic gun vibrations produce a localised heat of the laminate which reduces the resin viscosity and facilitates the pin insertion. Z-pins are commercialised in preforms which are placed over the laminate to be reinforced and squashed under the pressure of the gun. A schematic of the z-pin insertion process is depicted in Fig. 2.6a. In Fig. 2.6b a picture of the insertion gun.

Z-pinning is a relatively low-cost process and applicable to pre-preg laminates [8]. Z-pin insertion affects the in-plane mechanical properties of composite laminates, e.g., a 10 to 15 per cent loss of in-plane mechanical properties is found in pinned laminates. However, the out-of-plane stiffness is significantly increased by 25%. When delamination crack propagates, z-pins act as through-thickness reinforcements that provide bridging traction forces increasing the interlaminar toughness.

2.2.2 Energy balance during crack bridging

When a delamination crack is forming and then propagating over a bonded interface, the energy balance under the bridging effect of TTR can be written as follows. Let be da an infinitesimal extension of the crack length, the strain energy release rate G can be expressed as:

$$G = -\frac{d\Pi}{da} = \frac{1}{B}\left(\frac{dW}{da} - \frac{dU}{da}\right) \tag{2.3}$$

where d , dW and dU are respectively the increase of the potential energy, work done by external force and elastic strain energy of the system, and B the width of test specimen. The critical strain energy release rate (G_C^{total}) required for unit crack extension in TTR laminates can be regarded as the sum of two contributions: the material intrinsic fracture toughness needed for creating new crack surface (G_C)and the increased energy dissipation rate due to bridging effect of the reinforcement (G_C^{TTR}) , Eq. (2.4):

$$G_C^{total} = G_C + G_C^{TTR} \tag{2.4}$$

According to the Griffith theory [59], fracture occurs when:

$$G > G_C + G_C^{TTR} \tag{2.5}$$

Fracture toughness of unreinforced laminate (G_C) is a material property, but the energy dissipation rate due to the pins (G_C^{TTR}) is a material-structure attribute that depends also on the pin geometry and insertion density, as well as the crack opening displacement. G_C^{TTR} is the energy absorption of the TTR during the failure process (usually either rupture under tensile strain for stitching or frictional pullout for tufting and z-pinning). G_C^{TTR} can be calculated by:

$$G_C^{TTR} = \frac{1}{B} = \frac{d\left(\sum_i \int P_i(u_i)du_i\right)}{da} \tag{2.6}$$

where P_i is the bridge force exerted by an active reinforcement in the crack wake and (u_i)the crack opening displacement at its respective location. For a fracture process such as in-plane fibre bridging characterised by having a crack wake bridging area that is smaller than any other specimen dimension, the delamination suppression mechanism is called small scale bridging (SSB). For stitched, tufted and z-pinned laminates, due to the pin frictional pullout process, the bridging length is usually of the same order of the laminate thickness resulting in the large scale bridging (LSB) mechanism. Some researchers consider the bridging effect provided by the through-thickness reinforcements to have a constant bridging length and therefore, can be calculated by averaging the energy dissipation rates over the reinforced area [60, 61]. However,

others believe this assumption being more appropriate for SSB than LSB; in the latter case the pin bridging force varies during the fracture process and thus, is not a constant value. Therefore, enhanced fracture toughness should be evaluated by accounting for the two energy contributions separately [57].

2.2.3 Knockdown of in-plane properties

The increase of delamination resistance does not come without costs: z-protrusion insertion into the laminate plies causes a considerable fibre misalignment, as shown in Fig. 2.7a. Z-pin insertion deflects the fibres and creates a void. During the curing cycle this void is filled with resin, forming a typical eyelet resin rich areas elongated in the fibre direction. The dimension of this area is proportional to the z-pin diameter (usually 4-6 diameters for carbon fibre laminates).

The fibre misalignment reduces the in-plane elastic properties of the laminate and promotes micro-buckling under compressive load. Effective three-dimensional elastic constants and knockdown properties of laminate reinforced by TTR have been studied considering the periodicity of the structure by Dickinson et al. in [62]. It was found that adding a few percentage of TTR has a small negative effect on the in-plane moduli (less than 10%), but allows to increase sensibly the transverse modulus (up to 60%). Grassi [63] modelled a representative unit cell (RUC) of a CFRP laminate reinforced by a 2% pinning , predicting a reduction of 7-10% in equivalent Young's modulus in the fibre direction. The fibre realignment was modelled modifying the material orientation of the laminate close to the pin. The boundary conditions applied were to constrain the opposite surfaces of the unit cell to remain parallel (plane-remain-plane). This was found to over-constrain the RUC predicting a higher elastic modulus [64].

Xia et al. developed a FE model using periodical boundary conditions that allows the RUC to deform in the configuration of minimal strain energy [64, 65]. This was achieved assuming two opposite surfaces of the cell to have the same deformed shape (periodical deformation u_i^*) and an average strain component($\overline{\epsilon_{ik}}$):

$$u_i = \overline{\epsilon_{ik}} x_k + u^*, \quad u_i^* \text{ periodical} \tag{2.7}$$

The subscripts i and k indicate respectively the displacement component and the RUC outer surface direction whose average strain is calculated of, as shown in Fig. 2.7b. One of the major achievement was that, using periodical boundary conditions, it is possible to satisfy not only the boundary displacement periodicity but also boundary traction periodicity.

Studying the knock down of laminate properties is very important for applications where z-pins are used to improve the fracture toughness of the laminate. However, when applied to joints, the loss of elastic in-plane properties

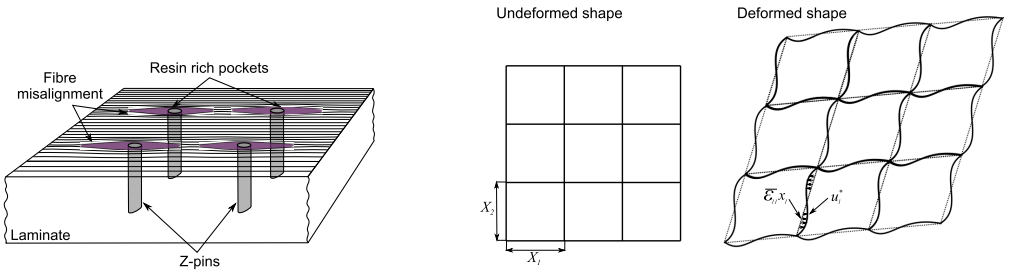

(a) (b)

Figure 2.7: (a) Fibre misalignment induced by z-pin intertion, (b) periodic boundary conditions for the study of a representative unit cell.

is confined to the overlapping region, which continues to be stiffer than the adherend, either being made of metal or laminate. The increase of compliance of the structure will be therefore negligible. Nevertheless, the reduced bearing strength of the laminate surrounding the pin will affect the bridging force that the z-protrusion carries.

2.2.4 Single pin bridging law

Failure mechanisms of the pin

When loaded in mode I (pullout), failure process of z-pins involves three phases; (1) stretching of tread, (2) progressive disbonding from surrounding laminate and (3) sliding out. The main mechanism which introduces axial stress in the pin is transverse shear. The cohesion between fibre and laminate is initially guaranteed by chemical bonding and then, after the failure of the connection between pin and laminate, by friction resistance. This, in turn, is due to the cure residual stress with induced a compressive state at the pin/laminate interface.

Z-pin pullout occurs asymmetrically: one side of the pin remains anchored to the laminate and only the other slides out. Usually the side having the chamfer head to facilitate insertion is the one that more likely fails. The progressive disbonding phase starts as soon as the maximum shear stress reaches the shear strength of the bond interface [66]. The average shear stress (τ_a) at debonding and the maximum elastic pullout force (P_{max}) will be:

$$\tau_a = \frac{1}{h^*}\int_0^{h^*} \tau(z)dz, \qquad P_{max} = \pi d h^* \tau_a \tag{2.8}$$

Where τ_z is the shear stress acting over the fibre surface, h^* is the pin embedded length and d is the fibre diameter. The pin pullout phase takes place

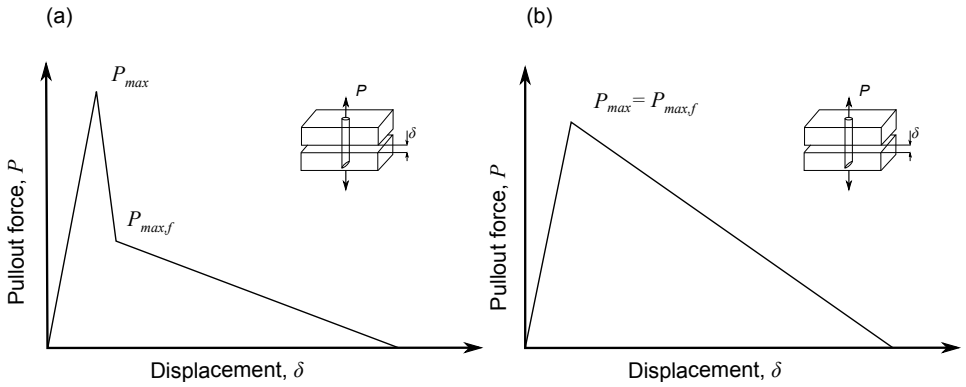

Figure 2.8: Pin pullout force vs. crack opening displacement showing two characteristic behaviour of z-pin pullout: (a) low friction resistance, (b) high friction resistance.

immediately after the disbond onset. The average friction stress τ_f and the maximum friction force at the beginning of the pullout phase are respectively:

$$\tau_f = \frac{1}{h^*}\int_0^{h^*} \tau(z)dz, \qquad P_{max,f} = \pi d h^* \tau_a \tag{2.9}$$

Fig. 2.8 shows two typical pin pullout behaviours observed from experiments [67–69]. First, the pullout force will reach its maximum, at which point disbond occurs at the pin/laminate interface. After this point there could be a sudden load drop before the frictional pullout phase (Fig. 2.8a) depending on the friction resistance that can be represented by the ratio of τ_a/τ_f. Force drop occurs if the ratio is greater than one; and the higher the ratio, the larger the drop. If $\tau_a/\tau_f \leq 1$, then there is no sudden force drop and the force vs. displacement curve has a characteristic bilinear shape (Fig. 2.8b).

When loaded in mode II z-pin shows much more complicated behaviour. Z-pin failure process can be divided into three phases: (1) pin has an initial elastic response, (2) pin then ploughs into the laminate (this is particularly pronounced for the unidirectional laminates), and (3) pin either ruptures under tension or is pulled out [70, 71]. The shear stress transfer is initially due to the mechanical bond and then to the friction resistance caused by the contact stresses at the pin/laminate interface. The shear stress at the pin/laminate interface is the main mechanism putting the pin under axial stress. Before applying mechanical load, the initial normal stresses between pin and laminate are compressive due to the mismatch of the coefficients of thermal expansion; this contact stress will then increase when the pin is pulled out due to the laminate shear deformation. The laminate supports the pin laterally causing large deformation in the surrounding resin matrix, which can cause a plastic deformation of the resin [72]; subsequently, due to the high circumferential tensile stresses, the laminate eventually fractures allowing the pin to plough into it. Transverse stresses on the pin exerted by the surrounding laminate make the pin subject to bending deformation during the elastic response phase. When

the transverse shear strength of the pin is exceeded the pin splits internally in several threads, loosing bending stiffness and increasing shear deformation. From this point onwards the pin behaves like a truss (subject to axial stress only) and subject to large rotation at the fracture plane. Depending on the pin geometry and laminate stacking sequence, the pin can either be pulled out resulting in a progressive and monotonic reduction of bridging force, or rupture with a sudden load drop [68]. Experimental tests have also shown that, when the pin is being pulled out, usually only one side of the pin slides out while the other side remains anchored to the laminate.

Experimental methods for measuring bridging laws

The bridging law of a single reinforcement can be measured experimentally either by using specially designed test specimens, containing a single reinforcement [68, 73, 74] or an array of those [75], or by using the inverse calculation method [56, 76]. The most commonly used test specimen consist of a single reinforcements inserted into a laminate block containing a central crack. The central crack is realised using a thin non-stick film (typically polyamide or PTFE). Pullout test is arranged gluing the top and bottom surfaces of the sample glued to two T-shaped metal grips, as depicted in Fig. 2.9a. The shank of each grip is held by the jaws of testing machine which apply the pullout load [68, 73]. Tan et al. used similar configuration called in "interlaminar tension test" to investigate the mode I bridging law of single stitch fibre [74]. In this configuration the artificial crack does not extends to the whole laminate surface: two lateral cuts facilitate the separation of the two laminate halves. However, this second configuration is more complex, therefore the first one is usually preferred.

Due to manufacturing defects such as pin insertion angle or resin rich area dimension, single pin test usually show a considerable scatter of experimental data. A multiple pin test can be used to reduce this variability: for instance this technique was used by Dai et al. [75], employing a 3x3 pin array configuration to study the bridging law for a z-pin in carbon fibre/epoxy laminate. Nevertheless, one of the major advantages of the single pin configuration is that the same specimen can be used for both mode I and II test. Whereas the pin-to-pin interaction in pullout test can be considered negligible, this is not generally true for shear test, therefore, for test campaign addressed to a complete characterization of the reinforcement (which comprises both mode I and II testing), the single pin configuration is still the most desirable.

Cartiè et al. used a specially designed testing rig to measure the bridging force of single pins in mode II [68]. The testing rig comprises two shear loading grips, each one of those holding one half of the test specimen. The shear relative displacement of the two laminate halves is imposed at the delamination plane.

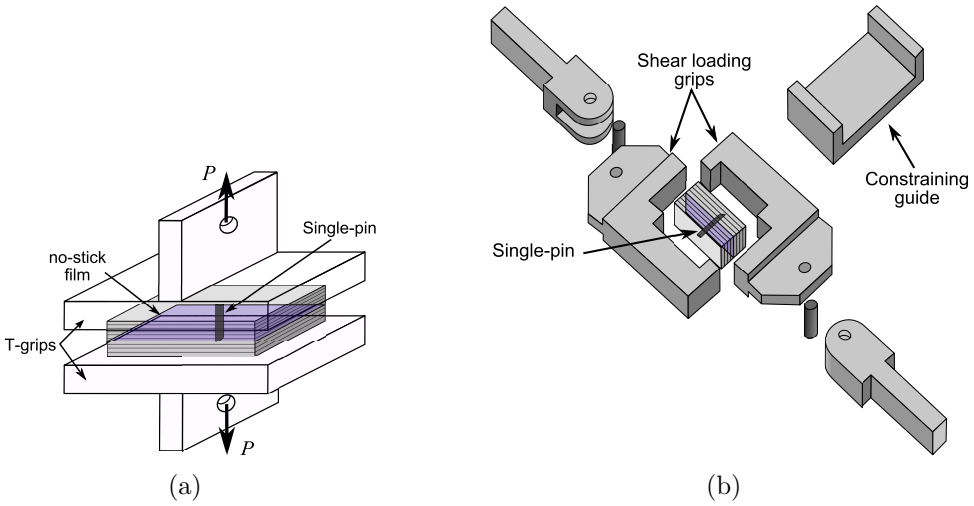

Figure 2.9: Single pin tests for measuring bridging laws: (a) pullout loading, (b) shear loading.

The test rig allows to perform the test either locking the opening or leaving the top and bottom surface to separate out of the plane. A schematic of the testing rig used in depicted in Fig. 2.9b.

Multiple pin configuration has been used by Cartiè et al. in [77]. This new form of mechanical test was designed to investigate the pullout of pins from thick laminates. The test rig imposed shear loading to a block of laminate containing several pins. The limitation of the pin number is dictated by the load cell capability used for the test. It was found that for mode II the crack opening constraint and the failure modes of the Z-pin depend on the interaction between the testing fixture the z-pin themselves.

By using either single or multiple pin test methods, a direct measurement of the bridging law is taken. Since the load carrying capability of the reinforcement was found to be affected by the testing fixtures, a different technique has been used in [76] and Massabò and Cox in [56]. An inverse calculation method was used to deduce the bridging forces of stitches by testing a mode II delamination test of stitched laminates (ENF configuration). This was done using a model of the test specimen and varying the bridging force in order to fit the experimental data. However, the bridging force so calculated is accurate for that specific application, but it might not be representative for different loading conditions. What's really necessary is a single-pin model.

Existing models for evaluating bridging laws

Although experimental testing is of crucial importance for understanding the behaviour and fracture mechanisms, as well as for measuring the basic proper-

ties for the reinforcement itself, modelling capability is fundamental for evaluating the influence of geometric parameters on the bridging law generated by the reinforcement and how these in turn affects the structural response of joints. Modelling enables estimating the effects of different pin configurations without the need of expensive and time-consuming test campaigns.

Current available models are either analytical or numerical (using the FE method). First pullout models of through-thickness reinforcements were developed using the existent knowledge on fibre composite laminates. The bridging effect of long fibres on the mode I matrix crack on fibrous composites was studied in [78, 79]. It was found that when a crack forms in the matrix, the load is transferred from matrix to fibres through shear stress, opposing the crack to growth further. The bridging process involves fibres debond and pullout. It was demonstrated that a necessary condition for having fibre bridging is the ultimate strain of fibres being larger than the matrix. Jain and Mai developed a simple shear lag analytical model for predicting the pullout force of stitch reinforcements [80]. The model was able to predict the bridging force of both interconnected and independent stitches by varying the model boundary conditions. Is was shown that independent stitches are able to absorb much more energy that interconnected ones due to the friction resistance during pullout.

A three-dimensional FE model has been used by Meo et al. to study the pullout of a single TTR under quasi-static conditions and in the presence of frictional contact between the fibre-matrix interface [81]. A tailored constitutive equation for the contact shear stress at the interface along the TTR axis was used to reproduce the pullout behaviour of the pin. When a maximum shear stress (τ_{max}) was exceeded the two parts were assumed to slide each other and the friction stress at their interface was imposed equal to τ_{max} regardless the value of compressive stress at interface. However, this insensitivity of the dynamic friction stress to contact force does not seem to have any physical background.

Allegri and Zhang used an analytical framework to develop a constitutive model of Z-fibre response under mixed mode loading condition. This was achieved by assuming the Z-fibre being a perfectly rigid body embedded in an orthotropic elastic foundation representing the surrounding composite laminate. Z-fibre behaviour was than idealised by considering two distinct stages of the pin response: pure elastic deformation of Z-fibre before it debonds from the base laminate and the progressive pullout of Z-fibre [82].

Cox and Shidhar developed a model for inclined through-thickness reinforcements accounting for the matrix deformation effect [83]. Cox subsequently improved the model to include the snubbing effect of z-pin pullout [84]. The model accounted for two possible ultimate failure of the pin: rupture under tension and pullout of the laminate. The plastic deformation of the pin close to the delamination plane makes the pin axis to orient towards the load direction as depicted in Fig. 2.10a. The resistance of the laminate to ploughing was

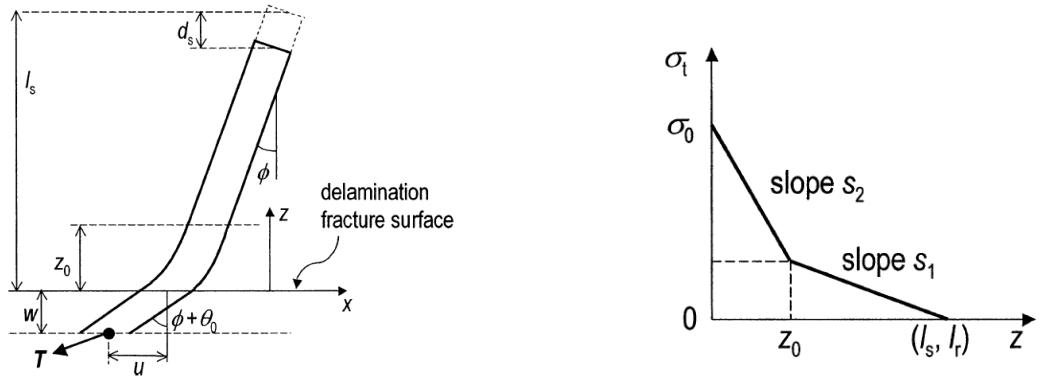

(a) (b)

Figure 2.10: (a) Cox's single pin model, (b) typical bi-linear shape of the axial stress along the pin axis as consequence of the two-friction assumption.

idealised as an elastic/perfectly plastic foundation. The hydrostatic pressure ahead of the pin deflection is assumed to increase friction resistance in the area close to the delamination plane (snubbing effect). To account for this effect a two-friction model was used. Simple shear lag theory is used to calculate the axial stress (σ_t) on the pin along its axis, z:

$$\frac{\sigma_t(z)}{dz} = -\frac{s \cdot \tau(z)}{A_t \cos\Phi} \tag{2.10}$$

Where $\tau(z)$ is the axial shear stress at the interface (accounted as constant all round the circumference), s is the pin circumference, A_t the cross sectional area and Φ the shear deformation of the pin as defined in Fig. 2.10b. The term $s/\cos\Phi$ accounts for the variation of pin circumference due to the shear deformation. Integrating Eq. (2.10) the axial stress along the pin axis can be calculated, an example is shown in Fig. 2.10b. It is worth noticing than the two different slopes of the curve are a direct consequence of two-friction model.

The effect of metallic z-rods under bending was also modelled by Tong and Sun [85, 86]. The z-rod was modelled as an elastic beam supported by an elastic/perfectly plastic foundation. The rod's lateral deformation (W_Z) in function of the through-thickness coordinate (ξ) was given by the solution of the following differential equation:

$$E_f I_f \frac{d^4 W_Z}{d\xi^4} + q(\xi) = 0 \tag{2.11}$$

Where $E_f I_f$ is the bending rigidity of the rod and $q(\xi)$ the lateral force that the laminate opposes to the pin deformation. The relative rotation of the two laminate blocks containing each half length of the rod was also accounted.

However, the model did not include a failure model for the rod, which is considered to behave elastically even at large deformations.

Plain and Tong developed an analytical model for stitch reinforcement under mixed mode loading conditions and subjected to large rotation [72] and very large rotation [87]. The stitch is treated as a rope supported by a plastic foundation, after the punch strength of the laminate is exceeded, the stitch ploughs into its support. The snubbing effect was included, but only the semi-circumference of the stitch in contact with the laminate was assumed having friction. As the stitch deforms, the embedded length of the stitch in assumed to change due to the stitch pushing into or pulling out of the matrix.

A plane strain FE model was developed by Cui et al. for evaluating the z-pin bridging force under mixed mode delamination. The splitting and rupturing of the z-pin were simulated by a cohesive zone model [88]. The pin was modelled as a bunch of threads connected each other by a cohesive interface. The number of cohesive interfaces was arbitrary set high enough to be able to catch the loss of bending rigidity of the pin. Pin debond and progressive pullout was simulated using a taylor friction coefficient which linearly varies from zero (when interface is still bonded) to one when the pullout phase starts over.

2.2.5 Models of TTR reinforced laminates

Once the pin bridging law is determined, no matter if calculated through a single-pin model or measured experimentally, the global behaviour of through-thickness reinforced laminates can be modelled. Whereas the three-dimensionality of the structure sometimes is important, in most of the cases the width dimension is omitted and the structure is modelled as two dimensional, in a plane strain stress state. Any existing crack is therefore assumed to run straight through the entire width of the specimen. Two main approaches are commonly used to account for the effect of TTR: (1) individual bridging forces are averaged over the bridging area and the average traction force is treated as function of the local crack opening displacement; (2) each pin traction is treated as a concentrated force acting at the pin location and governed by a nonlinear law (in most of the cases bi-linear). The two modelling approaches are illustrated in Fig. 2.11

Averaged bridging forces

Jain and Mai developed an analytical model of a stitched double cantilever beam, using the Euler-Bernoulli beam theory [80]. A cohesive law was used to model the bridging traction as function of the crack opening displacement. This cohesive relation was calculated multiplying the stitch bridging force by the relative stitch density. Using this approach the stitch force is smeared

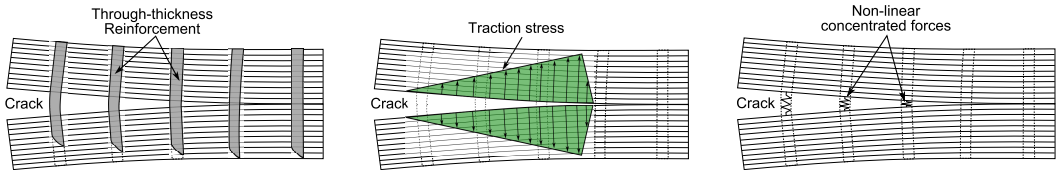

Figure 2.11: (a) Through-thickness reinforcements bridging a delamination crack, (b) bridging forces smeared over the bridging area, (c) TTR bridging modelled as concentrated forces.

evenly over the bridging area. An inverse calculation method was used by Robinson and Das to evaluate the bridging traction exerted by z-pins over the bridging area of DCB test specimen. The initial load carrying pin stiffness was assumed infinitely high and the bridging traction was therefore idealised as a linearly decreasing function of the crack opening displacement. The beam theory was used to calculate the sectional bending moment of the DCB arms and fracture was assumed to occur when a critical bending moment was exceeded. Byrd and Birman studied the effect of z-pins on the strain release rate, fracture and fatigue in composite laminates [89]. A DCB specimen was modelled as two cantilever beams connected over the bridging area by elastic foundation, mimicking the pin forces.

Ming and Cox used equivalent continuous bridging springs acting on the delamination fracture surface to model the effects of through-thickness reinforcements in enhancing the fracture toughness of curved laminar structures [90]. Two stages of delamination were identified: an initial continuously increasing delamination resistance and a steady crack propagation. The transition point between these two phases was called AKC limit (after Aveston, Cooper and Kelly, who first studied crack bridging in brittle matrix composites [79]). The mode II delamination of a stitch reinforced ENF test specimen was modelled by Massabò et al. using an analytical framework [76]. The bridging action of the stitches is deduced, using the inverse calculation method, from both crack profile measurements and load-displacement curve of the ENF specimen. The bridging force is smeared over the bridging area and the so obtained transverse shear stress is treated as a function of the relative shear displacement between the two crack surfaces. The effect of stitches was evaluated considering the superposition of two sub-problems: (1) a beam without delamination and (2) a beam with surface traction mimicking the effects of stitches. The shear displacement at stitch failure defines the ACK limit. After this limit is passed the equivalent fracture toughness of the laminate reaches a steady state value.

Concentrated bridging forces

The beam theory was used by Ratcliffe and O'Brien to predict delamination growth in DCB specimens reinforced in the thickness direction with z-pins [91]. The specimen arms were modeled as cantilever beams supported by discrete springs governed by a bi-linear damage law. Closed-form solutions were developed for specimens having an increasing number of pins. The solution was then generalised for an infinite number or reinforcements.

The mode I interlaminar fracture of carbon/epoxy composite laminates was studied numerically by Grassi and Zhang [57] using the FE method. Enhanced delamination resistance of a z-pin reinforced DCB specimen was simulated using a plane strain model. The crack advancement was calculated using the VCCT method and the pin bridging force simulated by non-linear springs. The bridging law (i.e. force vs. displacement) provided by a single pin was multiplied by the number of pins over the specimen width to calculate the spring constitutive equation. This approach has been subsequently used to simulate the structural response of structural joints [92]. A similar approach was used by Allegri and Zhang to study the benefit of z-fibre pinning to improve the bonding strength of composite joints [82]. A three-dimensional FE model was developed using shell elements for the laminate and spring elements, governed by a non-linear damage law, for the pin bridging. The model was used to simulate the structural behaviours of a conventional T-joint and a novel cruciform joint. More recently a multi-scale modelling approach has been employed to simulate the structural behaviour and fracture of a T-joint [93]. The pin bridging force at interface between the web and the skin is modelled by non-linear springs, governed by a trilinear relation.

The delamination toughness of z-pinned laminates was studied by Yan et al. with a similar numerical approach [94]. In their model the z-pin pullout process was simulated by the deformation of a set of non-linear springs distributed over the laminate thickness. A plane strain FE model was developed to simulate the crack propagation of a z-pin reinforced DCB specimen. The crack growth was calculated using a critical crack opening displacement (COD) criterion.

The mode I interlaminar fracture in z-pin reinforced composite laminates is simulated using a cohesive zone model by Dantuluri et al. [61]. A bilinear cohesive traction-separation law is employed to model the fracture of the unreinforced composite and nonlinear spring elements to simulate the pin bridging force. A second model was also developed to further reduce computational efforts. The model used an equivalent distributed cohesive model as a substitute for the discrete nonlinear spring elements.

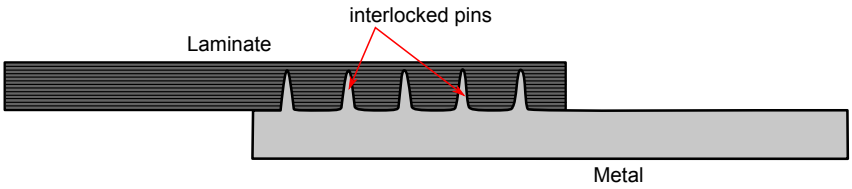

Figure 2.12: Sketch of pin interlocking reinforcement technique.

2.3 Hybrid metal-composite joints by pin interlocking

Improving the adhesion between two adherends by producing on the metallic surface physical features that stick into the laminate is a recently developed technique called surface structuring. Bonding strength and toughness are improved by bridging mechanisms analogue to through-thickness reinforcements. Moreover, for joint structures, the laminate stiffness reduction due to protrusion insertion should not be accounted as a real drawback: on the contrary this brings an actual benefit to the hybrid interface by better distributing the shear stress. Although several shapes of the protrusion may be used to obtain the goal, researchers' attention focused mainly on pin-shaped features, produced vertically or with an angle on the metal surface. This is the concept of pin interlocking; Fig. 2.12 shows a sketch of the reinforcement technique. Metallic pins can be manufactured using several techniques, among these, the most interesting ones for industrial applications have to allow high productivity low-cost manufacturing. Some of the most promising technologies are reviewed below.

2.3.1 Pins fabricated by additive layer manufacturing

Additive layer manufacturing is a modern fabrication process that can use a wide range of materials (such as titanium, stainless steel or aluminium)to be grown from a fine powder to a final product. Three dimensional parts are built up in two-dimensional layers as little as 0.05 mm thick. Additive manufacturing (sometimes also known as 3D printing [95–97]) offers great flexibility and opportunities for creating new products at low cost. Recent development of laser processing [98–100] and electron beam melting [101, 102] have contributed to enhance the industrial interest on this technology.

A powder nozzle additive layer manufacture (ALM) technique was used to produce a hybrid titanium/CFRP pin reinforced double lap joint. It was found that the laser power was an important parameter to determine the pin shape, particularly the laser power needed to be diminished during the pin manufacture in order to obtain a cylindrical pin. It was also shown that increasing the

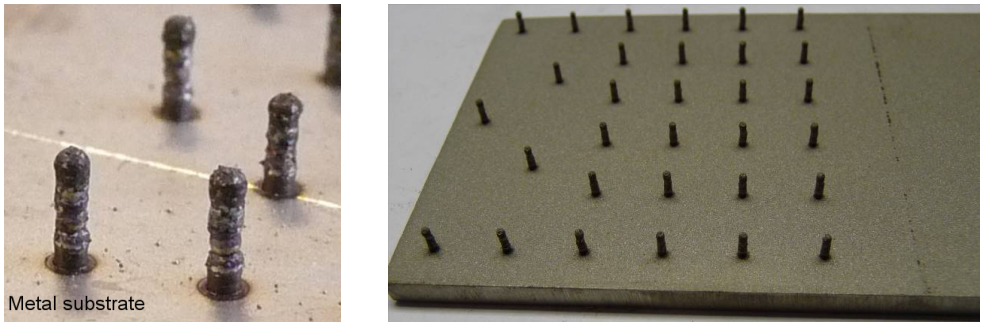

(a) (b)

Figure 2.13: (a) Metal pin reinforcements manufactured by ALM technology, (b) pin arrangement used to reinforce an hybrid double lap joint.

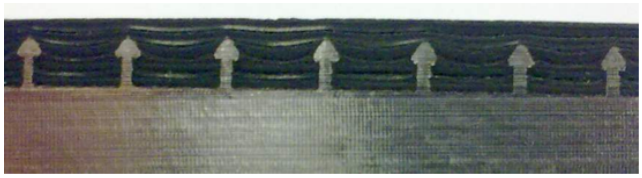

Figure 2.14: Cross section of a hyper joint along one pin row.

metal substrate temperature increases the adhesion of the pin.

An ALM technique has been used to manufacture an arrow-shaped pins to increase the mode I delamination resistance. The pointed head on the pin was designed to facilitate the laminate insertion, the arrow-head to oppose pullout after consolidation. This technology was called "hyper joint". Fig. 2.14 shows a hyper joint section along one row of reinforcements. The good compaction of laminate and the absence of macroscopic defects around the pin can be noticed. The joint was demonstrated to have good compaction of the laminate. A 7x7 pin array specimen was tested in pullout showing good performance in bridging mode I delamination cracks.

2.3.2 Pins by Surfi-Sculpt

Surfi-Sculpt technology by TWI [103] that uses a power electron beam to create surface textures. This technique is applicable to a wide range of materials (e.g. aluminium alloys, steels and titanium), allowing the creation of a range of hole and patterns, which can be precisely controlled. This technology has been used to produce pin-shaped surface features. The material melted by the beam moves, in part, due to the surface tension generated by a temperature gradient created across the molten material surface. How the material moves and ultimately the shape of the features produced, can be determined by precisely controlling the beam path and speed over the surface [104]. A schematic

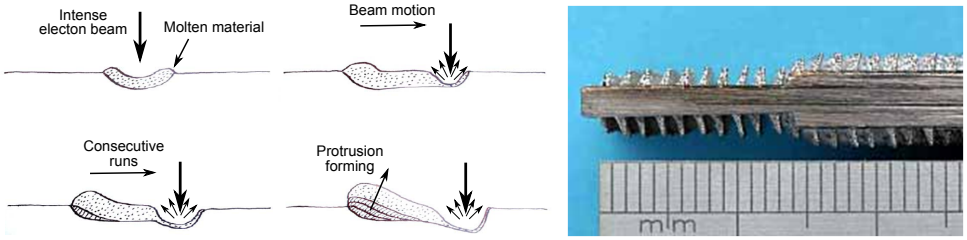

(a) (b)

Figure 2.15: Sulfi-Sculpt technology (a) schematic of the protrusion formation process, (b) a Comeld double lap joint.

of the process is depicted in Fig. 2.15a.

Surfi-Sculpt provides an attractive solution for the manufacture of composite to metal (Comeld) joints. The protrusions penetrate the fibres in the composite, preventing sudden bond-line failure from occurring. Tests revealed that Comeld joints absorbed twice as much energy before failure than control joints and displayed a more progressive and consequently detectable failure mode [105, 106]. Fig. 2.15b shows the outlook of the sulfi-sculpt surface feature used for the Comeld joint.

Guild et al. studied the effect of sculpted surface geometry on the stress distribution at the boned interface [22]. A multi-scale approach was used: the global strain deformation was extracted by a global model, then the stress distribution of the mostly loaded surface protrusion was evaluated by a local FE model. Wu et al. developed an element-free Galerkin method, based on the variation principle of the potential energy, with radial basis function interpolations to solve Comeld joints two dimensional stress distributions [23]. The stress distribution at the hybrid interface was been studied using a unit cell models with a single protrusion. These results were compared with an FE stress analysis of the joint showing the element free methods to provide an efficient, time-saving tool to study damage initiation of surface structured joints. Wu et al. further used the aforementioned model to optimise the protrusion geometry on the sculpted metal surface [24]. In the model was simplified considering that the damage onset always occurs at runout, thus the geometry was reduced to the two metal protrusions closest to the joint end.

2.3.3 Pins by Cold metal transfer (CMT)

Cold Metal Transfer is welding technology similar to MIG welding, but with the difference that weld zones remain considerably "colder" in the CMT than they would with conventional gas metal arc welding. The CMT process is based on short circuiting transfer, or more accurately, on a deliberate, systematic

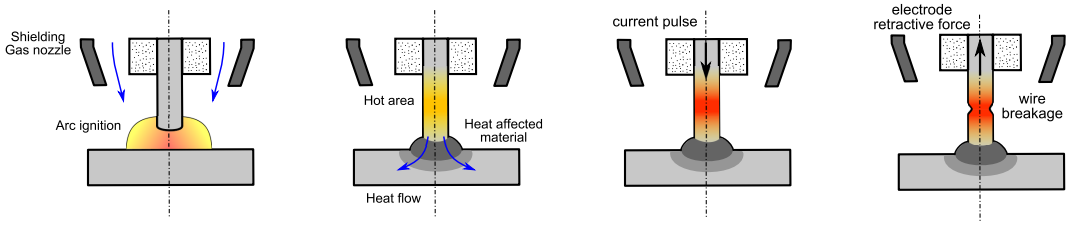

Figure 2.16: Schematic of CMT welding for the pin manufacturing process.

discontinuing of the arc. This method significantly reduces the arc pressure and minimises the electrode distortion while being dipped into the weld pool. The motions of the wire is integrated into the welding process and into the overall management of the procedure. Every time short circuiting occurs, power supply is interrupted and the wire retracted. The forward and back motion takes place at a rate of up to 90 Hz. The wire retraction motion aides droplet detachment during the short circuit [107]. The reduced thermal input offers advantages such as low distortion and higher precision. Benefits include higher-quality welded joints, minimal spatter, ability to weld light-gauge sheet as thin as 0.3 mm, as well as the ability to join both steel to aluminum.

CMT can be used to manufacture pin-reinforced hybrid metal composite joints. The pin-manufacture process is divided in four steps: (a) a first arc weld connects the electrode to the metal substrate, then (b) the circuit is opened, the power supply is cut and the wire is let cool down. (2) After a time delay of about 0.5-2 seconds, (c) the circuit is closed again letting the current pass. Temperature of the wire increases proportional to the resistance R, due to the Joule effect. The part of the wire closer to the metal plate has a larger mass to exchange heat with. The hotter spot is at about 3-5 mm from the metal surface. Finally (d) a combination of wire tension produced by the retraction force of the electrode and high temperature then cause the wire breakage [108]. A schematic of the process is depicted in Fig. 2.16, Fig. 2.17 shows pictures of the the welding process during the four aforementioned phases. The weld is shielded by a inert gas (composition of argon, helium and carbon dioxide). The grade of oxidation the heat affected area depends on the shielding gas compound: initial finding showed that the most relevant parameter is the percentage of carbon dioxide. High percentage of carbon dioxide increases the grade of oxidation embrittling the weld. However, low percentage of this gas is necessary to have a stable arc ignition.

The shape of the pin tip can also be controlled by the welding parameters (current, retraction force and time delays: (1) between arc and second current pulse and (2) between current pulse and retraction force). The most sensitive parameter for the pin shape is the time delay between current pulse and retraction force apply. The longer the material is let heat up, the larger mass of materials retouches from the electrode and goes making up the pin tip. Wether

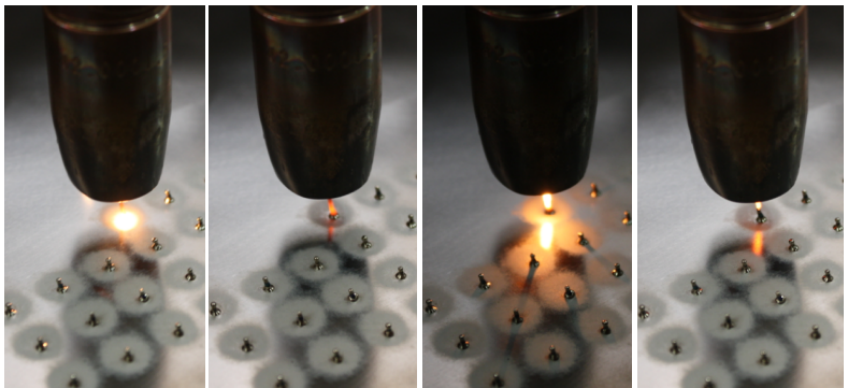

Figure 2.17: Photographs of CMT welding during the four phases of the pin manufacturing process.

a small delay produces a pike pin tip, a longer delay forms a ball head. After a critical size of the ball head diameter (about 1.5 times the electrode diameter) the material consolidation over the pin tip is no longer stable and the pin head deforms sideways.

Ucsnik et al. showed that the failure modes of the joint can vary from pullout to shear failure of the pin or a combination of the two, depending on the pin geometry. Whereas cylindrical pins promote pullout failure mode, ball-head pin tip increases the resistance of these from being withdrawn form the composite part. Pins therefore more likely fail in shear [21]. Fig. 2.18a shows the pin pullout failure of a double lap joint reinforce by cylindrical pins, Fig. 2.18b shows the quality of the pin reinforcements. Compared to cylindrical pins, ball-head pin reinforced joint showed higher strength (+40%) and energy absorption (+8%).

Joesbury el al. studied the structural performance of pin reinforced steel-CFRP double lap joints [109]. The joint configuration was similar to the one used by Ucsnik et at., but in this study the pins were embedded through the entire section of the laminate. It was found that the bondline failure was leaded by the yielding of the metal substrate. The joint strength was limited by the axial force the metal adherend could carry before having large yielding deformations. The pin reinforcements changed the failure mode of the joint from unstable to progressive debond, the energy absorption at failure was almost doubled.

2.4 Cohesive zone modelling

A cohesive relationship in modelling is a law that describes the progressive damaging of material, which gradually decreases its stiffness properties down to zero, when material final failure occurs. This relationship can be applied to

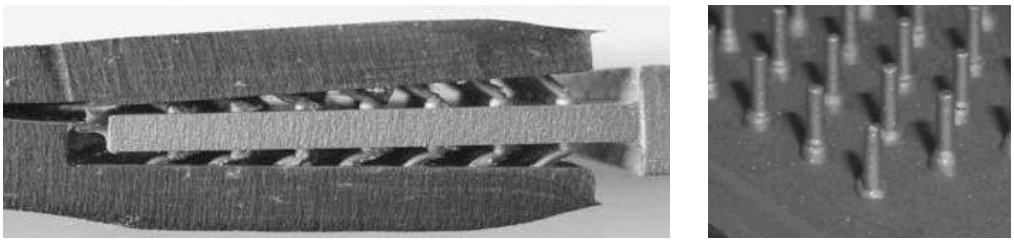

Figure 2.18: Example of a surface structured joint, (a) failure mode of a double-lap pin-joint, (b) particular of the pin surface features [21].

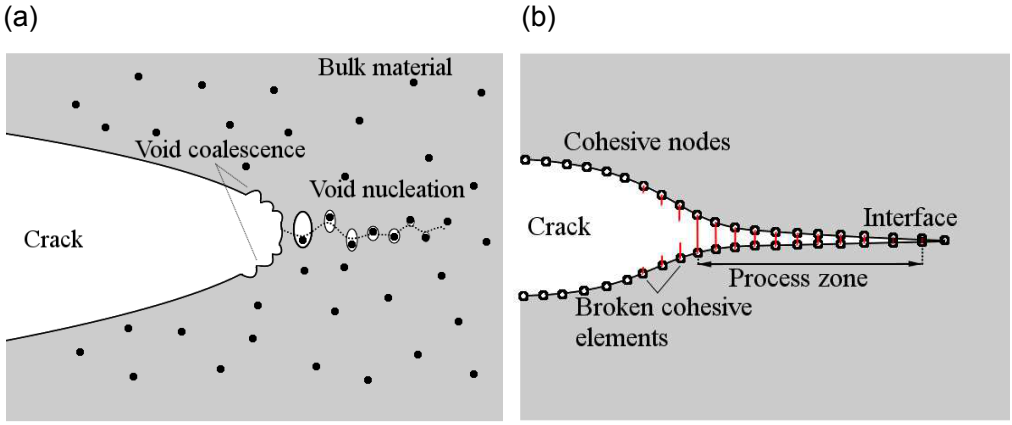

Figure 2.19: Microscopic processes that lead to material fracture: (a) Real case, (b) Process idealization [111].

model the bulk material fracture (continuum cohesive modelling) or only its separation (CZM). Using continuum cohesive modelling is possible to predict the fracture inside the bulk material by embedding a cohesive relationship in the material element formulation. In this way the fracture is allowed to move in any direction through the material. However this technique requires large computational efforts, which sometimes could be saved imposing the damage to initiate and propagate along well defined paths (as for CZM). Nevertheless , it worth noticing the for most of the engineering applications critical location usually known a-priori.

CZM attempts to model the material fracture by defining the traction between two initially bonded surfaces that progressively separate. The cohesive model is based on the premise that fracture is not simply the snap material failure, but several microscopic processes, such as void nucleation and coalescence, lead to a local and gradual decrease of material stiffness properties (Fig. 2.19). The area ahead of the crack tip where the interface progressively degrades is called process zone [110].

Dugdale [111] was the first one to apply a cohesive model for predicting the fracture of ductile material; a strip-yield force was introduced for preventing

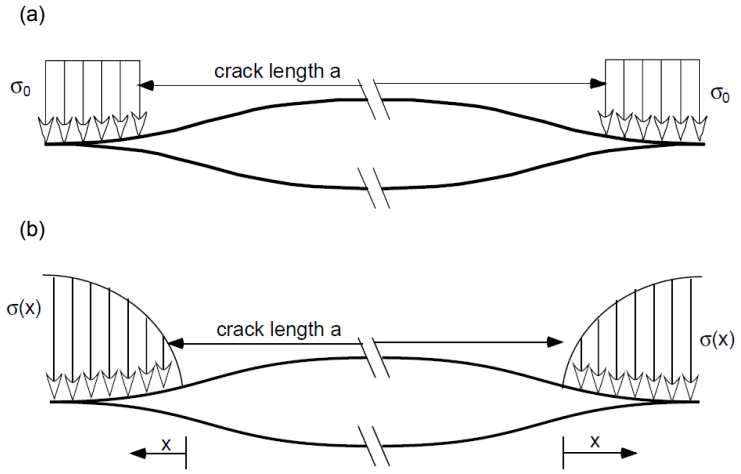

Figure 2.20: Cohesive zone models: (a) Dugdale's model, (b) Barenblatt's model.

a crack from extending, as depicted in Fig. 2.20a. The stress equal to the material strength was applied to the two separated surfaces, for a characteristic length (plastic zone). In this way the unrealistic occurrence of singularity at the crack tip was avoided. Barenblatt [112] develop a similar model with a cohesive law to account for the atomic lattices decohesion. In this way, the plastic zone was replaced by a process zone to account for void nucleation and coalescence, and other micro cracking processes (Fig. 2.20b). The first model using a cohesive law in terms of a traction separation law (earlier models a direct relationship between traction and distance from the crack tip was used) was developed by Hillenborg et al. [113] to study fracture behaviours of concrete.

The relationship between surface traction and separation is called traction-separation law (TSL), or also cohesive law. Several TSLs have been suggested in order to model different material classes. Fig. 2.21 gives an overview of frequently used shapes [110]. There is a dispute whether the TSL should start with a finite traction for a null separation or not. If the TSL starts from the axis origin, also a small stress would lead a separation; on the other hand also the unloaded case would have a surface traction. However, in FE modelling the TSLs starting from the axes origin seem to find more agreement.

2.4.1 Formulation

Given the shape of the TSL, only two parameters are sufficient to completely define the cohesive behaviour: the cohesive strength (T_0) and the displacement at failure δ_f. The first parameter is used to define the damage initiation, the second is for damage propagation. This latter parameter is also viewed as characterizing the cohesive material ductility to failure (the larger δ_f the longer

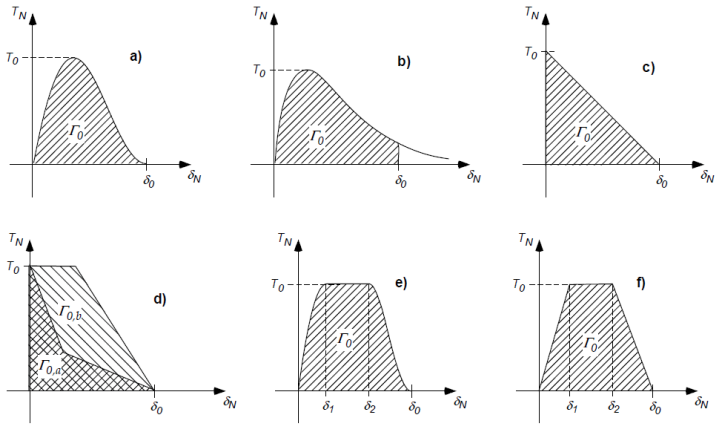

tbp

Figure 2.21: Typical traction separation laws: a) Needleman, b) Needleman with cut tail, c) Hillerborg, d) Bazant, e) Scheider, f) Tvergaard and Hutchinson.

the length of the process zone, the more enhanced material plasticity). The area subscribed by the TSL represents the work necessary to create a unit area of fracture surface, also known as the critical strain energy release rate G_C:

$$G_C = \int_0^{\delta_f} (T(\delta) d\delta) \tag{2.12}$$

In a FE framework the TSL is implemented in cohesive elements (4-node quadrilateral for 2D analysis or 8-node brick for 3D). The initial part of the cohesive law is usually linear: this part represents the traction capability of the interface before the any fracture process takes place degrading material properties. In general stress can be coupled with displacement: each stress component depended on the three of displacement:

$$\left\{ \begin{array}{c} T_N \\ T_S \\ T_T \end{array} \right\} = \left[\begin{array}{ccc} K_{NN} & K_{NS} & K_{NT} \\ K_{SN} & K_{SS} & K_{ST} \\ K_{TN} & K_{TS} & K_{TT} \end{array} \right] \left\{ \begin{array}{c} \delta_N \\ \delta_S \\ \delta_T \end{array} \right\} \tag{2.13}$$

Where the subscripts N, S and T stand for respectively "normal", "shear" and "tear"; K_{ij} represents the element of the stiffness matrix that couples stress and displacement. However, often the stress caused by non-corresponding displacement components is negligible or null, therefore the stiffness matrix reduces to be diagonal. In this case the elastic law is uncoupled and Eq. (2.13) can be simplified as follows:

$$\left\{ \begin{array}{c} T_N \\ T_S \\ T_T \end{array} \right\} = \left\{ \begin{array}{c} K_N \cdot \delta_N \\ K_S \cdot \delta_S \\ K_T \cdot \delta_T \end{array} \right\} \tag{2.14}$$

When a threshold stress value is reached (cohesive strength T_0) the TSL loses the linear behaviour and a softening part starts, following the predefined shape.

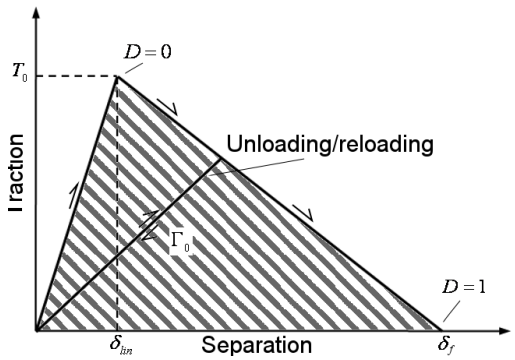

Figure 2.22: Cohesive traction separation law.

A damage parameter D is used to account for the element loading history: if the element undergoes a certain offset of damage due to a peak of load, its stiffness is permanently decreased, when the load in discharged, the element keep the modified stiffness for any further loading condition (Fig. 2.22 [114]). The stiffness reduction of the TSL can be express as below:

$$T = (1 - D)[K]\{\delta\} \tag{2.15}$$

The undamaged condition is characterised by $D = 0$ and the failure occurs when $D = 1$. For a linear softening, the damage evolution parameter D can be defined using the effective and relative displacement at failure. The following expression was proposed by Camanho and Davila [115]:

$$D = \frac{\delta_f \left(\delta - \delta_{lin}\right)}{\delta \left(\delta_f - \delta_{lin}\right)} \tag{2.16}$$

Where δ_{lin} is the displacement at damage initiation, namely $\delta_{lin} = T_0/K$ and δ_f is the displacement at complete failure, as depicted in Fig. 2.22. Due to the inevitable loss of stiffness during crack propagation and the irreversible nature of the event, the system equilibrium configurations changes widely during the crack opening. Sometimes the crack propagation is unstable and the system jumps from one equilibrium point to the next one though a sudden drop of load. In order to speed up the solution convergence velocity of the FE model, in quasi-static simulations, a viscosity parameter ν is often used [116, 117]. This parameter add an artificial term to the nodal force balance of the model, proportional to nodal velocity:

$$\{F_i\} = [K] \cdot \{U\} + \nu \left\{\frac{\partial U}{\partial T}\right\} \tag{2.17}$$

Where $\{F\}$ is the vector of nodal forces, $\{U\}$ nodal displacements and $[K]$ is the stiffness matrix. The derivative of nodal displacement (nodal velocity)

is calculated using the numerical time domain (quasi-static approximation) where the FE code seeks for the solution. The name viscosity is given after the formal similitude of the term with the resistance of a body within a fluid. The viscosity is a numerical artefact that introduces an error term. This parameter has to be set large enough to help solution convergence, but sufficiently small not to affect results. The viscous term depends on the derivative of the nodal displacements, thus as a rule of thumb the viscosity parameter has to be set at least the order of one magnitude smaller that the smallest time increment.

2.4.2 Existing models for delamination of composites

The CZM is most wide-spread damage mechanics model for delamination of composite laminates. Cohesive parameters are usually set on simple delamination tests such as double cantilever beam (DCB) for mode I (as for instance in [114, 118–120]), end notch flexure (ENF)[118, 121] or end loaded split (ELS) [122, 123] for mode II. These test configurations are designed to measure the interlaminar fracture toughness or the laminate. All of these have an embedded artificial crack that propagates when a critical load is reached up. The most meaningful cohesive parameter for the damage evolution is G_C, the others (initial stiffness K and cohesive strength T_0) can be regarded as "penalty" parameters to be set in a range that speed up the solution convergence [124, 125]. Usually the cohesive strength is set equal to the interlaminar laminate strength and the initial stiffness is set high enough not to vary the compliance of the system [126].

When studying structures without pre-cracks, the cohesive strength T_0, as well and the shape of the TSL, assumes much more importance for simulating the crack nucleation transitory. Gustafson and Waas studied the influence of cohesive parameters in the behaviour of adhesively bonded joints. They concluded that, regarding the prediction of the joint strength, T_0 is almost as important as the critical strain energy release rate G_C [42]. Sun et al. used a CZM formulation to study the ductile-brittle transitions in the fracture of plastically deforming, adhesively bonded structures [127]. Due to the insensitivity of DCB test to T_0, an alternative tensile wedge test was developed to determine the cohesive strength.

The hybrid bonded interface delamination of CFRP-titanium interleaved joints was studied by Camanho et al. using a cohesive zone model [20]. The interleaved laminate was designed to increase the bolt bearing resistance of the composite laminate. The model employed shell elements for the laminate plies and cohesive elements at interlaminar interfaces, which were able to simulate progressive delamination due to the bolt bearing load.

In most of the common cases the CZM has been also found to be nearly insensitive to the cohesive law shape; no matter which one is used as far as the

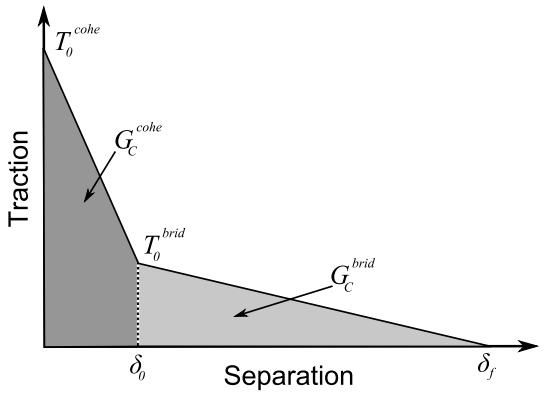

Figure 2.23: Cohesive-bridging traction separation law.

area underneath remains the same [128]. For this reason the bilinear shape is the most commonly used for modelling interlaminar delamination damage in composite laminates. This assumption is usually valid for all the fracture process where the process zone ahead of the crack remains small ($< a/10$, where a is the crack length). However, for small scale bridging (SSB) problems, such as in-plane fibre bridging or fracture of short-fibre materials, the shape of the TSL assumes more importance. Yang et al. [129] used a cohesive-bridging law to model the fracture of human cortical bones. The fracture process was characterised by having several ligaments bridging the crack along the wake. The cohesive-bridging law used in the model is depicted in Fig. 2.23; the high peak triangular area is representative of the first phase of the fracture process (at tip), whereas the wide-base triangular area simulates the bridging effect of ligaments.

Sun and Jin carried out a study on the usage of cohesive-bridging law for modelling the in-plane fibre bridging and the z-fibre bridging [130]. One of the main conclusions was that, because different mechanisms are involved in the bridging and cohesive zones, they should be treated separately in general. When cohesive and bridging are combined into a single traction separation law, parameters such as cohesive/bridging energy density (G_C^{cohe}/G_C^{brid}) and peak cohesive/bridging traction (T_0^{cohe}/T_0^{brid}) strongly influence the results.

CHAPTER 3

MODELLING METHODOLOGY

3.1 Introduction

Experimental and theoretical analyses have been performed on through-thickness reinforced laminates under the mode-I, mode-II and mixed mode load conditions [56, 68, 77]. Models have been developed to predict the enhanced fracture toughness and delamination crack suppression of through-thickness reinforced laminates. Two main approaches are: (1) z-reinforcement forces are averaged over the bridging area and their contribution is counted as traction stress, which is function of the local delamination displacement [60, 80, 89]; (2) each reinforcement traction is treated as a concentrated force acting at the pin location and governed by a non-linear force-displacement relation [57, 61, 86, 92, 94]. When the first approach is employed, the bridging relation is defined as either a stress-displacement relation [56, 80] or the stiffness of an elastic foundation [89]. However, modelling the z-reinforcement forces as an average surface traction is more appropriate for small and dense reinforcements such as stitches. When larger and more sparse reinforcements are used (z-pins, z-rods or surface-structured pins for hybrid joints), the characteristic slip-stick behaviour usually exists. This phenomenon, is due to the localised force of the pin, therefore cannot be well represented by this modelling technique. The second approach accounts for the local pin effect and better represents the behaviour of large reinforcements, however, when associated with a FE framework, the concentrated force causes stress singularity issues and the solution results to be mesh sensitive.

Cohesive zone modelling for studying delamination of unpinned laminates under the mode-I, mode-II and mixed mode I/II loading conditions, as well as

for adhesively bonded joints, is gaining more and more recognition within researchers. Owing to the mixed strength/energy based failure criterion, initial crack is not needed in the model. Recently, attempts have been made to use CZM to model through-thickness reinforcement in mode-I condition. Sun and Jin developed a FE model using a cohesive-bridging law to account for the energy contribution of in-plane fibre bridging and Z-fibres [130]. A similar approach was adopted by Dantuluri et al. to simulate delamination in z-pinned double cantilever beam (DCB) [61]. However, the TSL used in both works was based on the average value of strain energy dissipation rate due to the pins over the whole fracture surface. This kind of approach is more suitable to the SSB where the energy contribution due to bridging can be considered as an improved material property.

The objective of this research is to develop a FEA tools for predicting the structural properties and failure of through-thickness reinforced joints. No matter if composite or hybrid metal-composite joints, the modelling strategy adopted is identical: the bridging effect of reinforcements is accounted for as a material-structure attribute rather than an improved material property. The strategy is presented in Fig. 3.1. The idea is to use a cohesive zone model for predicting the delamination of the the unpinned area and the bridging effect of pins. The unpinned CZM is governed by the laminate intrinsic toughness, whereas much enhanced delamination toughness due to the pin bridging force is used in the pin location.

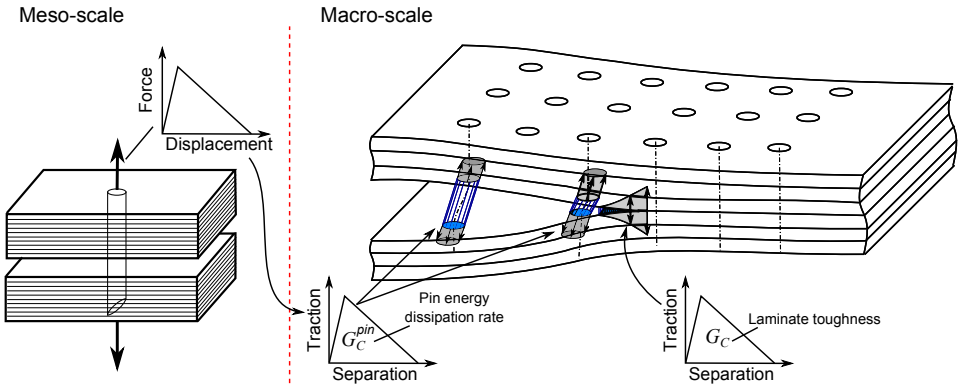

Figure 3.1: Multi-scale modelling approach

This approach can account for the local effect caused by z-pins, avoiding either averaging the pin forces over the whole reinforcement area or using concentrated traction forces. The large scale bridging effect of pins is therefore better represented, especially for lower pin densities, permitting more accurate analysis.

3.2 Multi-scale approach

The modelling approach is schematically represented in Fig. 3.1, the problem is studied at two modelling levels: (1) a unit-cell single pin model to analyse the bridging of an individual reinforcement and (2) a macro-scale model to simulate the structural response of the joint. The bridging force generated by a single pin reinforcement is assumed to be fully characterised by two basic loading conditions: tensile stress normal to the crack plane (induced by mode I interlaminar stress) and shear stress along the crack plane (induced by mode II interlaminar stress). The pin bridging force generated by the pin under these two loading conditions is evaluated by two distinct models. Any mixed mode displacement of the pin is divided into its two components (in-plane and out-of-plane) and the bridging force exerted by the pin is calculated as the vectorial summation of the two model responses (i.e. neglecting any reciprocal interaction)

Two independent cohesive zone models are used for evaluating the delamination damage of bonded interface and pin bridging forces. The unpinned CZM is governed by the laminate intrinsic toughness, whereas enhanced delamination toughness is used in the pin locations. A bilinear TSL is used to define the constitutive response of cohesive elements. A mixed-mode failure criterion is used to calculate the crack propagation:

$$\frac{G_I}{G_{IC}} + \frac{G_{II}}{G_{IIC}} + \frac{G_{III}}{G_{IIIC}} \geq 1 \tag{3.1}$$

where G_I, G_{II} and G_{III} are the instantaneous traction strain energy release rate values of the system under crack opening, sliding and tearing displacements, respectively. G_{IIC} and G_{IIIC} are assumed equal (isotropic shear delamination resistance).

3.3 Unit-cell for calculating single-pin bridging laws

The bridging force exerted by an individual pin is calculated using a unit-cell model loaded either under tensile stress normal to the crack plane (induced by mode I crack opening displacement) or shear stress along the crack plane (induced by mode II interlaminar stress). The interface between upper and lower laminate shells (for composite joints) or metal and composite adherends (for hybrid joints) is assumed completely failed and the pin bridging the only feature connecting the two parts.

It worth noticing that the local crack tip boundary condition of the bonded interface (completely failed) is formally different from the macro-scale model

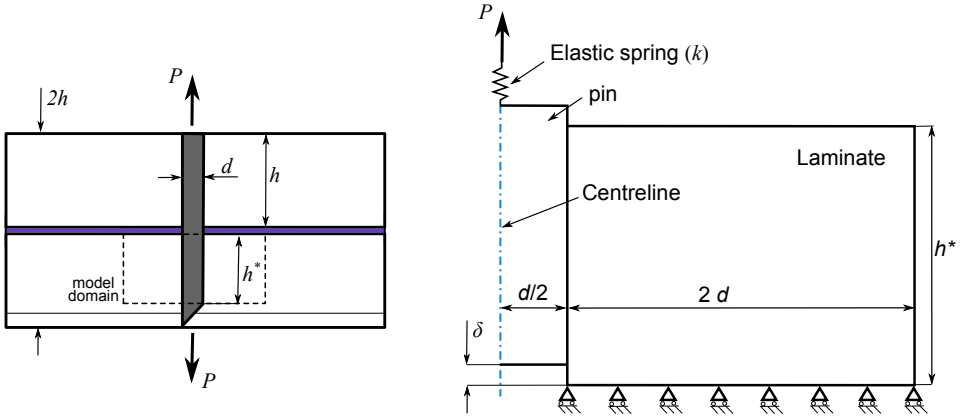

Figure 3.2: Single-pin unit-cell model: (a) model domain (b) FE model and boundary conditions applied.

where the bridging law is then used to calculate the evolution of the delamination crack. This is an assumption of the model: the pin bridging contribution is only relevant when the crack has passed it, i.e. pin is far behind the advancing crack tip; thus boundary conditions of the delamination interface for both single pin and macro-scale structural models. However, the hypothesis is supported by the physical observation that the effect of pin reinforcements to enhance delamination fracture toughness of composite laminates is negligible until the damage has reached a considerable dimension (5–10 pin diameters), i.e. the crack passes the reinforcement [10, 67, 131].

3.3.1 Pin under mode I loading

The bridging force exerted by a single pin under tensile stress normal to the crack plane is estimated using an axi-symmetric FE model, as shown in Fig. 3.2. The pin is assumed to be perpendicular to the delamination plane and the applied force aligned with the pin axis. The pin is also assumed to pullout from the side having the chamfer head (for ease of insertion purpose). The tip tip of the pin does not contribute to the pullout resistance, therefore the modelled pin height (h^*) is reduced of one diameter with respect the regular height of the pin. The model is based on the observation of a resin-rich pocket around the pin, of about 5–6 pin diameters, caused by the pin insertion. Considering that laminate properties in the cross fibre direction are dominated by the resin matrix, material surrounding the pin is assumed as homogeneous and isotropic.

Experimental observation has pointed out that the initial debonding phase gives a negligible contribution to the energy absorption, therefore the pullout resistance is considered being caused by the friction force only [80, 81]. This friction resistance results from the compressive residual stresses around the pin due to the curing process. The resin matrix shrinks more than the pin

during cooling down from the elevated cure temperature to room temperature, resulting in compressive residual stress state along the pin in the radial direction.

The model uses a surface to surface algorithm to calculate the normal contact stress and the Coulomb friction. The curing process is modelled by applying a temperature change from cure to room conditions (i.e. imposing a thermal strain contraction of $\alpha\Delta T$). Thermal residual stresses are calculated and saved in the model as the initial condition in order to maintain displacement compatibility. A pullout force is then applied at the pin top surface under the displacement controlled loading condition. Numerical simulation runs until the pin is completely pulled out.

It should be noted that the main energy dissipation mechanism accounted by this model is the friction resistance during the z-pin pullout process. However, when small pins are inserted into thick laminates (e.g. when the ratio between laminate thickness and pin diameter h/d is larger than 15–20), pin failure mode may switch from pullout to pin rupture. The latter failure mode is not accounted for by the present model, which limits the model application to only the thinner laminates. However, energy dissipation in the pin final rupture failure is much smaller than that in the pin pullout process.

3.3.2 Pin under mode II loading

For evaluating bridging force carried by single pin reinforcements loaded under shear stress along the crack plane (induced by mode II interlaminar stress) a distinction between carbon and metal pins is made. Despite the geometrical similarity these two reinforcement types show very different failure mechanisms, which characterise their mechanical response to shear loading. Both metal and carbon pins has a similar elastic response, dominated by bending of the pin along its axis. However, this phase is followed by a nonlinear hardening response of the force-displacement curve. Whereas for carbon fibre pins failure is driven by the axial shear strength of the z-pin, which cause the typical pin splitting into several ligaments when the shear stress exceeds the material strength, metal pins instead deforms plastically, carrying almost a constant shear stress.

In both cases the pin damage is accompanied by a loss of bending stiffness, which allows the pin to allocate large shear displacements. However, whereas for z-pins the lack of plastic behaviour implies a steep drop of bending stiffness, for metal pins the process is more gradual thus more difficult to implement into a model. Due to this so different behaviours, different approaches are used for each specific case: (1) an analytical model for carbon fibre z-pins and (2) a FE model for metal pins.

(a) Analytical model for carbon fibre pins

The bridging force exerted by a single carbon fibre z-pin under shear stress along the crack plane is estimated using an analytical micro-mechanical model. The model is based on the observation that z-pin failure process can be divided into three phases: (1) pin has an initial elastic response, (2) pin then ploughs into the laminate (this is particularly pronounced for the unidirectional laminates), and (3) pin either ruptures under tension or is pulled out [70, 71]. The shear stress transfer is initially due to the mechanical bond and then to the friction resistance caused by the contact stresses at the pin/laminate interface. The shear stress at the pin/laminate interface is the main mechanism putting the pin under axial stress. Before applying mechanical load, the initial normal stresses between pin and laminate are compressive due to the mismatch of the coefficients of thermal expansion; this contact stress will then increase when the pin is pulled out due to the laminate shear deformation.

The laminate supports the pin laterally causing large deformation in the surrounding resin matrix, which can cause the resin under plastic deformation [72]; subsequently, due to the high circumferential tensile stresses, the laminate eventually fractures allowing the pin to plough into it. Transverse stresses on the pin exerted by the surrounding laminate make the pin subjected to bending deformation during the elastic response phase. When the transverse shear strength of the pin is exceeded the pin splits internally in several threads, loosing bending stiffness and increasing shear deformation. From this point onwards the pin behaves like a truss (capable to carry axial stress only) and subjects to large rotation at the fracture plane. Depending on the pin geometry and laminate stacking sequence, the pin can either be pulled out resulting in a progressive and monotonic reduction of bridging force, or rupture with a sudden load drop [68].

The model comprises a composite laminate containing a centre delamination and a z-pin bridging the two crack surfaces (Fig. 3.3a). Assuming the chamfer head at one end of the pin is negligible, the specimen is symmetric with respect to the central plane and it is loaded anti-symmetrically. Therefore only one side of the pin is modelled. However, considering that pin pullout is more likely to occur at the side having the chamfer, the pin height (pin insertion depth) in the model is reduced by the chamfer height.

The model comprises all aforementioned three phases of pin bridging. During the elastic response the pin is assumed to react as a beam supported by an elastic spring foundation. Stiffness of the spring foundation is estimated considering the elasticity of the laminate nearby and the dimension of the resin rich zone close to the pin. Since the resin rich pocket extends in the fibre direction and the laminate properties in cross-fibre direction are dominated by the resin, material properties close to the pin are assumed to be homogeneous

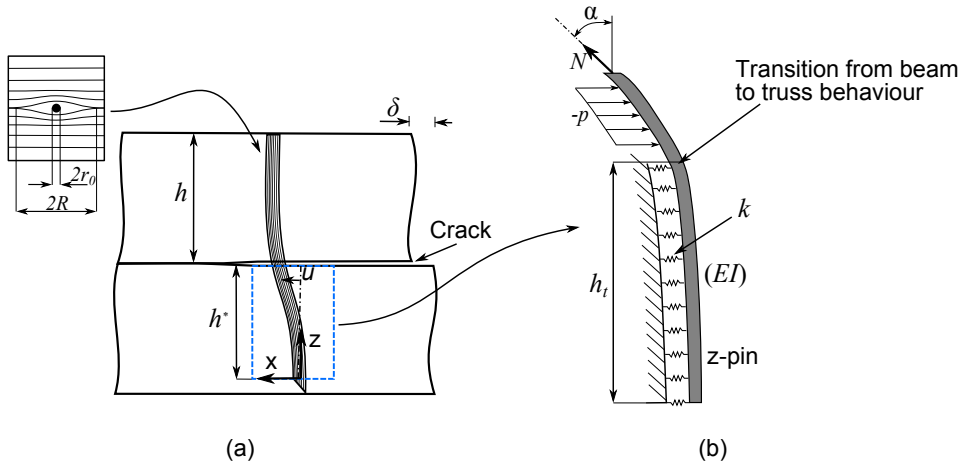

Figure 3.3: (a) Schematic of single-pin bridging a mode-II delamination crack, (b) micro-mechanical beam model for evaluating the mode-II bridging law.

and isotropic, and equivalent to the transverse stiffness of the laminate surrounding the pin. During the elastic loading phase pin lateral displacement u can be expressed by following differential equation:

$$EI\frac{\partial^4 u}{\partial z^4} + ku = 0 \tag{3.2}$$

where EI is the pin bending rigidity, k the elastic constant of the spring foundation mimicking the stress distribution in the laminate acting on the pin, which is calculated by:

$$k = \frac{\pi}{2}\frac{E_{lam}}{\ln\frac{R}{r_0}} \tag{3.3}$$

where r_0 is the pin radius and R is radius of circular area of laminate close to the pin dominated by the resin properties. R is assumed equal to the dimension of the resin rich zone, which is usually 4-6 times the pin radius ($R = 5r_0$ is used for this model). Detailed derivation of Eq. (3.3) is given in Appendix A. Let δ be the applied shear displacement between the two laminate parts. Relative boundary conditions are:

$$u\big|_{z=h^*} = \frac{\delta}{2},\ \left.\frac{\partial^2 u}{\partial z^2}\right|_{z=0} = 0,\ \left.\frac{\partial^2 u}{\partial z^2}\right|_{z=h^*} = 0,\ \left.\frac{\partial^2 u}{\partial z^2}\right|_{z=0} = 0,\ \left.\frac{\partial^3 u}{\partial z^3}\right|_{z=0} = 0 \tag{3.4}$$

During the ploughing phase laminate is assumed to react as a perfectly plastic material; the lateral force exerted on the pin is therefore constant and independent of the displacement. This force per unit length p represents the resistance of the laminate being punched by a blunt notch [72, 132]. The model is depicted in Fig. 3.3b. Following differential equation describes the pin lateral displacement in the ploughing zone.

$$N\frac{\partial^2 u}{\partial z^2} + \frac{\partial N}{\partial z}\frac{\partial u}{\partial z} = -p \tag{3.5}$$

where N is the axial force on the pin and $-p$ [1] the lateral reaction force per unit length acting on the laminate. Derivation of Eq. (3.5) can be found in Appendix B. Differential Eq. (3.2) and Eq. (3.5) describe z-pin displacement in the transverse direction. Eq. (3.5) depends on the distribution of the axial stress in the pin. The friction resistance is the physical mechanism with which z-pin carries axial load. Following differential equation, deriving from the force balance in the axial direction of the z-pin, describes pin axial stress distributed along the axis:

$$\begin{cases} \frac{\partial N}{\partial z} = \mu(\frac{\pi}{2} r_0 \sigma_0 + k|u|) & z \leq h_t \\ \frac{\partial N}{\partial z} = \mu p & h_t < z \leq h \end{cases} \tag{3.6}$$

where μ is the Coulomb friction coefficient between pin and laminate, σ_0 the compressive residual stress due to the curing process and h_t the length of transition between elastic and plastic behaviour. The transition is assumed to occur when the pin starts having large lateral displacements, thus when the maximum shear stress is exceeded the pin starts splitting into several threads. The initial compressive residual stress σ_0 is estimated using the following equation:

$$\sigma_0 = \frac{\Delta T(\alpha_{lam} - \alpha_{pin}) E_{lam} E_{pin}}{E_{lam} + E_{pin}} \tag{3.7}$$

where ΔT is the temperature variation during the curing process of the test specimen and α_{pin} and α_{lam} the coefficients of thermal expansion (in the radial direction) of the pin and the laminate, respectively. The mathematical problem can be solved using the boundary condition of the axial stress (Fig. 3.3b):

$$N(L) = F \sin \alpha \tag{3.8}$$

The transition length h_t between beam and truss behaviour depends on the applied load (it becomes bigger as the load increases); therefore the nonlinear solution is found using an iterative scheme as illustrated in Fig. 3.4 and implemented in Matlab 7. The maximum bridging force is estimated by considering two critic conditions that lead two distinct failure modes: (1) axial stress exceeds the friction resistance resulting in pin being pulled out; (2) axial stress overcomes z-pin tensile strength causing the pin rupture failure.

(b) FE model for interlocked metal pins

The bridging force exerted by a single metal pin under shear stress along the crack plane is estimated using a 3D FE model. The modelled geometry and the applied boundary conditions are defined in order to simulate the loading condition of the test sample, as shown in Fig. 3.5. The specimen is composed of a single pin realised on a thick metallic substrate of cylindrical shape (pin is

[1] Ploughing resistance $-p$ is indicated with the sign minus because always opposite to displacement direction

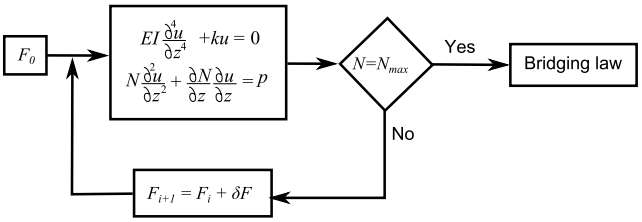

Figure 3.4: Iterative scheme used to determine the single-pin bridging force.

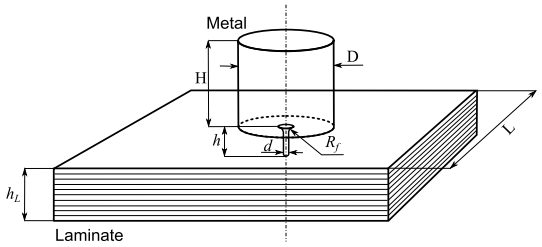

Figure 3.5: Specimen geometry used for shear tests of metal pins.

welded on the surface of metal substrate) and a square block of laminate with quasi-isotropic layup, where the pin is inserted. Metal and laminate blocks are separated by a thin FEP (fluorinated ethylene propylene) film at the metal cylinder base. The film is mimicking a debond crack and the pin is the only mechanical connection between the two halves of the specimen.

Due to the fibre rearrangement induced by the pin insertion process, resin rich areas and voids form in the area near the pin, as shown in Fig. 3.6. On the presented section these areas are visible at the plies oriented at 0° and ±45° (as shown on the left-hand side of Fig. 3.6a); due to eyelet resin rich areas oriented in the fibre direction. However, the percentage of these defects is of the same order of z-pinning technology and the relative global reduction of the laminate in-plane properties is usually smaller than 15% [8]. The percentage content of fibres, resin and voids (calculated basing on the colours of the different compounds in the photograph: fibres in light grey, resin in dark grey and voids in black), is plotted in Fig. 3.6b. The average content of fibres growth monotonically from zero to an asymptotic value of about 60% (fibre content of the unenforced laminate); the resin and voids content function is the complement to 100% of the fibre volume content. Data are interpolated using a cosine function as reported in Fig. 3.6b insertion.

The model is based on the following experimental observation: (1) single pin has an initial linear-elastic response. (2) This linear-elastic phase is followed by a non-linear increasingly-compliant response of the pin. During this phase the pin bends over due to the high bending moment at the root and starts deforming plastically. Due to the high pressure at the root, the pin also ploughs into the resin rich areas of the laminate. This phenomenon is also believed to be related to the closure of the voids embedded in the resin rich areas. (3)

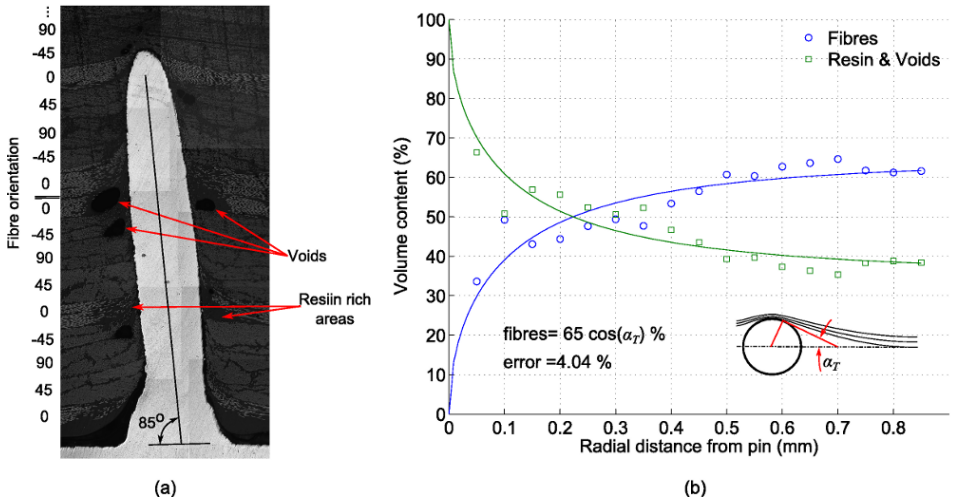

Figure 3.6: (a) Micrograph section of a CMT pike pin, (b) average fibre percentage content in function of the radial distance from pin.

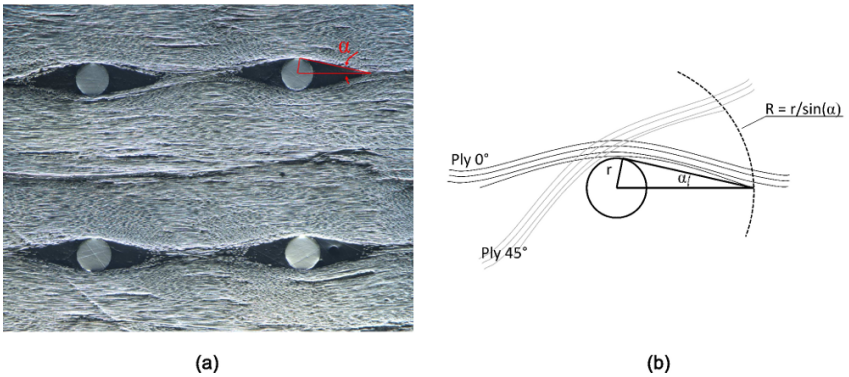

Figure 3.7: Fibre misalignment caused by pin insertion: (a) laminate horizontal section of pin reinforced metal-composite joint (courtesy of Adam Joesbury's), (b) schematic used to evaluate the dimension of the laminate area around the pin with reduced properties.

The final failure of the pin occurs either due to shear plastic failure at the pin root or by pin pulled out of the laminate.

The laminate close to the pin has characteristic eyelet shaped resin rich pockets in the local fibre-directions as visible in Fig. 3.7a. The length of these areas is typically 4–5 pin diameters. Considering the quasi-isotropic layup, the laminate properties have been homogenised according to the different fibre percentage. The region closest to the pin (within one pin radius) is assumed to have pure resin properties; an intermediate region (up to the boundary of the eyelet resin pockets), due to fibre misalignment, is assumed to have material properties equal to 50% of the base laminate (Fig. 3.7b).

The presence of voids and the pin ploughing phenomenon has been modelled assuming a perfectly plastic behaviour of the resin near the pin. Material behaves elastically until the yielding stress is reached. After that the stress

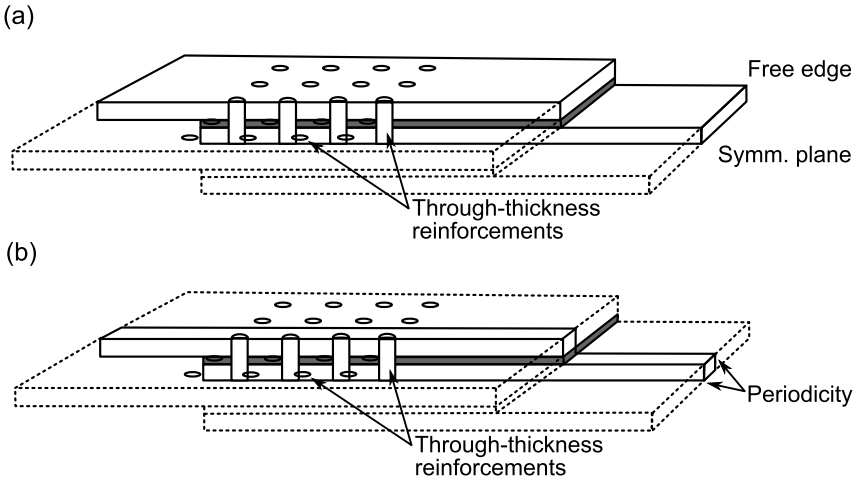

Figure 3.8: Sketches of the two models used to simulate the structural response of through-thickness reinforced joints: (a) whole model representing half of the geometry (b) unit-strip model for half of a pin row.

remains constant and material interaction allows large strain deformation. The yield stress and all the properties of the resin rich zone have to be considered as parameters of the model and they have to be set over a reference test. Yielding stress particularly is expected to depend upon the laminate layup as well. Laminate properties at the far field are assumed homogeneous and are calculated using the laminate theory. The contact force between pin and laminate is modelled using a penalty surface to surface algorithm with a friction coefficient μ equal to the one used for the mode-I pin pullout model.

3.4 Cohesive zone model for through-thickness reinforced structures

The structural properties and failure of through-thickness reinforced structures is studied using a macro-scale cohesive zone model. Two different FE models have been developed: a complete model (referred as "whole" model from now on) representing the entire geometry (Fig. 3.8a), and a simplified "unit-strip" model (Fig. 3.8b) by exploiting the periodic pin arrangement. The unit-strip represents one pin row (in the longitudinal direction of the joint) in the mid-width and the surrounding laminate of the dimension of a periodical repeating unit. Longitudinal planes of symmetry are eventually exploited (either reducing the model geometry to half. The y-axis deformation is constrained; hence it neglects the free-edge effects. However, the much reduced model size allows significant saving in computational effort.

In both models, 8-node linear continuum shell elements with reduced integration (designated as CS8R in Abaqus) were used for the laminate beams and

8-node cohesive elements (COH8) for the bonding interface. Element size in cohesive zone is one fifth of the adjacent shell element, in order to achieve numerical stability. This is essentially a 2D shell element model using one layer shell elements for the adherends and cohesive elements for the interface between them. Continuum shell element that has independent displacement degree of freedom enabling calculation of the rotation variables from the difference in nodal displacement between the element top and bottom surfaces.

Cohesive elements at the interface are governed by two different traction-separation laws: one for the unpinned laminate toughness and the other for pin enhanced toughness. For the unpinned laminate, cohesive model parameters are estimated by delamination test such as DCB for mode-I and ENF for mode-II loading conditions. Whereas, parameters of the bridging cohesive law were calculated from the bridging law of individual reinforcements.

3.4.1 Pin models

The pin bridging effect is implemented into the macro-scale structural model using two distinct pin models, obtained as follows. A traction-separation law in terms of the pin stress versus crack opening is deduced from the bridging force shown in Fig. 3.9; it is expressed as

$$T(u) = \frac{P(u)}{\pi r_0^2} \tag{3.9}$$

where u is the delamination opening displacement, $T(u)$ is the bridging stress in the cohesive law and $P(u)$ is the pullout force (derived from the unit-cell model). Eq. (3.9) is plotted in Fig. 3.9b (solid line represents the realistic traction-separation law). The bilinear curve (dashed line) is an approximation. The two curves are equivalent in terms of the enhanced fracture energy (G_C^{pin}), which is the area under the traction-separation curve; both curves describe same energy absorption rate due to pin bridging effect. For mode-I bridging the two curves always remains very close each other, whereas, due to the nonlinear response of pin reinforcements in mode-II, in this latter loading case the difference is larger.

This pin response was implemented into the global FE model using two different pin models to represent the nonlinear and bilinear bridging laws as shown in Fig. 3.10. (1) The "spring-pin" model employs nonlinear spring elements with a user-defined force-displacement relation, which is the nonlinear curve in Fig. 3.9b. As depicted in Fig. 3.10 insertion (a) these springs are connected to the two adherends through Multiple-Point Constraints (MPCs). The size of the connection points equals the pin cross-sectional area. (2) The "cohesive-pin" model uses cohesive elements at the interface, as shown in Fig. 3.10b, that are governed by the simplified bilinear traction-separation law.

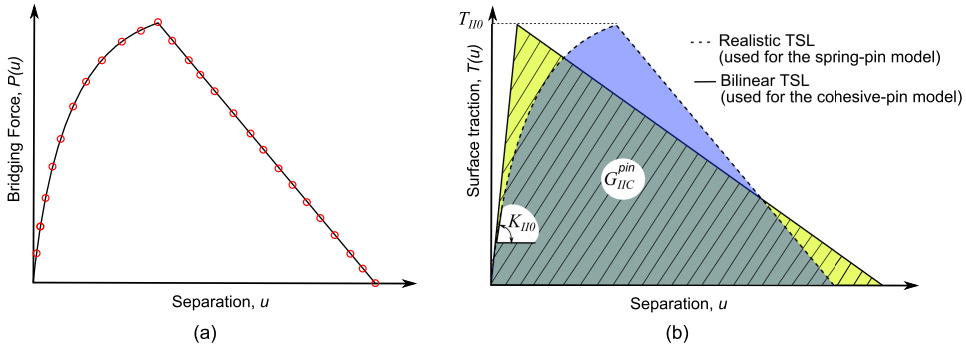

Figure 3.9: Schematic of the two traction-separation laws used to simulate pin bridging into the global FE model: (a) bridging force of a single pin, (b) traction-separation law used for analyses (solid line for the realistic TSL, dash line for its bilinear approximation).

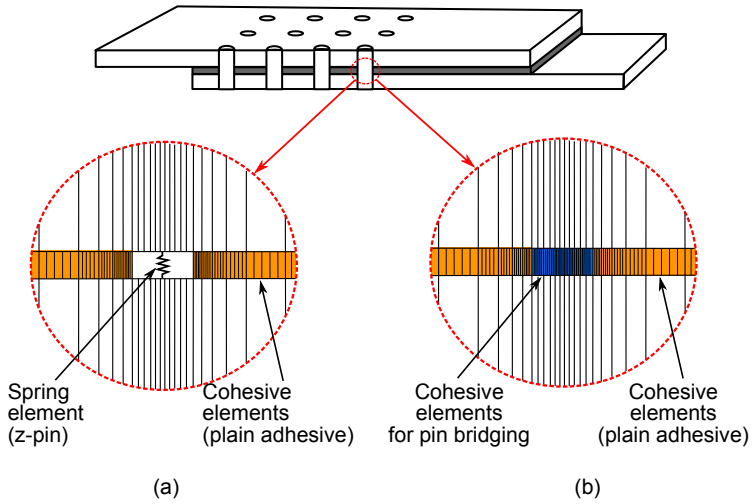

Figure 3.10: Schematic of the two traction-separation laws used to simulate pin bridging into the global FE model: (a) bridging force of a single pin, (b) traction-separation law used for analyses (solid line for the realistic TSL, dash line for its bilinear approximation).

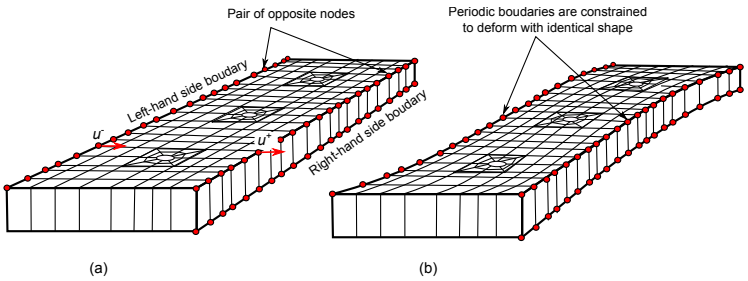

Figure 3.11: Schematic of periodicity boundary condition used in the unit strip model. (a) undeformed and (b) deformed shape.

3.4.2 Unit-strip model for periodical pin arrangements

In order to save computational time and thus having a model more suitable for parametric studies and optimization of the joint configuration, a simplified model has been developed. The unit-strip model consists of strip of width equal to the repetitive unit of the pin arrangement (i.e. one row of pin for a matrix arrangement), as shown in Fig. 3.8b. The idea is to use periodic boundary conditions at the two longitudinal planes that defines the unit-strip in order to represent an infinitely wide pin arrangement.

To satisfy the deformation periodicity at boundaries the nodal displacement are constrained to respect the following:

$$u_i^+ = \overline{\epsilon_{ik}} x_k + u^- \tag{3.10}$$

Where u_i^+ and u_i^- are the i-component of nodal displacement at the two opposite boundaries, x_k is the distance between the two boundaries and $\overline{\epsilon_{ik}}$ is the (i,k) term of the average strain tensor. The displacement functions at the two boundaries have the same shape. This boundary condition has been demonstrated by Xia et al. to respect also the stress periodicity [64, 65]. However, when the repetitive cell of the pin arrangement and the loading conditions are symmetric with respect the longitudinal central plane the displacements at boundaries have to respect also the following relation:

$$u_i^+ = \begin{cases} u_i^- & \text{parallel to the symmetry plane} \\ -u_i^- & \text{perpendicular to the symmetry plane} \end{cases} \tag{3.11}$$

Boundary conditions defined by Eq. (3.11) and Eq. (3.10) are implemented into the model by constraining the displacement perpendicular to the boundary plane to be constant over the entire boundary plane, in order to allow the strip having lateral contraction due to the Poisson's effect. The position of plane (lateral contraction) is calculated by the FE code in order to respect the force balance. Fig. 3.11 shows the unit-strip model boundary conditions.

The model calculates the external applied load that to the strip bears (P_{strip}). The load carried by the joint (P) can be calculated then using the following

relation:

$$P = \frac{W}{0.5\,p_y} P_{strip} \tag{3.12}$$

Where W is the joint width and p_y the pin pitch in the width direction. The scaling factor between the two model is simply the ratio between the joint and the model width (i.e the number of strips necessary to cover the joint along its width).

Due to the finite width of the structure, the number of pins bridging the crack over the joint width (N_{pin}) generally differs from the scaling factor calculated by Eq. (3.12). The pin bridging traction used in the unit-strip model (T_{strip}) is therefore corrected in order to account for this effect:

$$T_{strip} = \frac{0.5\,p_y}{W} N_{pin} T \tag{3.13}$$

It should be noticed that for large structures such as large fuselage or wing panels, this correcting factor is close to unit, whereas for small samples where the free-edge effect in more relevant, varying within a range of $(N_{pin} \pm 1)/N_{pin}$.

Part II

Development for composite joints

CHAPTER 4

MODEL VALIDATION FOR PREDICTION OF DAMAGE PROPAGATION

4.1 Introduction

The first step for the validation of the modelling approach is demonstrating the suitability of the model to predict delamination damage of composite laminates under mode-I and mode-II loading conditions. The first part of this chapter deals with modelling of mode-I delamination samples (DCB tests) of plain and z-pin reinforced laminates. The second part of the chapter is dedicated to pinned and unpinned delamination tests under mode-II loading conditions (ENF tests).

Two-dimensional (plane strain) and three-dimensional models of unreinforced DCB and ENF delamination tests were constructed and compared with experiments in order to validate the cohesive model. The numerical results of the two models (i.e. 2D and 3D) are then compared to demonstrate their equivalence in terms of load and crack extension prediction. For the reinforced DCB and ENF delamination tests, the plane strain model was not viable due to the pin presence; therefore, the unit-strip model was used and compared with experimental test data for validation.

Table 4.1: Material mechanical properties used in FE analyses of unrenforced DCB tests [118].

E_{11}	$E_{22} = E_{33}$	$G_{12} = G_{13}$	$\nu_{12} = \nu_{13}$
	(GPa)		
146	10.5	5.25	0.3

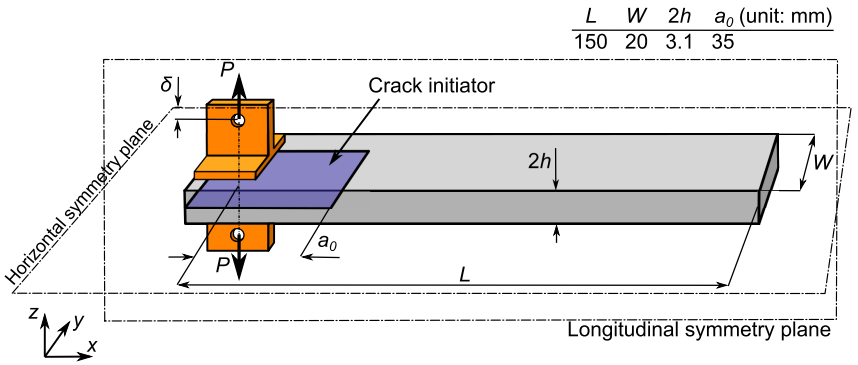

Figure 4.1: Geometry of unreinforced mode-I delamination test

4.2 Unreinforced mode-I delamination test

4.2.1 Geometry and model description

Experimental data for model validation are from Asp [133], who carried out an extensive testing campaign to investigate the effects of moisture and temperature on the interlaminar delamination toughness of a carbon/epoxy composite laminate. Fig. 4.1 shows the DCB test set up, specimen geometry and loading conditions. The specimen is fabricated from toughened resin HTA/6376C carbon/epoxy prepreg supplied by Cibe Geigy (material properties are summarised in Table 4.1). The specimen is composed of two sub-laminates of equal number thickness and layup respectively $[0_{24}]$ and $[\pm 5/0_4]_s$, with an initial crack of 35 mm created by inserting at the central delamination plane a thin polyamide film (thickness 7.5 μm). This layup was chosen in order to avoid fibre bridging effects which can manifest when delamination occurs between plies with same fibre orientation. However, the change of flexural stiffness from unidirectional layup is negligible and thus the specimen can be considered symmetric with respect the delamination plane.

Two-dimensional plane strain model

A two-dimensional FE model was constructed to predict the interlaminar delamination growth under mode-I loading. The model uses 4-node linear plane strain elements with reduced integration (designated as CPE4R in Abaqus)

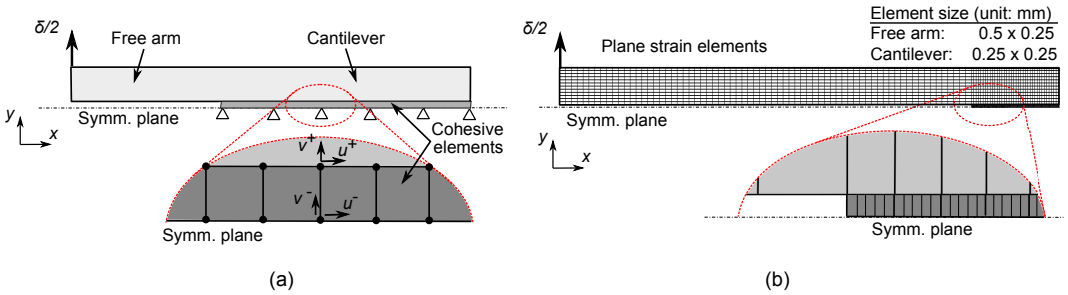

Figure 4.2: Plane strain model of the unpinned DCB specimen (a) geometry and boundary conditions, (b) mesh used for analysis.

for the composite laminate beams and 4-node cohesive elements, governed by a bilinear traction separation law, for the bonded interface. The symmetry of the specimen geometry is exploited and only the top half of DCB geometry modelled (a sketch of model geometry and applied boundary conditions are shown in Fig. 4.2a). The simulation was run under displacement loading control by imposing a displacement of $\delta/2$ (half of the total applied displacement) to the top-left corner node (Fig. 4.2a). The cohesive elements properties used for analysis are summarised in Table 4.2. Because of the symmetry, the cohesive element separation calculated during analysis represents half of the real crack opening displacement, i.e. initial stiffness K_{I0} and fracture toughness G_{IC} are scaled as follows:

$$\begin{cases} K_{I0}^{(symm)} = 2\,K_{I0} \\ G_{IC}^{(symm)} = 0.5\,G_{IC} \end{cases} \tag{4.1}$$

Symmetry boundary condition (i.e. no shear stress at the symmetry plane) was then employed by allowing the cohesive element nodes at boundary to move free over the symmetry plane. However, due to absence of transverse shear stiffness of cohesive elements, the symmetry boundary condition allows a zero-energy, hourglass deformation of cohesive elements which cause convergence problems. In order to avoid this to happen the the relative shear displacement between top and bottom surfaces was also constrained:

$$u^+ = u^-, \qquad \text{for each couple of points} \tag{4.2}$$

Where u^+ and u^- are nodal in-plane displacements of two opposite nodes belonging respectively to the top and bottom surfaces of the cohesive elements, as shown in Fig. 4.2a. Eq. (4.2) forces the cohesive elements to have a deformation compatible with the constrain of no-shear stress at the symmetry plane. A mesh sensitivity analysis was conduct and the mesh depicted in Fig. 4.2b was found to be the best compromise between accuracy and computational time. The cohesive element size was set one fifth of the adjacent composite laminate in order to achieve numerical stability and convergence.

Table 4.2: Cohesive elements parameters for unreinforced DCB model

Initial stiffness K_{I0}	Cohesive strength T_{I0}	Fracture toughness G_{IC}
2 x 10^{14} N/m^3	30 MPa	240 J/m^{-2} *

* [57]
Other cohesive parameters have been set to achieve numerical stability as described in [124-125]

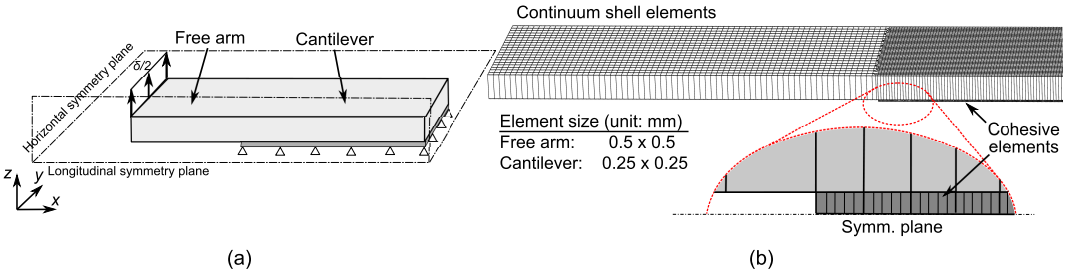

Figure 4.3: Three-dimensional model of the unpinned DCB specimen (a) geometry and boundary conditions, (b) mesh used for analysis.

Three-dimensional model

A three-dimensional model of the unreinforced DCB was constructed using 8-node linear continuum shell elements with reduced integration (designated CS8R in Abaqus) for the composite laminate beams and 8-node cohesive elements for the bonded interface. Continuum shells elements with nodal displacement degree of freedom (u, v, w), use the differential displacement of top and bottom surfaces to calculate the shell rotation. Boundary conditions, and material and cohesive properties were kept the same as for the plane strain model. Both longitudinal and horizontal symmetry planes (Fig. 4.1)are exploited, thus only one quarter of geometry is modelled. Fig. 4.3 shows model geometry and mesh used for analysis.

4.2.2 Numerical results

Two-dimensional plane strain model

Calculated force versus displacement and crack extension versus prescribed displacement, and comparison with the test results in [133] are presented in Fig. 4.4. The FE analysis shows excellent agreement with experimental data. The model was able to predict the initial linear elastic response of the cantilever beam and the peak load at which a continuous and stable delamination crack started propagating, as shown in Fig. 4.4a. After the peak the load decreases

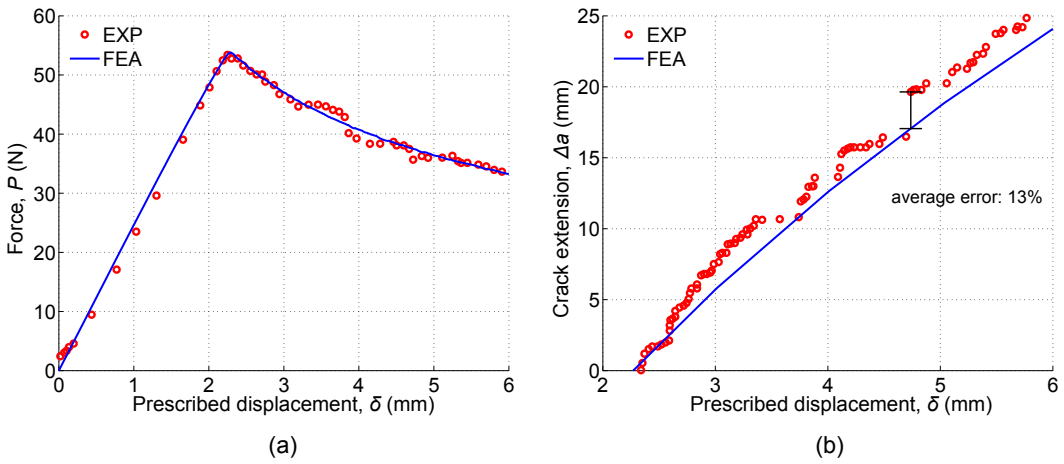

Figure 4.4: Comparison between FEA and experiment: (a) force vs. prescribed displacement and (b) crack extension vs. prescribed displacement curves.

monotonically with increasing the prescribed applied displacement at the beam free end. The crack starts propagating at $\delta = 2.27$ mm, as shown in Fig. 4.4b. The model slightly underestimates the extension, however the error always remains smaller that 13%.

Fig. 4.5 shows the contour plots of stress components (σ_{11}, σ_{22} and τ_{12}) during the crack propagation phase (at applied displacement $\delta = 3$ mm; crack extension $\Delta a = 5.7$ mm). The lighter gray area represents the laminate, in darker gray the cohesive part. Due to the loading condition of the composite beam, flexural bending stress (σ_{11}) is the dominant stress contribution (Fig. 4.5a). However, despite its lower amplitude compared with axial bending stress, peel stress at interface is the stress component influencing the crack advancement. Fig. 4.5b shows the σ_{22} stress concentration at the crack tip. Shear stress (τ_{12}, as shown in Fig. 4.5c has a stress concentration at the centre of the laminate beam, however, this stress component goes to zero at interface (i.e. on the symmetry plane).

Shear and peel stress distributions over the delamination plane are plotted in Fig. 4.4. Near the crack tip peel stress has a peak value up to the cohesive strength of 30 MPa (Fig. 4.4a). The distance between the peak stress and the crack tip (where stress drops to zero) is the so-called process zone (i.e. where cohesive element stiffness is progressively softened to zero). Consistently with the applied boundary condition, the shear stress is null all over the interface (over the symmetry surface). The small deviation in the stress distribution close to the process zone is due to numerical errors. However, this stress error remains small compared with the peel stress, i.e. negligible (Fig. 4.4b).

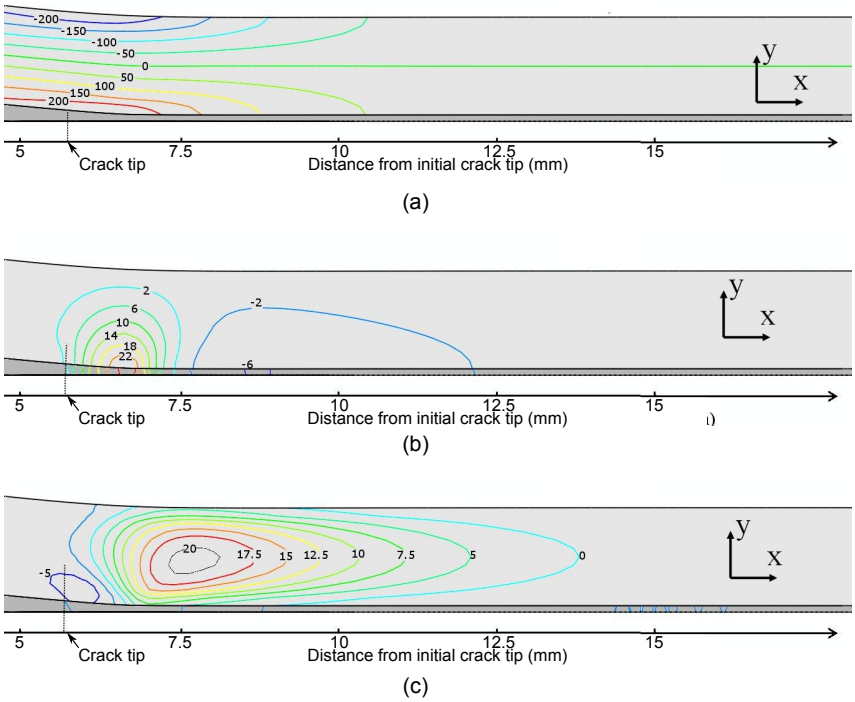

Figure 4.5: Stress contour plots at prescribed displacement $\delta = 3$ mm (crack extension $\Delta a = 5.7$ mm: (a) flexural bending stress (σ_{11}), (b) Normal stress in y-direction (σ_{22}), (c) In-plane shear (τ_{12}). Unit: MPa.

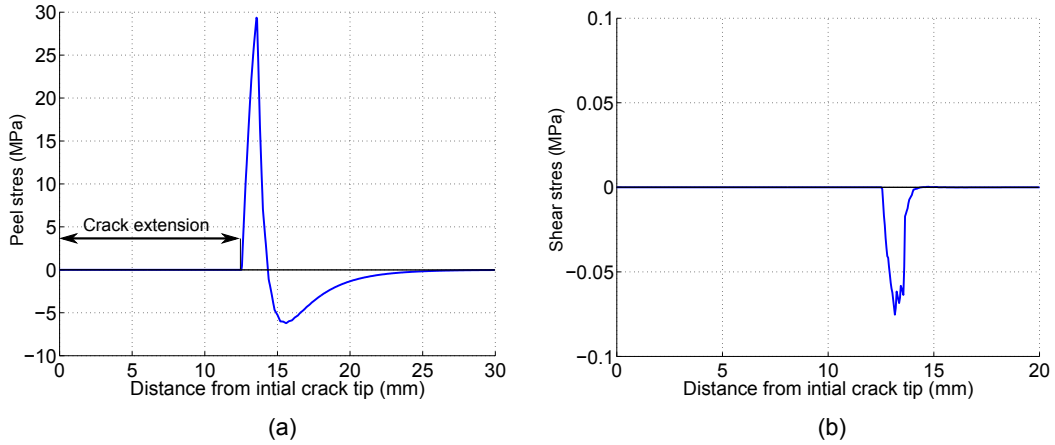

Figure 4.6: Interfacial (a) peel and (b) shear stresses over the delamination plane at prescribed displacement $\delta = 3$ mm (crack extension $\Delta a = 5.7$ mm).

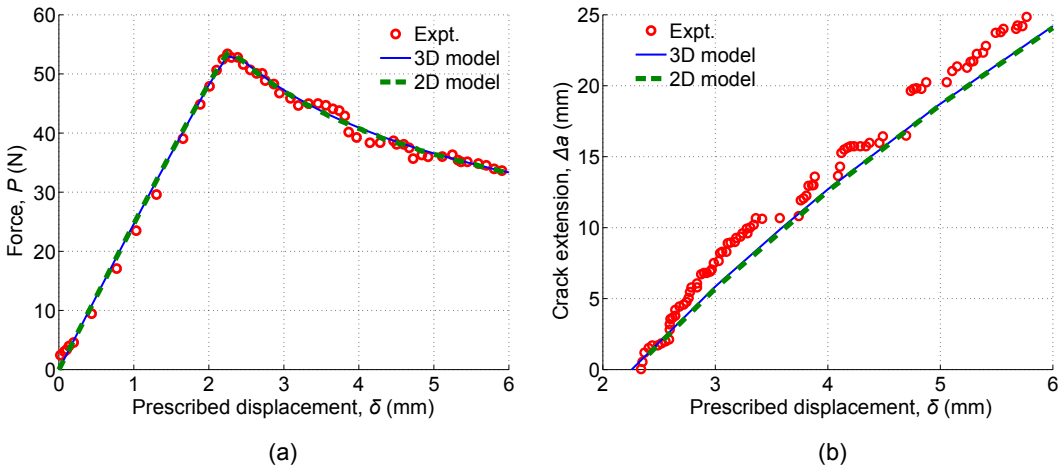

Figure 4.7: Comparison between 2D plane strain and 3D models: (a) force vs. prescribed displacement and (b) crack extension vs. prescribed displacement curves.

Three-dimensional model

The 3D model prediction of force versus relative displacement is compared with the 2D model and experimental results in Fig. 4.7a. The difference of prediction between the two models is very small ($< 0.1\%$). The crack extension predicted by the two models, plotted in Fig. 4.7b, is also consistent with the experimental data. The crack length of the 3D model is taken at the specimen XZ mid-plane in order to be comparable with the plane strain condition of the 2D plane strain model. As shown in Fig. 4.8, due to the free edge effect, the crack front assumes a thumb-nail shape, crack extension is more deep at the XZ symmetry plane (i.e. in the middle of the specimen).

Interfacial stresses along the XZ-symmetry plane are plotted in Fig. 4.8: on the left hand side peel stress of both 2D and 3D cases are presented; a slight difference can be noticed in the peak load position. On the right hand side shear stress distributions of the two models are plotted. The 3D model predicts a slightly higher stress peak than plane strain model, however, the maximum shear stress still remains small enough to be considered negligible.

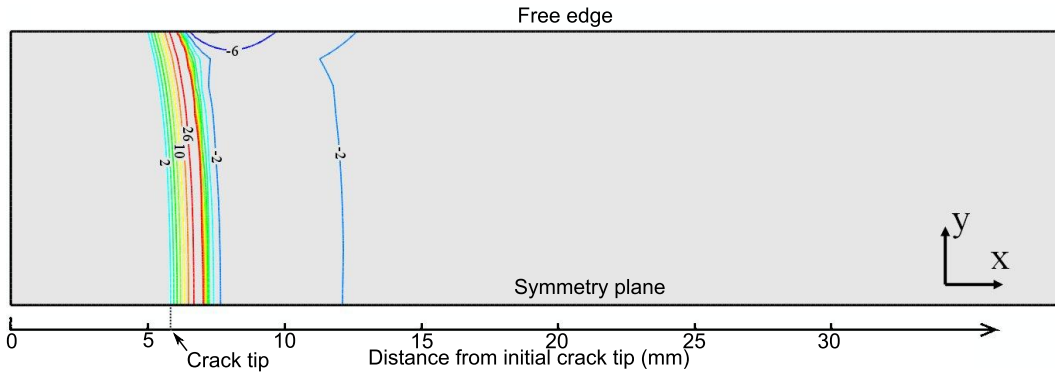

Figure 4.8: Peel stress ($sigma_{33}$) contour plot at prescribed displacement $\delta = 3$ mm (crack extension $\Delta a = 5.85$ mm. Unit: MPa.

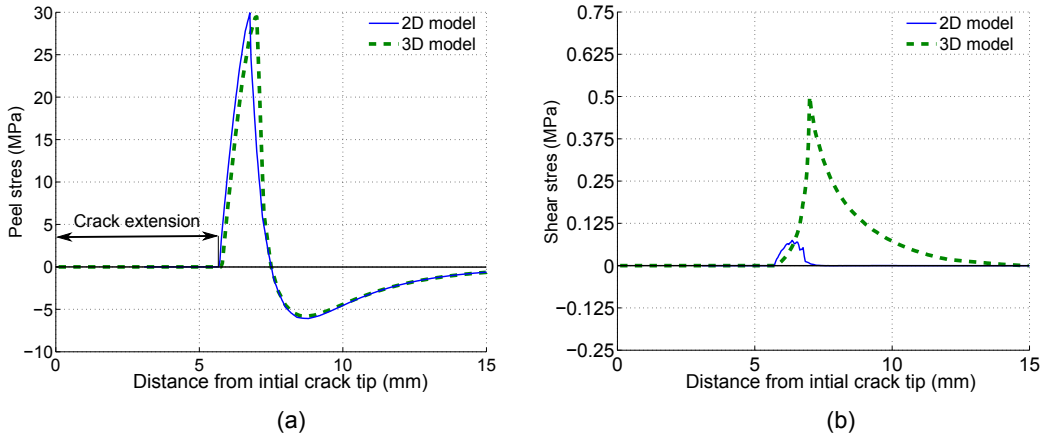

Figure 4.9: Interfacial (a) peel and (b) shear stresses over the delamination plane at prescribed displacement $\delta = 3$ mm (crack extension $a\Delta = 5.85$ mm).

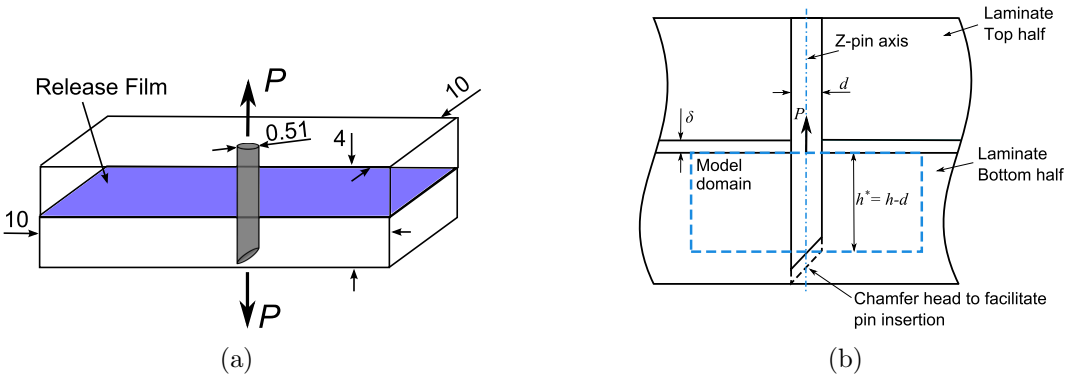

Figure 4.10: Geometry of single pin pullout test: (a) schematic of a test specimen; b) FE model domain.

4.3 Z-pin reinforced mode-I delamination test

4.3.1 Single-pin pullout model

Test geometry and model description

Numerical model presented here is taken from the experimental test published in [68]. Test specimen was made of 32 unidirectional plies of IMS/924 prepreg resulting in 4 mm nominal thickness. A thin film was inserted in the mid plane to separate the laminate into two halves to avoid any interaction between the two parts. A z-pin of 0.51 mm diameter was inserted by an ultrasonic hammer. A 10 x 10 mm test piece was then cut off with the z-pin positioned in the middle as shown in Fig. 4.10a. Two end-tabs were bonded to the laminate free surfaces to facilitate load application in the test machine. The test was performed under displacement-controlled loading condition and the resultant force was recorded.

Only the part of the specimen in the half containing the pin chamfer tip was modelled as indicated in Fig. 4.10b. The chamfer is not considered to influence the pin pullout resistance; hence the model thickness (h^*) is reduced by the height of the chamfer (d). The remaining part of the specimen beyond the model domain is assumed to have linear elastic behaviour that was modelled by an elastic spring with stiffness k. Fig. 4.11a shows half of the model domain due to symmetric geometry.

An axi-symmetric FE model was used as shown in Fig. 4.11b. The model uses a surface to surface algorithm to calculate the normal contact stress and the coulomb friction. The curing process is modelled by applying a temperature variatioin from 180° C to 25° C. Thermal residual stresses are calculated and saved in the model as the initial condition in order to maintain displacement compatibility. A pullout force is then applied at the pin top surface under

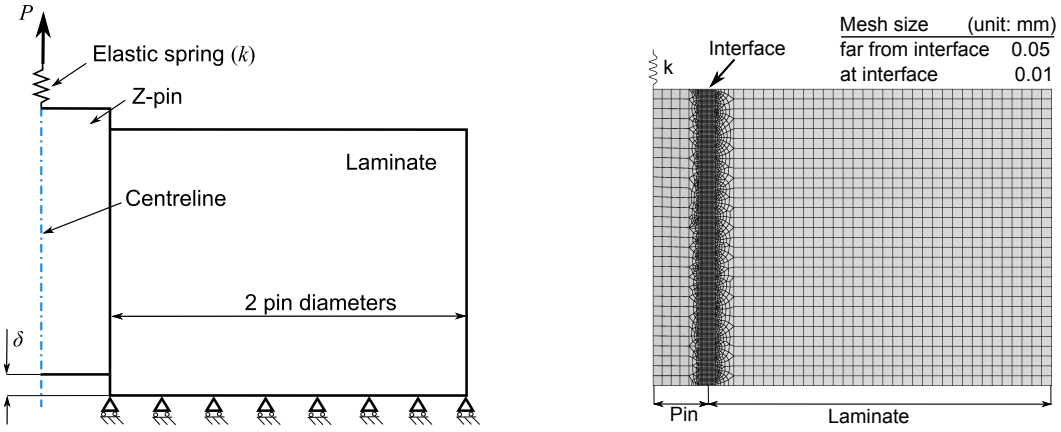

Figure 4.11: Single-pin unit-cell model: (a) axi-symmetric model and boundary conditions; (b) Mesh used for the FE analysis.

Table 4.3: Z-pin material properties used for the single-pin pullout model (T300/BMI). Material properties from [67]

E_{11}	E_{22}	E_{33}	G_{12}	G_{13}	G_{23}	ν_{12}	ν_{13}	ν_{23}	α
GPa									K^{-1}
120	30	30	4.6	4.6	3.9	0.35	0.35	0.4	0

the displacement controlled loading condition. Non-linear geometry effects are included. Numerical simulation runs until the pin is completely pulled out.

Numerical results

Commercial FE software package Abaqus v6.9 was used for the analysis. Axi-symmetric quadrilateral quadratic elements (CAX8) are used in the model. Converged numerical results were achieved using the mesh shown in Fig. 4.11b; a refined mesh at pin-laminate interface, where the stresses are higher, and a relatively coarse mesh away from it. Material properties used in the analysis are given in Table 4.3 (z-pin) and Table 4.4 (laminate).

Mechanical properties of the pin surrounding laminate material used in the single-pin model are: $E = 11$ GPa, $\nu = 0.4$ and coefficient of thermal expansion

Table 4.4: Mechanical properties of IMS/924 used for z-pin reinforced DCB test samples [57]

E_{11}	E_{22}	E_{33}	G_{12}	G_{13}	ν_{12}	ν_{13}	G_{IC}
GPa							kJ m^{-2}
138	11	11	4.4	4.4	0.34	0.34	0.25

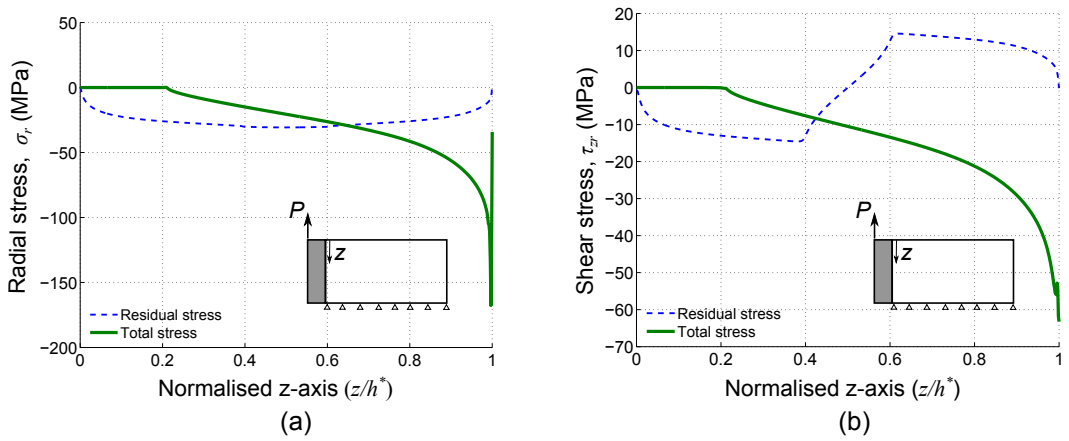

Figure 4.12: Stress distribution along the pin at pin/laminate interface: dash line represents thermal residual stress after the curing process, solid line is the total stress at the peak pullout load. (a) Normal (radial) stress, σ_r ; (b) Shear stress, τ_{zr}.

$\alpha = 2.4\text{x}10^{-5}$ K^{-1}. Although pin surrounding material is mainly the resin matrix, the mechanical property is not the same as the pure resin due to the existence of fibres. Therefore, laminate transverse properties were used for the material close to the pin. The temperature difference applied to simulate the curing process is $\Delta T = -155°$ C. Residual stress field is a function of the temperature change, model dimension, coefficients of thermal expansion and Young's modulus of the pin and surrounding material in the radial direction.

The normal and shear stresses along the pin/laminate interface are presented in Fig. 4.12. Following observations can be made. First, curing process induced thermal residual stress in the pin radial direction (σ_r) is negative, about 30 MPa, indicating that the pin is under compression by surrounding material. This initial contact stress causes friction resistance when a pullout load is applied. The residual shear stress (τ_{zr}) is a balanced distribution of 15 MPa. Second, at the maximum applied load, the surrounding laminate is subjected to shear deformation resulting in the pin under high shear stress at the pin end (Fig. 4.12b), which in turn increases the contact pressure at the lower part of the pin (Fig. 4.12a). This increased contact pressure adds extra resistance to the pin pullout. The level of this contact stress is related to the laminate shear deformation, which depends on the aspect ratio of embedded pin length to pin diameter, h^*/d (Fig. 4.10b). Therefore, the average friction resistance cannot be regarded as a constant for different geometries. Fig. 4.13 shows the dependency of average shear stress on the ratio h^*/d. The larger the ratio, the lower the average shear stress will be.

Calculated pin pullout force versus displacement relation under displacement controlled loading condition was correlated with the test measurement in [68] in order to calibrate two constants used in the numerical model: the stiffness of the elastic spring (k), see Fig. 4.11a, and the friction coefficient (μ). Parameter

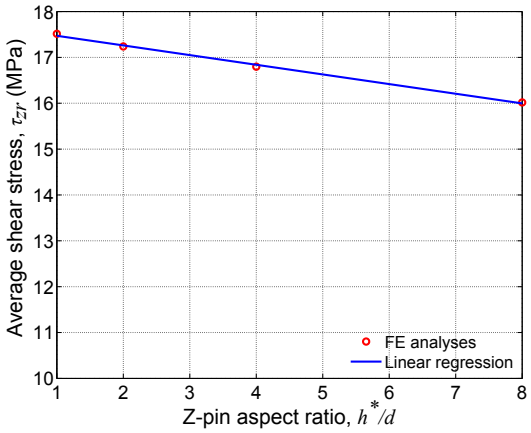

Figure 4.13: Influence of z-pin aspect ratio (h^*/d) on the average shear stress.

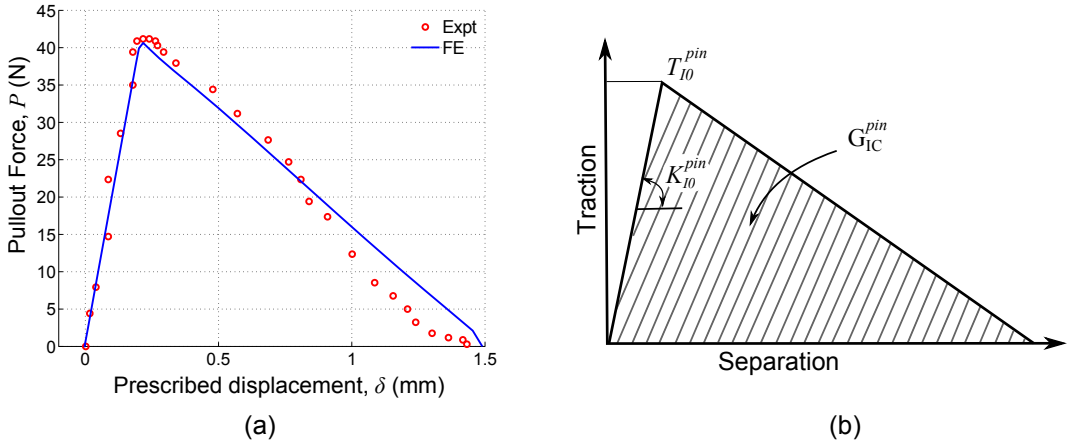

Figure 4.14: (a) Pin pullout force vs. displacement comparison between FE analysis and test measurement [68], (b) schematic of traction–separation law based on the derived force–displacement relation.

k influences mainly the initial slope, whereas μ affects the slope of the second part of the curve. With $k = 200$ kN/m and $\mu = 0.75$, the model agrees with the test result very well as shown in Fig. 4.14a.

These two parameters were then kept constant to evaluate z-pin bridging forces of other geometries. The curve second part where the pin is progressively pulled out of the laminate has a constant descending slope until the last point where the slope of the curve slightly increases. This is due to the lower contact stresses close to the laminate free surface and the consequently reduced friction resistance (Fig. 4.11a).

Fig. 4.14b is a schematic of the traction-separation law, i.e. cohesive zone model, describing the pin bridging effect. It is deduced from the pin pullout force versus displacement relation in Fig. 4.14a. The law is defined by three parameters, i.e. the initial stiffness (K_{IO}^{pin}), the cohesive strength (T_{I0}^{pin}) and

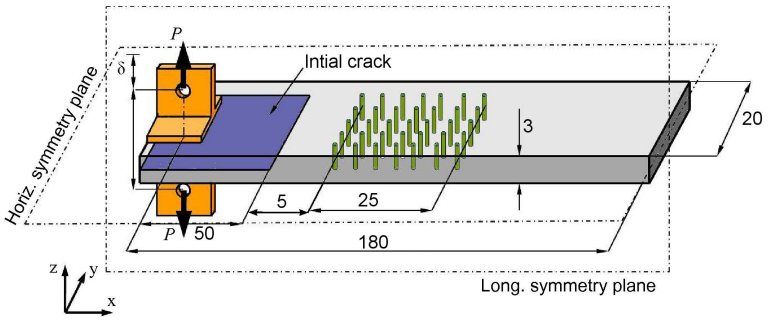

Z-pin parameters

Pinned area (%)	Pin diameter (mm)	Pin Pitch (mm)
2	0.51	3.1
2	0.28	1.55
0.5	0.28	3.5

Figure 4.15: Geometry and dimension of the z-pinned DCB test specimen (unit: mm).

Table 4.5: Cohesive law parameters used for the z-pin reinforced mode-II delamination tests.

Plain laminate			Pin bridging cohesive law			
K_{I0} (N/m^3)	T_{I0} (MPa)	G_{IC} (kJ/m^2)	Pin diameter: d (mm)	K_{I0}^{pin} (N/m^3)	T_{I0}^{pin} (MPa)	G_{IC}^{pin} (kJ/m^2)
$1x10^{14}$	30	0.25	0.28	$1.97x10^{12}$	360	240
			0.51	$8.10x10^{11}$	160	89

the fracture toughness (G_{IC}^{pin}). This law can be implemented into a macro-scale structural model (DCB in this specific case) for calculating delamination growth in pinned laminates.

4.3.2 Marco-scale model of DCB tests

Geometry and model description

Pinned and unpinned DCB test specimens taken from [68] were modelled. Geometry and dimension are shown in Fig. 4.15. Each specimen was made of 24 plies of unidirectional prepreg of IMS/924 resulting in 3 mm nominal thickness[1]. Mechanical properties of the laminate are summarised in Table 4.4. An initial crack of 50 mm length was made by inserting a thin polyamide film in the mid-plane of the specimen. Z-pins were made of pultruded T300/BMI. Pinned area starts 5 mm from the initial crack tip[2] lasting 25 mm in length and covering the entire specimen width. Three pin configurations of variable pin diameter and pin areal density were modelled; these parameters are summarised in Fig. 4.15 insert.

Two different FE models have been developed: a complete model ("whole" model) representing half of the specimen geometry (Fig. 4.16a), and a sim-

[1]Measured laminate thickness is 3.2 mm for unpinned and 3.3 for pinned specimens.

[2]The distance of reinforced area from initial crack tip is only 1 mm in the configuration 3 specimen (as labelled in Fig. 4.15)

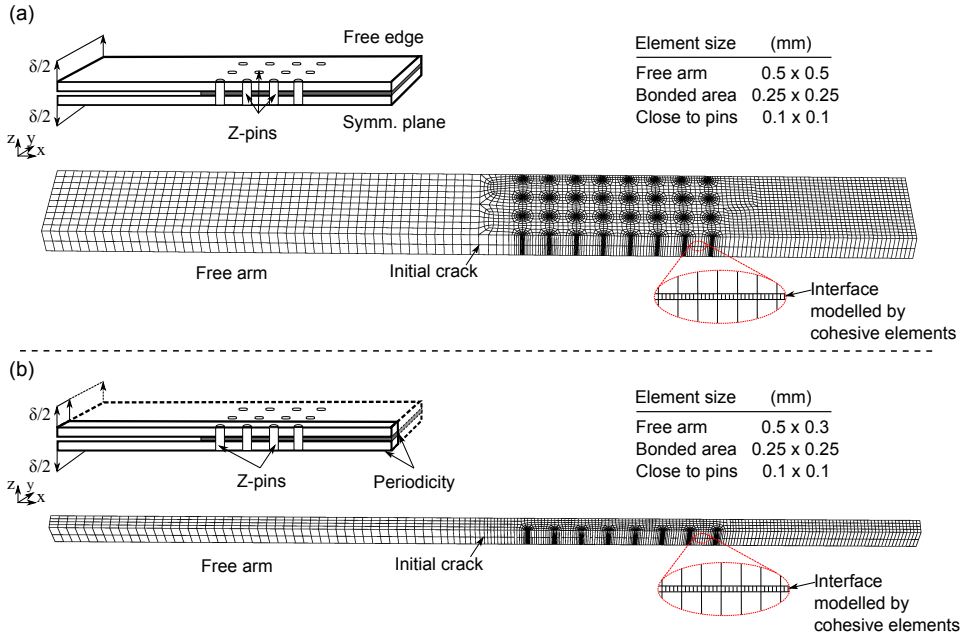

Figure 4.16: FE models of DCB specimen using two layers of shell elements and cohesive elements at interface: (a) whole model representing half of the DCB specimen (b) unit strip model for half of a pin row.

plified "unit-strip" model (Fig. 4.16b) by exploiting the periodic pin arrangement. The unit-strip represents one half of a pin row in the mid-width and the surrounding laminate of the dimension of a periodical repeating unit. The y-axis deformation is constrained; hence it neglects the free-edge effects. However, the much reduced model size allows significant saving in computational effort. In both models, 8-node linear continuum shell elements with reduced integration (CS8R) were used for the laminate beams and 8-node cohesive elements (COH8) for the bonding interface. Cohesive element parameters used for analyses are summarised in Table 4.5. Element size in cohesive zone is one fifth of the adjacent shell element (Fig. 4.16 insert), in order to achieve numerical stability.

Numerical results

Calculated force versus displacement and crack extension versus applied displacement for the three pin configurations and comparison with the test results in [68] are presented in Figs. 4.17–4.19. The first two cases (pin areal density $A_p = 2\%$ with pin diameter $d = 0.51$ mm, and $A_p = 0.5\%$ with $d = 0.28$ mm) were simulated by both the whole and unit-strip models; the third case ($A_p = 2\%$ with $d = 0.28$ mm) was modelled only by the unit-strip model due to the excessive computational cost of the complete model.

All three cases show similar trends in the load-displacement curves that are

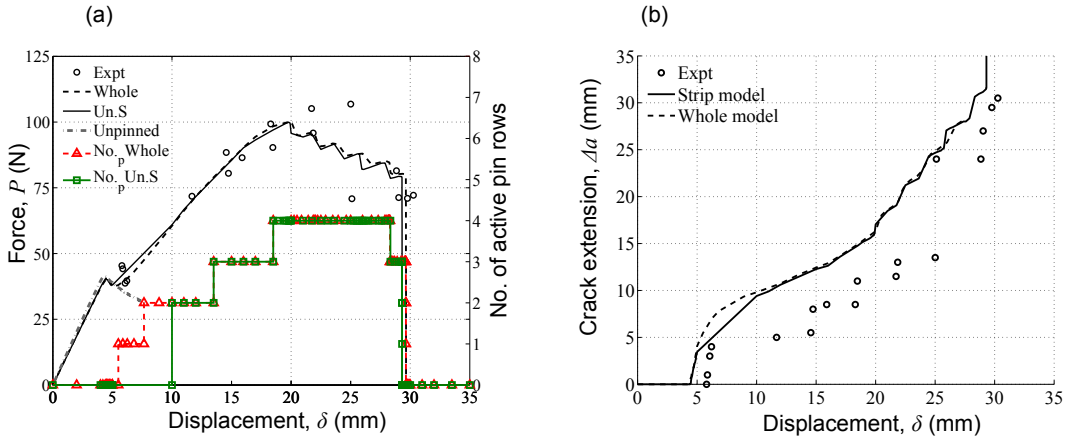

Figure 4.17: Comparison between experiment and simulation (pinned laminate: $A_p = 2\%$, $d = 0.51$ mm), (a) Applied force vs. opening displacement; also showing the number of active pin rows in the crack wake (right-hand y-axis), (b) crack extension vs. opening displacement.

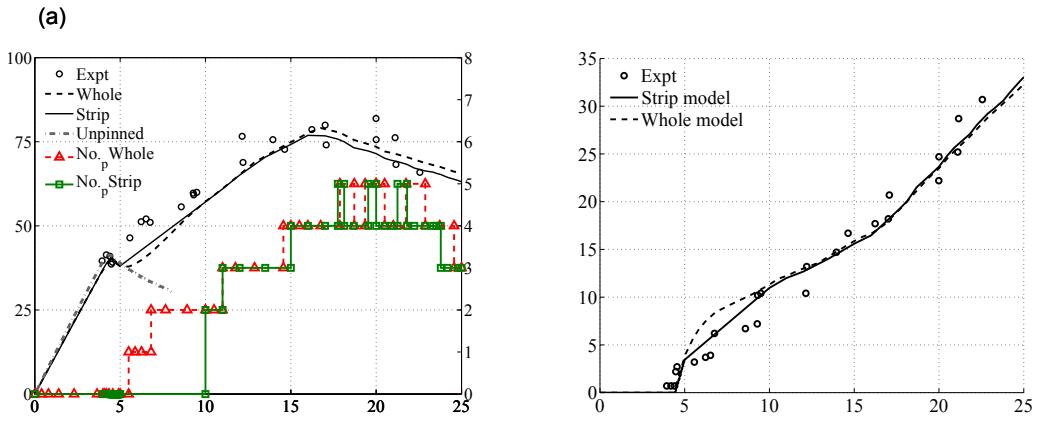

Figure 4.18: Comparison between experiment and simulation (pinned laminate: $A_p = 0.5\%$, $d = 0.28$ mm): (a) Applied force vs. opening displacement; also showing the number of active pin rows in the crack wake (right-hand y-axis), (b) crack extension vs. opening displacement.

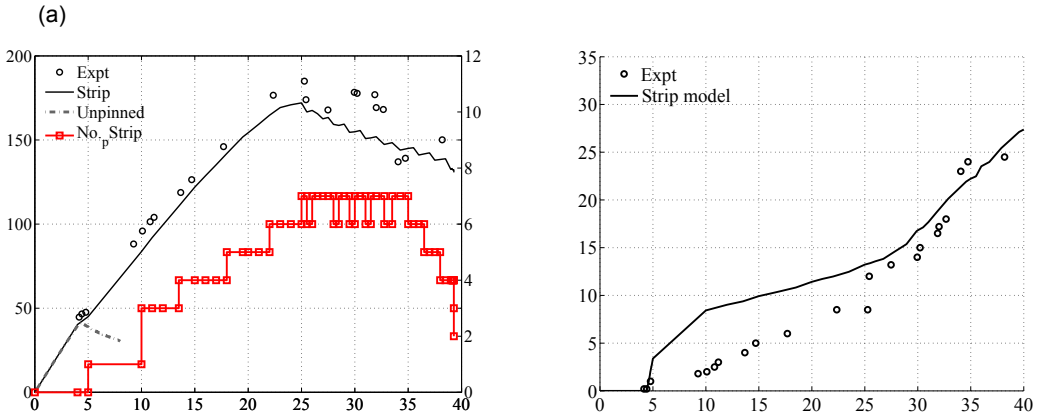

Figure 4.19: Comparison between experiment and simulation (pinned laminate: $A_p = 2\%$, $d = 0.28$ mm): (a) Applied force vs. opening displacement; also showing the number of active pin rows in the crack wake (right-hand y-axis), (b) crack extension vs. opening displacement.

also plotted together in Fig. 4.20. Following observations are made. First, an elastic response is observed at the beginning, and the initial delamination crack starts propagating at the same load level (about 41 N) for the pinned and unpinned specimens. This indicates that initial delamination growth before the crack tip entering the pinned region is controlled by the toughness of the plain resin regardless the specimen is pinned or not. Second, as soon the delamination crack starts growing the load has a small drop (at about 41 N). For the unpinned specimen the load decreases from here continuously and monotonically after the peak, whereas all pinned specimens can recover after the small load drop and pick up much more loads. Pin bridging effect starts as soon as the delamination crack passes the first pin row. Crack tip is shielded from the crack opening force when pins are bridging the crack wake; consequently crack growth slows down (Fig. 4.20b) and the load recovers from the small drop at the delamination onset and increases to a maximum. Third, the crack bridging length is a good indicator of the bridging effect. The parameter is defined as the length of the crack wake where the pins are still active, i.e. not yet being pullout completely. This information is presented in terms of the number of active pin rows indicated on the right-hand-side y-axis of Figs. 4.17a–4.19a. It shows that the bridging length increases as the number of active pins rises. Active pin number reaches a saturate value at the maximum load; from this point onwards, whenever the delamination crack passes a new pin row, pins in the far end row of the bridging area will be pulled out, maintaining the "active" pin number almost constant. However, the bridging force of the active pins in the crack wake is not constant during delamination growth. This causes the characteristic "slip-stick" behaviour, which is demonstrated by the oscillating force curve after the peak force.

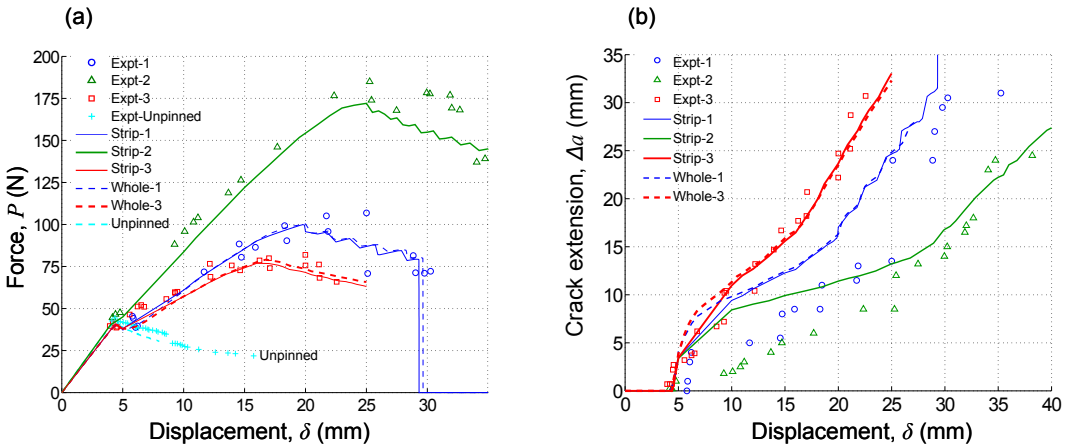

Figure 4.20: Summary of numerical results: (a) applied force vs. opening displacement, (b) crack extension vs. opening displacement. Plotted configurations: case 1: $A_p = 2\%$, $d = 0.51$ mm, case 2: $A_p = 2\%$, $d = 0.28$ mm, case 3: $A_p = 0.5\%$, $d = 0.28$ mm.

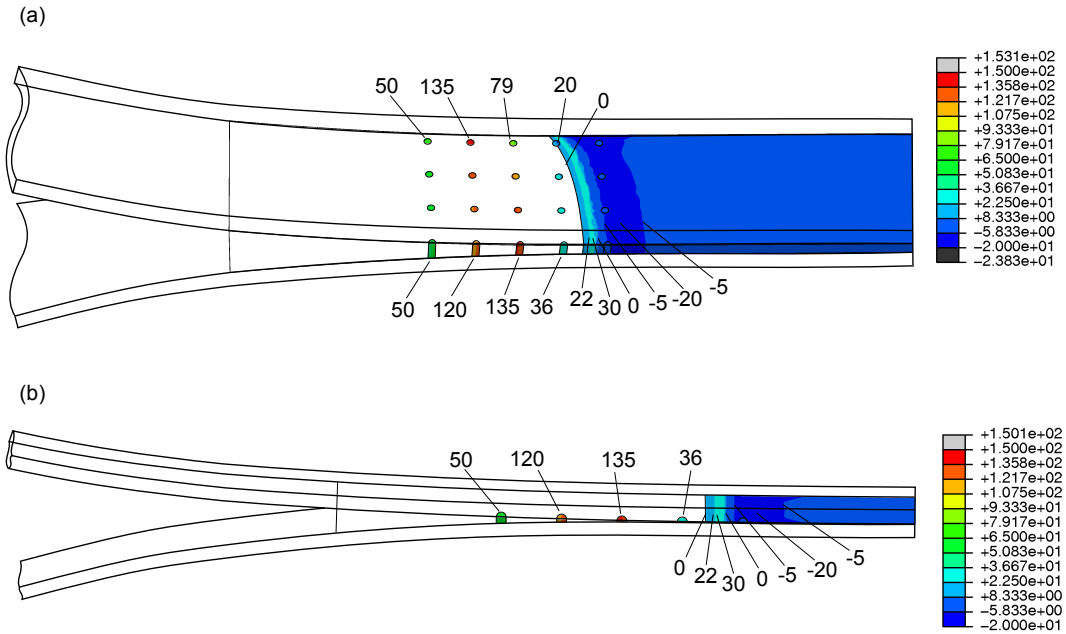

Figure 4.21: Peel stresses at interface: (a) whole model, (b) unit strip mode (Unit: MPa).

For the same specimens, crack extension length versus applied displacement is plotted in Figs. 4.17b–4.19b and also in Fig. 4.20b. It should be pointed out that in the experiment crack lengths were measured by visual observation; therefore the comparison of this parameter may be more qualitative than quantitative. For all three cases delamination crack starts growing at the same applied displacement. After an initial fast growth, crack growth rate become much slower in the first stage when the number of "active" pin at the crack wake increases. After the peak force, crack growth rate increases again. Final unstable failure occurs when the crack tip passes the pin reinforced area and the number of active pins in the crack wake drops to zero. In all three cases the model has slightly underestimated the load capability, i.e. the model is conservative, with an error range of 5-10% (Fig. 4.20a). For the crack extension prediction (Fig. 4.20b), discrepancy between the model and experiment is much larger especially at the early crack growth stage ($\Delta a = 0 - 15$ mm), after which the model and experimental results are in reasonably good agreement.

Fig. 4.21 shows the values of interlaminar peel stresses at the delamination plane during the steady crack growth stage at applied displacement $\delta = 25$ mm (for z-pin parameter $A_p = 2\%$; $d = 0.51$ mm). It demonstrates that active pins in the crack wake shield the crack from suffering the full crack opening displacement. Consequently the pins are subject to high peel stresses. The whole model predicts faster crack growth at the specimen centre (on the longitudinal symmetry plane) as depicted crack front profiles in Fig. 4.21a. Since the unit-strip model represents a centre strip of the specimen containing the mid-row pins and neglects the free edge effect, the modelled crack front is just the crack tip position. Both models predict a bridging length equal to four pin pitch size (as indicated by the four active pins subjected to tensile stress), demonstrating therefore the large-scale bridging scenario.

Both the whole and unit-strip models predict the same delamination growth and failure loads with negligible difference. However, the computation effort required by the whole model is significantly greater as the computing time is seven times higher. Comparison of the computational effort of the two models is given in Table 4.6. Finally, this modelling approach can be applied for through-thickness reinforcement using larger diameter pins or rods in lower areal density.

4.4 Unreinforced mode-II delamination test

4.4.1 Geometry and model description

Experimental data used for validating the model were gathered Asp in [133]. Specimen geometry and preparation is the same as for mode-I test, described in

Table 4.6: Summary of computational efforts of whole and unit-strip models.

Case	No. of elements		Computational time (h)	
	Unit-strip (k)	Whole model (k)	Unit-strip	Whole model
Unpinned DCB	–	15	–	0.5
$d = 0.51$ mm, $A_p = 2\%$	30	80	0.8	6.5
$d = 0.28$ mm, $A_p = 0.5\%$	35	90	1	7
$d = 0.28$ mm, $A_p = 2\%$	40	120	1.2	–

Sec.4.2.1 (material properties are summarised in Table 4.1). The delamination test is performed using a three-point bending testing rig. Fig. 4.22 shows 3-pt bend ENF test set up, geometry and load conditions. The initial crack length plays a crucial role in the failure behaviours of this testing configuration: in order to have a stable crack propagation the initial crack length has to be longer than a critical dimension. The stable crack propagation analysis summarised in the following section is important to understand and interpreter test results presented later in this chapter.

Stable crack propagation condition

Let consider the ENF test geometry, as depicted Fig. 4.22. Load characteristic generated by the load applied in the 3-pt bending test are depicted in Fig. 4.23. The strain energy release rate (G_{II}) is the energy delivered by the system due to a small crack increment da is:

$$G_{II} = \frac{P^2}{2B}\frac{dC}{da} \tag{4.3}$$

Where C is the system compliance, the inverse of stiffness:

$$C = \frac{\delta}{P} \tag{4.4}$$

According to the elementary beam theory the relationship between applied force and centre line displacement of a beam having two different bending properties, for respectively the cracked and undamaged parts, is:

$$\delta = \frac{P}{(EI)_2}\left[\frac{L^3}{48} + \frac{a^3}{12}\left(\frac{(EI)_1}{(EI)_2} - 1\right)\right] \quad 0 \leq a \leq L/2 \tag{4.5}$$

Where $(EI)_1$ and $(EI)_2$ are the bending stiffness of respectively cracked and integer beam sections. Note that the first term in the square bracket of Eq. (4.5) represents the solution of the simply supported beam. The solution for

$a \geq L/2$ can be found mirroring the problem. The relationship between applied force and centre line displacement is therefore:

$$\begin{cases} \delta = \frac{P}{8WEh^3}\left[\frac{L^3}{4} + 3a^3\right] & 0 \leq a \leq L \\ \delta = \frac{P}{8WEh^3}\left[3a^3 - 9a^2L + 9aL^2 - 2L^3\right] & L/2 \leq a \leq L \end{cases} \tag{4.6}$$

Using Eq. (4.6) to calculate the compliance derivative and substituting in Eq. (4.3), it is possible to obtain the following relation:

$$\begin{cases} G_{II}(P,a) = \frac{9P^2}{16W^2}\frac{a^2}{Eh^3} & 0 \leq a \leq L/2 \\ G_{II}(P,a) = \frac{9P^2}{16W^2}\frac{(L-a)^2}{Eh^3} & L/2 \leq a \leq L \end{cases} \tag{4.7}$$

Expression 4.7 gives the strain energy release rate (G_{II}) for any combination of force P and crack length a. G_{II} is a quadratic function of the applied load; when the critical strain energy release rate (G_{IIC}) is reached crack stars opening. It worth noticing that, at fixed load (P constant) the derivative of G_{IIC} respect to the crack length is positive for any a, P until $a < L/2$, i.e. the crack propagation is unstable until crack dimension is smaller than half of the specimen length, then it becomes stable. However, delamination tests are performed under displacement loading control. For the first part of delamination ($a \leq L/2$),Eq. (4.7) can be written in function of prescribed displacement:

$$G_{IIC} = 4Eh^3\delta^2\frac{9a^2}{\left(\frac{L^3}{4} + 3a^3\right)^2} \tag{4.8}$$

Calculating then the derivative of G with respect to the crack length a for fixed displacement (δ constant), it is possible to obtain the stable crack growth condition:

$$\frac{\partial G_{IIC}}{\partial a} \leq 0 \tag{4.9}$$

$$\frac{a}{L} \geq \frac{1}{2\sqrt[3]{3}} \tag{4.10}$$

Eq. (4.10) shows that for small cracks, delamination growth is unstable. For a specimen of length $L = 100$ mm, the minimum crack length that meet the stable crack propagation requirement is $a_0 = 35$ mm.

Two-dimensional plane strain model

A two-dimensional FE model was constructed to predict the mode-II interlaminar delamination growth of composite laminates. The model used 8-node quadratic plane strain elements with reduced integration (designated as CPE8R in Abaqus) for the composite laminate beams and 4-node cohesive elements, governed by a bilinear traction separation law, for the bonded

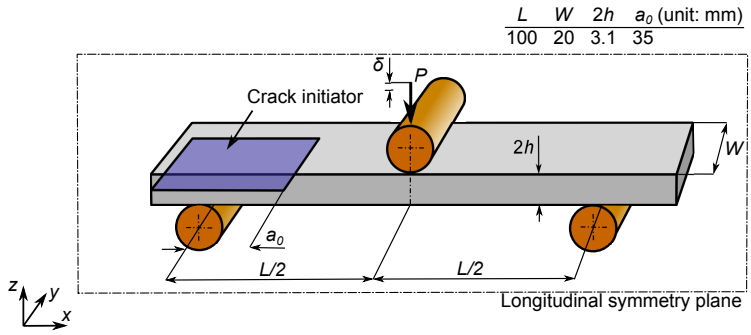

Figure 4.22: Geometry of unreinforced mode-II delamination test.

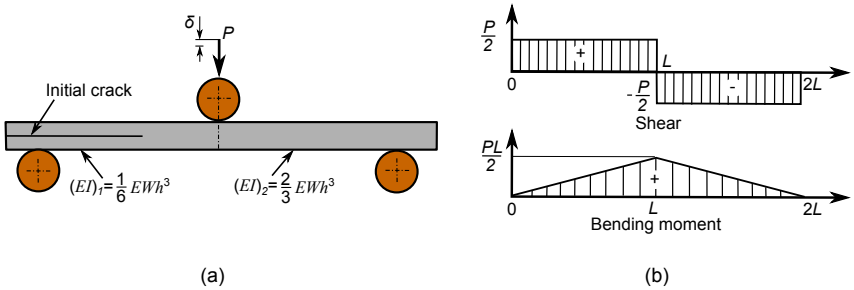

Figure 4.23: ENF test specimen: (a) beam bending properties, (b) load characteristics.

interface. The interaction between top and bottom laminate beams was modelled as a friction less contact using a surface-to-surface algorithm. Quadratic elements have been preferred to linear ones (used for modelling the mode-I DCB delamination test instead) due to their better performance with the contact algorithm. The simulation was run under displacement loading control by imposing a displacement of δ to the node of the top laminate beam at the centreline between the two simple supports (Fig. 4.24a).

Zero thickness cohesive elements have been used to model the crack propagation in order to maintain the beam section properties, which would be modified if the two beams were separated of the cohesive element thickness. The mesh size depicted in Fig. 4.24a was chosen after a mesh sensitivity study; the co-

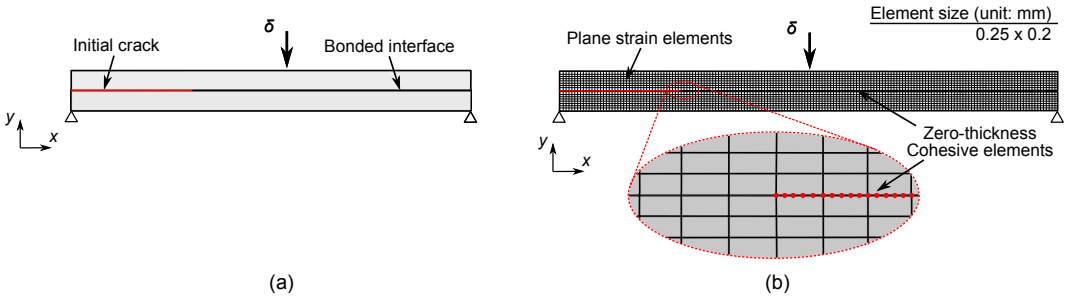

Figure 4.24: Plane strain model of the unpinned ENF specimen (a) geometry and boundary conditions, (b) mesh used for analysis.

Table 4.7: Cohesive elements parameters for unreinforced ENF model

Initial stiffness K_{II0}	Cohesive strength T_{II0}	Fracture toughness G_{IIC}
2 x 10^{14} N/m^3	90 MPa	880 J/m^{-2}

* [57]
Other cohesive parameters have been set to achieve numerical stability as described in [124-125]

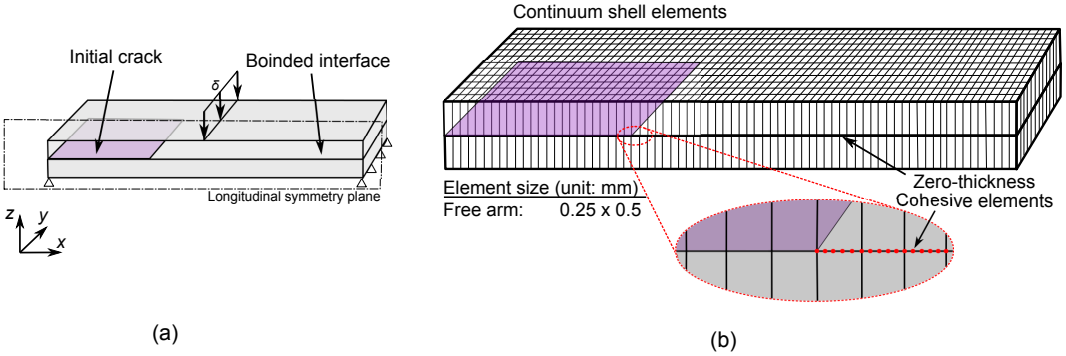

Figure 4.25: Three-dimensional model of the unpinned ENF specimen (a) geometry and boundary conditions, (b) mesh used for analysis.

hesive element size is one fifth of the laminate element size in order to achieve numerical stability during the crack propagation (Fig. 4.24b). Cohesive element properties used for analysis are summarised in Table 4.7.

Three-dimensional model

A three-dimensional model of the unreinforced ENF was constructed using 8-node linear continuum shell elements with reduced integration (designated CS8R in Abaqus) for the composite laminate beams and 8-node cohesive elements for the bonded interface. Boundary conditions, and material and cohesive properties were kept the same as for the plane strain model. Longitudinal symmetry (Fig. 4.1) was exploited, thus only one half of geometry modelled. Fig. 4.25 shows model geometry and mesh used for analysis.

4.4.2 Numerical results

Two-dimensional plane strain model

Calculated force versus displacement and crack extension versus prescribed displacement and comparison with the test results in [133] are presented in

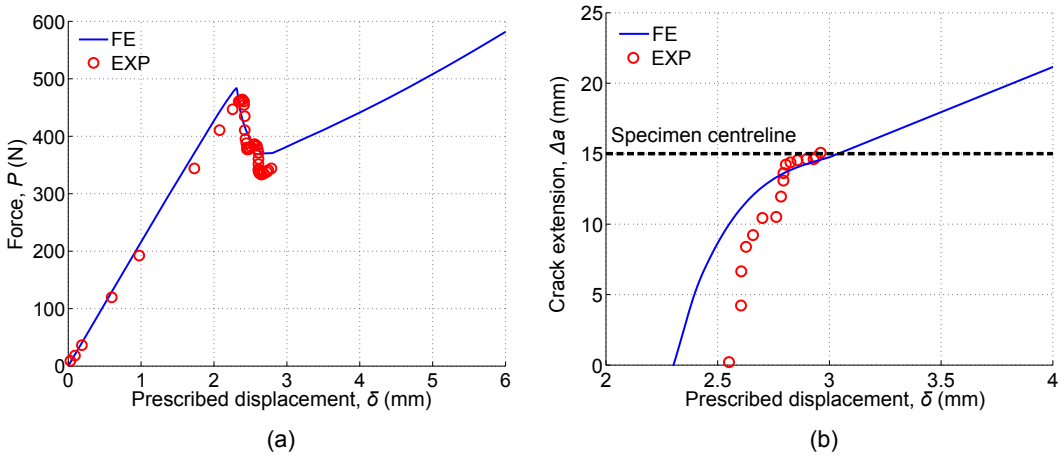

Figure 4.26: Comparison between FEA and experiment: (a) force vs. prescribed displacement and (b) crack extension vs. prescribed displacement curves.

Fig. 4.26. The FE analysis shows excellent agreement with experimental data. The model was able to predict the initial linear elastic response of the simply supported beam beam and the peak load at which a continuous and stable delamination crack started propagating, as shown in Fig. 4.26a.

When crack starts opening (at a prescribed displacement $\delta = 2.29$ mm) applied force drops quickly with displacement. The crack grows rapidly from initial value up to specimen centreline (crack extension $\Delta a = 15$ mm). As reported by Asp in [133], crack extension lengths are recorded during experimental test by visual observation using microscope. Visual detection of crack extension under sliding fracture mode is difficult because there is no actual separation between the two fractured surfaces. For this reason, some differences between FE prediction and experimental data are visible.

A slight difference in the initial stiffness of force-displacement curve can be noticed in Fig. 4.26a. This is attributed to the presence of a resin rich pocket at the initial crack front due to thickness film used to create the artificial crack. Specimen compliance is highly sensitive to the initial crack dimension. Due to this resin rich pocket the specimen behaves as if the initial crack was slightly longer. This effect is not modelled in the FE analysis and therefore, the consequence is a slight steeper slope of the model response. However, this difference of initial conditions does not affect the stable crack propagation behaviour.

Specimen failure is reached when the crack extension is approximately $\Delta a = 15$ mm (i.e. when the crack tip reaches the specimen centreline) due to the high bending stresses. In the FE analysis this failure mode is not taken into account and for this reason the model shows further load capabilities and crack continues propagating even beyond specimen centreline.

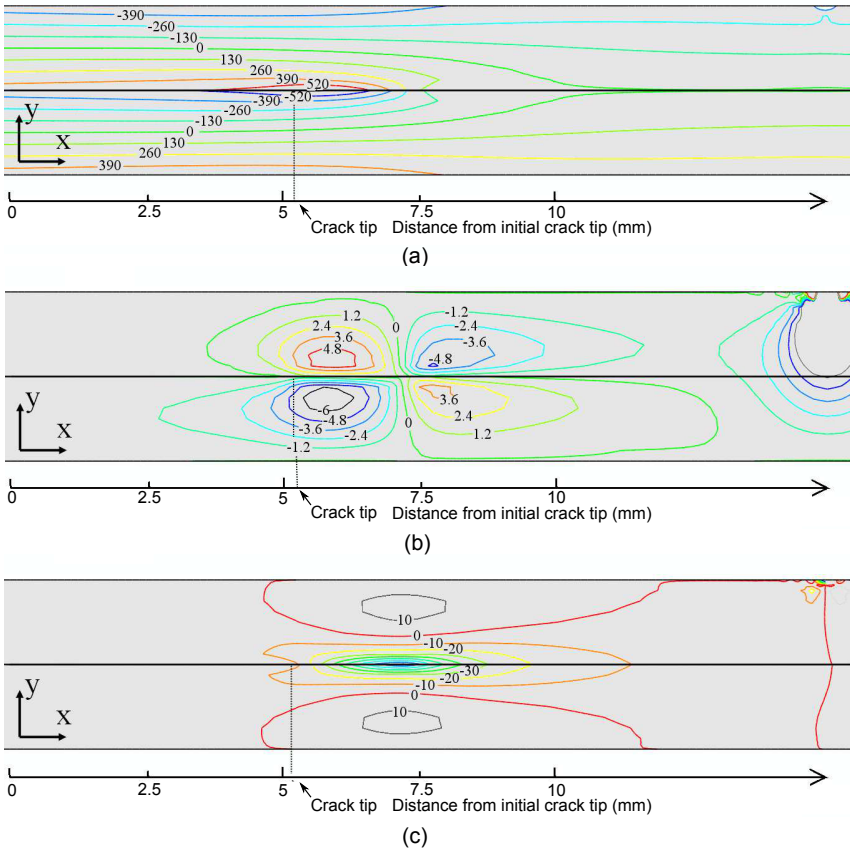

Figure 4.27: Stress contour plots at prescribed displacement $\delta = 2.4$ mm (crack extension $\Delta a = 5.2$ mm: (a) flexural bending stress (σ_{11}), (b) Normal stress in y-direction (σ_{22}), (c) In-plane shear (τ_{12}). Unit: MPa.

Fig. 4.5 shows the contour plots of stress components (σ_{11}, σ_{22} and τ_{12}) during the crack propagation phase (at applied displacement $\delta = 2.4$ mm; $\Delta a = 5.2$ mm). Due to the loading condition of the composite beam flexural bending stress (σ_{11}) is the dominant stress contribution (Fig. 4.27a). Fig. 4.5b shows the σ_{22} stress concentration at the crack tip. Due to the geometry symmetry and the anti-symmetric loading condition, peel stress goes down to zero at the interface between the two beams. Shear stress (τ_{12}) at interface is the stress component influencing the crack advancement, as shown in Fig. 4.5c.

Shear and peel stress distributions over the delamination plane are plotted in Fig. 4.28. Near the crack tip shear stress has a peak value up to the cohesive strength of 90 MPa (Fig. 4.28b). Peel stress is compressive all over the interface a part the at process zone (Fig. 4.28b).

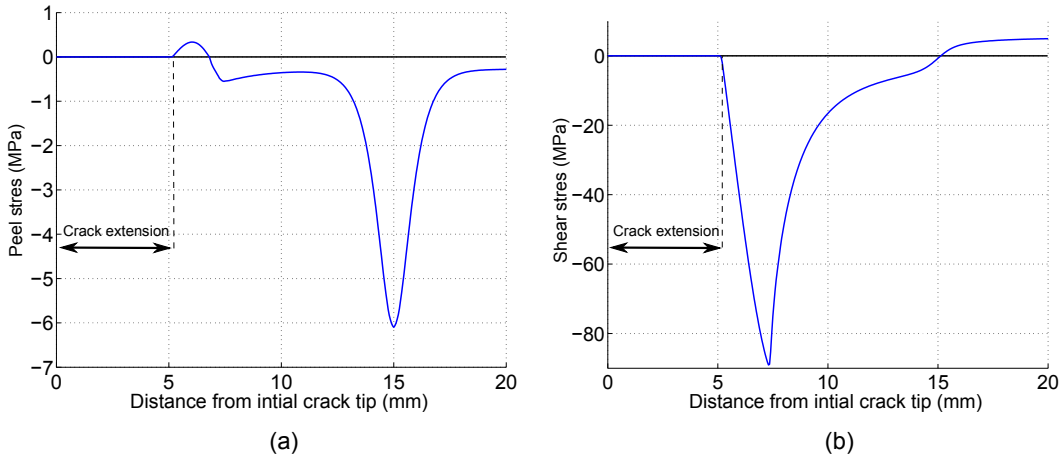

Figure 4.28: Interfacial (a) peel and (b) shear stresses over the delamination plane at prescribed displacement $\delta = 2.4$ mm (crack extension $a = 5.2$ mm).

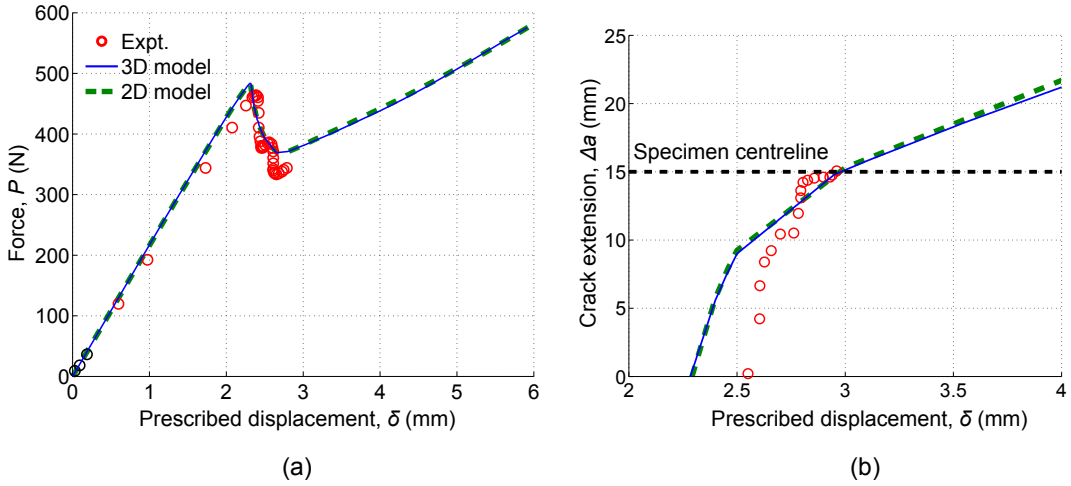

Figure 4.29: Comparison between 2D plane strain and 3D models: (a) force vs. prescribed displacement and (b) crack extension vs. prescribed displacement curves.

Three-dimensional model

The 3D model prediction of force versus relative displacement is compared with the 2D model and experimental results in Fig. 4.7a. The difference of prediction between the two models is very small ($< 0.5\%$). The crack extension predicted by the two models, plotted in Fig. 4.7b, is also consistent with the experimental data. The crack length of the 3D model is taken at the specimen XZ mid-plane in order to be comparable with the plane strain condition of the 2D plane strain model. Like in 2D case crack grows rapidly in from initial dimension to the centreline (crack extension 15 mm) and FE model over-esteems crack dimension respect to experimental results at early stages of crack propagation, when crack reaches dimensions close to the centreline FE model and measurements find more agreement.

As shown in Fig. 4.30, the free edge effect has a smaller effect on the shape of the crack front, which remains almost straight (i.e. in agreement with plane strain assumption).

Interfacial stresses along the XZ-symmetry plane are plotted in Fig. 4.30: on the left hand side peel stress of both 2D and 3D cases are presented. On the right hand side shear stress distributions of the two models are plotted; a slight difference can be noticed in the peak load position.

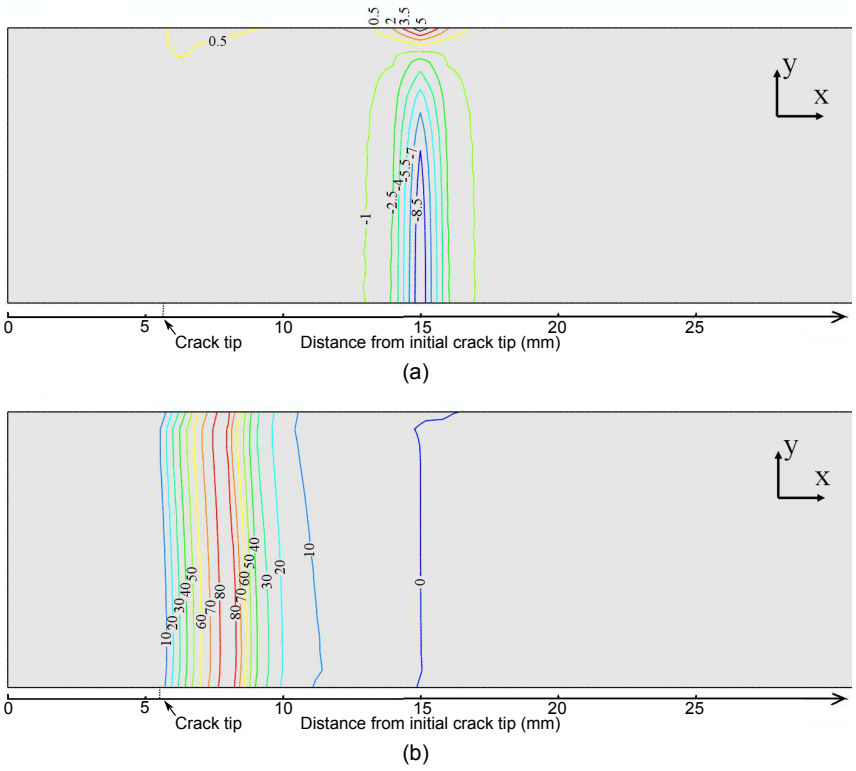

Figure 4.30: Contour plots of interfacial stress at prescribed displacement $\delta = 2.4$ mm (crack extension $\Delta a = 5.6$ mm. (a) peel stress ($sigma_{33}$), (b)shear stress (τ_{13}). Unit: MPa.

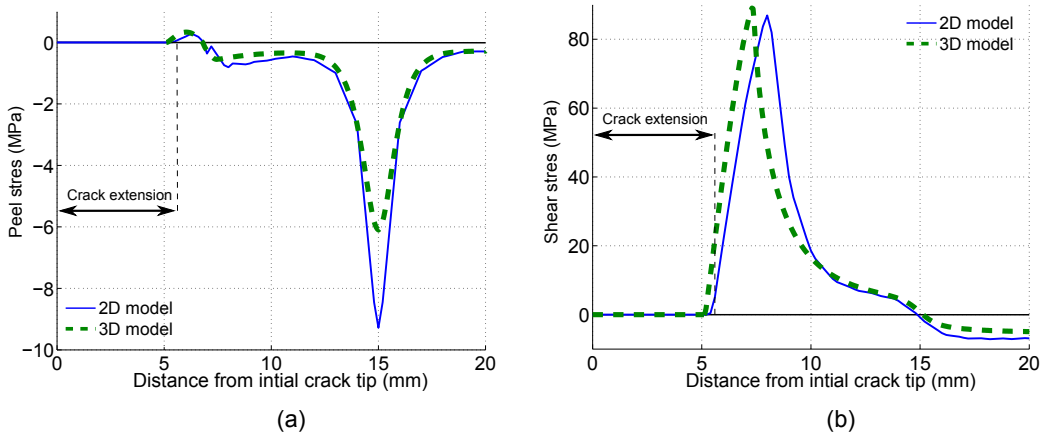

Figure 4.31: Interfacial (a) peel and (b) shear stresses over the delamination plane at prescribed displacement $\delta = 2.4$ mm (crack extension $a = 5.6$ mm).

4.5 Z-pin reinforced mode-II delamination test

4.5.1 Single-pin pullout model

Test geometry and model description

The analytical micro-mechanical model of single-pin pullout behaviour under mode II loading described in Sec.3.3.2 is used to evaluate the bridging force exerted by a carbon/epoxy z-pin. Experimental data presented here are taken from [68]. The test specimen comprises a 10 x 10 block of composite laminate, made of 32 unidirectional plies of IMS/924 prepreg resulting in 4 mm thickness, containing a centre delamination crack and a z-pin, made of carbon/epoxy T300/BMI of diameter $d = 0.51$ mm.

The z-pin was inserted into the fresh prepreg laminate using an ultrasonic hammer in order to minimize fibre breakage. Z-pin was provided with a chamfer head to facilitate insertion. However, the chamfer is not considered to influence the bridging behaviours of the pin, hence the model thickness (h^*) is reduced by the height of the chamfer.

The initial compressive residual stress σ_0 is estimated using Eq. (3.7), by imposing a temperature variation $\Delta T = 150°\text{C}$ during the curing process of the test specimen. Coefficients of thermal expansion of the pin and laminate are set as: $\alpha_{pin} = 0$ and $\alpha_{lam} = 2.4\,\text{x}\,10^{-5}$ K^{-1}.

Numerical results

Fig. 4.32 shows the force versus displacement curves of different configurations: variable pin diameter at fixed laminate thickness (Fig. 4.32a), and variable laminate thickness for a given pin diameter (Fig. 4.32b). All curves show similar characteristics as described below: (1) an initial linear elastic response before the force reaches 20 N, after which point the pin is subjected to larger deformation and ploughing into the laminate. During the ploughing phase despite the curve becomes more compliant it continuously increases to a maximum value. At this peak point one of the two failure criteria is met. One failure mode is the pin being gradually pulled out manifesting a linear decrease of the bridging force. When the pin is completely pullout, the displacement equals to the pin embed length. Another failure mode is abrupt pin rupture manifesting a sudden force drop (Fig. 4.32). Following consideration can be drawn: (1) both laminate thickness and pin diameter affect the pin pullout behaviour, and the load carrying capability is higher for larger pin diameter and thicker laminates; (2) pin rupture occurs more likely for smaller diameter pins inserted into thicker laminates; (3) the initial stiffness and maximum elastic force are higher for larger pins.

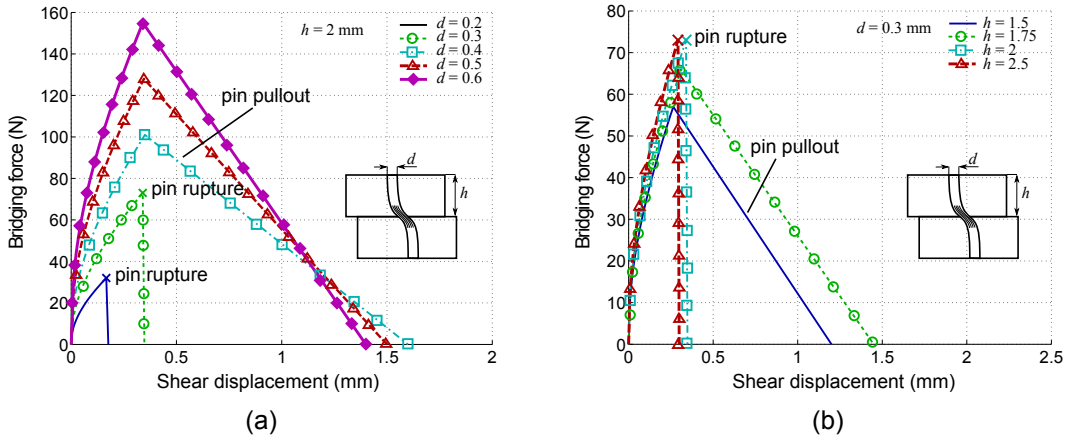

Figure 4.32: Influence of pin parameters bridging force: (a) effect of pin diameter, (b) effect of laminate thickness.

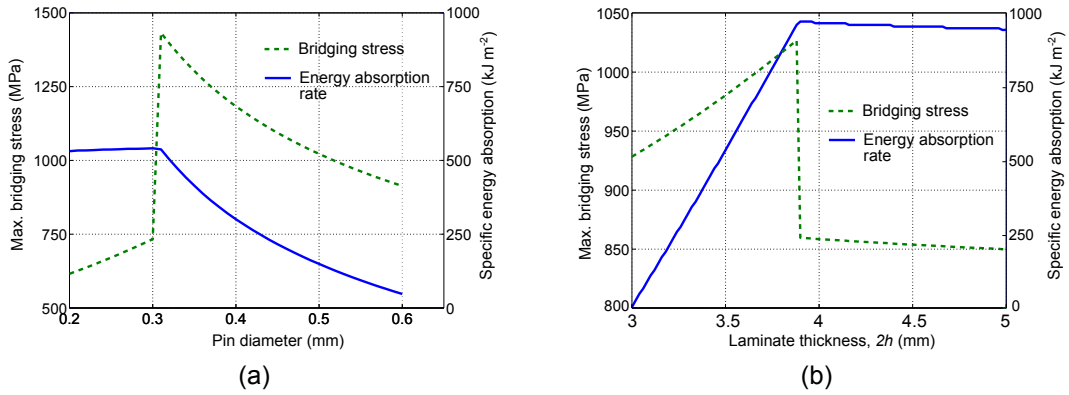

Figure 4.33: Maximum bridging stress and specific energy absorption as function of: (a) pin diameter and (b) laminate thickness ($2h$).

However, more meaningful parameters for the effectiveness of z-pins are the pin maximum bridging stress (force divided by pin cross-section area) and energy absorption rate (absorbed energy divided by pin cross-section area). Therefore graphs in Fig. 4.32 are re-plotted in Fig. 4.33 in terms of the two new parameters, on the left and right y-axis respectively. Model sensitivity to pin diameter and pin embedded length are plotted respectively in Figs. Fig. 4.33a-b. The big jumps in the curves (at $d = 0.31$ mm in Fig. 4.33a and $h = 1.9$ mm in Fig. 4.33b) indicate change of the failure mode. Smaller pin diameter or thicker laminate promotes pin rupture, resulting in much lower energy absorption rate by the pin. The most effective pin configuration is the one that fails in the pullout mode, but close to the pin rupture condition.

Calibration of model parameters has been performed using the single-pin test data published in [68]. Fig. 4.34 shows a comparison of the predicted and test measured bridging force versus displacement curves. The pins were not

Table 4.8: Micro-mechanical model parameters for the mode-II unit-cell model for carbon/epoxy z-pin.

Z-pin Young's modulus[a]	Laminate Young's modulus[b]	Friction coefficient[c]	Pin axial strength[a]	Pin shear strength[a]	Laminate punch strength[c]
E_{pin} (GPa)	E_{lam} (GPa)	μ	S_{pin} (MPa)	S_u (MPa)	p (N/mm)
123	11	0.77	1200	100	700

[a] Material properties from [88]

[b] Transverse stiffness of IMS/924 (Table 4.4).

[c] Calibrated by the experimental test [68]

placed exactly perpendicularly to the laminate surface as intended; they came out with a small variability of intended insertion angle[3] (Fig. 4.34). This insertion angle variability is characteristic of the technology used; therefore, the more realistic traction-separation law should be an average of all the possible bridging forces coming from different insertion angles. However, these considerations are beyond the scope of this thesis; the pin is thus supposed to be perfectly perpendicular to the laminate surface.

Two parameters have been used to calibrate the model: the friction coefficient μ and the laminate punch strength p (defined in Sec.3.3.2). The first parameter controls the occurrence of the fibre pullout; the higher the friction coefficient, the longer the pullout is delayed and the higher the ultimate force. The second changes the curvature of the pin response during the nonlinear phase. A higher punch strength results in a smaller portion of material affected by the pin ploughing and thus in a stiffer response of the pin (upward curve). The calibrated model parameters used in analyses are reported in Table 4.8

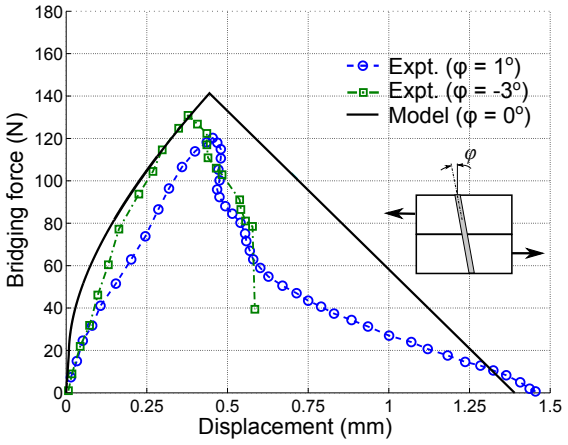

Figure 4.34: Comparison of the analytical model with experimental test result [68].

[3]Minus sign in the pin angle means that the pin tip points opposite to the direction of applied load.

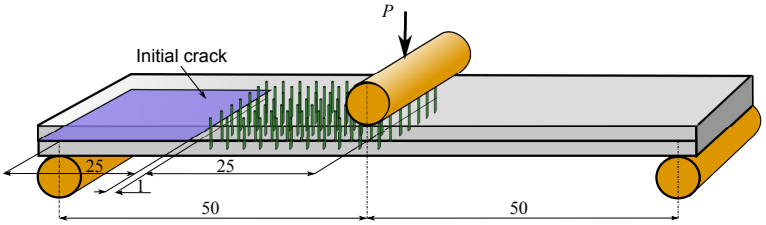

Z-pin parameters

Config. No.	Pin areal density (%)	Pin diameter (mm)	Pin pitch (mm)
1	2	0.51	3.1
2	2	0.28	1.55
3	0.5	0.28	3.5

Figure 4.35: Geometry and dimension of the z-pinned ENF test specimen (unit: mm).

4.5.2 Marco-scale model of ENF tests

Geometry and model description

Pinned and unpinned ENF specimens taken from [68] were modelled as shown in Fig. 4.35. Each specimen was made of 24 plies of unidirectional prepreg IMS/924 resulting in 3 mm nominal thickness[4]. Mechanical properties of the laminate are listed in Table 4.4. An initial crack of 25 mm length was made by inserting a thin polyamide film in the mid-plane of each specimen. Z-pins were made of pultruded T300/BMI. Reinforced area was designed 5 mm from the initial crack tip extending for 25 mm length covering the entire specimen width. Three configurations of different pin areal density or diameter were simulated; these parameters are summarised in Fig. 4.35 insert.

Considering the unpinned ENF model results, the free edge effect was assumed negligible, thus only the unit-strip model was used to simulate delamination of z-pin reinforced ENF test specimens (i.e. only half of a pin row and the surrounding laminate were modelled). Mesh used for analysis is shown in Fig. 4.36.

Z-pin bridging force (calculated using the unit-cell analytical model, as show in section 4.5.1 was implemented into the global FE model of the ENF specimen using both spring-pin and cohesive-pin models (fully described in Sec.3.4.1), as shown in Fig. 4.36 insert. Published test data of unreinforced ENF were used to correlate the cohesive model parameters, which are given in Table 4.9. Load is applied by displacement controlled loading condition, i.e. a transverse displacement δ is imposed at the centre of the ENF.

Numerical results

Force versus applied displacement
Predicted force versus displacement of three z-pin configurations are shown in Figs. 4.37a–4.39a. Both the cohesive-pin and spring-pin models predict similar force-displacement responses. Cohesive-pin model predicts a slightly

[4]Measured laminate thickness is 3.2 mm for unpinned and pinned configuration 1 specimens, 3.3 mm for pinned specimens in configurations 2 and 3 (Fig. 4.35 insert).

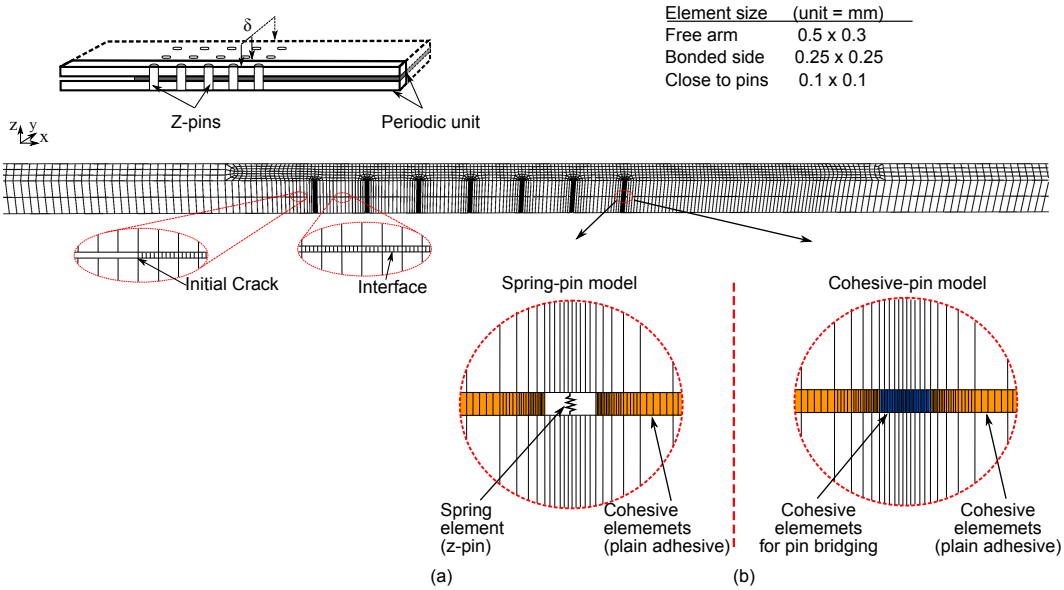

Figure 4.36: Models of z-pinned ENF specimen using two layers of shell elements and cohesive elements at interface: insertion (a) spring model using a non-linear spring element for the pin bridging (b) cohesive model using two different cohesive traction-separation laws for plain laminate and enhanced toughness at pin location.

Table 4.9: Cohesive law parameters used for the z-pin reinforced mode-II delamination tests.

Plain laminate			Pin bridging cohesive law			
K_{II0} (N/m^3)	T_{II0} (MPa)	G_{IIC} (kJ/m^2)	Pin diameter: d (mm)	K_{II0}^{pin} (N/m^3)	T_{II0}^{pin} (MPa)	G_{IIC}^{pin} (kJ/m^2)
1x10^{14}	70	0.77	0.28	4.2x10^{13}	1050	740
			0.51	1.9x10^{13}	630	370

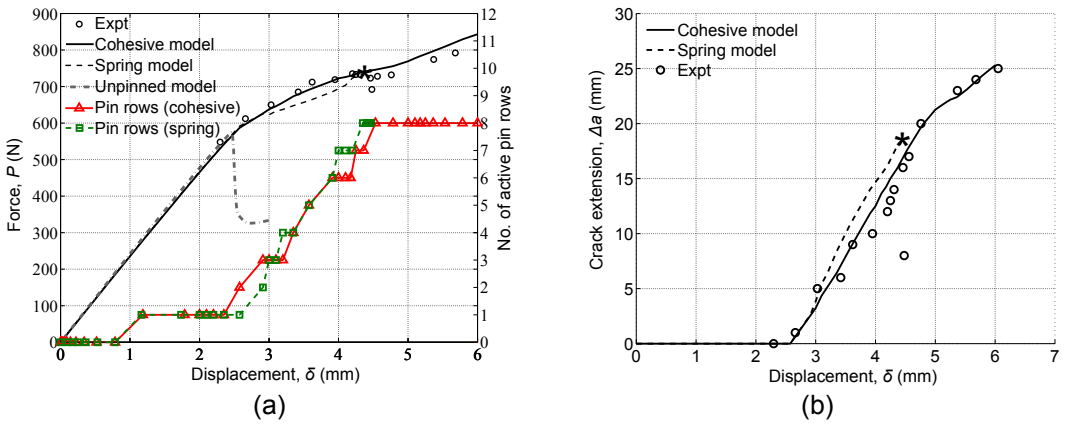

Figure 4.37: Comparison between experiment and simulation (pinned laminate: $A_p = 2\%$, $d = 0.51$ mm), (a) applied force vs. displacement; also showing the number of active pins in the crack wake (right-hand y-axis), (b) crack extension vs. displacement.

higher force and shorter crack extension when the crack size is small (< 4 mm), and two models get closer for larger crack lengths. Difference between the two model predictions always remains smaller than 5%, demonstrating that the simplified bilinear bridging law works well. For the 2% pin density cases, the spring-pin model had some difficulty to converge, as the simulation stopped at about 4 mm applied displacement that is marked by the asterisk sign in Figs. 4.37a and 4.38a. On contrast the cohesive-pin model always reached the end of simulation due to its built-in stabilisation features [124, 125]. For the lower pin density ($A_p = 0.5\%$), spring-pin model ran through. Due to the convergence difficulties the number of incremental steps to analysis completion is much higher for spring-pin model than that of the cohesive-pin model; consequently, the computing time for the spring-pin model is about four times higher. Overall predicted force-displacement curves are in good agreement with the test results in [68] for all the three cases.

Crack bridging length

The pin bridging effect starts as soon as the delamination crack passed the first pin row. Crack tip is shielded from shear force when pins are bridging the crack wake; hence the applied load recovers and increases to a maximum. Crack bridging length is a good indicator of the bridging effect, which is defined as the length of the crack wake where the pins are still active, i.e. not yet failed completely due to either rupture or being pulled out. This information is presented in terms of number of active pin rows indicated on the right-hand side y-axis of 4.37a–4.39a. In all three cases the number of active pin rows increases continuously and does not reach a saturate value: it increases up to the totality of the pin rows inserted into the laminate. Final failure of the specimen occurs due to crushing of the laminate under bending. This result is in agreement with the constantly rising resistance curve (R-curve) in [68], where Cartié et al. reported that the mode-II fracture toughness of z-pinned

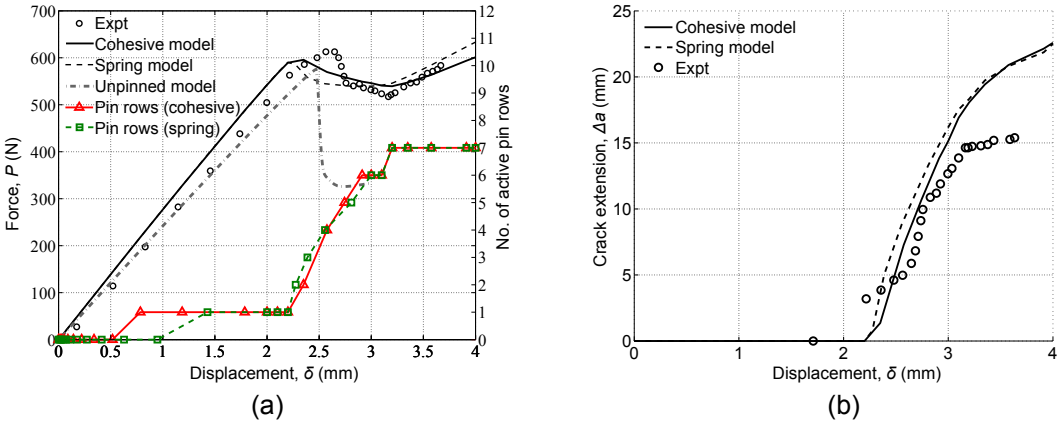

Figure 4.38: Comparison between experiment and simulation (pinned laminate: $A_p = 2\%$, $d = 0.28$ mm), (a) applied force vs. displacement; also showing the number of active pins in the crack wake (right-hand y-axis), (b) crack extension vs. displacement.

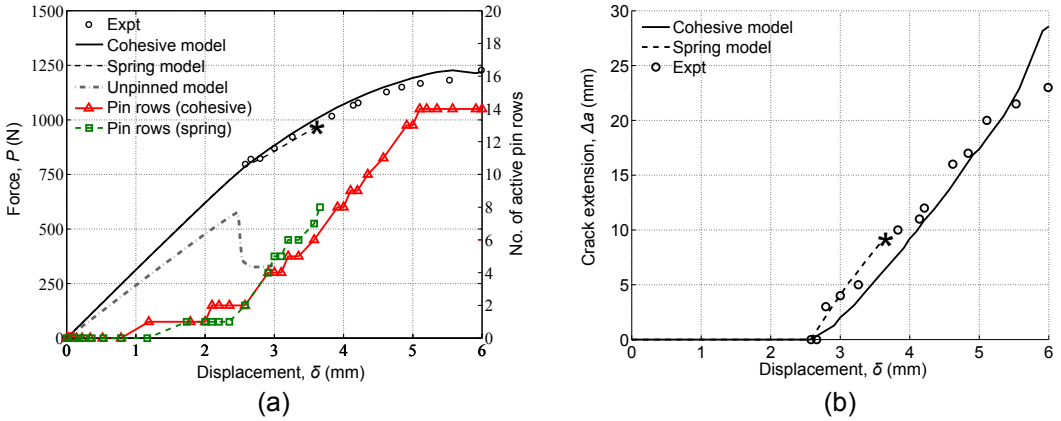

Figure 4.39: Comparison between experiment and simulation (pinned laminate: $A_p = 0.5\%$, $d = 0.51$ mm), (a) applied force vs. displacement; also showing the number of active pins in the crack wake (right-hand y-axis), (b) crack extension vs. displacement.

configurations constantly increases with the crack length. The absence of a plateau value in the R-curve indicates that the number of active pins in the crack wake was still increasing when final failure of the specimen occurred due to exceeding the laminate in-plane tensile stress.

Crack extension behaviour
For the same specimens, crack extension length versus applied displacement is plotted in Figs. 4.37b–4.39b. It worth noting that in the experiment crack lengths were measured by visual observation; therefore, the comparison of this parameter is more for the trend rather than being quantitative. The agreement between the simulation and experiment is reasonably good, particularly for the 2% density cases and for 0.5% case when crack is smaller than 15 mm; percentage error in this region is less than 20%. Larger difference is noted for longer cracks (> 15 mm). Nevertheless, these larger discrepancies occur when it is close to the specimen final failure, which is due to exceeding the laminate in-plane tensile strength. The model does not take into account this failure mode; therefore, deeper crack propagation is predicted.

Comparison of the three cases
Trend of the load-displacement curve are similar and are summarised in Fig. 4.40a. It should be noted that the difference in initial compliance of the three configurations is due to the small variations of the test sample geometry (laminate thickness and initial crack length), which were incorporated into the models in order to have good comparison between model and experiment. This initial compliance mismatch is not due to the z-pin bridging effect; hence it is not discussed in this thesis. Following observations can be made: First, the ENF test specimen has a linear elastic response at the beginning, and the initial delamination crack starts propagating at the same applied displacement of about $\delta = 2.5$ mm for all pinned and unpinned specimens. Second, as soon as the delamination crack starts propagating the applied load drops. For the unpinned case crack propagates unstably leading to rapid final failure, whereas in all pinned configurations crack propagates in stable manner and the specimens pick up much more loads.

Interlaminar shear stresses
Numerical modelling also reveals that active pins in the crack wake shield the crack from suffering from the full crack opening displacement. Consequently the pins are subject to high shear stress. Fig. 4.41 shows the values of interlaminar shear stresses at the delamination plane at applied displacement $\delta = 4$ mm (for z-pin parameter $A_p = 2\%$; $d = 0.51$ mm). Cohesive-pin model predicts slightly smaller crack extension (Figs. 4.37b–4.39b) and higher shear stresses on the pin rows close to the crack tip. This is the consequence of the simplified bilinear traction-separation law employed; the pins modelled with the cohesive law are able to pick up bridging load quicker than the ones modelled with springs. However, after an initial different evolution of the crack,

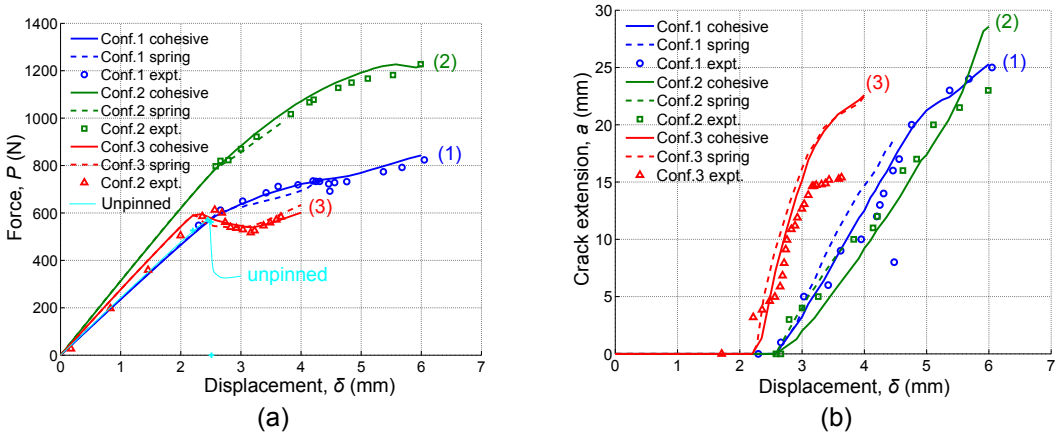

Figure 4.40: Summary of numerical results: (a) applied force vs. displacement, (b) crack extension vs. opening displacement. Configuration: (1): $A_p = 2\%$, $d = 0.51$ mm, (2): $A_p = 2\%$, $d = 0.28$ mm, (3): $A_p = 0.5\%$, $d = 0.28$ mm.

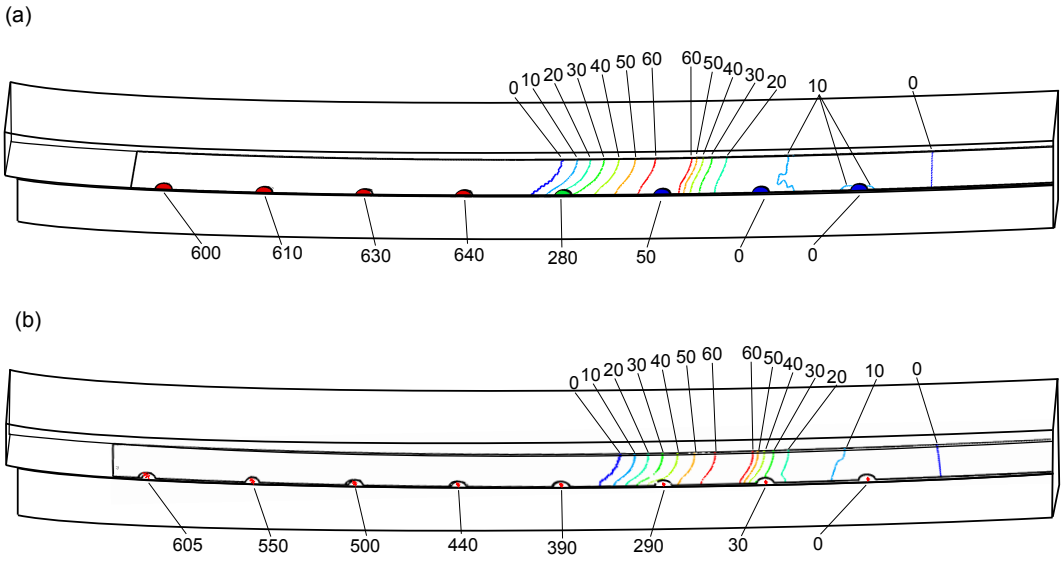

Figure 4.41: Interlaminar shear stresses at delamination plane, (a) cohesive model, (b) spring mode. (Stress unit: MPa). Pinning parameters: $A_p = 2\%$, $d = 0.51$ mm; applied displacement: $\delta = 4$ mm.

due to the energetic equivalence of the two bridging laws, the predictions of the two models converge in all modelled cases (Figs. 4.40a-b).

4.6 Summary of results

A new cohesive zone model has been developed for evaluating enhanced fracture toughness of through-thickness reinforced laminates. The model have been validated under both mode-I and mode-II loading conditions by comparing model results with experiments. Main contributions to the development of predictive models are:

1. Two separate cohesive laws are employed: one for the pins locations and another for the unpinned areas. It has enabled modelling the large scale bridging phenomenon manifested by z-pinned laminates. Once the specific pin bridging law is determined by either testing or modelling, the approach can be used for different pin arrangements.

2. Adhesive properties of the resin and structural response of the through thickness are used separately allowing to evaluate the effect of different pin reinforcement size and densities.

3. For mode-I delamination tests, where the crack front was demonstrated to assume a thumb-nail shape due to the free-edge effect, unit-strip and whole model predictions have been compared, showing excellent agreement. Computing time for the unit-strip model is about 14% of that required by the whole model. Hence, the unit-strip model can replace a complete model if pins are placed in a periodical pattern.

4. For mode-II delamination tests, characterised by having a strongly non-linear pin bridging law, two pin-models have been used: spring-pin and cohesive-pin models. Both models well predicted the delamination behaviour of the ENF test sample, showing good agreement with the experimental data.

CHAPTER 5

ANALYSIS OF Z-PIN REINFORCED T-JOINT STRUCTURES

5.1 Introduction

In this chapter an FE model was developed to analyse the structural properties and failure of a z-pinned T-shaped composite joint subjected to a tensile (pull-off) load applied to the stiffener. Experimental data presented here has been used for validation purposes only and are available in the open literature in [131].

The analysis was based on a multi-scale modelling approach performed at the unit-cell and structural levels, as presented in Chapter 3. The joint was reinforced along the skin-stiffener flange region only, which is where delamination failure occurs, and outside of this region the joint was not pinned.

A cohesive zone model of the unreinforced joint has been used to demonstrate the model capabilities of capturing the failure modes and structural properties of the joint. The effect of z-pin reinforcements have been evaluated in the second part of the chapter. The joint structural properties have been simulated using the unit-strip model (presented in Sec.3.4.2). Z-pin bridging law has been estimated by the unit-cell model and then implemented into the structural model by cohesive elements.

Table 5.1: Material mechanical properties used in FE analyses of unrenforced T-joint tests [131].

E_{11}	$E_{22} = E_{33}$	$G_{12} = G_{13}$	G_{23}	$\nu_{12} = \nu_{13}$	ν_{23}
	(GPa)				
120	7.5	5.25	3	0.32	0.32

5.2 Geometry and model description

5.2.1 Experimental testing of the joint

T-joint specimens were made of unidirectional T700 carbon/epoxy prepreg tape (VTM 264 supplied by Advanced Composites Group). The material properties of the carbon/epoxy laminate are provided in Table 5.1, and it was assumed they were not affect by the pins. The joint geometry and dimensions are shown in Fig. 5.1. The plies to the skin, stiffener and flange were stacked in a cross-ply $[90/0/90/0/90]_S$ pattern. The Δ-fillet region at the stiffener base was filled with the unidirectional prepreg tape. Before curing, the skin-flange section to the T-joint was pinned with pultruded rods of unidirectional T300 carbon fibre/bismaleimide (Albany Engineered Composites Pty Ltd). The pins were inserted in the orthogonal (through-thickness) direction of the skin-stiffener flange section using an ultrasonic hand-held device operated at the frequency of 20 kHz. The entire length of the skin-flange connection was reinforced with pins, whereas the regions outside of this connection were not pinned (as indicated in Fig. 5.1). A full description of the z-pinning process used to reinforce the T-joint is given by Koh et. al. [131]. The volume content and diameter of the pins was 2% and 0.28 mm, respectively. The pins were arranged in a square grid pattern aligned along the length and across the width of the skin-flange section to the joint. The spacing between the pins both along and across the joint was 1.75 mm.

Control T-joint specimens (without pins) were also made with the same geometry as the pinned specimens. Both the unpinned and pinned joint specimens were cured in an autoclave at 120°C and 620 kPa for one hour. The joints were bonded by co-curing without the use of adhesive. The average volume content of carbon fibres in the skin, flange and stiffener of the joints was about 60%.

A stiffener pull-off test was performed on the T-joint specimen to validate the FE model. A tensile load was applied to the stiffener using a 50 kN Instron machine at a constant displacement rate of 1 mm/min until final failure. The ends of the skin were clamped to a rigid support plate, although some slippage occurred during testing which was accounted for by the FE model. At least five specimens of the unpinned and pinned joints were tested under identical conditions to validate the FE model.

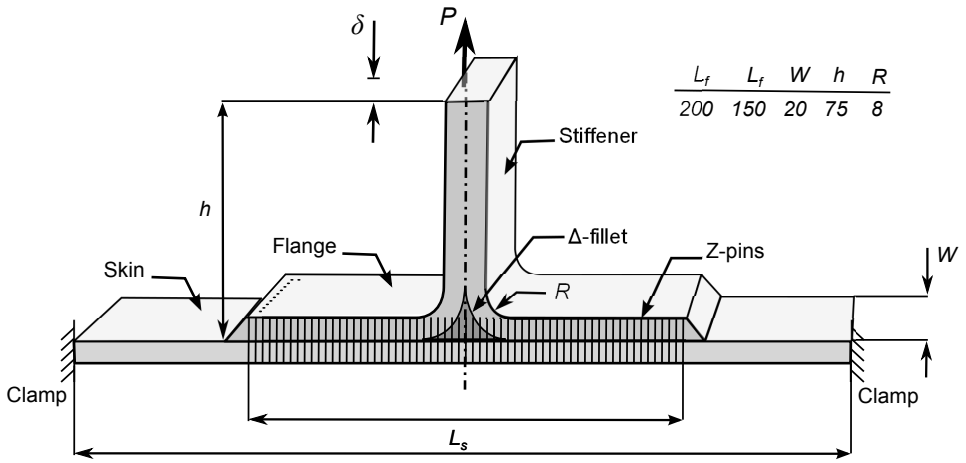

Figure 5.1: Geometry, loading and boundary conditions of the pinned T-joint.

5.2.2 Model description

A finite element model of the unpinned joint was created using quadratic plane strain shell elements with reduced integration (designated as CPE8R in Abaqus), as shown in Fig. 5.2. The model was constructed to capture the progressive delamination along the stiffener centreline and the skin/stiffener bondline. Mesh sensitivity and element sensitivity analysis was performed, and the mesh shown in Fig. 5.2 was found to give the optimum compromise between numerical accuracy and computation time. The orthotropic elastic properties of the cross-ply $[0/90]_S$ carbon fibre/epoxy laminate used for the skin, flange and stiffener of the joint are given in Table 5.1. The triangular Δ-fillet region at the stiffener based was filled with unidirectional laminate with the fibre direction perpendicular to the modelling plane. The triangular region at the taper run-out at the flange ends was assumed to have the mechanical properties of epoxy resin ($E = 3$ GPa, $\nu = 0.4$).

According to experimental observation of the failure of T-joints under tensile loading [131], discrete delamination cracks grow along the interface between the skin and flange (a_1 - horizontal path), centre-line of the stiffener (a_1 - vertical path), and centre of the web (a_2), as illustrated in Fig. 5.2-b. These crack paths were modelled by placing a layer of cohesive elements between the plies.

Cohesive elements (COH2D4) were used to model the delamination cracks along these paths, with the cohesive interface element size being one-fifth of the adjacent ply element size in order to achieve numerical stability [125]. Cohesive element property values were selected based on the delamination toughness properties of the carbon/epoxy laminate used in the joint ($G_{IC} = 0.6$ and $G_{IIC} = 1.2$ kJ/m^2). The parameters and their values used for the cohesive fracture analysis are provided in Table 5.2.

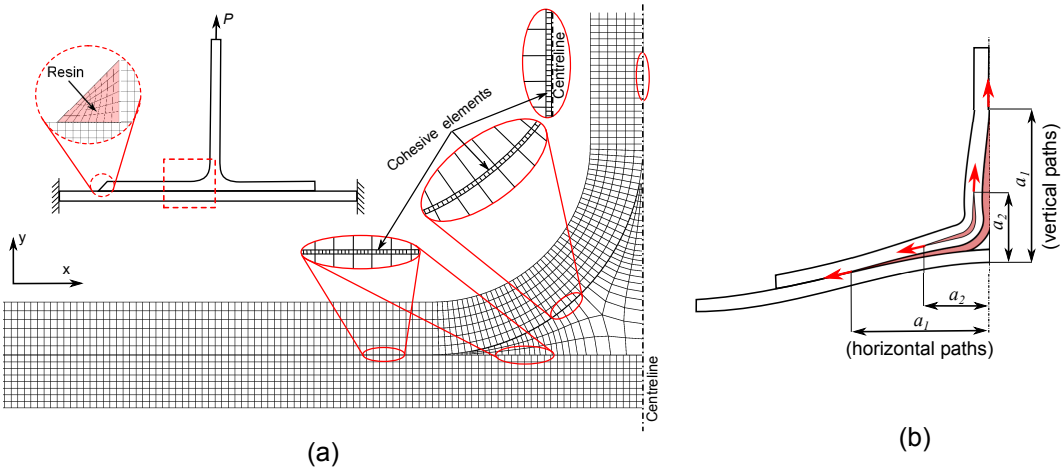

Figure 5.2: (a) Unpinned joint model. (b) Location of discrete delamination cracks.

Table 5.2: Cohesive elements parameters for unreinforced T-joint model

Initial stiffness		Cohesive strength		Fracture toughness	
K_{I0}	K_{II0}	T_{I0}	T_{II0}	G_{IC}	G_{IIC}
(N/m^3)		(MPa)		(J/m^{-2})	
5 x 10^{13}	5 x 10^{13}	30	70	600	1200

The FE simulations were run under displacement-controlled loading by applying a monotonically increasing tensile displacement as the boundary condition on the nodes at the upper extremity of the stiffener. In order to avoid hourglass deformation of cohesive elements on the symmetry plane, the y-direction displacement of each cohesive element node was constrained to be the same as its corresponding node on the other face of the element (i.e. no shear strain at the symmetry). The ends of the skin were clamped to prevent vertical displacement and rotation of the joint. However, it was found that the axial displacement constraint (perfect clamping) or assuming the clamp does not to react in the axial direction (sliding clamps) resulted in the joint being either too stiff or too compliance compared to the experimental results (which are presented later). The clamp was therefore assumed to constrain the axial displacement until a maximum axial force. From this point the joint was assumed to slide axially with a constant friction force. The maximum friction force exerted by clamps depends on material and surface roughness which clamps were made of, and upon the force applied to close the clamps them-selves. This boundary condition was modelled using a non-linear spring element (designated SPRING1 in Abaqus). Non-linear spring properties were calibrated on the experimental results in order to match the joint stiffness. A sensitivity analysis of this parameters has been also included in Sec. 5.2.3. Spring initial stiffness of 1x10^8 N/m and maximum axial force of 9 kN were found to best represent the joint boundary conditions.

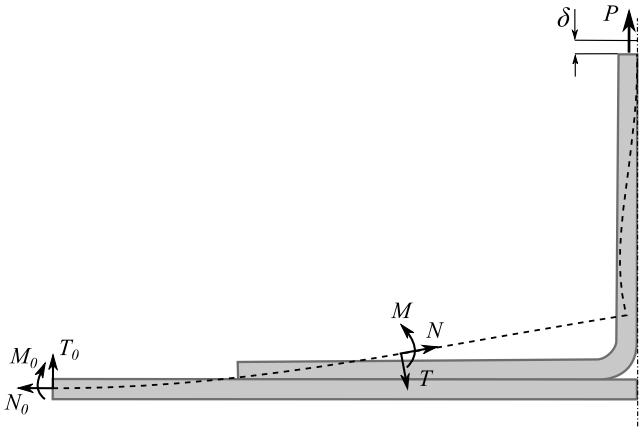

Figure 5.3: Joint stress characteristics along the joint skin.

5.2.3 Effect of clamps on the joint stiffness

The membrane stress introduced by clamps, due to the large joint deformations, affects the joint overall stiffness. Let consider the stress characteristics along the joint skin as depicted in Fig. 5.3. Due to the nonlinear geometry introduced by deformation (large displacement hypothesis), the force balance can be written as follows:

$$\begin{cases} T = T_0 \cos v' + N_0 \sin v' \\ N = -T_0 \sin v' + N_0 \cos v' \end{cases} \tag{5.1}$$

Where v is the vertical displacement of the skin and the apostrophe indicated the derivative with respect to the beam axial coordinate. Assuming of being in a small deformation regime ($\sin v' = v'$ and $\cos v' = 1$) Eq. (5.1) can be written as follows:

$$\begin{cases} T = T_0 + N_0 v' \\ N = -T_0 v' + N_0 \end{cases} \tag{5.2}$$

For the external force equilibrium $T_0 = -P$. Thus the bending moment of the joint can be calculated as follows:

$$M = M_0 + (-P + N_0 v')x \tag{5.3}$$

If axial deformation at clamps is constrained the N_0 is proportional to the variation of joint length, i.e. to v^2. Shear force and bending moment have a cubic dependence on the applied load. Assuming the membrane stiffness (EA) much larger than the bending stiffness (EI), the joint stiffness can approximated considering the work dome the force P:

$$P\delta = \int \frac{M^2}{EI} dx \tag{5.4}$$

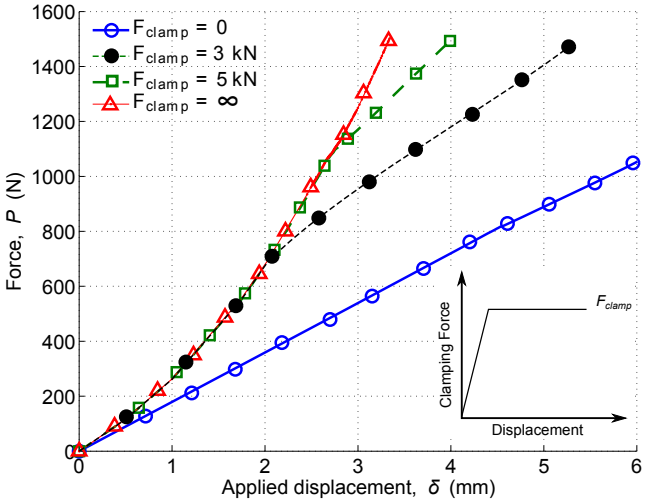

Figure 5.4: Effect of the axial force introduced by clamps on the joint response.

Fig. 5.4 shows the effects of the axial force introduced by clamps to the joint response. If the skin is free to slide axially over the clamps, no axial stress is introduced into the structure (i.e. $F_{clamp} = 0$) the force-displacement curve of the joint has a linear relation. Vice-versa if the clamps constrain the skin axially, the joint shows a cubic force-displacement curve. However, the axial force introduced by the clamps is limited by the friction resistance between clamps and skin. The two curves plotted in Fig. 5.4 ($F_{clamp} = 3$ kN and $F_{clamp} = 5$ kN) represent the joint response for a clamping axial force with a linear response, proportional to the axial displacement, up to a saturation value (F_{clamp}) and then constant.

5.3 Numerical results

5.3.1 Unpinned joint

Fig. 5.5 shows the applied force-vertical displacement curves for the unpinned joint that were calculated using the FE model and measured using the stiffener pull-off test. There is excellent agreement between the calculated and measured curves, which validates the numerical accuracy of the FE model for the unpinned joint. The FE model accurately predicted the non-linear rise in the stiffness and the peak load of the unpinned joint, after which it was predicted that the load capacity would drop abruptly due to splitting cracking along the centre-line of the stiffener (at point 1 in Fig. 5.5) followed by delamination cracking along the skin/flange interface (at point 2). These two fracture modes were observed in the unpinned experimental test specimens [131].

Fig. 5.6 shows the normal (y-direction) stress contour map for the unpinned

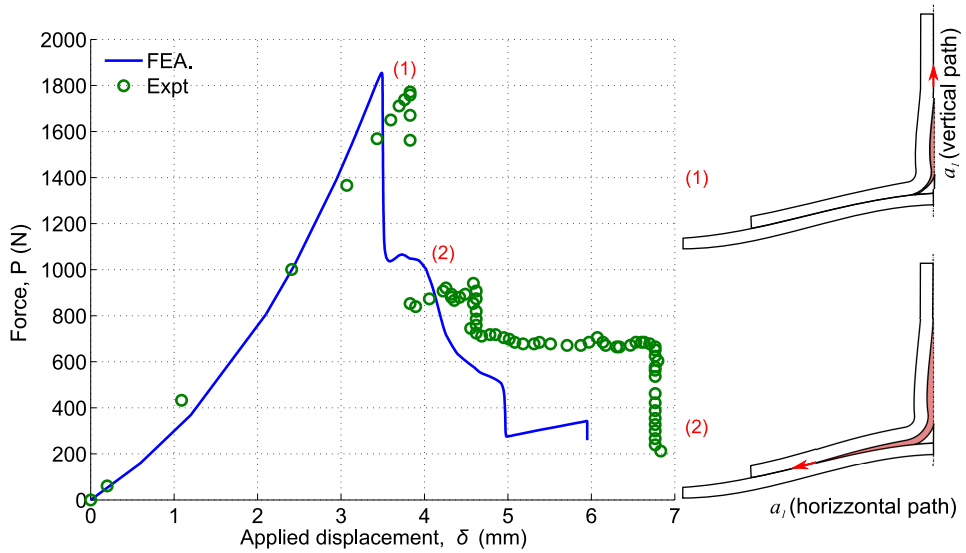

Figure 5.5: Comparison of the calculated and measured applied force-displacement curves for the unpinned joint. The diagrams on the right-side indicate the onset of vertical cracking along the centre-line of the stiffener at point 1 and horizontal cracking along the skin/stiffener interface at point 2.

joint calculated using the FE model. The numerical analysis showed that crack initiation occurred when the normal tensile stress exceeded the peel strength of the cohesive elements in the FE model. It was determined that the splitting crack along the centre-line of the stiffener was due to a pure mode I stress, which at the crack tip was about 30 MPa. The delamination crack at the skin/flange interface propagated under a mixed mode I/II stress condition, and therefore the peel stress was calculated to be slightly lower at about 18 MPa.

A sensitivity analysis of the cohesive element parameters on the joint response has been carried out in this section. The three parameters that defines the mode-I and mode-II cohesive laws have been varied between a lower and an upper bound, one at time each keeping the others constant. The effect on the model response of each of parameter is illustrated in Fig. 5.7. Where not differently specified in the graph the values of cohesive parameters are the same an in Table 5.2.

Due to the insensitivity of initial stiffness K_{I0} and K_{II0}, the relative plots have not been reported. As concluded by many other authors, this parameter has no particular physical meaning and it has to be set high enough not to vary the global compliance of the joint [124, 125].

Cohesive strengths T_{I0} and T_{II0} (which physically represents respectively the adhesive peel and shear strength) affect the damage initiation point and thus the peak load. Delamination initiates at the round region, where peel is critical. For this reason the model shows high sensitivity to T_{I0}.

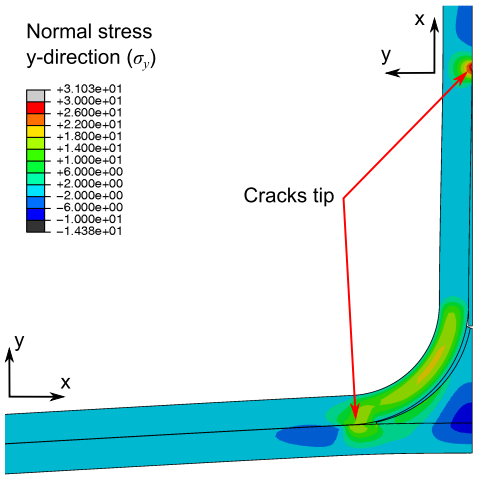

Figure 5.6: FE stress contour map of the normal stress in the y-direction of the unpinned joint (the coordinate system follows laminate orientation).

Peak load is almost insensitive to the cohesive energy G_C (which physically represents the delamination toughness); G_{IC} and G_{IIC} characterise the behaviour of the joint after damage initiation. Although the crack at the skin/stiffener interface propagates under mixed mode, the high sensitivity of the model to G_{IC} shows that mode-I is dominant.

5.3.2 Z-pin reinforced joint

A FE model was created for a pinned joint that had the same geometry as the unpinned joint. A unit-strip model was constructed with the pins spaced at regular intervals (1.25 mm) along the skin/flange region, as shown in Fig. 5.10. Because a unit-strip model was used, it was possible to model the pins as one-half of a single row of pins. Due to the pinned joint having a higher ultimate load limit than the unpinned joint, the central interlaminar planes of the stiffener are important for delamination damage progression after crack growth between the skin and flange. For this reason an extra layer of cohesive elements was added between the plies close to the centre-line of the stiffener (illustrated as crack a2 in Fig. 5.2b). Each sub-laminate was modelled using one layer of shell elements (designated continuum shell SC8R in Abaqus).

The pins were modelled using cohesive elements for the pin traction load-displacement law (TSL) determined using the single pin unit-cell model. For mode II loading near the delamination crack tip, the non-linear shear deformation of the pins was neglected and a simplified bi-linear TSL was used. Cohesive element properties used for the FE analysis are provided in Table 5.1.

Fig. 5.10 compares the calculated and measured applied load-displacement

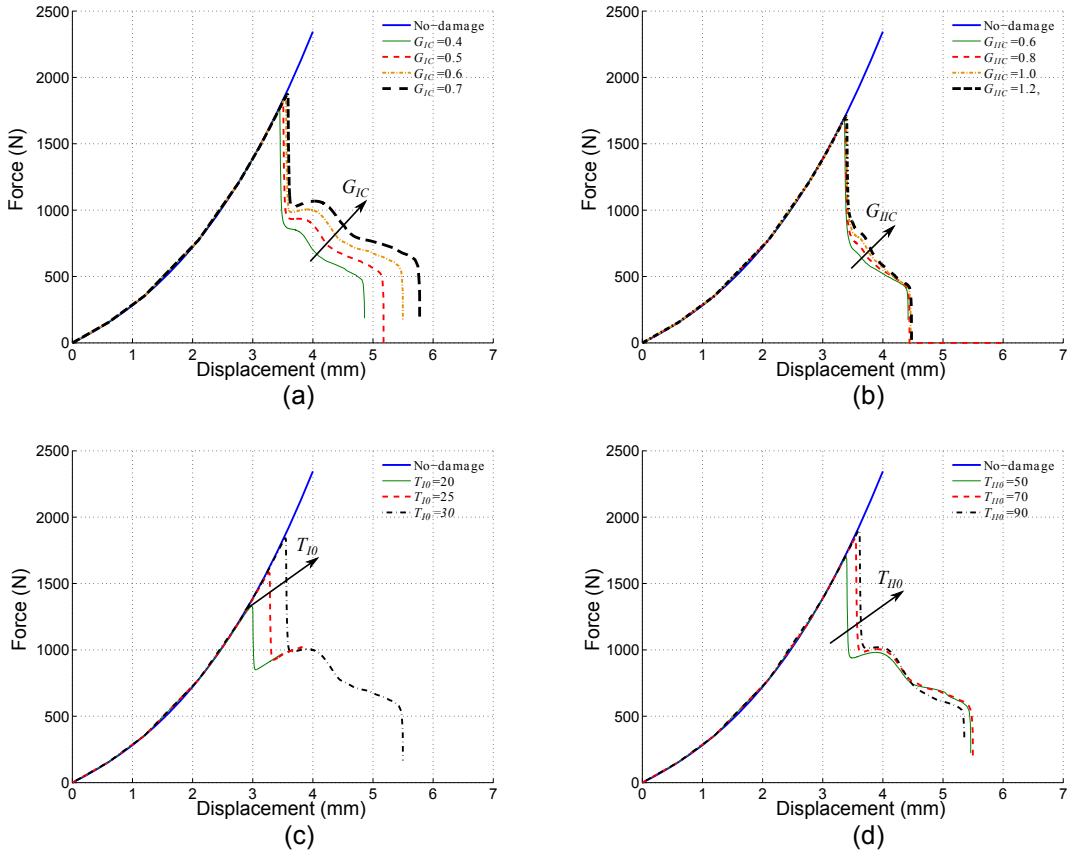

Figure 5.7: Sensitivity analysis of the cohesive element parameters: (a) Mode-I fracture toughness (G_{IC}), (b) mode-II fracture toughness (G_{IIC}), (c) peel strength (T_{I0}), (d) shear strength (T_{II0}).

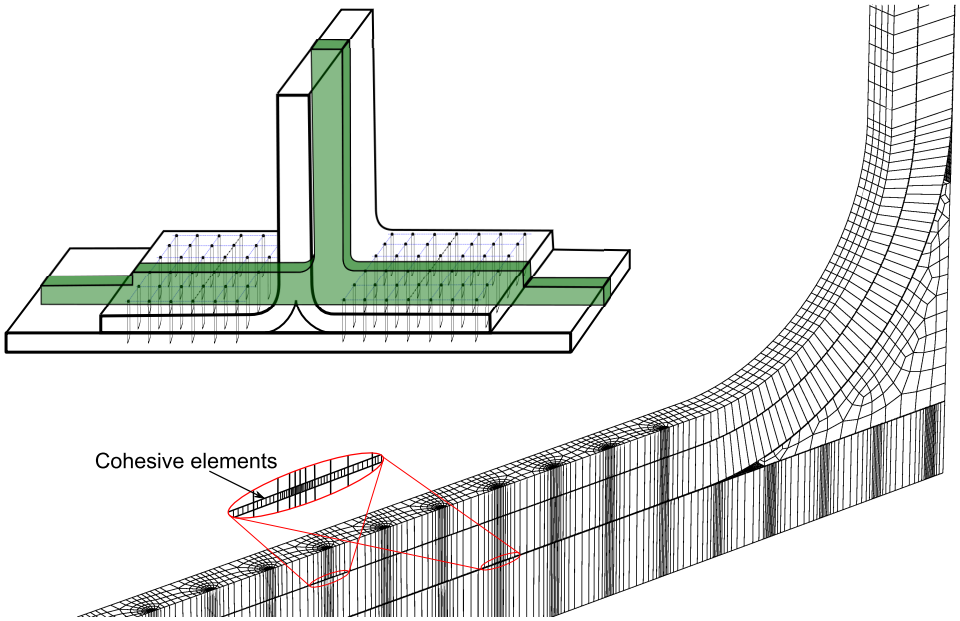

Figure 5.8: Unit-strip FE model of the pinned joint.

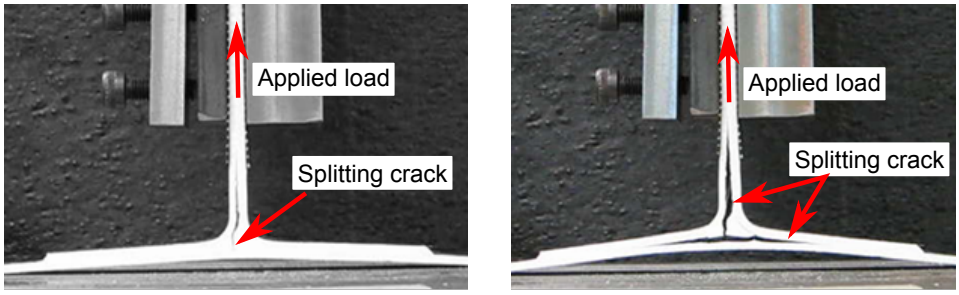

Figure 5.9: Pinned joint showing (a) splitting cracking along the stiffener centre-line at the initial load drop and (b) delamination cracking along the skin/stiffener flange interface at the second (ultimate) load drop.

curves for the pinned joint, and again there is excellent agreement. The stiffness of the pinned joint was calculated using the FE model to be the same as the unpinned joint, and this was confirmed by experimental testing. Pins do not significantly alter the in-plane elastic modulus of carbon/epoxy laminate [21,22], and therefore the stiffness of the joint was not changed by pinning. The pinned joint experienced an initial load drop (at $\delta = 4$ mm), and the FE model determined that it was caused by the initiation from the Δ-fillet region of a splitting crack along the centre-line of the stiffener. This was immediately followed with the initiation of a delamination crack along the skin/flange interface. Again, this was confirmed by experimental testing with both stiffener splitting and skin/flange delamination cracking spreading from the Δ-fillet region of the pinned joint specimen following the initial load drop (Fig. 5.9). The FE model predicted that the pinned joint does not fail catastrophically at the initial load drop point (unlike the unpinned joint) due to bridging traction loads generated by the pins along the delamination crack between the skin and flange. The pin traction loads caused a recovery in strength and consequently the pinned joint was able to withstand further loading up to the ultimate load limit of about 3800 N, which was over twice as high as the unpinned joint. The FE model determined that the second (and much larger load drop at $\delta = 10.7$ mm) was caused by the formation of a second crack within the web region (a_2), and this was also observed experimentally.

Between the initial and second load drop points, the FE model predicted that an increasing number of pins generated traction loads as the delamination crack grew in length along the skin/flange interface, and this was the cause for the progressive increase in joint strength between the two points, as shown in figure 9b. The spacing between the pin rows along the skin/stiffener interface was 1.75 mm, and it was calculated that seven rows of pins were bridging the delamination crack to promote maximum interlaminar toughening. The FE analysis revealed that once the delamination crack length exceeded the pin bridging traction zone length of about 12.25 mm, the last row of pins in the

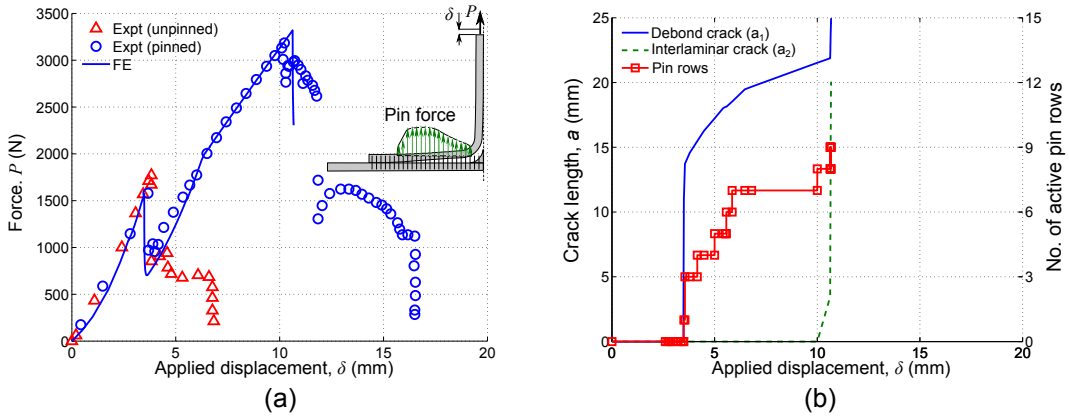

Figure 5.10: (a) FEA and measured applied force vs. displacement curves for the pinned joint. (b) FEA of the crack length vs. applied displacement and number of active pin rows along the skin/stiffener flange delamination crack.

crack wave failed by pull-out as a new row of pins began to generate traction loads near the crack tip. Again, this was confirmed by experimental testing with the pin bridging zone along the skin/flange interface being 10-15 mm long.

FE analysis was performed to calculate the pin traction loads along the skin-flange delamination crack at two points: (a) when the pins first formed a fully-developed bridging zone which occurred at $\delta = 6$ mm (figure 11) and (b) at the maximum load point which occurred at $\delta = 10.7$ mm (figure 12). The FE model computed both the normal tensile and transverse shear traction stresses for each row of pins along the delamination crack. (The stresses represent the traction loads per pin unit area). The analysis showed that the traction stresses were non-uniformly distributed between the pin rows along the crack. Both the tensile and shear traction stresses increased with distance behind the crack tip due to increasing crack opening/sliding displacement and reached a maximum at about one-half along the crack length. The traction stresses then decreased towards the rear of the bridging zone due to the reduced friction stress generated by the pins when they were nearly pulled out from the laminate. Fig. 5.11 also shows that the normal traction stresses generated along the upper (a_2) crack were lower than those generated along the skin/flange interface crack (a_1). This was due to the smaller opening displacement in the a_2 crack and the shorter embedded pin length which induced a lower shear load along the pin/laminate interface. However, the transverse shear stresses were higher along the a_2 crack due to the higher shear sliding displacement compared to the a_1 crack. This analysis revealed the complexity of the bridging traction loads generated in pinned joints which increased the strength and toughness properties.

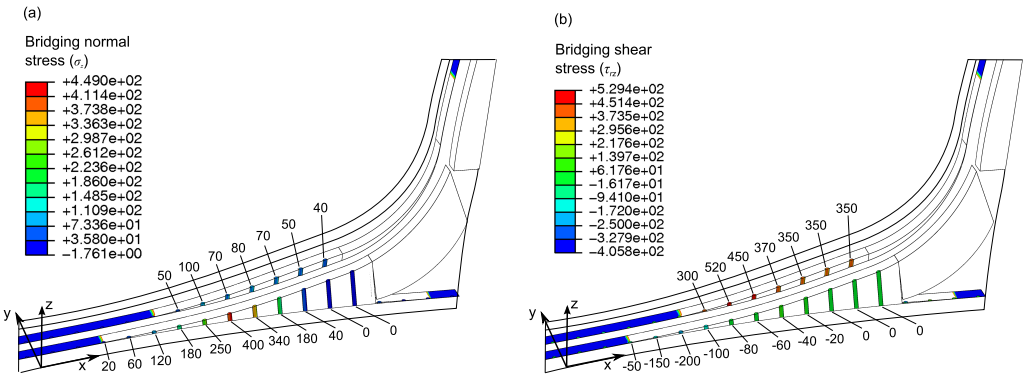

Figure 5.11: Pin bridging stresses at ultimate load, applied displacement $\delta = 10.67$ mm. (a) Normal stress in z-direction (through-thickness). (b) Transverse shear stress. The stresses represent the bridging force per pin unit area. Unit MPa.

5.4 Summary of results

A validated FE model has been developed which can analyse the structural properties and fracture behaviour of pinned T-shaped composite joints when subjected to a tensile (stiffener pull-off) load. The FE model analyses the crack bridging traction loads of a single pin under modes I and II interlaminar stresses at the unit-cell scale, and this analysis is then used to calculate the strength and delamination fracture properties of pinned joints at the structural level. The FE model provides important insights into the strengthening and toughening of pinned joints, such as failure initiation being determined by mode I splitting cracking along the vertical stiffener and the ultimate strength being controlled by the modes I/II pin traction loads, which are unevenly distributed along the bridging zone between the skin and stiffener flange. The FE model also revealed that both the traction loads generated within the web region (a_2-type crack) and along the skin/flange interface (a_1 crack) are important in the strengthening and toughening of pinned joints. The FE model computed that the traction loads are mainly mode II shear stresses in the a_2 crack and mode I tensile stresses in the a_1 cracks. Despite the complexities of the internal stress distribution, pin traction laws and crack growth behaviour for the pinned joint, the FE model accurately calculated the stiffness, strength and fracture modes when compared to experimental test results. This validation study demonstrates that the FE model can be used in the optimum design of pinned T-joints when subjected to tensile loading.

Part III

Development for hybrid metal-composite joints

CHAPTER 6

METAL PIN BRIDGING FORCES FOR HYBRID METAL-COMPOSITE JOINTS

6.1 Introduction

In this chapter the bridging force exerted by interlocked metal pins inserted into carbon/epoxy laminate is analysed. Two FE models have been constructed to simulate both mode-I (pullout force perpendicular to the laminate plane) and mode-II (shear force planar to the laminate plane) loading conditions. Specific experimental tests were carried out to demonstrate the model validity. These were also part of a larger testing campaign finalised towards the characterization of bridging performance of this type of reinforcement. However, to-date the results of this testing campaign are not yet published; for this reason in the first part of the chapter specimen preparation, testing rig and loading conditions were briefly described.

The analyses of single-pin tests were carried out reproducing loading and boundary conditions of experiments in order to validate the model. A detailed description of the FE models used in this chapter, their validity and limits are also reported in Sec.3.3.1 and Sec.3.3.2 for mode-I and mode-II loading conditions respectively. The models were then used to evaluate the effect of geometric parameters on the bridging force exerted by pins. These bridging force will be then used in the next chapter to evaluate the structural properties of pin reinforced metal-composite joints.

6.2 Single-pin pullout test

6.2.1 Test geometry and model description

Mode-I bridging force exerted by metal pins was measured by single-pin pull-out test. This test was also simulated by FE modelling and compared with experimental results. Test specimen was composed of pike-shape single-pin of height $h = 3.4$ mm and diameter $d = 0.7$ mm, CMT welded[1] on a thick cylindrical metallic substrate and a 30x30 square block of laminate where the pin was inserted (Fig. 6.3a). Stainless steel AISI 304 was used to manufacture the metal half of the specimen, whereas the laminate was made of 32 plies of T700-M21 prepreg in a quasi-isotropic layup, resulting in 4 mm nominal thickness. The stacking sequence of the laminate was $[0°/45°/90°/-45°]_{2S}$. Metal and laminate parts were separated by a thin FEP (fluorinated ethylene propylene) film at the base, mimicking a debond crack at metal/laminate interface. The purpose of the test is to measure the pin stand-alone pullout resisting force that bridges the two parts when completely delaminated.

Specimens were prepared using special purpose moulding made of Rohacell PMI foam (density 210 g/mm^3). This moulding material was selected basing on the thermal expansion coefficient (22 μm/m K^{-1}, which is very close to the one of the laminate) in order to minimise the residual thermal stress and bending of the specimen during the cooling down after cure. Moulding was provided with cylindrical holes, used to hold the metal base of the specimens. Laminate was laid up in bars of 270x30 mm which were wrapped in polyimide film (A photograph of the set-up used is shown is Fig. 6.1). The surface of pins was sand blasted and cleaned in an ultrasonic bath of acetone before being inserted into the laminate. The pin insertion was done using an ultrasonic horn at 20 kHz vibration frequency, with a procedure similar to [68, 77]. The horn was placed on the bases of the metal specimens, using a piece of damping material in between the two to avoid cavitation of the ultrasonic hammer. The high frequency pressure waves generated by the horn produce local heating of the laminate at the pin location. The localised heating reduced the viscosity of the resin and the long carbon fibre are allowed to move around the pin during the insertion with minimal fibre breakage.

Moulding was cured in autoclave at 180°C temperature and 4 bar pressure, accordingly to the supplier's specification. Individual specimens were then realised cutting the laminate bar with diamond saw and demoulded from the PMI foam. Pullout tests were then carried out under displacement loading control with a speed of 1 mm/min, using a 1 kN INSTRON testing machine. Specimen was clamped at the lateral surface of the laminate block and the

[1]Details of the welding process are reported in 2.3.3.

Figure 6.1: Photograph of the moulded single-pin specimens before curing cycle.

pullout load applied by a self-centering chuck where the metal part of the specimen was held. A schematic of the test set-up is depicted in Fig. 6.2.

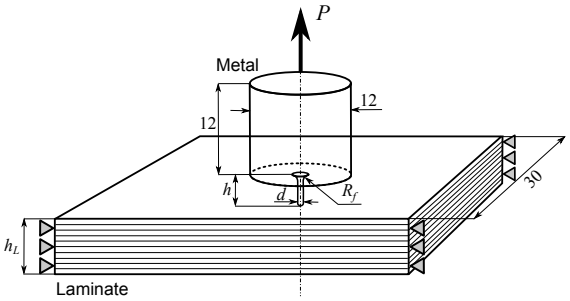

Figure 6.2: Schematic of single-pin pullout test geometry and fixturing. (Unit: mm)

An axi-symmetric FE model, similar to the one used for carbon fibre pins presented in Sec.3.3.1, was constructed to simulate the pullout test. Specimen geometry is depicted in Fig. 6.3a. The model is based on the observation of a resin-rich pocket around the pin, of about 5-6 pin diameters, caused by the pin insertion. Considering that laminate properties in the cross fibre direction are dominated by the resin matrix, material surrounding the pin is assumed as homogeneous and isotropic. The contact force between metal and composite parts was calculated using a surface to surface algorithm and Coulomb friction friction model (i.e. maximum shear force proportional to the contact pressure).

Metal pin and surrounding laminate were modelled using axi-symmetric quadrilateral quadratic elements with reduced integration (CAX8R). Converged numerical results were achieved increasing the mesh size at the pin-laminate interface, due to the high contact stress caused by friction, whereas a relative coarse mesh was used far from the interface . Fig. 6.3b shows the FE model mesh. Material properties used in the analysis are given in Table 6.1 [27] (for the metallic pin) and for the surrounding resin rich laminate the following properties are used: $E = 11GPa$, $\nu = 0.4$ and $\alpha = 2.4$ x 10^{-5}. The residual stress state due to the cure process was calculated imposing a temperature variation of -155°C to the whole model. The residual stress field is a function of the temperature change, model dimension, coefficients of thermal expansion and Young's modulus of the pin and surrounding material in the radial direction. Once calculated, this residual stress field was saved into the model before applying the pullout force. Loading was introduced by imposing an increasing pullout displacement at the bottom of the metal pin base and keeping

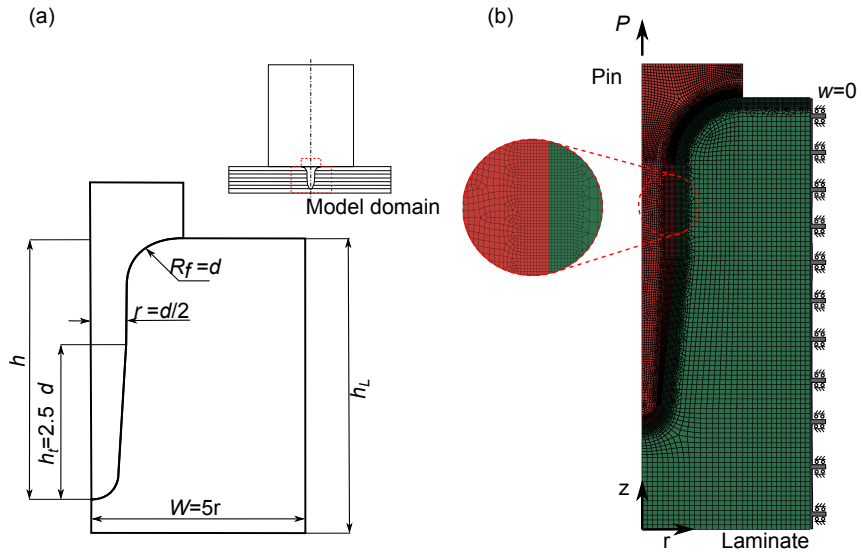

Figure 6.3: Single-pin pullout model: (a) pike pin geometry, (b) model mesh and boundary conditions.

Table 6.1: Material properties uses for interlocked metal single-pin pullout analysis.

Stainless steel AISI 304		
E	ν	α
190 GPa	0.33	11 μm/m

Material properties from [27]

the laminate constrained at boundaries in order to reproduce the experimental boundary conditions (Fig. 6.2).

6.2.2 Numerical results

The radial (σ_r), circumferential (σ_θ) and shear (τ_{rz}) residual stress distributions due to the cure process are presented in Fig. 6.4. The following observations can be made. First, the curing process induced thermal residual stress in radial direction (σ_r) is negative at the pin/laminate interface, about 20 MPa (Fig. 6.4a), indicating that the pin is under compression by surrounding materials. This initial contact stress causes friction resistance when pullout load is applied. At the pin tip the compressive radial stress (σ_r) is balanced by a tension on the lower part of the laminate; at pin central section the by high circumferential stress (σ_θ) on the laminate close to the pin (Fig. 6.4b). The residual shear stress distribution is balanced (no external force applied) and it is higher at the extremities of the pin (Fig. 6.4c).

When the pullout load is applied there is an initial linear-elastic response. At

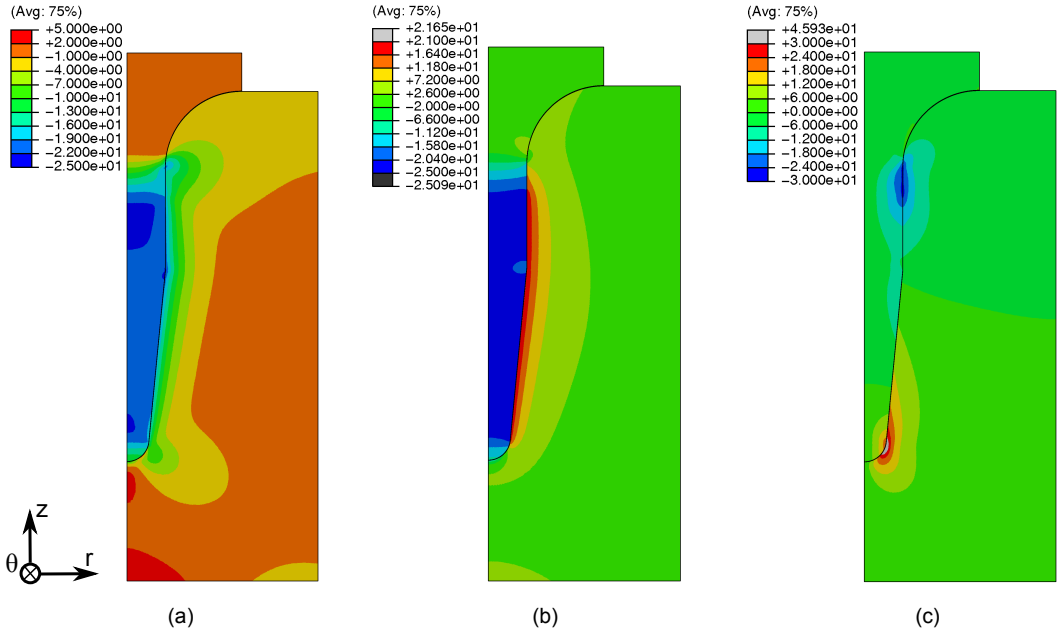

Figure 6.4: Residual stress due to cure: (a) radial stress (σ_r), (b) circumferential stress (σ_θ), (c) shear stress (τ_{rz}). Unit (MPa).

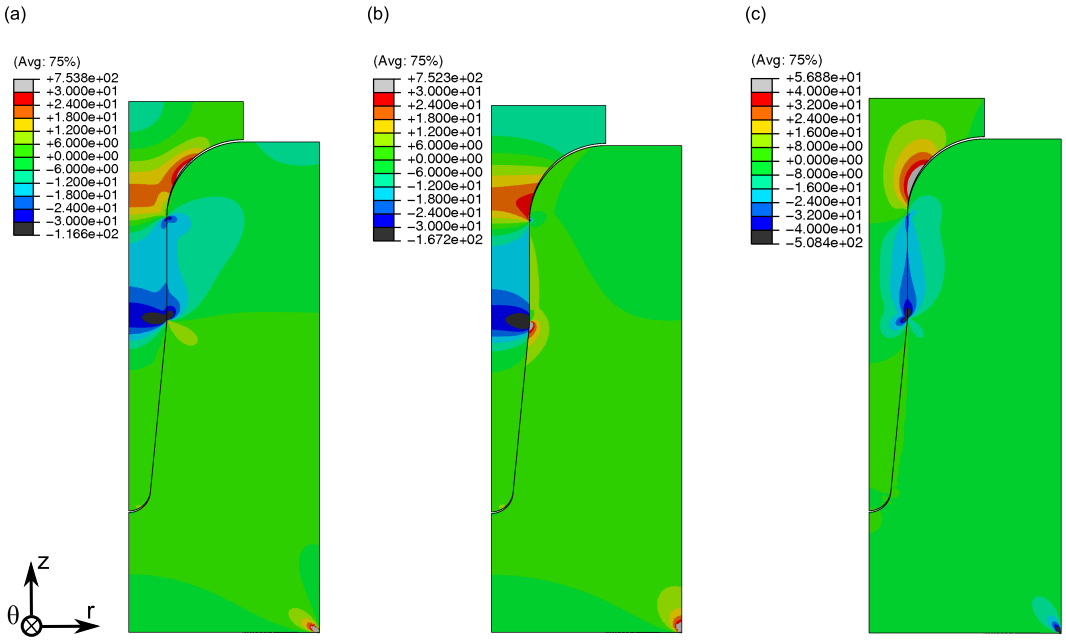

Figure 6.5: Mechanical + Residual stress: (a) radial stress (σ_r), (b) circumferential stress (σ_θ), (c) shear stress (τ_{rz}). Unit (MPa).

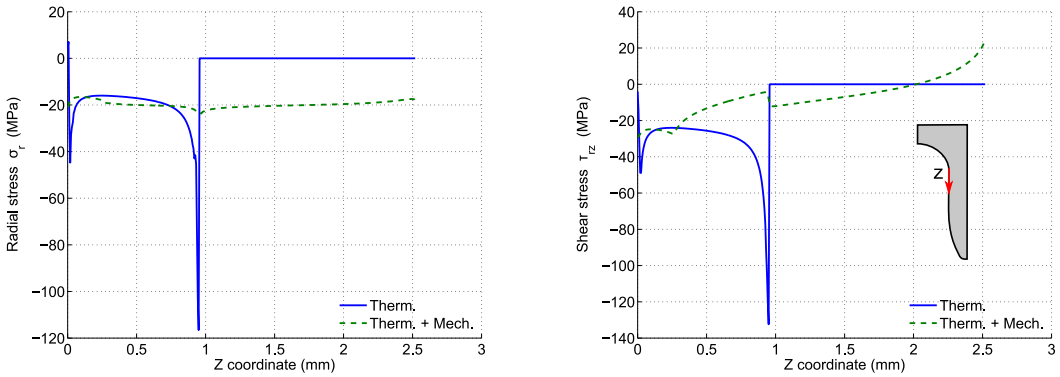

Figure 6.6: Thermal and mechanical stress distributions at pin interface: (a) radial stress (σ_r), (b) shear stress (τ_{rz}).

this phase the applied force is not enough to beat the friction resistance, therefore the pin remains steady in its position. When the force exceeds a threshold value (about 70N in this case) and the applied force becomes higher than the maximum friction resistance and pin starts sliding. As soon as this occurs a void is generated between pin tip and laminate; all surfaces not perfectly parallel to the pin pullout displacements separate and only the cylindrical portion of the pin remains in contact (Fig. 6.3a). This practically reduces the effective height of the pin that resists to pullout. When this section is completely pulled out the resisting force drops to zero. The effective height of the pin can be written as follows:

$$h^* = h - h_t - r_f \tag{6.1}$$

During the sliding regime: the shear stress at the interface is proportional to the contact pressure (Fig. 6.5). The shear deformation due to loading increases the contact pressure and shear at the lower part of the pin. This non-linear effect adds extra resistance to the pin pullout. The level of this contact stress is related to the laminate shear deformation, which depends on the aspect ratio of pin embedded length to pin diameter, h^*/d. Radial normal stress and shear stress at the pin interface are plotted in Fig. 6.6. Calculated pin pullout force vs. displacement is compared with the test measurement in Fig. 6.7a. The model is calibrated by setting the friction coefficient (μ). This coefficient is characteristic of the pin surface roughness and the manufacturing technology.

It worth noting that, due to the lateral constraint of the pin, small variations of the pin surface position results in a quite high contact stress. Therefore the coefficient μ also takes into account the average effect of the surface imperfections which cause over-pressure and higher pullout resistance. When the coefficient of friction is set to 1.5 the model agrees with the test result very well as shown in Fig. 6.7a.

Fig. 6.7b is a schematic of the traction-separation law, i.e. cohesive zone model, describing the pin bridging effect. It is deduced from the pin pullout

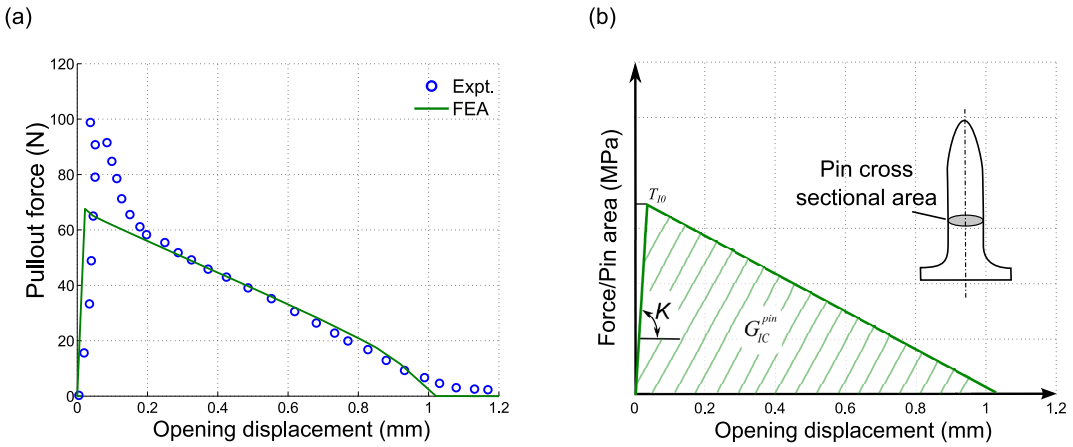

Figure 6.7: Mechanical + Residual stress: (a) radial stress (σ_r), (b) circumferential stress (σ_θ), (c) shear stress (τ_{rz}). Unit (MPa).

force vs. displacement relation in Fig. 6.7a. The law is defined by three parameters, i.e. the initial stiffness (K_I), the cohesive strength (T_{I0}) and the fracture toughness (G_{IC}^{pin}). This law can be implemented into a macro-scale structural model for calculating the energy absorption of the pins for a crack propagating purely in mode-I.

6.2.3 Pin aspect ratio effect

As shown in previous paragraph the maximum resisting force (P_{max}) of a single-pin to pullout can be expressed in function of the following parameters: pin diameter d, effective pin height h^* and coefficient of friction μ:

$$P_{max} = \mu \int_0^{2\pi} \int_0^{h^*} \sigma_r r d\theta dz \tag{6.2}$$

Where σ_r is the contact stress around the pin, which is function of the initial curing thermal stress and the shear deformation of the laminate due to strain. The pullout force can be written as follows:

$$P_{max} = \mu \pi d h^* \overline{\sigma_r} \, (h^*/d) \tag{6.3}$$

Where $\overline{\sigma_r}$ is the average compressive stress over the pin interface, function of the pin aspect ratio h^*/d. A graph representing the variation of this parameter is plotted in Fig. 6.8. The graph shows that the more elongated the pin is the less the effect of strain of the increase of pullout resistance. However, it should be noticed that increasing pin height (i.e. aspect ratio) provokes a reduction of the average compressive stress at the pin interface, but globally produces an increase of pullout resistance due to the higher pin height. Nevertheless, the results of this study shows that this increment is as much as one would expect

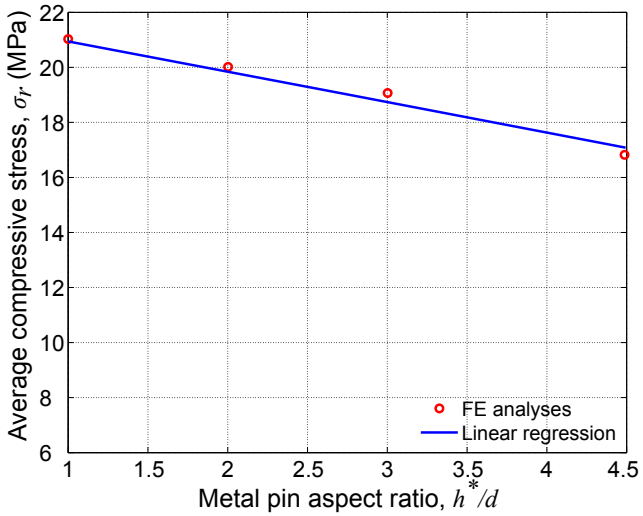

Figure 6.8: Influence of pin aspect ratio (h^*/d) on the average compressive stress ($\overline{\sigma_r}$).

considering a the average compressive stress constant. Eq. (6.3) together with Fig. 6.8 give a simple analytical tool for calculating the pullout resistance force of a generic geometry single-pin.

6.3 Single-pin shear test

6.3.1 Test geometry and model description

Mode-II bridging force exerted by metal pins was measured by single-pin shear test. This test was also simulated by FE modelling and compared with experimental results. In order to reduce the uncertainly, especially on material properties at the pin root, single-pin specimens were manufactured using a precision milling machine from a stainless steel AISI 304 rod, instead of CMT welded. The geometry of the pin was: diameter $d = 0.8$ mm, height $h = 2.5$ mm, fillet radius $r_f = 0.4$ mm. Specimen preparation, laminate material, layup and curing process was then kept the same as for the mode-I test samples, described in the previous section.

The testing rig used for shear tests was designed to constrain metal and composite part to have a relative displacement of pure shear, i.e. avoiding any opening displacement. The test rig comprises two arms in which the metallic and composite halves of the specimen are respectively clamped. The arm containing the composite part has an adjustable screw-driven clamp to lock the specimen; the other part has a fitting hole where the metallic base cylinder is positioned at the beginning of the test. A schematic of the testing rig is depicted in Fig. 6.9. An additional clamp with PTFE rollers is used to lock

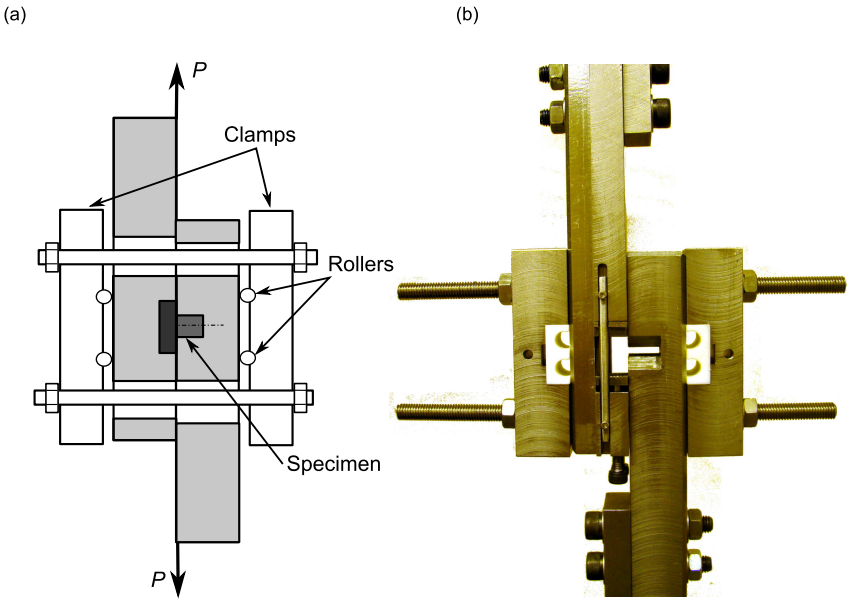

Figure 6.9: Testing rig used for mode-II single-pin tests. (a) schematic of the rig, (b) picture the assembled rig ready for testing.

the backing surfaces of the rig, i.e. to constrain any opening displacement. These tests were part of a larger testing campaign carried out by John Butler as part of the bridging the divide project. Further detail can be found in [108].

Due to the dimension of the rig, the compliance of this has been found to be of the same order of magnitude as the specimen. For this reason the displacement recorded at the crosshead is considerably bigger than the real specimen displacement. A digital image correlation system (DANTEC) was used to measure the actual shear displacement and the rig stiffness (K_R). The stiffness of the system (rig+specimen) is given by the following relation:

$$\frac{1}{K_T} = \frac{1}{K_S} + \frac{1}{K_R} \tag{6.4}$$

Where subscripts "T", "S" and "R" respectively stand for: total, specimen and rig. Considering that the stiffness of the rig remains constant during the test, any loss of stiffness is due to specimen failure only. The stiffness of the rig can be used therefore to correct the crosshead measured displacement. Given the crosshead displacement, applied force and shear rig stiffness, the following relation provides the effective shear displacement of the sample (δ_s):

$$\delta_s = \delta_c - \frac{P}{K_R} \tag{6.5}$$

A 3D FE model of the sample geometry has been created as described in Sec.3.3.2. Considering the quasi isotropic layup, the laminate properties have

Table 6.2: Material properties uses for interlocked metal single-pin shear analysis.

Stainless steel AISI 304

E	ν	α	σ_Y	σ_U	n^*
190 GPa	0.33	11 μm/m	300 MPa	600 MPa	3.8

Resin rich zone

E	ν	α	σ_Y
3 GPa	0.4	24 μm/m	100 MPa

Laminate prepreg.

E_{11}	E_{22}	E_{33}	G_{12}	G_{13}	G_{23}	ν_{12}	ν_{13}	ν_{23}	α_1	α_2	α_3
(GPa)								(μm/m)			
120	8.5	8.5	4.2	4.2	4.2	0.35	0.35	0.4	2.1	24	24

* Ramber-Osgood parameter used in 6.6

been homogenised according to the different fibre percentage. The region closest to the pin (within one pin radius) is assumed to have pure resin properties; an intermediate region (up to the boundary of the eyelet resin pockets), due to fibre misalignment, is assumed to have material properties equal to 50% of the base laminate. The presence of voids and the pin ploughing phenomenon, as described in Sec.3.3.2, has been modelled assuming a perfectly plastic behaviour of the resin near the pin. Material behaves elastically until the yielding stress is reached. After that the stress remains constant and material interaction allows large strain deformation. The yield stress and all the properties of the resin rich zone have to be considered as parameters of the model and they are meant to be set over a reference test. Yielding stress particularly is expected to depend upon the laminate layup as well. Laminate properties at the far field are assumed homogeneous and are calculated using the laminate theory. Material properties used in the analysis are summarised in Table 6.2. The contact force between pin and laminate is modelled using a penalty surface to surface algorithm with a friction coefficient $\mu = 1.5$ (same as the one used in the pullout model). Plastic deformation of the metal part is calculated by an iteration procedure using the Ramberg-Osgood stress-strain relation:

$$\epsilon = \frac{\sigma}{E} + 0.002 \left(\frac{\sigma}{\sigma_Y} \right)^n \tag{6.6}$$

Model domain and boundary condition applied are depicted in Fig. 6.10a. Loading is introduced applying a pure mode-II displacement between top surface of the laminate and metal base. In order to reproduce the stiffness of the clamp, used to constrain the opening displacement of the sample, top and bottom surfaces of the sample were connected by a linear spring element of stiffness 500 N/mm.

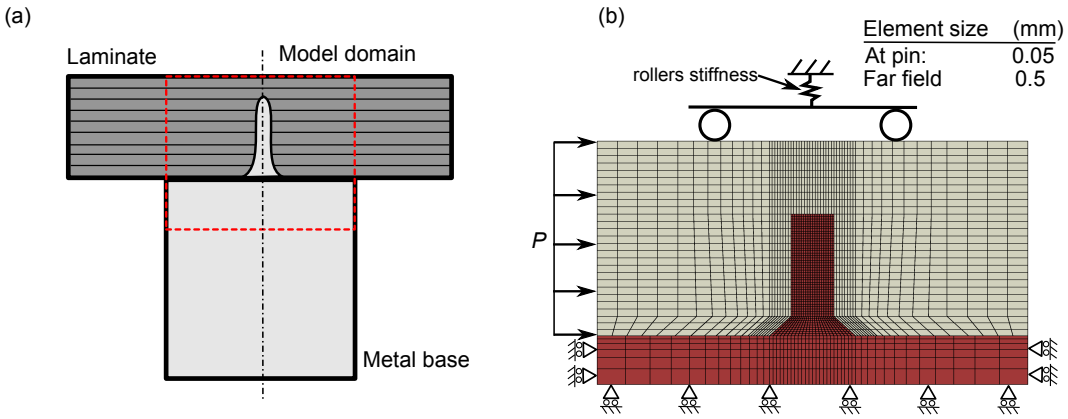

Figure 6.10: (a) Cartoon of the model geometry and the applied boundary conditions, (b) mesh used in analysis (fillet radius of the depicted geometry: $r_f = 0.4$ mm).

Three dimensional quadratic brick elements with reduced integration (C3D20R elements) have been used to model both metal and composite parts. A mesh sensitivity analysis has been performed to set the element size. Mesh depicted in Figure Fig. 6.10b showed best compromise between accuracy and computational time.

6.3.2 Numerical results

When shear load is applied, the pin strains mainly in bending. The maximum stressed areas are the the pin root, just above the fillet radius. Fig. 6.11 shows the distribution of normal stress (σ_{33}) and shear stress (τ_{13}) during the linear-elastic response of the pin. Normal stress in maximum far from the neutral axis and the shear stress is maximum at the centre of the pin. With increasing the shear strain, material at the pin root exceeds the yielding limit and behaves plastically and the high lateral force makes the pin lean in the direction of applied load. The normal stress peak moves upward, where material is still in plastic field (Fig. 6.11c), whereas at the pin root shear stress becomes critical, as shown in Fig. 6.11d. Stress level increases up to the ultimate load and the pin starts failing at pin root. At the same time the resin rich area around the pin behaves non-linearly, allowing the pin to plough in. The entire cross section of pin fails plastically at root, shearing off the entire pin, still almost completely embedded into the laminate (no pin pullout effect). This behaviour found agreement with experimental results.

Fig. 6.12 shows a comparison of the force vs. displacement curve predicted by the model and the experimental data. Following consideration can be done: (1) initial linear-elastic response of the pin is very stiff (about 7500 N/mm). (2) This linear-elastic phase is followed by a non-linear response of the pin due to the plastic deformation of the pin. (3) Due to the high pressure at

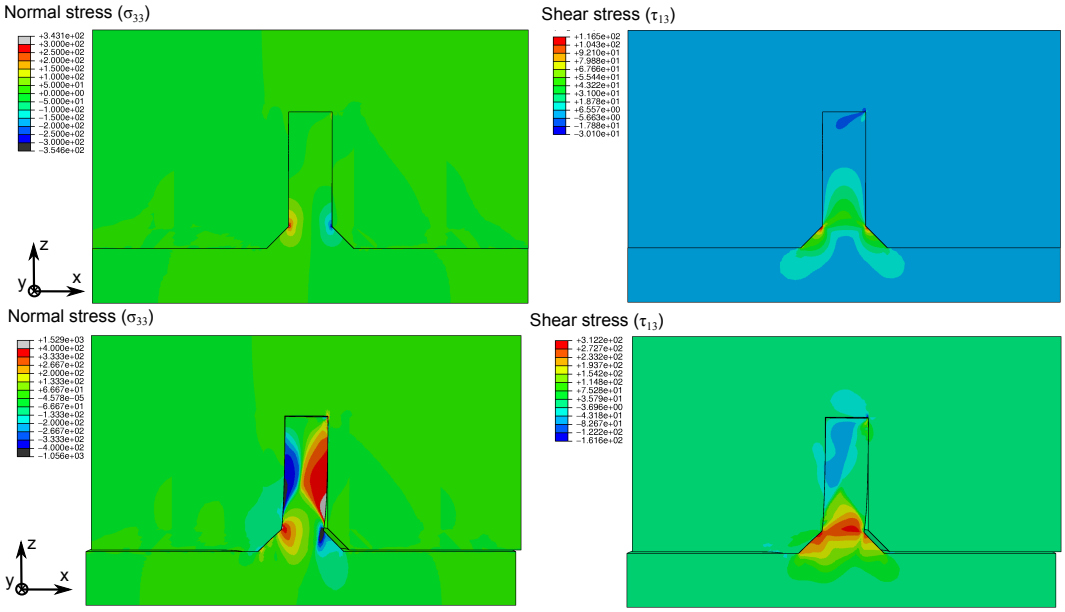

Figure 6.11: Stress distribution on the pin: (a) and (c) normal stress in z-direction (σ_{33}) during the linear-elastic and non-linear phases respectively, (b) and (d) transverse shear stress (τ_{13}) during the linear-elastic and non-linear phases respectively. Unit: MPa.

the root, the pin also ploughs into the resin rich areas of the laminate. This phenomenon is also believed to be related to the closure of the voids embedded in the resin rich areas. This explains the large variability of experimental test results during this phase.

The model shows good agreement with experimental results: initial stiffness, transition load between linear/non-linear behaviour were very well predicted. Also the model prediction during the ploughing phase shows relatively good agreement with experiments, always remaining within the experimental scatter.

The mode-II bridging law can be used to obtain the traction-separation law, i.e. cohesive zone model, describing the pin bridging effect. It is deduced from the pin bridging force vs. displacement relation in Fig. 6.12. The law is calculated by dividing the pin bridging force by the pin cross section area, as described in Sec.3.4.1. This law can be implemented into a macro-scale structural model for calculating the energy absorption of the pins for a crack propagating purely in mode-II.

6.3.3 Effect of geometric parameters

Differently form mode-I bridging law, mode-II pin bridging involves a much larger number of parameters, particularly it will be a function of geometrical parameters and material properties. In order to better understand the effect of

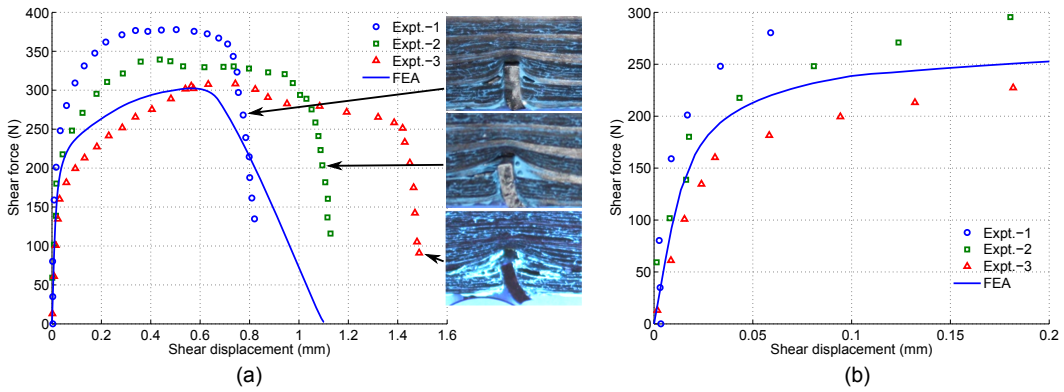

Figure 6.12: Comparison between FE analysis and experimental data of the mode-II bridging force exerted by the pin: (a) force versus applied displacement curve up to pin ultimate failure, (b) zoom of the first part of the curve.

these parameters a parametric study has been carried out. In particular three parameters have been identified to affect the most pin bridging: pin height (h), pin diameter (d) and pin fillet radius (r_f).

The way these parameters affect the elastic response and the non-linear response of the curve gives a clear insight to the physics of the phenomenon, i.e. an indication of who to modify the pin configuration to obtain specific characteristics of the bridging curve. Whereas the linear elastic response of the pin is fully characterised by the initial stiffness (slope of the straight line passing through the origin, tangent to the curve), the non-linear response of pin can be described by three parameters of the curve: yielding load, ultimate load and displacement at failure (as shown in Fig. 6.13).

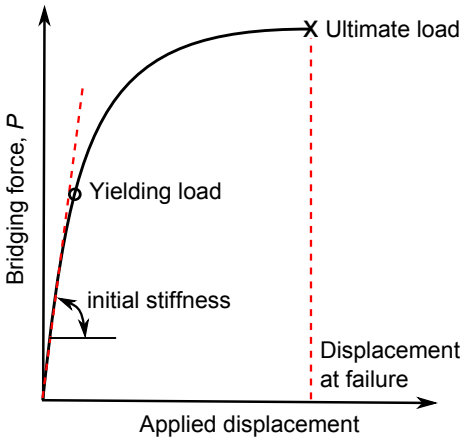

Figure 6.13: Schematic diagram of the mode-II bridging law.

However, considering the large variability of the measured bridging curve during the non-linear response of the pin (i.e. large scatter of ultimate load), the yielding load can be considered a more accurate indication of pin strength. Furthermore, another consideration that should be done is that, differently from mode-I bridging where the two adherents show large out-of-plane displacements after delamination, for mode-II bridging shear displacement between the adherents is usually much smaller, i.e. the most relevant part of the curve is the linear elastic response. For these reasons only the pin stiffness and yielding load (pin elastic limit load) were presented in the follow-

Table 6.3: Range of parameters used in for sensitivity study.

	Pin height, h	Pin diameter, d	Pin fillet radius, r_f
		(mm)	
Lower bound	1.5	0.4	0.4
Reference value	2.5	0.8	0.4
Upper bound	3.5	1.6	1.2

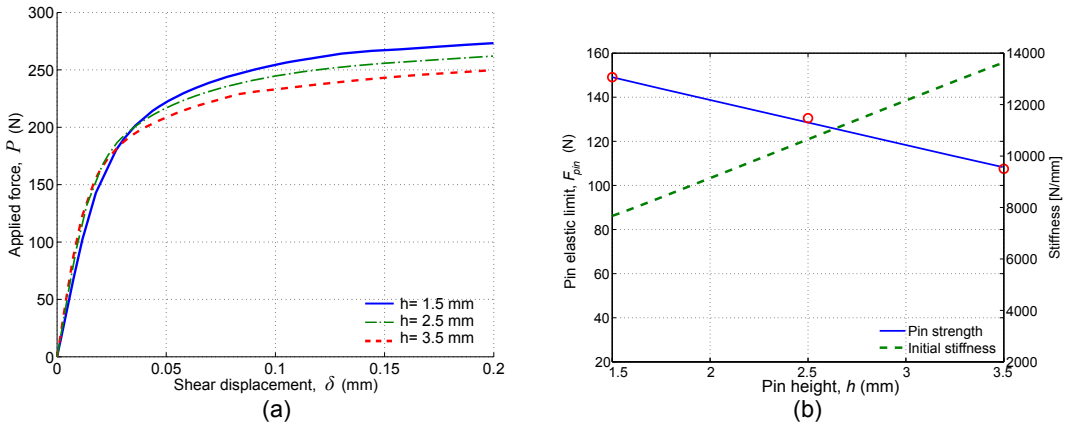

Figure 6.14: Sensitivity of the pin bridging force to the pin height (h): (a) force vs. displacement curves of different configurations, (b) interpolation curves of the pin elastic limit and initial stiffness in function of the pin height.

ing graphs.

The influence of each parameter was studied one time each using as reference the pin configuration analysed in Sec.6.3.1 ($d = 0.8$, $h = 2.5$, $r_f = 0.4$,). Each singular parameters was varied within the range indicated in Table 6.3 keeping the others unchanged and equal to the reference configuration.

Figs 6.14a–6.16a show the pin bridging curves of the analysed configurations with different geometries. The global behaviour of all of them is always the same, showing that there is no change in failure mode (from shear to pullout of the pin from the laminate). The model shows a relatively low sensitivity to the pin height (Fig. 6.14a): a variation of this parameter of 60% produces a very modest change in the force-displacement curve. Increasing the pin height enhance lateral support of the pin provided by the surrounding and therefore the pin initial stiffness, as visible in Fig. 6.14a. Whereas stress level at the pin root due to bending get slightly worse by increasing the pin height, i.e. the elastic limit load decreases.

The influence of pin diameter on the pin bridging force is plotted in Fig. 6.15. This is the parameter the model shows the highest sensitivity to. As visible in Fig. 6.15b the pin elastic limit load (i.e. the pin strength) shows a quadratic

dependence to this parameter. This confirms the fact that the failure mode of all configurations always remain the same and the pin strength is therefore proportional to the pin cross section. The dependence of pin initial stiffness on the pin diameter shows linear correlation. This indicates that the elastic response of the pin is mainly influenced by the stiffness of the elastic foundation that supports the pin rather than the bending rigidity of the pin.

Fig. 6.16 shows the influence of the pin fillet radius. This parameter affects both pin elastic limit and initial stiffness. Whereas initial stiffness to have a strong liner dependence on this parameter (an increase of 50% of pin fillet radius correspond to a + 25% of stiffness), the elastic limit shows a logarithmic behaviour: an increase of 50% of radius provokes a relatively small increment (8%). On the other hand reducing the fillet radius of 50% causes a knock down of the elastic limit of abut -40%. This result clearly indicates that the fillet radius should never be smaller than the pin radius.

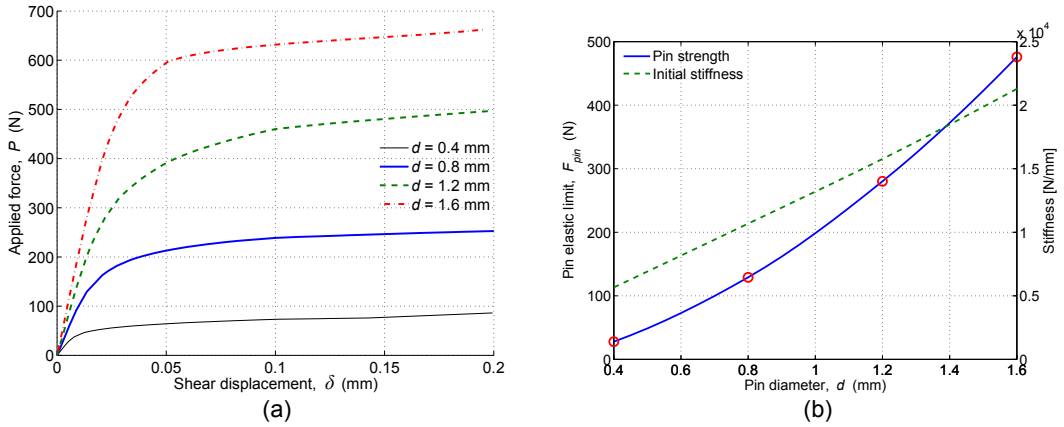

Figure 6.15: Sensitivity of the pin bridging force to the pin diameter (d): (a) force vs. displacement curves of different configurations, (b) interpolation curves of the pin elastic limit and initial stiffness in function of the pin diameter.

6.4 Summary of results

Two validated FE models have been developed which can analyse respectively the mode-I and mode-II bridging properties of interlocked metal pin reinforcements for hybrid metal/composite structures. These models were able to accurately predict both mode-I and mode-II bridging laws of single-pin reinforcement. The FE model provides important insights into the strengthening and toughening of interlocked pin joints. Main results can be summaries as below:

- Mode-I bridging is characterised by friction between pin and surrounding laminate. This friction resistance in generated by the thermal compressive stress induced by the cure process of the laminate. The pin pullout

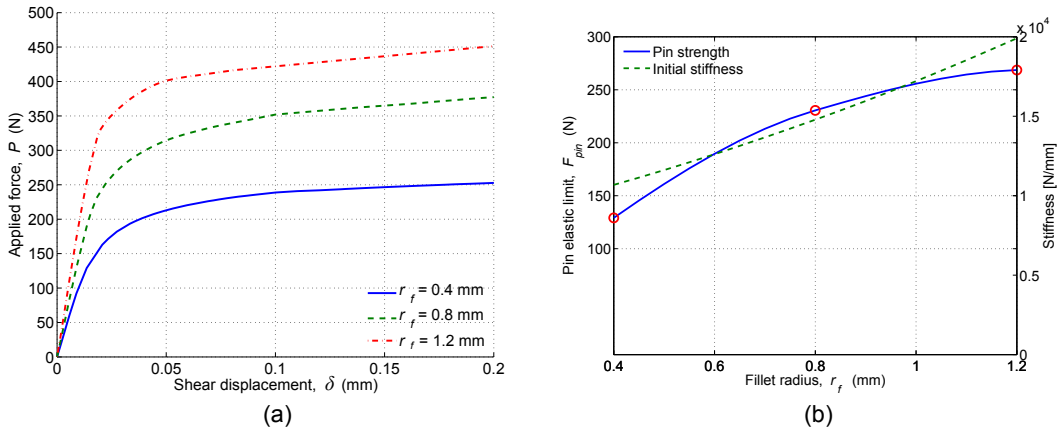

Figure 6.16: Sensitivity of the pin bridging force to the pin fillet radius (r_f): (a) force vs. displacement curves of different configurations, (b) interpolation curves of the pin elastic limit and initial stiffness in function of the pin fillet radius.

force is therefore proportional to the lateral surface of the pin embedded into the laminate. This result implies that, keeping the percentage of reinforcement constant, the way to improve the bridging performance of pins is to increase the wet-surface, i.e. increase aspect ration;

- Due to the shear strain of the laminate, the pin bridging force shows a small sensitivity to the pin aspect ration. The average compressive stress around the pin (i.e. also friction resistance) slightly decreases by increasing the pin aspect ratio. However, this reduction of pin performance always remains much smaller than the increment due to the enhancement of wet-surface resisting pullout.

- The model also shows that for pike-shaped pins the only portion of the embedded length of the pin that contributes to bridging is the cylindrical part of the pin (i.e. the pin head should not be accounted).

- Mode-II bridging is characterised by the pin bending, plastic deformation at the pin root, ploughing into the surrounding laminate and shear failure. Despite the complexity of the phenomenon the model was able to accurately predict the pin failure mode and the bridging force of the pin.

- The bridging curve shows an initial linear elastic response, followed by a continuous compliance-increasing phase. This phase is characterised by large plastic deformation of the pin and pin ploughing into the laminate.

- It was found that the first part of the bridging curve is highly influenced by the stiffness of the elastic foundation that supports the pin (i.e. the laminate), whereas the pin strength is mostly influenced by the pin diameter.

- It was also found that a small fillet radius (< than pin radius) strongly deteriorates the bridging performance of pin, both is terms of strength and stiffness.

CHAPTER 7

ANALYSIS OF PIN REINFORCED HYBRID METAL/COMPOSITE DOUBLE-LAP JOINTS

7.1 Introduction

This chapter presents an FE model for predicting the performance and failure behaviour of a novel hybrid metal-composite joint with interlocking pins to increase resistance to debonding failure. A unit-strip model with cohesive interface elements at bond line was constructed to simulate the onset and propagation of debonding cracks. Two separate traction-separation laws for the cohesive elements are employed; one represents unreinforced adhesive properties and the other is used for the pin enhanced toughness. This approach can account for the so-called large scale bridging effect and also avoids using concentrated pin forces in the numerical models, thus removing mesh-size dependency and permitting more accurate and reliable computational solution.

In the first part of the chapter model prediction are compared with experimental data for validation purposes. The second part of the chapter analyses the model sensitivity to main bridging parameters.

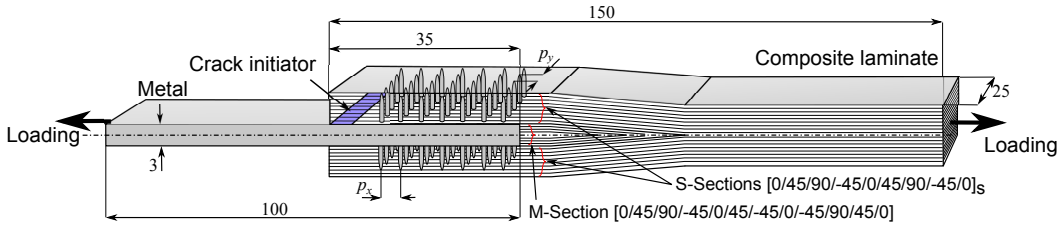

Figure 7.1: Joint geometry and dimension; pin pitch p_x and p_y are given in the next section (unit: mm).

7.2 Geometry and model description

7.2.1 Experimental testing of the joint

Unreinforced and pin-reinforced double lap joints were produced and tested under tensile load. The geometry and dimension are given in Fig. 7.1. Unreinforced configuration was used as a baseline reference to assess the effects of pin reinforcement. Steel AISI 304 and carbon fibre epoxy prepreg T700-M21 were used respectively for fabricating the metallic and composite parts. The adhesive bonding was reinforced by pins arranged in an array of 5x7. Spike head pins of 0.8 mm diameter and 4 mm height were manufactured using the CMT technology on the metallic surface. The metal part of the overlap was then sand blasted in order to improve the adhesion between composite and metal. The composite part was made of a central section (M-section) and two side sections (S-section) as shown in Fig. 7.1. A quasi-isotropic layup was used, [0/45/90/-45/0/45/-45/0/-45/90/45/0] and $[0/45/90/-45/0/45/90/-45/0]_S$ for "M" and "S" sections respectively; each lamina ply having a nominal thickness of 0.25 mm. An initial crack of 5 mm length was created by inserting a thin FEP (fluorinated ethylene propylene) film at the runout of the composite part. In order to insert the pins into the prepreg without damaging the in-plane carbon fibres, an ultrasonic horn device was used. Mechanical testing was performed using a 100 kN Instron test machine under displacement controlled loading at speed of 1 mm per minute.

7.2.2 Model description

FE model was developed to analyse the structural properties and failure of a pin-reinforced double lap joint (DLJ) subjected to a tensile load, as schematically shown in Fig. 7.1. The analysis was based on a cohesive zone model where the bridging effect of pin reinforcements is assumed to be fully characterised by the load carrying capability of a single-pin. The bridging law of a single pin under shear loading was measured experimentally and used to define the structural response of pin in the model. Cohesive zone modelling (CMZ)

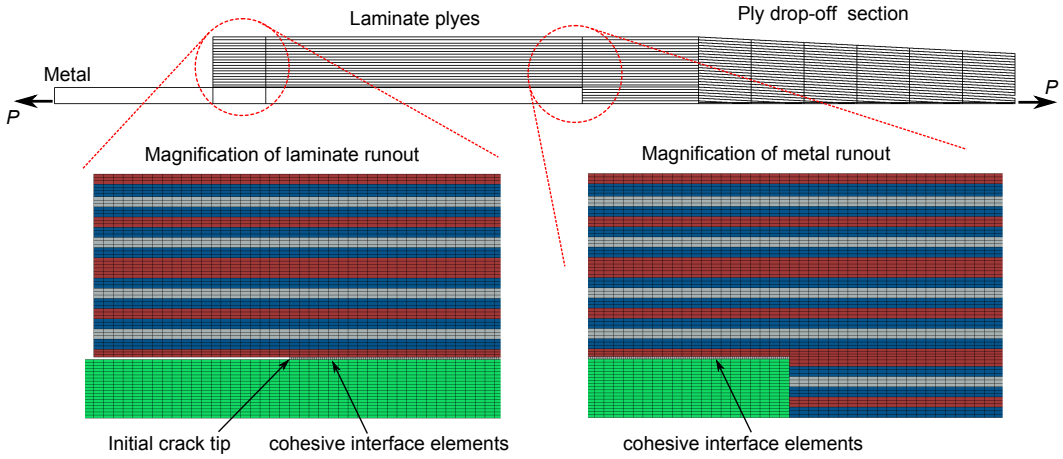

Figure 7.2: Model of the unreinforced joint (plane strain model).

was used to calculate initiation and growth of delamination cracks in the joint. Two models are proposed in this paper to simulate the pin bridging effects: a spring-pin model that reproduces the nonlinear response of the pin, and a cohesive-pin model based on a simplified traction separation law (TLS).

Unpinned

A finite element model of the unreinforced joint was created using quadratic plane strain elements with reduced integration (designated as CPE8R in Abaqus), as shown in Fig. 7.2. The model was developed to calibrate the cohesive element properties along the bonded interface and to validate the cohesive zone model used for analysing crack growth. After performing mesh size sensitivity analysis, the mesh shown in Fig. 7.2 was found to give acceptable compromise between accuracy and computation time. Composite laminate was modelled with three elements per ply thickness. Elastic properties of each ply were calculated according to the local fibre orientation in relation to the main coordinate axis. Material properties of the carbon fibre/epoxy laminate and the stainless steel used for the two adherends of the joint are given in Table 7.1. Plastic deformation of the metal part is calculated by an iteration procedure using the Ramberg-Osgood stress-strain relation:

$$\epsilon = \frac{\sigma}{E} + 0.002 \left(\frac{\sigma}{\sigma_Y} \right)^n \tag{7.1}$$

Due to the symmetry of the joint only half of the geometry is modelled; vertical displacement of the elements nodes on the symmetry plane is constrained. Cohesive elements (designated as COH2D4 in Abaqus) were used to model the debonding crack along the bondline interface with cohesive element size being one-fifth of the adjacent ply element size in order to achieve numerical

Table 7.1: Material properties and cohesive element parameters used in the Double lap joint FE model.

Laminate (Unidirectional carbon fibre/epoxy Hexcel T700-M21)	
In-plane Young's modulus (E_{11})	120 GPa
Transverse Young's moduli (E_{22}, E_{33})	190 GPa
Shear moduli (G_{12}, G_{13}, G_{23})	4.6 GPa
Poisson's ratio (ν_{12}, ν_{13}, ν_{23})	0.35

Metal adherend (Stainless steel AISI-304)	
Young's modulus (E)	190 GPa
Poisson's ratio (ν)	0.33 GPa
Yield strength (σ_Y)	290 MPa
Ramberg-Osgood parameter (n) used in Eq. (7.1)	3.8

Cohesive Element Properties of Adhesive (It is cobonding - the adhesive is the laminate resin: M21)	
Mode I traction stiffness of laminate (K_I)	2.5 x 10^{13} N/m^3
Mode II traction stiffness of laminate (K_{II})	2.5 x 10^{13} N/m^3
Mode I failure load of laminate (T_{I0})	30 MPa
Mode II failure load of laminate (T_{II0})	70 MPa
Mode I fracture toughness of laminate (G_{IC})	200 J/m^2
Mode II fracture of laminate (G_{IIC})	550 J/m^2

stability [124, 125]. A bilinear traction-separation law was used to define the constitutive response of cohesive elements. A mixed-mode failure criterion was used to calculate the crack propagation:

$$\frac{G_I}{G_{IC}} + \frac{G_{II}}{G_{IIC}} = 1 \tag{7.2}$$

where G_I and G_{II} are the crack tip strain energy release rate values corresponding to the crack opening (mode-I) and crack sliding (mode-II) movement, respectively. Values of parameters used for the cohesive fracture analysis are provided in Table 7.1. FE simulations were run under displacement-controlled loading condition by applying a monotonically increasing tensile displacement as the boundary condition on the nodes at the joint ends (Fig. 7.2).

Pin-locked joint model

The pin reinforced joint model has the same geometry as the unpinned joint. Because of the pins, the use of a plane strain model is not viable. Due to the periodic pin arrangement of the pins, a unit-strip model is used to represent a basic "repetitive unit" of the joint that contains half pin row. The unit-strip model was constructed with the pins spaced at regular intervals to respect the pin pitch in the longitudinal direction ($p_x = 3.75$ mm); the width of the strip is half of the pin pitch in the lateral direction ($p_y = 4.16$ mm, as shown in Fig. 7.3. However, the model is representative of an infinitely wide pin arrangement (i.e. similar to a plane strain model). The implications and influence of model results are discussed in Sec.7.3.2. The insets of Fig. 7.3 show the two different pin-models used for analyses, which are described later in this section.

Eight-node linear continuum shell elements with reduced integration (designated as CS8R in ABAQUS) were used for composite and metal adherends, whereas the bonding interface was modelled by a layer of 8-node cohesive elements (COH8). The bridging force carried by each individual pin was measured experimentally using the testing rig shown in Fig. 7.4a. The specimen consisted of a square block of unit-cell laminate (20x20x4.6 mm) having the same composite layup as the joint, containing a single pin (with dimension and material identical to the pin used to reinforce the joint) CMT welded over a thick cylindrical metal substrate (of diameter 12 mm and height 12 mm). The test was carried out by constraining the crack opening displacement in order to avoid any mixed mode loading condition. Due to the yielding and bending of the pin the bridging force exerted by the pin was strongly nonlinear in the rising part of the pin force vs. displacement curve.

In order to implement this nonlinear relation into the FE model for DLJ, a traction-separation law in terms of the pin cross-sectional stress is deduced

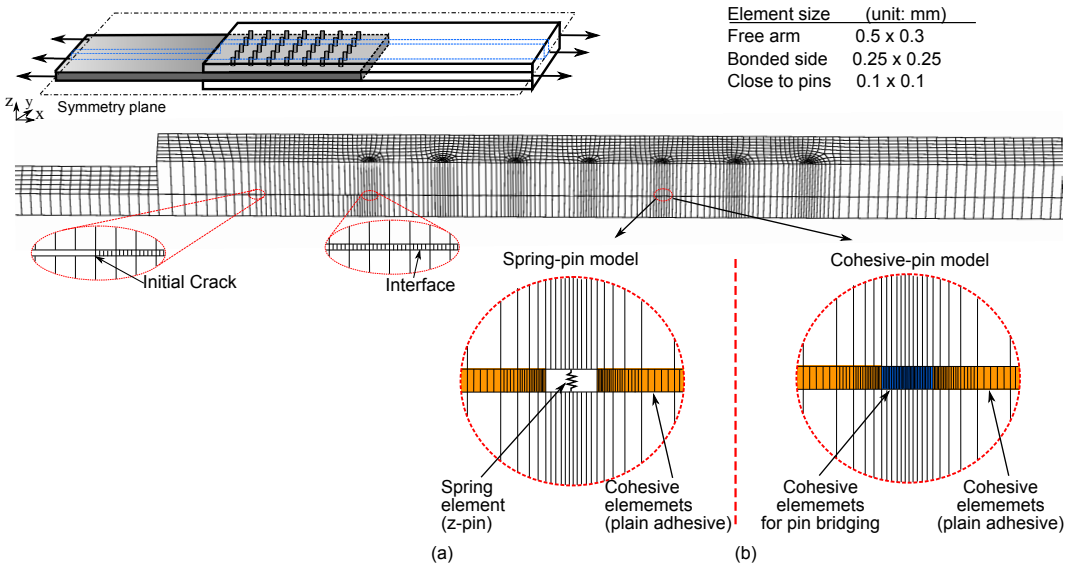

Figure 7.3: Unit strip model for pin reinforced double lap joint.

from the bridging force, as described in Sec.3.4.1.

$$T(u) = \frac{P(u)}{\pi r_0^2} \tag{7.3}$$

Where u is the shear displacement, $T(u)$ the pin bridging stress and $P(u)$ the bridging force. The bridging traction given by Eq. (7.3) is plotted in Fig. 7.4b (solid line represents the measured bridging law). The bilinear curve (dashed line) is an approximation. The two curves are equivalent in terms of: (1) initial stiffness (K_{II0}^{pin}), cohesive strength (T_{II0}^{pin}) and enhanced fracture toughness (G_{IIC}^{pin}), which is the area under the stress-displacement curve; both curves have same energy absorption rate due to the pin bridging effect. Pin bridging parameters are reported in Fig. 7.4b insert.

This pin response was implemented into the global FE model of the DLJ specimen using two different models to represent respectively the nonlinear and bilinear bridging laws as shown in Fig. 7.3 insets. (1) The "spring-pin" model employs nonlinear spring elements with a user-defined force-displacement relation, which is the nonlinear curve in Fig. 7.4b. As depicted in Fig. 7.3 inset (a), these springs are connected to the two adherends through Multiple-Point Constraints (MPCs). (2) The "cohesive-pin" model uses cohesive interface elements (Fig. 7.3 inset (b)) governed by the simplified bilinear traction-separation law.

Boundary condition of the unit-strip model is set according to the periodic pin arrangement and it is representative of an infinitely wide pin distribution. The nodal displacement at periodical boundaries is constrained in the y-direction. The two planes that delimit the unit-strip are constrained to remain in-plane,

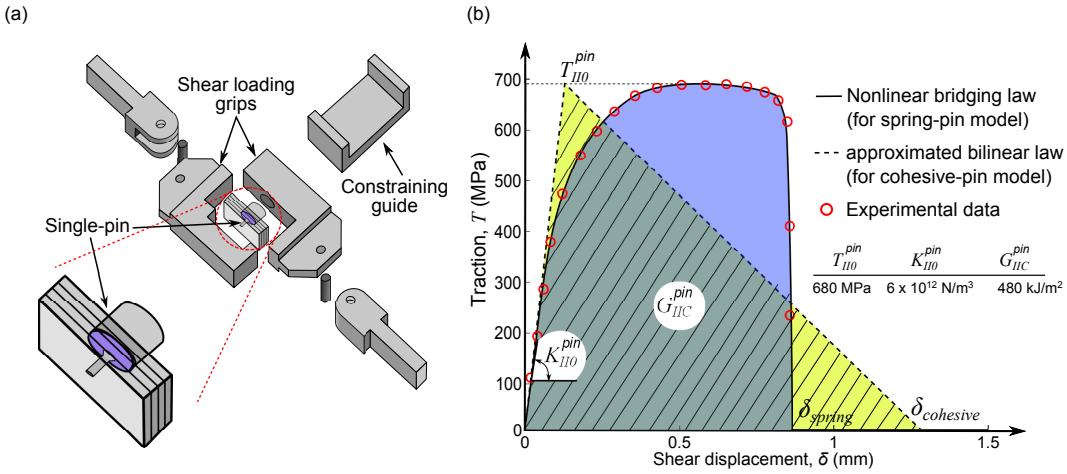

Figure 7.4: Determination of bridging law of single pin reinforcement, (a) a schematic of the testing rig, (b) pin bridging traction-separation laws used for the two pin models.

but also allowed to contract laterally to account for the Poisson's effect. The external applied force to the joint (P) is related to the force calculated through the unit-strip model (P_{strip}) using the following equation:

$$P = \frac{W}{0.5 p_y} P_{strip} \tag{7.4}$$

Where W is the joint width and p_y the pin pitch in the width direction. The scaling factor is simply the ratio between the joint and the model width (i.e the number of strips necessary to cover the joint width).

Due to the finite width of the structure, the number of pins bridging the crack over the joint width (N_{pin}) generally differs from the scaling factor calculated by Eq. (7.4). The pin bridging traction used in the unit-strip model (T_{strip}) is therefore corrected in order to account for this effect:

$$T_{strip} = \frac{0.5 p_y}{W} N_{pin} T \tag{7.5}$$

However, it should be noticed that this factor can vary in a range between $(N_{pin} \pm 1)/N_{pin}$. For large structures such as large fuselage or wing panels, this correcting factor is close to unit.

7.3 Numerical results

7.3.1 Unpinned joint

Figure 7.5a shows the force versus applied displacement curves calculated by the FE model and experimentally measured. There is excellent agreement

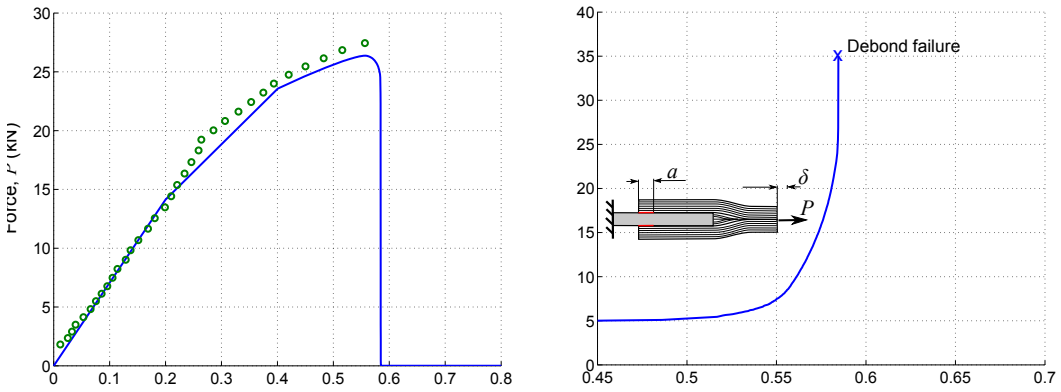

Figure 7.5: (a) Comparison between calculated and measured force vs. applied displacement, (b) Calculated crack length vs. applied displacement.

between the calculated and measured curves, which validates the cohesive FE model for the unpinned joint. The FE model accurately predicted the joint strength (error $< 2.5\%$). The joint response remains linear elastic until the yield stress of the metal substrate is exceeded. This point is identified in the force-displacement curve by the change of slope.

As shown in Fig. 7.5b. The crack starts propagating from the initial crack starter at about $\delta = 0.5$ mm (close to the the peak load and after the change of slope in the force-displacement curve). The crack groth rate monotonically increases with the applied displacement up to a crack length of $a = 25$ mm, where the propagation becomes unstable and the ultimate debond failure occurs abruptly.

The FE model also shows that the crack propagation is influenced by the yielding of the metal plate: when the axial stress exceeds the material strength, the large plastic deformation increases the shear stress at runout, causing propagation of the disbond crack. As shown in Fig. 7.6, the crack front corresponds to the point where the axial strain of the metal substrate (right-hand side of the y-axis) exceeds the plastic yield of 0.2%.

7.3.2 Pin reinforced joint

Force vs. applied displacement

Figure 7.7 compares the calculated and measured curves of force and crack extension versus applied displacement for the pinned joint. The agreement of the predicted curve and experimental data is excellent up the peak load point. Both the cohesive-pin and spring-pin models predict similar force-displacement responses up the peak load (which is expressed as no failure has occurred up

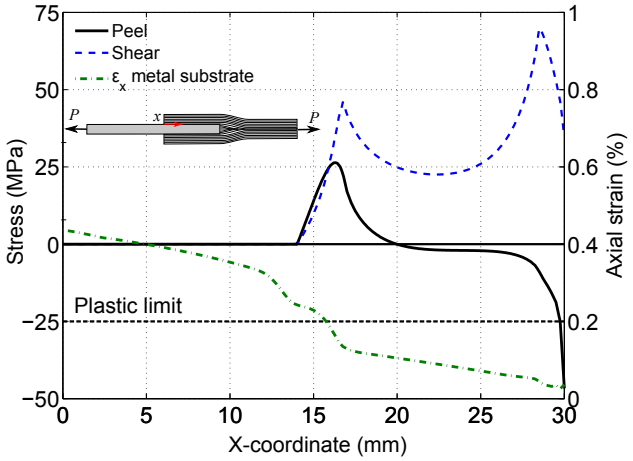

Figure 7.6: Peel (solid line) and shear stress (dash line) distribution over the bonded region during delamination (a = 14 mm). Axial strain over the metallic substrate (dash-pointed line).

to this point); the difference between prediction and measurement is of about 5%. The load drop corresponds to the debonding failure. The load carried by the pin at this point is defined as joint strength (as indicated in 7.7a), since from this point onward the bonded interface is completely failed; whereas the maximum force carried by the joint will be referred in this thesis as ultimate load. From this point onward the load is completely carried by the pin bridging action; the differences between the two models (i.e. cohesive-pin and spring-pin) are more significant.

Both models predict load recovery after the bondline failure. The cohesive-pin model shows a stiffer response after the bondline failure and a smaller displacement at failure. The spring-pin model, which more accurately modelled the pin bridging force (Fig. 7.4b), shows a better agreement with experimental results. For this reason this model has been used to assess the sensitivity analyses carried out in following sections.

Crack extension behaviour

The pin bridging effect starts as soon as delamination crack passes the first pin row (a = 10 mm). Crack tip is shielded from shear stress as the pins transfer load on the crack wake. This delays any further crack advance, slowing down crack propagation. The crack starts propagating at about the same applied load for both reinforced and unreinforced configurations (P = 26 kN - corresponding to δ = 0.55 mm), as shown in Fig. 7.7b. The crack front advances at about the same rate from initial crack length 5 mm up to 10 mm (when the crack front passes the first pin row), from this point onward the crack propagation slows down and the joint is able to pick up more load. The

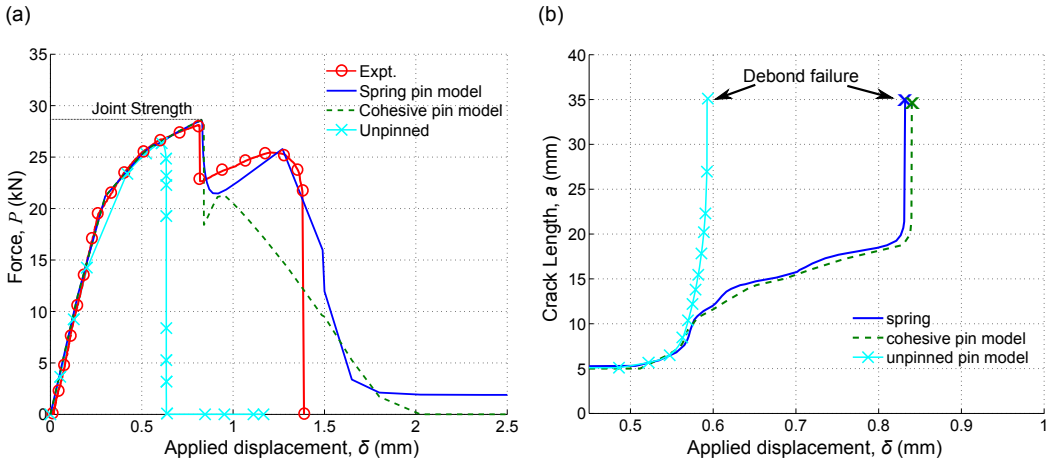

Figure 7.7: (a) Comparison between calculated (using cohesive spring-pin models) and measured force vs. applied displacement curves, (b) Calculated crack extension from its initial size of 5 mm vs. applied displacement.

cohesive-pin model predicts slightly shorter crack length due to employing the simplified bilinear traction-separation law. This is due to the cohesive pins having stiffer response than the pins modelled by the springs. However, the difference between the two models always remains smaller than 2%.

Interlaminar shear stresses

Figure 7.8 shows the interlaminar shear stresses at the dobonidng plane at overlap extension $\delta = 0.65$ mm (crack length $a = 14$ mm). Higher shear stresses are predicted by the cohesive-pin model on the pin rows close to the crack tip. This is because that the bilinear cohesive-pin model is stiffer than the spring-pin model before the force reaches the maximum (Fig. 7.4), hence the higher predicted pin reaction force. It is worth noting that the pin stresses in Fig. 7.8 should not be interpreted as the pin internal stress, but an equivalent stress derived from dividing the bridging force by the pin cross-sectional area.

The figure shows the crack retarding mechanisms, that is the pins in the crack wake (left-hand side) picking up stresses. It also shows the failure behaviour of the joint: increasing applied load a secondary disbond crack onsets at the other runout and propagates toward the main crack front. Final failure occurs when the two crack fronts meet at the centre of the joint. This behaviour was predicted by both cohesive-pin and spring-pin models.

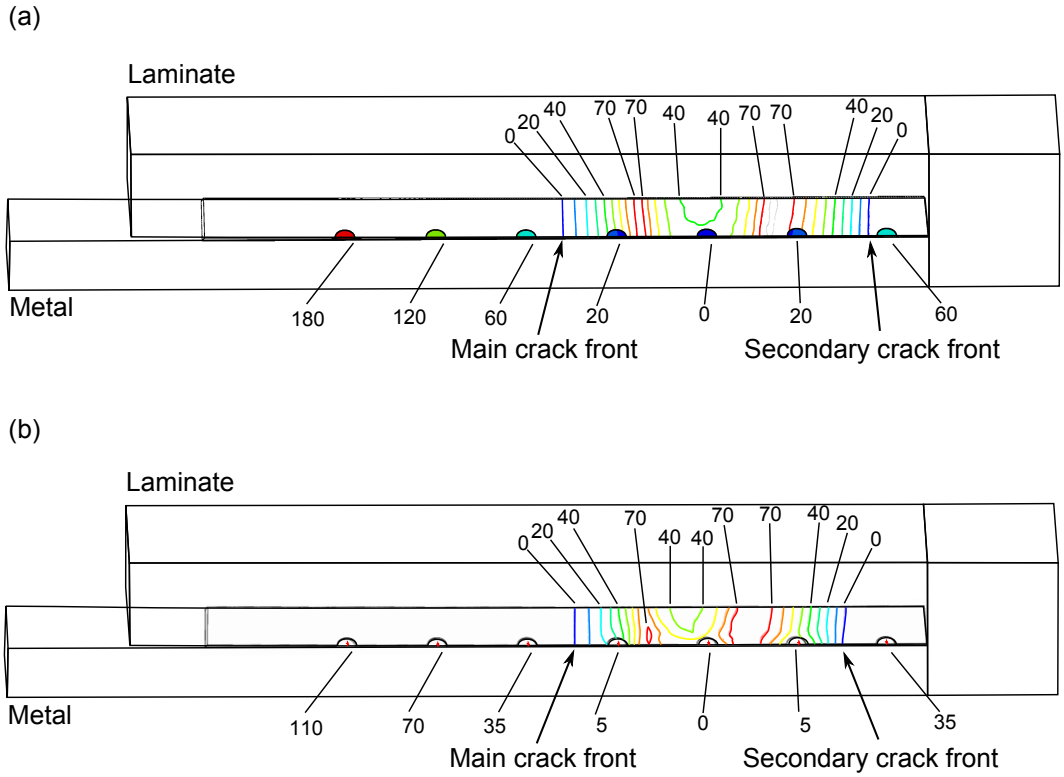

Figure 7.8: Shear stress distribution over the boned interface and pin bridging stresses (crack length, $a = 14$ mm). (a) cohesive-pin model, (b) spring-pin model. (Unit: MPa).

7.4 Geometrical parameter sensitivity

In order to better understand the bridging mechanisms of interlocked pins and the way to improve joint performance a sensitivity study of bridging parameters on the joint response has been carried out. Bridging parameters can be divided into two categories: geometrical and physical. Geometrical parameters are relative to macroscopic joint aspects such as adherend thickness, overlap length and pin arrangement, whereas physical bridging parameters parameters are the ones that define the traction-separation law of pins: initial stiffness (K_0^{pin}), cohesive strength (T_0^{pin}) and fracture toughness (G_C^{pin}). However, the effect of adhered geometry on the performance of bonded joints has been largely studied in the literature, for this reason the sensitivity on these parameters has been omitted. Nevertheless, as shown in Sec.7.3.1 and Sec.7.3.2, debond crack propagation is highly influenced by the thickness of the metal adherend. This parameter has been studied in order to select an appropriate value to be used for further analysis. The use of a too thin metal adhered would have affected the entire sensitivity study making the joint almost insensitive to all other parameters.

7.4.1 Metal substrate yielding

The FE analysis carried out in Sec.7.3.1 showed that the onset of delamination was led by the yielding of the metal substrate: when the stress exceeded the yielding limit the metal substrate starts having large axial plastic deformation. This large deformation increases locally the shear stress of the adhesive interface at run out. A sensitive study of the thickness of the metal plate was conducted to investigate this phenomenon. Joint response at variation of the metal substrate thickness is plotted in Fig. 7.9a. The graph shows that the initial non-liner behaviour of the joint is strongly influenced by yielding of the metal substrate: increasing the metal thickness joint response becomes stiffer, especially close to the peak load, where large plastic deformation occurs for thin joints. Then, after the load drop, the joint response becomes insensitive to the metal substrate thickness and all joint configurations respond in a similar way. This confirms that after the bondline failure (i.e. after the load drop) the entire strain is carried by pins and the joint response is totally characterised by the bridging force and the number of pins them-selves.

Figure 7.9b shows that the joint strength (peak load) rapidly increases as soon as the metal substrate is thickened (i.e. axial stress on the metal plate is reduced). Reducing yielding of the metal substrate decreases the shear deformation at the crack tip. The increment of axial stiffness of the substrate also enhances the effect of pin bridging, improving their shielding effect on the crack front. However, as soon as metal substrate yielding is limited, increasing

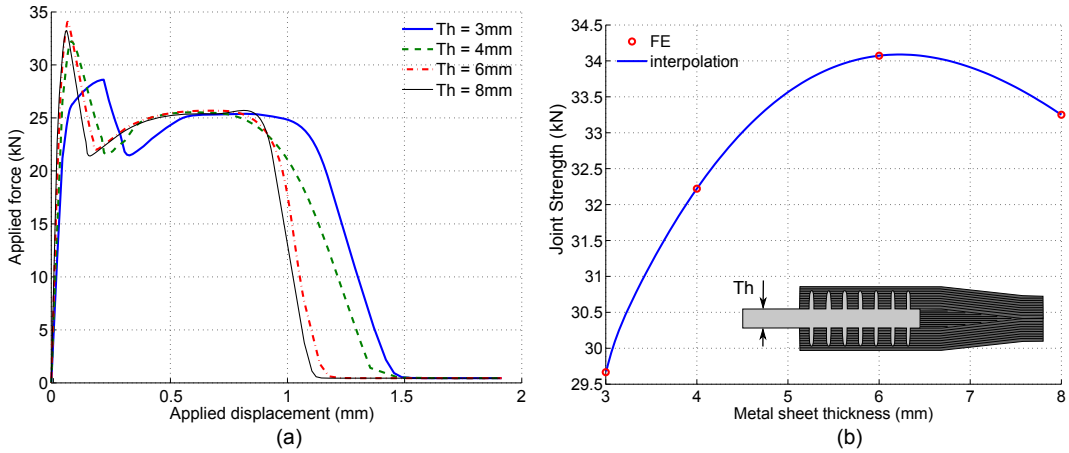

Figure 7.9: Effect of the metal substrate thickness on the joint performance: (a) structural response of different thickness joints, (b) strength of the joint - spline interpolation of FE results.

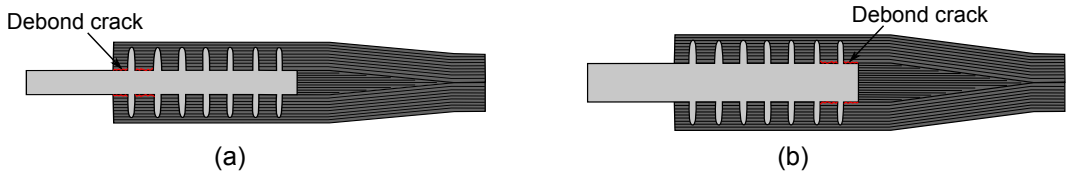

Figure 7.10: Effect of the metal substrate thickness on the joint failure mode: (a) thin metal substrate promotes failure from the laminate runout (left-hand side), (b) thick metal substrate starts failing at the metal runout (right-hand side).

the thickness has a negative effect on the joint strength due to the increase of secondary bending at the overlap (i.e. higher peel at runout). Another effect of increasing the metal substrate thickness is the change of the bonded interface failure mode: whereas thin metal substrate shows a delamination crack growing from the laminate end towards the centre of the joint (as schematically depicted in Fig. 7.10a), for thicker metal substrate the delamination crack starts at the opposite runout (Fig. 7.10b). This behaviour is due to the variation of axial stiffness of the metal adherend: higher shear stress peak is where axial strain is larger, increasing the thickness of the metal substrate reduces the stress peak at the laminate runout, i.e. the debond crack starts from the opposite side. The analysis revealed the configuration with metal substrate thickness of 6 mm achieved the maximum strength. For this reason this parameter was kept the same for all following analyses.

7.4.2 Number of pin rows

FE analysis in Sec.7.3.2 showed that at bondline failure no pin was completely fallen off. Moreover, analysis revealed that at all pins were still within their

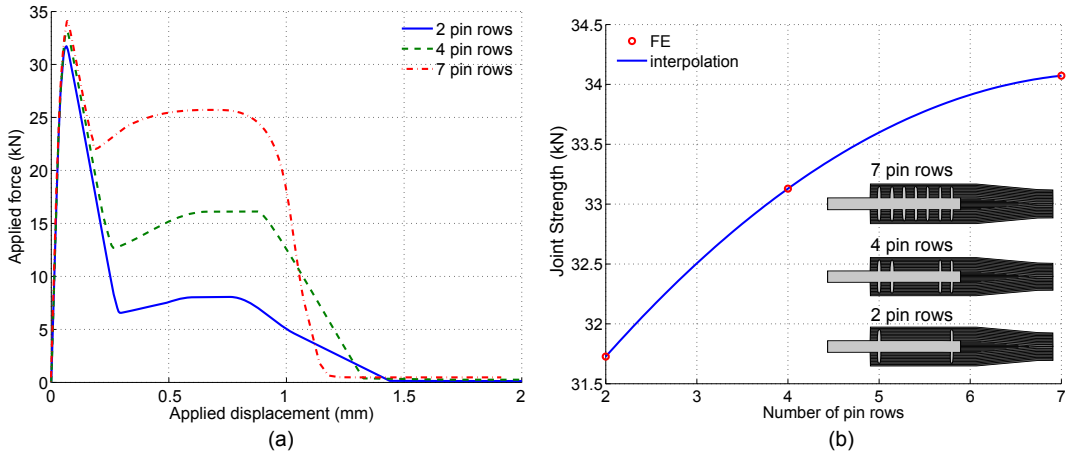

Figure 7.11: Effect of pin row number on the performance of the DLJ: (a) structural response of the joints having different pin row number, (b) strength of the joint - spline interpolation of FE results.

elastic limit and the most stressed pins were the ones closest to runouts (i.e. where shear deformation was larger). A study on the effect of the pin row number has been carried out in order to understand the relative importance of the deeper pin rows in bridging the bondline failure. As shown in Fig. 7.11 insert, the number of pin rows was varied removing the rows from the centre of the joint towards the two runouts, i.e. keeping the rows closest to runouts.

Figure 7.11a shows the joint response varying the number of pin rows. This parameter highly influences: (1) joint strength (peak load at which complete debond occurs), (2) load recovery after the load drop and (3) ultimate load of the joint. The joint strength increases with the number of pin rows, however, as visible in Fig. 7.11b, the increment per pin row is not constant and decreases with the increasing of the pin row number. This smaller effectiveness of additional pin rows is probably due to the larger distance from runout: the furthest the pin is from the joint runout the less bridging action exerts (i.e. bridging effect is less effective). Load recovery after complete failure of the bonded interface is totaly due to the pin load carrying capability, for this reason the distance from runout is irrelevant: the load recovery is proportional to the number of pins only.

7.4.3 Pin arrangement

In this section the effect of the pin arrangement has been studied. As showed in previous section pin rows at runouts are more stressed than the ones at the centre of the joint (i.e. they bridging action should be more effective), for this reason the effect of increasing the pin density at the two runouts, keeping the pin number unchanged, has been analysed. Geometry and dimensions of

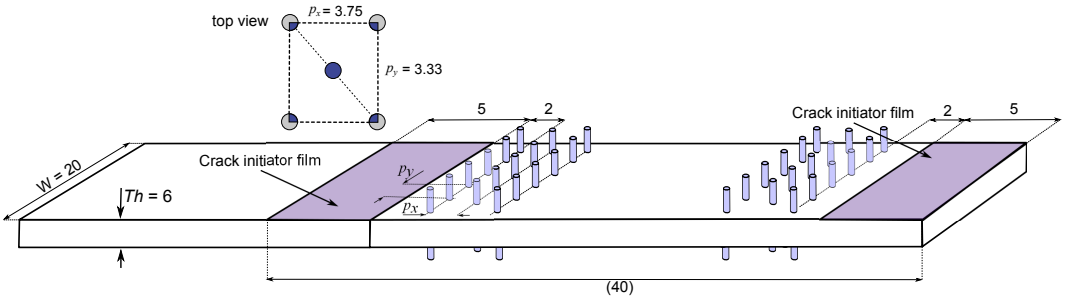

Figure 7.12: Sketch of the joint configuration with high pin density at runouts.

the high density pin arrangement are depicted in Fig. 7.12. The joint had a quincunx pin arrangement of 6-5-6 pins at both runouts, which makes a totality of 68 pins. The local pin density of this configuration can be estimated, as illustrated in Fig. 7.12 insert, by the ratio between reinforcement cross-section and total area of the repetitive cell:

$$A_p = \frac{2\,(\pi d^2/4)}{p_x p_y} = 0.08 \tag{7.6}$$

This configuration will be compared with the homogeneous 7x5 pin arrangement analysed in previous section (70 pins in total), where a pin density of $A_p = 3\%$ was evenly distributed over the entire overlap area.

A 6 mm thick metal substrate has been used in order to avoid large plastic deformation and the width of the joint was reduced to $W = 20$ mm to reduce the load carrying capability of the joint for testing facility issues. All the other dimensions were kept the same as previous configuration (Fig. 7.1). As shown in Fig. 7.10, a thick metal substrate promotes debond crack to start from the metal runout, for this reason a second crack starter of 5 mm length has been inserted also at this runout, as illustrated in Fig. 7.12.

Force vs. applied displacement

Joint response of the two configurations is compared in Fig. 7.13a. The two curves follows the same rising path: bonded interface starts debonding at about 10 kN where the force vs. displacement curves show an increase of compliance. Both curves, due to pin bridging effect, keep picking up load in a continuous compliance-increasing curve. Complete failure of the bondline comes with a load drop. High pin density fails at a lower load (about 18 kN) than homogeneous pin arrangement (about 20 kN). Reason of this phenomenon will be cleared later, when interlaminar shear stress at interface and bridging traction of pins will be presented. After the load drop in both configurations pins pick up the entire strain and the joint shows a load recovery. The ultimate load of homogeneous pin arrangement is about 3% higher than configuration

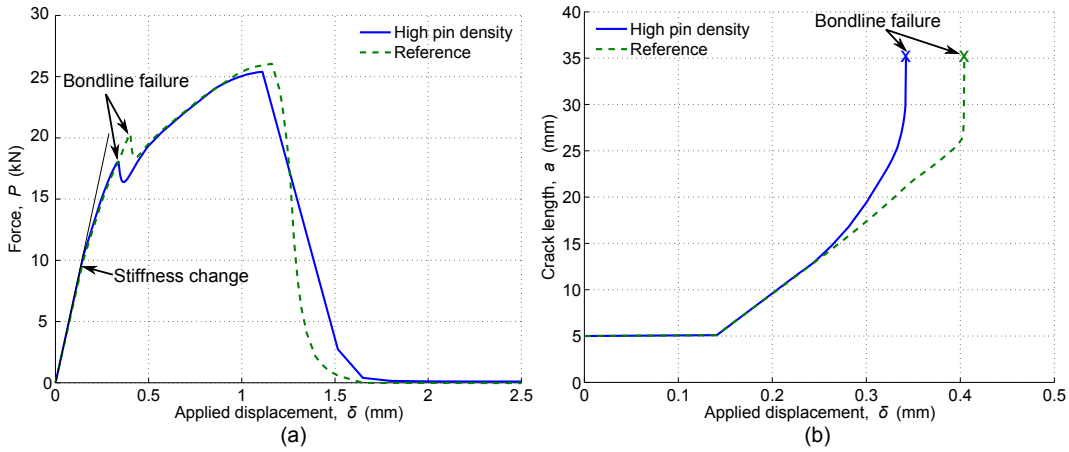

Figure 7.13: Comparison between calculated high pin-density and homogeneous pin arrangement: (a) force vs. applied displacement, (b) Calculated crack extension from its initial size of 5 mm vs. applied displacement.

with high pin density at runouts. This result is due to the slightly higher number of pins in the homogeneous pin arrangement (70 against 68 pins) and confirms that after the bondline failure the pin arrangement is irrelevant.

Crack extension behaviour

Figure 7.13b shows the crack extension behaviour of the two configurations. Damage initiation occurs at the same applied displacement (same load). The crack growth rate of both configuration remains the same up to a displacement of $\delta = 0.24$ mm. For homogeneous pin arrangement it remains almost constant up to a displacement of $\delta = 0.4$ mm, where delamination becomes unstable and crack propagates quickly to the end of the joint (bondline failure). Whereas for high pin-density configuration crack growth rate increases continuously for $\delta > 0.24$ mm and bondline failure occurs earlier. This shows a better bridging action of the homogeneous pin arrangement.

Interlaminar shear stress

Figure 7.13a and b show homogeneous pin arrangement performs better than the configuration with high pin density: bondline fails later in the first case, reaching a higher load. This behaviour highlights a better bridging action of homogeneously spaced pins. Figure 7.14 shows interlaminar shear stress at interface and bridging traction stresses at the load drop (just before the unstable crack propagation and the bondline failure). As visible in the figure, even though central pins bear a lower load than the ones closer to runout (Fig. 7.14a), the totality of load carried by the 7x5 pin arrangement is higher that other configuration. The bridging traction of the three pins close to the metal

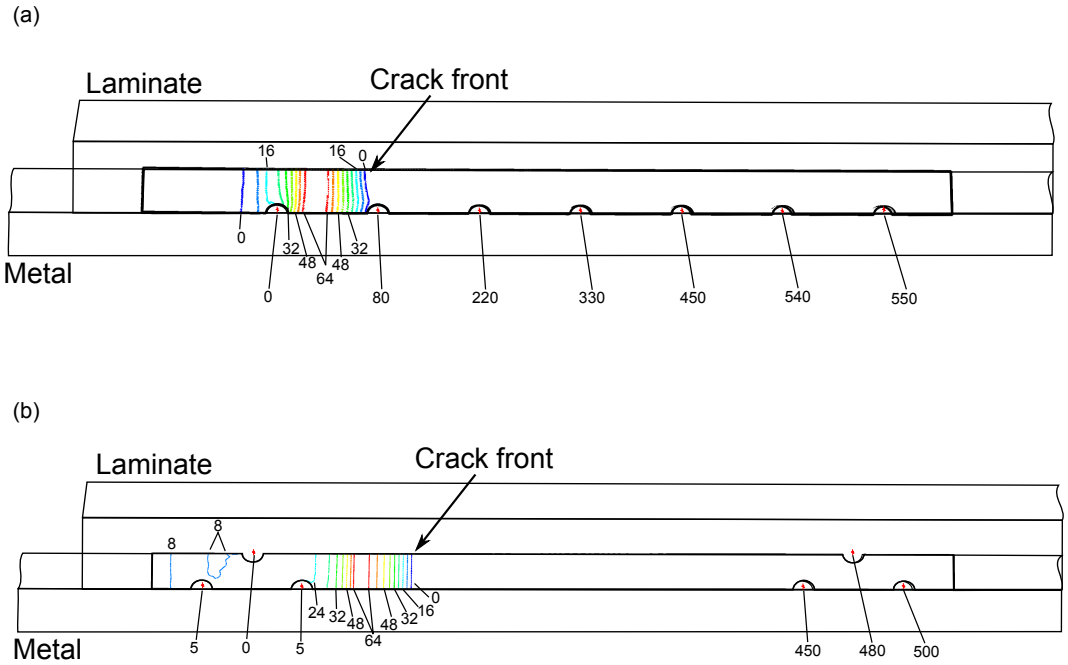

Figure 7.14: Shear stress distribution over the boned interface and pin bridging stresses (crack length, $a = 20$ mm). (a) homogeneous pin arrangement, (b) high pin-density configuration. (Unit: MPa).

runout (delamination onset) in the high pin-density configuration is relatively high, however the remaining three pins at the opposite runout are almost unloaded.

7.4.4 Pin bridging physical parameters

In this section the effects on the joint performance of load carrying characteristic of a single pin and the bridging law shape are analysed. As described in Sec. 6 pin traction separation laws, which depend directly by bridging force carried by a single pin, can be fully characterised by three parameters: initial stiffness (K_0^{pin}), cohesive strength (T_O^{pin}) and fracture toughness (G_C^{pin}). Bridging characteristics of pin reinforcements are defined by pullout and shear bridging forces. A sensitivity study of these parameters has been carried out in order to understand how much the performance of a single pin affects the response of the entire joint.

Model showed to be insensitive to mode-I bridging parameters, for this reason no graph will be presented in this section. This results highlights that failure mode of the joint is dominated by mode-II. Figure 7.15 shows the model sensitivity to the pin fracture toughness G_{IIC}^{pin} (i.e. the area underneath the mode-II traction-separation law of the pin reinforcement). The first part of the force versus displacement curves is almost identical, both linear elastic response and

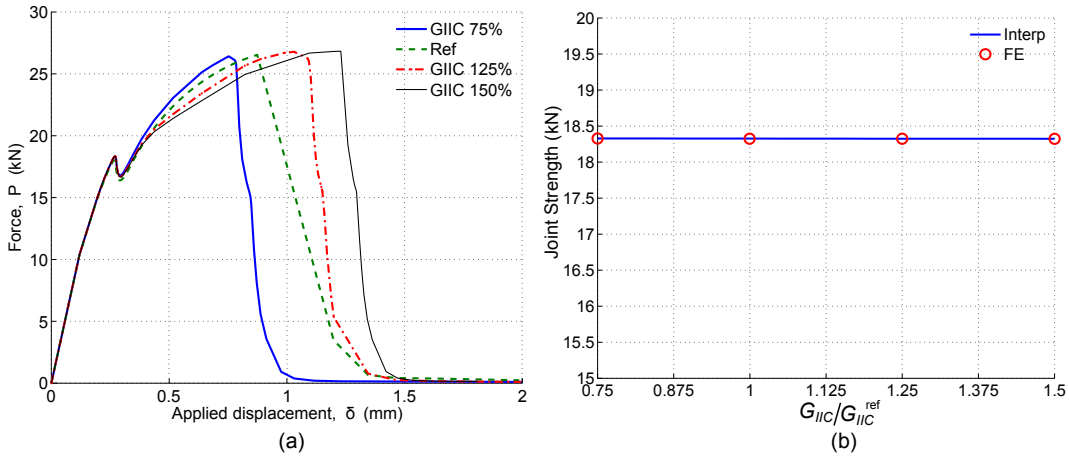

Figure 7.15: Effect of pin fracture toughness (G_{IIC}^{pin}) on the performance of the DLJ: (a) structural response of the joint varying G_{IIC}^{pin}, (b) strength of the joint - spline interpolation of FE results.

joint behaviour during the crack propagation phase seems to be insensitive to this parameter (Fig. 7.15a). Differences between different configurations become visible after the load drop (i.e. after complete failure of the bonded interface): higher G_{IIC}^{pin} results in an higher enlongation of the joint at ultimate failure. Figure 7.15b shows that the joint strength is completely insensitive to the pin energy absorption: any variation of G_{IIC}^{pin} produces no change in joint strength.

Figure 7.16 shows the model sensitivity to the initial stiffness K_{II0}^{pin} of the pin traction-separation law. Differently from G_{IIC}^{pin}, which was affecting the second part of the curve, this parameters modifies the first part of the joint response: as soon as the crack starts propagating pins with higher initial stiffness provide better bridging performance. As visible in Fig. 7.16a the higher K_{II0}^{pin} the steeper the curve during the crack propagation phase, the higher the joint strength. Figure 7.16b shows that joint strength is strongly affected by this parameter.

The effects of pin cohesive strength (T_{IIO}^{pin}) on the joint response is plotted in Fig. 7.16a. This parameter slightly affects the first part of the curve, giving only a small improvement to the joint strength(Fig. 7.16b). Whereas the sensitivity of the model response after the load drop shows a strong sensitivity.

This sensitivity study shows that joint strength and debond crack propagation are strongly influenced by the first part of the pin traction-separation curve (i.e. by initial stiffness K_{II0}^{pin}), whereas cohesive strength T_{II0}^{pin} and pin energy absorption G_{IIC}^{pin} affects the joint behaviour after the bondline failure and the global load capacity of the joint.

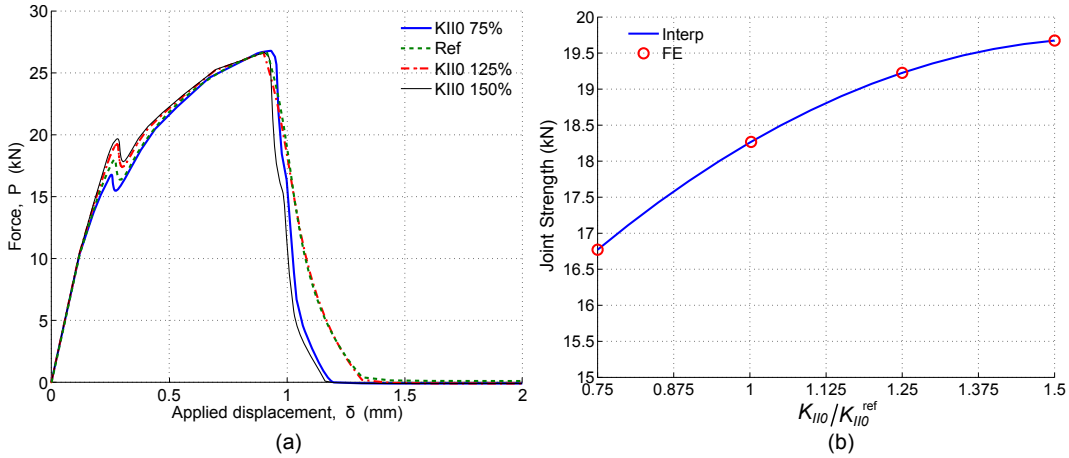

Figure 7.16: Effect of pin initial stiffness (K_{IIO}^{pin}) on the performance of the DLJ: (a) structural response of the joint varying K_{II0}^{pin}, (b) strength of the joint - spline interpolation of FE results.

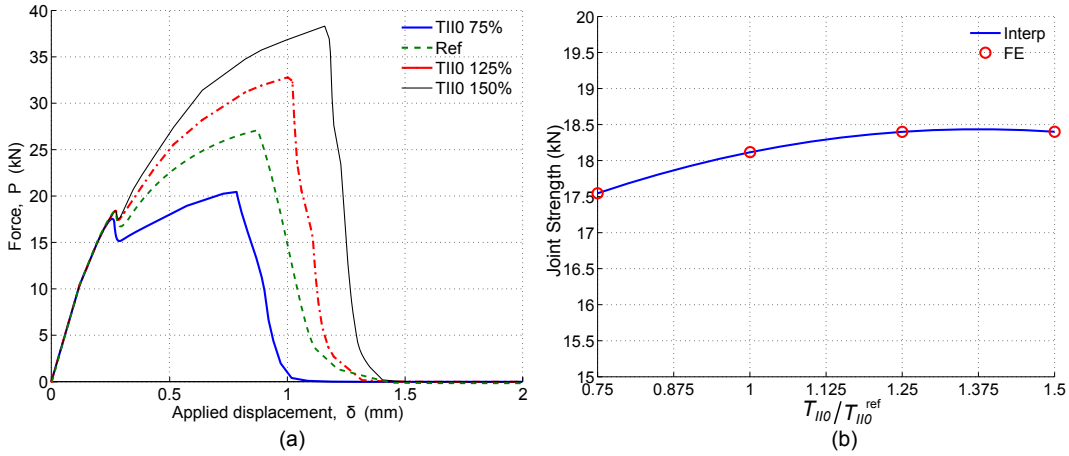

Figure 7.17: Effect of pin cohesive strength (T_{IIO}^{pin}) on the performance of the DLJ: (a) structural response of the joint varying T_{II0}^{pin}, (b) strength of the joint - spline interpolation of FE results.

7.5 Summary of results

A validated FE model has been developed which can analyse the structural properties and fracture behaviour of double lap metal-composite joints reinforced by interlocked pins when subjected to a tensile load. In this chapter it has been demonstrated that: (1) pin bridging action can be modelled by nonlinear springs as well as cohesive interface elements. Bridging laws governing these pin models can be obtained from either single-pin specimen tests or unit-cell models; (2) these pin models can be implemented into a commercial FE package for structural models. In the first part of the chapter the model has been validated by comparing with experimental results.

The two different pin-models are able to predict accurately the debonding of interface, demonstrating the suitability of the cohesive and spring-pin models up to the complete failure of bonding. The validity of the cohesive-pin model is limited up to this point, where the over-simplified traction-separation law used for the pin response results in poor agreement with experimental curve. The spring-pin model better simulates the joint response after the complete failure of the bonded interface.

In the second part of the chapter the spring-pin model has been used to evaluate the effects of geometrical and physical parameters on the joint performance. The metal substrate thickness resulted to be one of the parameters that mostly affects the joint behaviour: thin metal substrate showed large plastic axial deformation of the metal adherend, which caused an early delamination of the bonded interface. Increasing the metal thickness initially improves the joint strength by retarding the bondline failure. However, after this yielding effect is avoided, any further increment of the metal substrate thickness produces a slight decrease of joint strength due to the increase of secondary bending.

The number of pins rows reinforcing the joint (or pin areal density, which is an equivalent measure of the same characteristic) showed to affect both joint strength and ultimate load: the higher the pin number the better the joint performance. However, it should be noticed that increasing the pin density could promote failure modes not accounted in this model (such as in-plane tensile failure of the laminate). A sensitivity study on the pin arrangement showed also that pin position affects only the debond crack propagation behaviour (i.e. the first part of the joint response). Although pins bridging effect is higher far from the crack tip, a local increment of the pin density at runouts (delamination onset) produces a slight decrease of pin strength. This effect is due to the fact that delamination starts from one runout adn propagates towards the centre of the joint. The pin close to the opposite runout remains almost unloaded up to the complete failure of the bondline.

The model sensitivity to the pin bridging physical parameters (parameters that characterise the pin traction-separation law) have been also analysed. The

study showed that initial stiffness (K_{IIO}^{pin}) of the traction-separation law is the parameter that mostly affects the debond crack propagation behaviour: stiffer pins provide a better crack shielding effect achieving higher joint strength. Whereas cohesive strength (T_{II0}^{pin}) and energy absorption (G_{IIC}^{pin}) only slightly influence the crack propagation and strongly affect the joint behaviour after complete failure of the bonded interface.

CHAPTER 8

OVERALL DISCUSSION

After an exhaustive review of through thickness reinforcement methods for composite and hybrid metal-composite joints and state-of-art of research efforts, this thesis has been focused on developing numerical models to study the effect of through thickness reinforcements on structural joints. Main results has been summarised at the end of each chapter drawing specific conclusions. Main conclusions can be summarised as follows:

8.1 Unit-cell single pin models

8.1.1 Carbon fibre pin reinforcements for composite joints

The bridging laws both in mode-I and mode-II of carbon fibre pins have been studied in Chapter 4. For mode-I bridging a FE model of a single-pin pullout test was developed and validated by experimental results. The model then was used to analyse the mechanisms that lead the pin bridging, highlighting the importance of the pin aspect ratio (ratio between embedded length and pin diameter h^*/d) and how the shear deformation of the laminate can influence the bridging performance of the pin. This study shows that the main contribution to energy absorption of pins is given by the friction resistance of these during the pullout. This result indeed confirms previous studies carried out by Cartié et al. [68] and it is possible to conclude that maximising the wet surface of pins versus pin cross section (i.e. reducing the pin size at fixed reinforcing areal percentage A_p) increases the effectiveness of reinforcement. However, the model also revealed that, due to the effect of the pin aspect ratio, the

increment of specific energy absorption was less than it was predictable from previous available models, based of a shear lag approximation.

An analytical model was then developed to evaluate the mode-II bridging characteristics of carbon fibre pins. The model is presented in detail in Chapter 3 and then validated by experimental results in Chapter 4. The failure behaviour of carbon fibre z-pin under mode-II loading was deeply analysed and then implemented into a non-linear mono-dimensional beam model. The main assumption of the model is that when the resin matrix around the pin starts failing, allowing the pin to plough into the laminate, the large shear deformation of the pin induces the pin to split internally. From this point onward the pin is fragmented into several ligaments and it is no longer capable of carrying any bending. The model uses the Euler-Bernulli beam approximation for the part of the pin that still responds elastically and it treats the part of the pin after pin splitting as a truss (incapable of carrying any shear load or bending).

The model revealed that depending on the pin height and diameter the pin shows different failure modes: either pin pullout or pin rupture. Small pin diameters and heights promote pin pullout failure mode. Increasing the pin diameter has small effect on the specific energy absorption until the pin keeps failing in pin pullout, then, when failure mode changes in pin rupture, the pin performance rapidly drops down. Whereas increasing pin height shows a strong positive effect until the failure mode remains pullout and then performance deteriorates when the failure mode switches to rupture.

This analysis shows that the pin best performance are achieved by pins with high aspect ratio h/d, however, this aspect ratio should be kept small enough not to promote pin rupture failure.

8.1.2 Metal pin reinforcements for metal/composite joints

The bridging laws both in mode-I and mode-II of metal pins have been studied in Chapter 6. For mode-I an FE model of a single-pin pullout test was developed and validated by experimental results. The model showed that cylindrical pins loaded in pullout behave exactly as carbon-fibre pins, main results can be summarised as below:

- the energy absorption due to the failure of bonding between pin and laminate is negligible with respect to the energy involved in pullout. The pullout resistance during the pin sliding phase is due to to friction and it is caused by the compressive radial stress state around the pin. This result highlights that a good material to be used for pin reinforcements should have a small coefficient of thermal expansion (at least smaller that the laminate along any of its two main directions);

- as it was for the chamfer head of z-pins, the pin tip, or any part of the pin surface that tends to separate from the laminate during pin sliding out, does not contribute to the pin pullout resistance;

- at fixed pin areal percentage of reinforcement, pins with high aspect ratio (h^*/d) are more effective due to the increase of wet surface (surface in contact with the laminate). However, as it was for carbon fibre pins, the effect of shear deformation of the laminate reduces the average shear friction stress between pin and laminate reducing the increment of pullout resistance from the one predictable by a simple shear lag model.

An 3D FE model was developed to evaluate the mode-II bridging characteristics of metal pins. The model presented in details in Chap. 3 has been then validated by experimental results in Chap. 6. Failure behaviour of metal pin reinforcements under mode-II loading were deeply analysed and then implemented into a non-linear finite element model. The model uses an elastic/perfectly plastic model to simulate the response of the laminate close to the pin, characterised by having high resin content and void defects. This assumption allows to simulate the pin ploughing into the laminate. The model also uses the stress-strain curve of the material for the pin reinforcement metal and a damage model to simulate the pin fracture.

The model revealed that within the range of parameters analysed the pin loaded in mode-II always tends to fail at the pin root. The failure process involves large plastic deformation of the metal, pin ploughing, necking at the root of the pin and plastic failure of the pin. This failure process was difficult to simulate and some discrepancies between model and experimental test were found. However, the model was capable of predicting with good accuracy the non-linear response of the pin up to the ultimate load.

Three key parameters have been identified to characterise the bridging force: initial stiffness, yielding load (transition to non-linear response of the pin) and ultimate load. Since it was demonstrated the ultimate load being experimentally very variable, only the variation of initial stiffness and yielding load have been studied varying the pin geometry. Nevertheless, the effects of these three parameters on the global performance of the joint have been analysed in Chap. 7 in order to understand which features a good pin reinforcement should have.

A sensitivity study on the pin geometry showed that pin response is almost insensitive to the pin height. This result, relative to metal pin reinforcements, reveals a distinct difference between metal and carbon fibre pin reinforcements, For the latter indeed the pin aspect ratio was the parameter of highest sensitivity [134]. The pin fillet radius and the pin diameter have a strong effect on both pin initial stiffness and yielding stress. These two parameters have been also demonstrated in Chap. 7 being the most sensitive for the joint per-

formance. In particular it was found that stiff pin reinforcements better stop incipient delamination cracks.

Basing on the results of the analyses carried out in Chap. 6 one could conclude that large stiff pins perform better than small ones. However it should be noticed that at fixed areal percentage of pin reinforcing the stiffness per unit area (K_{II0}^{pin}) decreases with the pin diameter, i.e. small size pins with high pin density perform better than large sparse pins (Fig. 8.1).

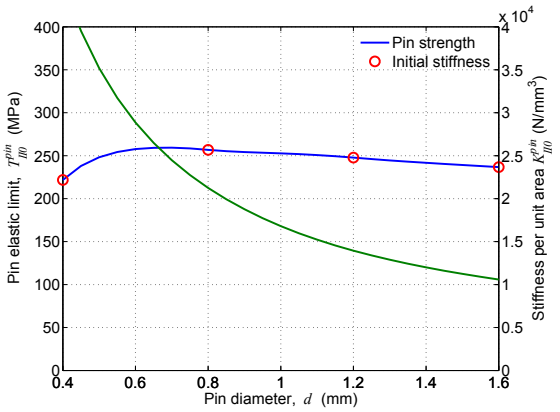

Figure 8.1: Sensitivity curves of the pin bridging traction (T_{II0}^{pin} and initial stiffness per unit of pin area (K_{II0}^{pin})) to the pin diameter.

Whereas the study showed that increasing the pin fillet radius has a positive effect on both pin strength and stiffness due to the enhancement of resisting section at the pin root. However, one should also bear in mind that increasing the pin radius excessively could increase the density of defects and make more difficult the pin insertion process. All these effects are not accounted by the FE model which assumes that the interface pin/laminate remains the same independently from pin geometry. It should be noticed that the percentage of defects in laminate close to the pin is an intrinsic characteristic of the material properties used to model the resin rich area.

8.2 Macro-scale structural models

A macro scale structural model has been developed and presented in details in Chap. 3. The model uses the bridging forces of pin reinforcement as input data to define the traction-separation laws of cohesive elements that reproduces the effect of pins onto the joint. In order to reduce the computational effort demanded a simplified model that uses periodical boundary conditions has been also created. This model assumes that the stress profile over the joint longitudinal cross section is the same as an infinitely wide panel and periodical with the pin pitch. The model has been applied for the following numerical cases:

- mode-I and mode-II delamination tests of z-pin reinforced laminates (results presented in Chap. 4)

- tensile tests of a z-pin reinforced T-joint (results are presented in Chap. 5)
- tensile tests of pin reinforced double-lap hybrid metal-composite joints (results presented in Chap. 7)

The numerical results of each of these cases has been extensively analysed and validated by comparing with experimental results. Main results can be summarised as below:

8.2.1 Carbon fibre pin reinforcements for composite/composite joints

The bridging effect of z-pin reinforcements on delamination samples loaded either in mode-I or in mode-II has been studied in Chap. 4. The model prediction was compared with experimental results; the effect of pin density and pin size on the resistance of the laminate to delamination was studied. It was pointed out that:

1. The bridging action of pins starts after the delamination crack has passed the first row of pin reinforcements, i.e. it does not affect damage initiation.
2. The bridging effect of pins increases with increasing the number of resisting pin rows on the crack wake that bridge the incipient crack. This number increases with increasing the delamination length up to a steady state where, as soon as one pin row is activated by the crack front passing it, another fails on the crack wake maintaining the number almost constant. This process has been fully described in Sec. 4.3.2 for test samples loaded in mode-I. However, for mode-II delamination, within the size of pins analysed, the crack length was never enough to establish a steady state of delamination growth.
3. For both mode-I and mode-II delamination test samples, at a fixed pin density, small pins perform better than large reinforcements.

The potential of the macro-scale model has been then demonstrated in Chap. 5, where the structural properties and failure behaviour of a z-pin reinforced T-joint loaded in traction over the stiffener have been accurately predicted. The model showed that, due to the high peel stress, the onset of disbond laid at the interface between the stiffener and the Δ-fillet region. The disbond crack then propagated unstably upward splitting the stiffener in two halves and finally started propagation at the interface between stiffener and skin. It was therefore demonstrated the model being capable of accurately predicting the propagation of delamination cracks under mixed mode loading.

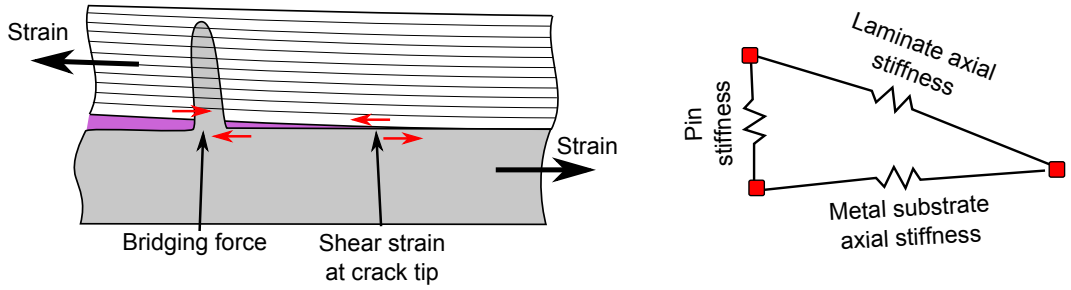

Figure 8.2: Cartoon of effect of the axial stiffness of adherends on the effectiveness of pin reinforcement in shielding the crack tip.

8.2.2 Metal pin reinforcements for metal-composite joints

The bridging effects of metal pin reinforcements on a double-lap metal-composite joints have been studied in Chap. 7. The model prediction was compared with experimental results for model validation purposes; the effect of geometrical parameters, pin arrangement and pin bridging properties on the structural performance of the joint was studied. Main results can be summarised as follows:

1. The onset and further propagation of debond always starts at the runout where the shear strain is maximum. This can be identified by a simple consideration: at the joint runout the axial strain is carried by only one of the two adherends (the one without interruption). The most critical runout is the one where the strain is carried by the adherend with the lower axial stiffness.

2. Usually, considering the elastic properties of the material used in the case under study, the critical runout should the one where the axial strain is carried entirely by the laminate. However, the model revealed, and it was confirmed by experimental results, that due to the local loss of stiffness caused by the metal entering into its plastic field, the onset of debond occurred at the opposite runout.

3. The model showed that increasing the thickness of the metal substrate would bring large benefit to the joint strength. Avoiding yielding of the metal substrate the stiffness of the system pin/laminate/metal-substrate increases, as depicted in Fig. 8.2. This implies that, at fixed bridging force exerted by the pin (i.e. fixed shear displacement δ), the shear strain at the crack tip is smaller if the system is stiffer. Therefore increasing the axial stiffness of adherends makes pins work better.

4. A sensitivity study of the pin bridging characteristics (initial stiffness K^{pin}_{II0}, strength T^{pin}_{II0} and energy absorption G^{pin}_{IIC}) on the performance

of the joint revealed that the most sensitive parameter was the initial stiffness of the pin. This can be explained by the fact that, within the range of parameters studied in this analysis, the complete failure of the bondline always occurred before any pin was completely failed, i.e. the part of the bridging law that most affects propagation of debond cracks is the linear elastic response.

5. The model revealed to be very sensitive to the pin distribution: any arrangement that increases the pin density along the path of the disbonding crack will increase the structural performance of the joint. However, in order to wisely place the pin reinforcements over the overlap a consideration on the damage onset should be done: bearing in mind what pointed out in point (1), the joint should be designed with a higher density of pin at the runout most critical for debond.

8.3 Conclusions

- Unit-cell single pin models to predict the reinforcement bridging laws under different loading conditions have been developed. These models are able to accurately predict the bridging force of the pin reinforcements which can be used as input data to evaluate the effect of these reinforcements on a macro-scale structural model.

- The effect of geometrical parameters on the pin performance have been deeply studied and it was concluded that either for z-pin or metal pin reinforcements, at equal pin density small size reinforcements perform better.

- A macro-scale structural model for predicting the effect of through-thickness reinforcements on the delamination/disbond resistance and the joint performance has been developed and validated. Comparison between numerical and experimental results showed excellent agreement.

- A simplified computational-time-efficient model has been also developed to predict joint structural performance. This model permitted to analyse a much larger number of different joint configurations. The model uses periodical boundary conditions at the sides of a joint strip which contains the minimal repetitive unit of the pin arrangement (i.e. unit-strip). This assumption basically implies that the joint performs as one strip of the same width of an infinitely wide joint.

- The effect of different pin bridging properties, pin densities and arrangements have been deeply studied using the unit-strip model. It was found that pin initial stiffness and pin density are the parameters that mostly

affect the joint performance. In particular the higher the stiffness the better pins bridge the incipient crack and therefore the better the joint performance. Whereas increasing pin density enhances the global pin bridging traction, obtaining a positive effect on the joint load carrying capability.

8.4 Future works

Basing on the conclusions of this thesis there are several ways to improve the bridging performance of pin reinforcements on increasing the structural performance of joints:

1. Reducing the pin diameter and increasing the pin density is one way. Of course there are technological limits to this: the minimum dimension of the pin is related to the technological limits of cold metal transfer welding (see Sec. 2.3.3 for further details) and it is also related to the pin insertion process: the pin has to remain straight while the uncured composite laminate is pressed in through the ultrasonic hammer (procedure described in detail in Sec. 3.3.2).

2. Increasing the pin initial stiffness per unit of cross section area (K_{IIO}^{pin}). This parameter has been demonstrated to increase by reducing the pin size, however, an enhancement of this could be also achieved by increasing the pin section at root, selecting a stiffer reinforcement metal or improving the elastic properties of the laminate close to the pin. This last parameter can be controlled by trying to reduce the size of the resin rich zone around the pin.

3. Increasing the axial stiffness of adherends at overlap. It has been demonstrated how the axial stiffness of adherend can affect the debond behaviour of a hybrid metal-composite double lap joint. The effectiveness of pin reinforcements is directly connected to the capability of the system of transferring the bridging load of the pin and reducing the shear strain at the crack tip. Modifying the laminate lay-up locally at the overlap region would probably increase the structural performance of the entire joint.

4. The importance of thermal induced stress due to the laminate curing process for both z-pins and metal reinforcement have been highlighted in Chapters 4 and 6. The compressive stress on the pin lateral surface is strictly related to the friction resistance of the pin during pullout which has been shown being the most important mechanism of energy absorption. Considering that the performance of the reinforcement and

strictly depending on this parameter, the effect of ageing (i.e. partial relaxation of this stress state) should be analysed in detail.

5. Another effect related to thermal induced stress which has been neglected in this thesis is the interaction between adjacent pins for hybrid metal/composite joints: due to the different coefficient of thermal expansion of the two adherends, during the cure process the material shrinkage produces a locking effect between pins. This effect increases the compressive stress at the pin lateral surface (i.e. providing a beneficial effect on pullout resistance and energy absorbtion during pullout). However, in numerical cases presented in this thesis metal pins always failed fracturing at the pin root, therefore the grade of inaccuracy produced by neglecting this effect is minimal. Nevertheless, when designing metal reinforcements which fail in pullout this effect is expected to be important.

APPENDIX A

DERIVATION OF LAMINATE ELASTIC FOUNDATION STIFFNESS

Let consider a section of the pin and surrounding laminate. A generic shear displacement δ is imposed to the pin cross section, which is assumed not to deform. The laminate subjected to a punch loading deforms and the hosting hole initially round assumes an eyelet shape as depicted in Fig. A.1. Through the following equations the reacting force provided by the laminate is expressed as a function of the applied shear displacement. The stiffness of the spring foundation (k) can be then calculated dividing the reaction force by the applied displacement.

Only one hemisphere of pin circumference is assumed to be in contact with the laminate. Assuming negligible the shear stress at the interface between pin and laminate interface, the lateral force that laminate exert on the pin can be expresses as follows:

$$F = \int_{-\frac{\pi}{2}}^{\frac{\pi}{2}} \sigma_{r\theta}\left(\theta\right) cos\left(\theta\right) r_0 d\theta \tag{A.1}$$

Considering the force balance in radial direction of element of unit surface the following relation can be written:

$$r\frac{\partial \sigma_r}{\partial r} + \sigma_r - \sigma_\theta = 0 \tag{A.2}$$

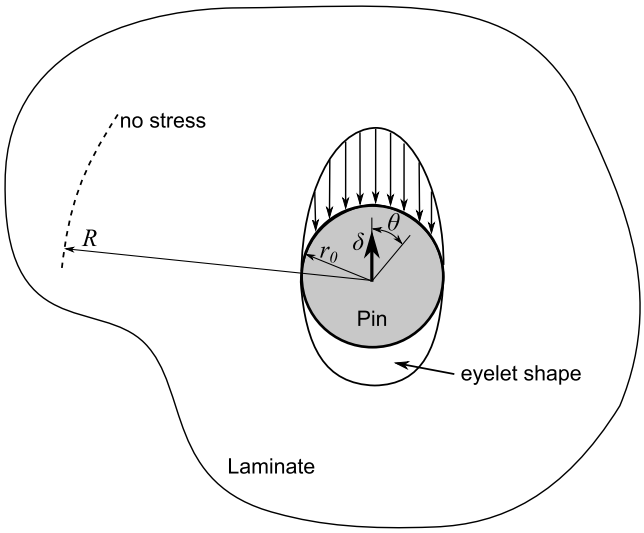

Figure A.1: Schematic of the reaction force provided by the laminate supporting the pin under lateral deflection.

Assuming circumferential stress σ_θ being small compared to σ_r, Eq. (A.2) can be written as:

$$\frac{1}{r}\frac{\partial\left(r\sigma_r\right)}{\partial r} = 0 \tag{A.3}$$

This means that at a given angle θ the radial stress flow $r\sigma_r$ remains constant along the radial direction and particularly this flow remains the same as at the pin interface ($r = r_0$), i.e. $r_0\sigma_{r_0}$. Assuming the lateral displacement of the laminate far enough from the pin ($r = R$, with $R \gg r_0$) being zero, we can express the radial displacement of the laminate at the pin interface as:

$$\delta_{r_0} = \int_{r_0}^{R} \frac{\sigma_r}{E_{lam}} dr = \frac{r_0\sigma_{r_0}}{E_{lam}} \int_{r_0}^{R} \frac{dr}{r} = \frac{r_0\sigma_{r_0}}{E_{lam}} \ln\frac{R}{r_0} \tag{A.4}$$

But the radial displacement has to be the same of the pin, which is imposed by the circular shape of the pin and can be expressed as:

$$\delta_{r_0} = \delta cos\left(\theta\right) \tag{A.5}$$

Therefore, using Eq. (A.4) and Eq. (A.5) we can obtain σ_{r_0} in function of the applied displacement δ; substituting then in Eq. (A.1) we have:

$$F = \frac{\delta E_{lam}}{\ln\frac{R}{r_0}} \int_{-\frac{\pi}{2}}^{\frac{\pi}{2}} cos^2\left(\theta\right) d\theta \tag{A.6}$$

$$F = k\delta, \qquad k = \frac{\pi}{2}\frac{E_{lam}}{\ln\frac{R}{r_0}} \tag{A.7}$$

Equation (A.6) gives the elastic response of the laminate being punched by the pin. The factor k that multiplies the displacement in Eq. (A.7) represents the stiffness of the spring foundation before any ploughing effect of the laminate.

APPENDIX B

DERIVATION OF DIFFERENTIAL EQUATION OF PIN LATERAL DISPLACEMENT AFTER PLOUGHING

Let consider at piece of z-pin of unit length dz. Large lateral displacement has already caused the internal z-pin splitting. The pin is completely flexible in bending and inextensible. The pin is able to carry only axial stress. Being $N = \pi r^2 \sigma$ the axial force of the pin, a schematic of the force acting over the pin is depicted in Fig. B.1. The force balance along the z and x-axis can be written as follows:

$$\begin{cases} \left(N + \frac{\partial N}{\partial z} dz\right) \cdot cos\left(\alpha + \frac{d\alpha}{dz} dz\right) - N\cos\alpha + q\cos\alpha dz = 0 \\ \left(N + \frac{\partial N}{\partial z} dz\right) \cdot sin\left(\alpha + \frac{d\alpha}{dz} dz\right) - N\sin\alpha + pdz = 0 \end{cases} \tag{B.1}$$

Assuming the derivative of α being small (small angle variations), system of equations (B.1) can be written as:

$$\begin{cases} \frac{\partial N}{\partial z} + q = 0 \\ \left(N + \frac{\partial N}{\partial z} dz\right) \cdot \left[sin(\alpha) \overbrace{cos\left(\frac{d\alpha}{dz} dz\right)}^{1} + cos(\alpha) \overbrace{sin\left((\frac{d\alpha}{dz} dz\right)}^{\frac{d\alpha}{dz} dz} \right] + \dots \\ \quad \dots - N sin(\alpha) + pdz = 0 \end{cases} \tag{B.2}$$

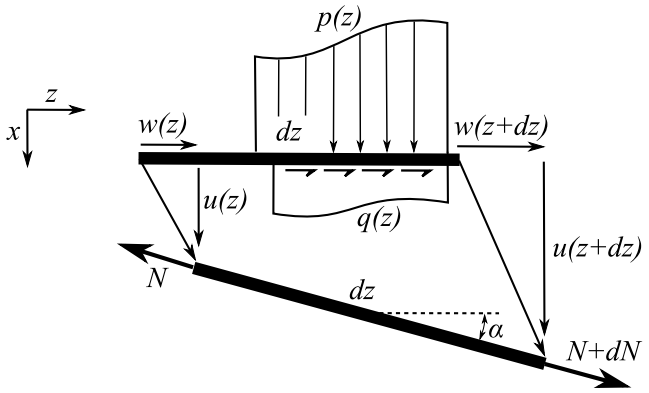

Figure B.1: Schematic of the forces acting over the pin (idealised as a truss) during the ploughing phase.

The first equation of Eq. (B.2) is a shear lag equation, which describes the axial load of the pin along the z-axis. The second equation instead is the force balance in the lateral direction, which describes the pin rotation within the laminate.

From geometrical consideration the following relation can be written:

$$\frac{du}{dz} = sin(\alpha), \quad \frac{d^2u}{dz^2} = cos(\alpha)d\alpha \tag{B.3}$$

Substituting then Eq. (B.3) in Eq. (B.2), we obtain the following differential equation:

$$\frac{dN}{dz}\frac{du}{dz} + N\frac{d^2u}{dz^2} + p = 0 \tag{B.4}$$

Which can be also expressed in the following simpler form:

$$\frac{\partial}{dz}\left(N\frac{du}{dz}\right) + p = 0 \tag{B.5}$$

Equation (B.6) can be integrated, obtaining the following form:

$$N(z)\frac{du}{dz} = -pz + N(z=0)\frac{du}{dz}|_{z=0} \tag{B.6}$$

Where $N(z=0)$ and $\frac{du}{dz}|_{z=0}$ are respectively the axial force and the z-pin rotation at the section $z=0$, which for the sake of simplicity will be called from now on respectively N_0 and α_0. The axial force carried by the pin ($N(z)$) can by calculated using the first equation of system B.2:

$$N(z) = N_0 - qz \tag{B.7}$$

Substituting Eq. (B.7) in Eq. (B.6) and integrating once again we can obtain a closed form of the lateral displacement of the z-pin in function of the friction

resistance of the pin to pullout (q) and the ploughing resistance of the laminate (p):

$$u - u_0 = \int_0^z \frac{-pz + N_0\alpha_0}{N_0 - qz} dz = \frac{p}{q}z + \frac{N_0}{q}\left(\frac{p}{q} - \alpha_0\right)\ln\left(1 - \frac{qz}{N_0}\right) \tag{B.8}$$

Derivation of differential equation of pin lateral displacement after ploughing

APPENDIX C

MODE-II ANALYTICAL MODEL OF CARBON PIN REINFORCEMENTS

Bridging performance of carbon pin reinforcements has been analysed by simulating a single-pin shear test. Hereafter it is reported the Matlab routine used for this purpose.

```
%% ESTIMATE OF THE MODE-II bridging law
%% Beam model to calculate the elastic response of the pin, pin ploughing
%% and failure.

function [d,Fout,Cohe,fib_rupt]=f_Zpin_Plough(L_lam,Phi,E,Emat,Su,SigmaU,...
            SigmaX,Sigma0,mu)

%% Input Variables
%L_lam                  %[mm]  Laminate half thichness
%Phi                    %[mm]  Pin diameter
%E                      %[MPa] Pin Young's modulus
%Emat                   %[MPa] Surrounding laminate Young's modulus
%Su                     %[MPa] Shear strength of the pin
%mu                     %      Coefficient of friction
%SigmaU                 %[MPa] Ploughing resistance
%SigmaX                 %[Mpa] Axial strength of the pin
%Sigma0                 %[MPa] Initial compression stress due to cure process

%% Output variables
%d                      %[mm] Shear displacement of the pin
%Fout                   %[N]  Bridging force of the pin
%rupt                   %     Fibre rupture: 1 fibre-breakage, 0 fibre-pullout
%Cohe                   %     Cohesive parameters [K0 TII0 GIIC]
%%-------------------------------------------------------------------------%%
%% Calculation foundamental quatities
```

```
%pin section: circular (J=pi/4*R^4)
R=Phi/2;
L=L_lam-Phi;    %pin embedded length (chamfer head of the pin does not
                %contribute to the pin response)
I=pi/4*R^4;     %Inertia moment with respect one principal axis
k=pi/2*Emat;    %stiffness of the distributed spring support
py=SigmaU*Phi;  %Force per unit length exerted by the laminate during
                %ploughing phase
%%%%%%%%%%%%%%%%%%%%%%%%%%%%%%%%%%%%%%%%%%%%%%%%%%%%%%%%%%%%%%%%%%%%
%% Solution of linear response phase (no ploughing)
%%Assumptions: the pin is assumed to behave initially as a beam supported
%% by an elastic foundation of stiffness k.
alpha=1/R*(Emat/E)^0.25;
xlin=L*(0:0.01:1);
%Solution is linear within input data (displacement at one end of the beam)
%boundary conditions applied: u''(0)=0, u'''(0)=0, u(L)=1 and u''(L)=0
Term1=cosh(alpha*L)*cos(alpha*L);Term2=cosh(alpha*L)*sin(alpha*L);
Term3=sinh(alpha*L)*cos(alpha*L);Term4=sinh(alpha*L)*sin(alpha*L);
A=[     0               0           0               1
        0               1           -1              0
    -Term4          Term3       -Term2          Term1
     Term1          Term2        Term3          Term4];
B=[0;0;0;1];
Xlin=(inv(A)*B)';
%third derivative in order to calculate transverse shear
X3_lin=alpha^3*2*[Xlin(2)-Xlin(3),-Xlin(1)-Xlin(4),-Xlin(1)+Xlin(4),...
            -Xlin(2)-Xlin(3)];
Send_lin=[Term1;Term2;Term3;Term4];
Slin=[cosh(alpha*xlin).*cos(alpha*xlin)     %General solution
    cosh(alpha*xlin).*sin(alpha*xlin)
    sinh(alpha*xlin).*cos(alpha*xlin)
    sinh(alpha*xlin).*sin(alpha*xlin)];
wlin=Xlin*Slin;
%% check soluiton
% X1=alpha*[Xlin(2)+Xlin(3),-Xlin(1)+Xlin(4),Xlin(1)+Xlin(4),...
            Xlin(2)-Xlin(3)];
% X2=alpha^2*2*[Xlin(4),-Xlin(3),Xlin(2),-Xlin(1)];
% X3=alpha^3*2*[Xlin(2)-Xlin(3),-Xlin(1)-Xlin(4),-Xlin(1)+...
            Xlin(4),-Xlin(2)-Xlin(3)];
% w1=X1*Slin;
% w2=X2*Slin;
% w3=X3*Slin;
% figure
% hold on
% plot(xlin,wlin,xlin,w1,xlin,w2,xlin,w3)
%solution is linear with applied displacement delta/2

%% Ploughing phase
fib_rupt=0;         %fibre rupture, initially assigned 0 (no-breakage)
d=0;                %initial applied shear displacement
Fout=0;             %initial bridging force
dF=0.1;             %force increment
```

```
F_i=dF;             %bridging force is step-by-step incremented and the
                    %solutionis then calculated for such applied force.
                    %Force keeps to be incremented until either fibre-breakage
                    %or fibre pullout conditions are met.
T0el=abs(-E*I*X3_lin*Send_lin);      %Force per unit of applied displacement
Nmax=1;                              %during elastic phase initial values of
                                     %maximum axial force and axial force
                                     %to enter the while cycle
N=0;
while Nmax>N
    if F_i<Su*pi*R^2                 %Condition for being in linear response
                                     %phase
        d_i=2*F_i/T0el;              %displacement is multiplied times 2
                                     %to account for the symmetry
        dlin=d_i;
        %updating output
        Fout=[Fout F_i];
        d=[d d_i];
        %updating applied force
        F_i=F_i+dF;
        %during elastic phase conditions of either fibre-breakage or
        %pullout are checked, therefore the cycle goes on
    else
       h_pl=(F_i-Su*pi*R^2)/py;      %height of pin which ploughs into
       Lt=L-h_pl;                    %the laminate remaining part of
                                     %the pin subjected to linear response
                                     %of the laminate
       %solution of elastic part
       x=Lt*(0:0.01:1);
        Term1=cosh(alpha*Lt)*cos(alpha*Lt);Term2=cosh(alpha*Lt)*sin(alpha*Lt);
        Term3=sinh(alpha*Lt)*cos(alpha*Lt);Term4=sinh(alpha*Lt)*sin(alpha*Lt);
        A=[     0               0           0               1
                0               1           -1              0
            -Term4          Term3       -Term2          Term1
            Term1          Term2        Term3          Term4];
        B=[0;0;0;1];
        X=(inv(A)*B)';
        X1=alpha*[X(2)+X(3),-X(1)+X(4),X(1)+X(4),X(2)-X(3)];
        X3=alpha^3*2*[X(2)-X(3),-X(1)-X(4),-X(1)+X(4),-X(2)-X(3)];
        Send=[Term1;Term2;Term3;Term4];
        S=[cosh(alpha*x).*cos(alpha*x)     %General solution
        cosh(alpha*x).*sin(alpha*x)
        sinh(alpha*x).*cos(alpha*x)
        sinh(alpha*x).*sin(alpha*x)];
        w=X*S;
        T0=-E*I*X3*Send;    %Force per unit of applied displacement
        d_el=Su*pi*R^2/T0;  %elastic displacement is equal to
                            %the displacement necessary to bring the pin
                                    % to exceed the shear strength
        Cforce=k*trapz(x,abs(w))*d_el+2*pi*R*Lt*Sigma0; %[N] contact force
                                                        %between pin
                                                        %and laminate
```

```
        N0=mu*Cforce;                                       %max axial force
                                                            %carried by
                                                            %the pin before
                                                            %sliding
        Sin_alpha0=X1*Send*d_el;                            %Sin of the angle
                                                            %at the boundary
                                                            %between elastic
                                                            %and plastic regions
        Sin_alpha=(py*Lt+N0*Sin_alpha0)/(N0+mu*py*Lt);      %Sin of the angle at
                                                            %the delamination plane
                                                            %(where bridging force
                                                            %is estimated)

        d_pl=h_pl/mu+N0/(mu*py)*(Sin_alpha0-1/mu)*...
            (log(h_pl+N0/(mu*py))-log(N0/(mu*py)));         %displacement in the
                                                            %ploughing area
        d_i=2*(d_el+d_pl);                                  %total displacement
        %updating output and checking fibre-breakage and pullout conditions
        d=[d d_i];
        %fibre-pullout condition (N>Nmax)
        N=F_i*Sin_alpha;
        Nmax=N0+mu*py*h_pl;
        sigma_x=N/(pi*R^2);
        if sigma_x>SigmaX       %fibre-breakage condition
            fib_rupt=1;
            F_i=0;
            Fout=[Fout F_i];
            break
        else
            Fout=[Fout F_i];
        end
        F_i=F_i+dF;
    end
end
%final failure occurs after at delta_f=L
%% Bridging law & cohesive element parameters
Fout=[Fout 0];
d=[d L];
K0=T0el/(pi*R^2);
TII0=max(Fout)/(pi*R^2);
GIIC=trapz(d,Fout/(pi*R^2));
Cohe=[K0 TII0 GIIC];
```

REFERENCES

[1] C. Soutis, Fibre reinforced composites in aircraft construction. *Progress in Aerospace Sciences* 2005; 41(2): 143–151.

[2] R.B. Deo, J.H. Starnes and R.C. Holzwarth, Low-cost composite materials and structures for aircraft applications. *RTO AVT Specialists, Meeting on "Low Cost Composite Structures"* 2001; .

[3] F.L. Matthews, P.F. Kilty and E.W. Godwin, A review of the strength of joints in fibre-reinforced plastics. Part 2. Adhesively bonded joints. *Composites* 1982; 13(1): 29–37.

[4] J.-K. Kim and Y.-W. Mai, High strength, high fracture toughness fibre composites with interface control – A review. *Composite Science and Technology* 1991; 41(4): 333–378.

[5] S. Singh and I.K. Partridge, Mixed-mode fracture in an interleaved carbon-fibre/epoxy composite. *Composites Science and Technology* 1995; 55(4): 319–327.

[6] J.H. Hodgkin, G.P. Simon and R.J. Varley, Thermoplastic toughening of epoxy resins: A critical review. *Polymers for Advanced Technologies* 1998; 9(1): 3–10.

[7] K. Dransfield, C. Baillie and Y.-W. Mai, Improving the delamination resistance of CFRP by stitching – A review. *Composites Science and Technology* 1994; 50(3): 305–317.

[8] A.P. Mouritz, Review of z-pinned composite laminates. *Composites Part A: Applied Science and Manufacturing* 2007; 38(12): 2383–2397.

[9] D.D.R. Cartié, G. Dell'Anno, E. Poulin and I.K. Partridge, 3D reinforcement of stiffener-to-skin T-joints by Z-pinning and tufting. *Engineering Fracture Mechanics* 2006; 73(16): 2532–2540.

[10] G. Dell'Anno, D.D.R Cartié, I.K. Partridge and A. Rezai, Exploring mechanical property balance in tufted carbon fabric/epoxy composites. *Composites Part A: Applied Science and Manufacturing* 2007; 38(11): 2366–2373.

[11] L.J. Hart-Smith, Bonded-Bolted Composite Joints. *Collection of Technical Papers - AIAA/ASME/ASCE/AHS/ASC Structures, Structural Dynamics and Materials Conference* 1984; (pt 1): 478–488.

[12] L.J. Hart-Smith, Design of repairable composite structures. *SAE Technical Paper Series* 1985; .

[13] L.J. Hart-Smith, Bonded-bolted composite joints. *Journal of Aircraft* 1985; 22(11): 993–1000.

[14] G. Kelly, Load transfer in hybrid (bonded/bolted) composite single-lap joints. *Composite Structures* 2005; 69(1): 35–43.

[15] G. Kelly, Quasi-static strength and fatigue life of hybrid (bonded/bolted) composite single-lap joints. *Composite Structures* 2006; 72(1): 119–129.

[16] V. Kradinov, E. Madenci and D.R. Ambur, Analysis of bolted laminates of varying thickness and lay-up with metallic inserts. *Collection of Technical Papers - AIAA/ASME/ASCE/AHS/ASC Structures, Structural Dynamics and Materials Conference* 2003; 7: 5435–5446.

[17] V. Kradinov, E. Madenci and D.R. Ambur, Bolted lap joints of laminates with varying thickness and metallic inserts. *Composite Structures* 2005; 68(1): 75–85.

[18] A. Fink, B. Kolesnikov and H. Wilmes, CFRP/titanium hybrid: Improving composite structure coupling. *JEC Composites Magazine* 2004; (7): 64–67.

[19] B. Kolesnikov, L. Herbeck and A. Fink, CFRP/titanium hybrid material for improving composite bolted joints. *Composite Structures* 2008; 83(4): 368–380.

[20] P.P. Camanho, A. Fink, A. Obst and S. Pimenta, Hybrid titanium-CFRP laminates for high-performance bolted joints. *Composites Part A: Applied Science and Manufacturing* 2009; 40(12): 1826–1837.

[21] S. Ucsnik, M. Scheerer, S. Zaremba and D.H. Pahr, Experimental investigation of a novel hybrid metal-composite joining technology. *Composites Part A: Applied Science and Manufacturing* 2010; 41(3): 369–374.

[22] F.J. Guild, P.J. Hogg and W. Tu, Comeld joints: A novel technique for bonding composites and metal. *Proceedings of ICCM International Conferences on Composite Materials* 2009; 1: 1–8.

[23] W. Tu, P.H. Wen and F.J. Guild, Multi-region mesh free method for Comeld joints. *Computational Materials Science* 2010; 48(3): 481–489.

[24] W. Tu, P.H. Wen, P.J. Hogg and F.J. Guild, Optimisation of the protrusion geometry in Comeld joints. *Composites Science and Technology* 2011; 71(6): 868–876.

[25] S.A. Ucsnik and G. Kirov, New possibility for the connection of metal sheets and fibre reinforced plastics. *Materials Science Forum* 2011; 690: 465–468.

[26] S.A. Ucsnik, R.a Gradinger, U. Noster and D.H. Pahr, Finite element based optimization of a novel metal-composite-joint. *VDI Berichte* 2008; 1(2028): 371–379.

[27] Military Materials Handbook 17. US Department of defense, 2002.

[28] P. Tan, L. Tong and G.P. Steven, Modelling for predicting the mechanical properties of textile composites - A review. *Composites Part A: Applied Science and Manufacturing* 1997; 28(11): 903–922.

[29] S.V. Lomov, D.S. Ivanov, Zako Verpoest, I., T. M., Kurashiki, H. Nakai and S. Hirosawa, Meso-FE modelling of textile composites: Road map, data flow and algorithms. *Composites Science and Technology* 2007; 67(9): 1870–1891.

[30] D5766/D5766-02a Standard Test Method for Hole Tensile Strength of Polymer-matrix Composite Laminates, volume 15.03. ASTM International, 2007.

[31] D6484/D6484M-04 Standard Test Method for Compressive Strength of Polymer-matrix Composite Laminates, volume 15.03. ASTM International, 2004.

[32] D6742/D6742-02 Standard practice for Filled-hole Tension and Compression Testing of Polymer-matrix Composite Laminates, volume 15.03. ASTM International, 2007.

[33] D5961/D5961M-05e1 Standard Test Method for Bearing Response of Polymer-matrix Composite Laminates, volume 15.03. ASTM International, 2005.

[34] P.P. Camanho and F.L. Matthews, Stress analysis and strength prediction of mechanically fastened joints in FRP: A review. *Composites Part A: Applied Science and Manufacturing* 1997; 28(6): 529–547.

[35] E.W. Godwin and F.L. Matthews, A review of the strength of joints in fibre-reinforced plastics. Part 1. Mechanically fastened joints. *Composites* 1980; 11(3): 155–160.

[36] R. F. Gibson, Principles of composite materials mechanics. aeronautical and aerospace engineering, McGraw-Hill, 1994.

[37] S.D. Thoppul, J. Finegan and R.F. Gibson, Mechanics of mechanically fastened joints in polymer-matrix composite structures - A review. *Composites Science and Technology* 2009; 69(3-4): 301–329.

[38] F.L. Matthews, P.F. Kilty and E.W. Godwin, A review of the strength of joints in fibre-reinforced plastics. Part 2. Adhesively bonded joints. *Composites* 1982; 13(1): 29–37.

[39] K.-S. Kim, J.-S. Yoo, Y.-M. Yi and C.-G. Kim, Failure mode and strength of uni-directional composite single lap bonded joints with different bonding methods. *Composite Structures* 2006; 72(4): 477–485.

[40] K.-S. Kim, Y.-M. Yi, G.-R. Cho and C.-G. Kim, Failure prediction and strength improvement of uni-directional composite single lap bonded joints. *Composite Structures* 2008; 82(4): 513–520.

[41] G. Li, P. Lee-Sullivan and R.W. Thring, Nonlinear finite element analysis of stress and strain distributions across the adhesive thickness in composite single-lap joints. *Composite Structures* 1999; 46(4): 395–403.

[42] P.A. Gustafson and A.M. Waas, The influence of adhesive constitutive parameters in cohesive zone finite element models of adhesively bonded joints. *International Journal of Solids and Structures* 2009; 46(10): 2201–2215.

[43] G. Richardson, A.D. Crocombe and P.A. Smith, A comparison of two- and three- dimensional finite element analyses of adhesive joints. *International Journal of Adhesion and Adhesives* 1993; 13(3): 193–200.

[44] Y. Zhang, A.P. Vassilopoulos and T. Keller, Mode I and II fracture behavior of adhesively-bonded pultruded composite joints. *Engineering Fracture Mechanics* 2010; 77(1): 128–143.

[45] Y. Zhang, A.P. Vassilopoulos and T. Keller, Mixed-mode fracture of adhesively-bonded pultruded composite lap joints. *Engineering Fracture Mechanics* 2010; 77(14): 2712–2726.

[46] S. Feih and H.R. Shercliff, Adhesive and composite failure prediction of single-L joint structures under tensile loading. *International Journal of Adhesion and Adhesives* 2005; 25(1): 47–59.

[47] M.F.S.F. De Moura and J.A.G. Chousal, Cohesive and continuum damage models applied to fracture characterization of bonded joints. *International Journal of Mechanical Sciences* 2006; 48(5): 493–503.

[48] M.F.S.F. De Moura, J.P.M. Gonçalves, J.A.G. Chousal and R.D.S.G. Campilho, Cohesive and continuum mixed-mode damage models applied to the simulation of the mechanical behaviour of bonded joints. *International Journal of Adhesion and Adhesives* 2008; 28(8): 419–426.

[49] A.D. Crocombe, Modelling and predicting the effects of test speed on the strength of joints made with FM73 adhesive. *International Journal of Adhesion and Adhesives* 1995; 15(1): 21–27.

[50] H.L. Groth, Stress singularities and fracture at interface corners in bonded joints. *International Journal of Adhesion and Adhesives* 1988; 8(2): 107–113.

[51] M. Quaresimin and M. Ricotta, Stress intensity factors and strain energy release rates in single lap bonded joints in composite materials. *Composites Science and Technology* 2006; 66(5): 647–656.

[52] A. Barroso, Mantič and F. V., París, Singularity parameter determination in adhesively bonded lap joints for use in failure criteria. *Composites Science and Technology* 2008; 68(13): 2671–2677.

[53] E.F. Rybicki and M.F. Kanninen, A finite element calculation of stress intensity factors by a modified crack closure integral. *Engineering Fracture Mechanics* 1977; 9(4): 931–938.

[54] R. Krueger, Virtual crack closure technique: History, approach, and applications. *Applied Mechanics Reviews* 2004; 57(1-6): 109–143.

[55] J. Lemaitre, How to use damage mechanics. *Nuclear Engineering and Design* 1984; 80(2): 233–245.

[56] R. Massabò and B.N. Cox, Concepts for bridged Mode II delamination cracks. *Journal of the Mechanics and Physics of Solids* 1999; 47(6): 1265–1300.

[57] M. Grassi and X. Zhang, Finite element analyses of mode I interlaminar delamination in z-fibre reinforced composite laminates. *Composites Science and Technology* 2003; 63(12): 1815–1832.

[58] Cox B.N. and Flanagan G., Handbook of analytical methods for textile composites. NASA contractor report 4750, March 1997.

[59] A.A. Griffits, The phenomena of rupture and flow in solids. Ph.D. thesis, Phisolofical transactions of the Royal Society of London, 1921.

[60] P. Robinson and S. Das, Mode I DCB testing of composite laminates reinforced with z-direction pins: A simple model for the investigation of data reduction strategies. *Engineering Fracture Mechanics* 2004; 71(3): 345–364.

[61] V. Dantuluri, S. Maiti, P.H. Geubelle, R. Patel and H. Kilic, Cohesive modeling of delamination in Z-pin reinforced composite laminates. *Composites Science and Technology* 2007; 67(3-4): 616–631.

[62] L.C. Dickinson, G.L. Farley and M.K. Hinders, Prediction of effective three-dimensional elastic constants of translaminar reinforced composites. *Journal of Composite Materials* 1999; 33(11): 1002–1029.

[63] M. Grassi, X. Zhang and M. Meo, Prediction of stiffness and stresses in z-fibre reinforced composite laminates. *Composites Part A: Applied Science and Manufacturing* 2002; 33(12): 1653–1664.

[64] Z. Xia, Y. Zhang and F. Ellyin, A unified periodical boundary conditions for representative volume elements of composites and applications. *International Journal of Solids and Structures* 2003; 40(8): 1907–1921.

[65] Z. Xia, C. Zhou, Q. Yong and X. Wang, On selection of repeated unit cell model and application of unified periodic boundary conditions in micro-mechanical analysis of composites. *International Journal of Solids and Structures* 2006; 43(2): 266–278.

[66] R.J. Gray, Analysis of the effect of embedded fibre length on fibre debonding and pull-out from an elastic matrix - Part 1 Review of theories. *Journal of Materials Science* 1984; 19(3): 861–870.

[67] D. D. R. Cartié, Effect of Z-fibres on the delamination behavior of carbon fibre/epoxy laminates. Ph.D. thesis, Cranfield University, 2000.

[68] D.D.R. Cartié, B.N. Cox and N.A. Fleck, Mechanisms of crack bridging by composite and metallic rods. *Composites Part A: Applied Science and Manufacturing* 2004; 35(11): 1325–1336.

[69] H.-Y. Liu, W. Yan, X.-Y. Yu and Y.-W. Mai, Experimental study on effect of loading rate on mode I delamination of z-pin reinforced laminates. *Composites Science and Technology* 2007; 67(7-8): 1294–1301.

[70] K.L. Rugg, B.N. Cox, K.E. Ward and G.O. Sherrick, Damage mechanisms for angled through-thickness rod reinforcement in carbon-epoxy laminates. *Composites Part A: Applied Science and Manufacturing* 1998; 29(12): 1603–1613.

[71] K.L. Rugg, B.N. Cox and R. Massabò, Mixed mode delamination of polymer composite laminates reinforced through the thickness by z-fibers. *Composites - Part A: Applied Science and Manufacturing* 2002; 33(2): 177–190.

[72] K.P. Plain and L. Tong, Experimental validation of theoretical traction law for inclined through-thickness reinforcement. *Composite Structures* 2009; 91(2): 148–157.

[73] J.W.G. Treiber, D.D.R. Cartiè and I.K. Partridge, Determination of crack bridging laws in tufted composites. *ICCM International Conferences on Composite Materials* 2009; .

[74] K.T. Tan, N. Watanabe and Y. Iwahori, Experimental investigation of bridging law for single stitch fibre using Interlaminar tension test. *Composite Structures* 2010; 92(6): 1399–1409.

[75] S.C. Dai, W. Yan, H.Y. Liu and Y.W. Mai, Experimental study on z-pin bridging law by pullout test. *Composites Science and Technology* 2004; 64(16): 2451 – 2457.

[76] R. Massabò, D.R. Mumm and B.N. Cox, Characterizing mode II delamination cracks in stitched composites. *International Journal of Fracture* 1998; 92(1): 1–38.

[77] D.D.R. Cartiè, M. Troulis and I. K. Partridge, Delamination of Z-pinned carbon fibre reinforced laminates. *Composites Science and Technology* 2006; 66(6): 855 – 861.

[78] J. Aveston, G.A. Cooper and A. Kelly, Single and multiple fracture. *Composites, national physics laboratory* 1971; pages 15–26.

[79] J. Aveston and A. Kelly, Theory of multiple fracture of fibrous composites. *Journal of Materials Science* 1973; 8(3): 352–362.

[80] L.K. Jain and Y.-W. Mai, On the effect of stitching on mode I delamination toughness of laminated composites. *Composites Science and Technology* 1994; 51(3): 331–345.

[81] M. Meo, F. Achard and M. Grassi, Finite element modelling of bridging micromechanics in through-thickness reinforced composite laminates. *Composite Structures* 2005; 71(3-4): 383–387.

[82] G. Allegri and X. Zhang, On the delamination and debond suppression in structural joints by Z-fibre pinning. *Composites Part A: Applied Science and Manufacturing* 2007; 38(4): 1107–1115.

[83] B.N. Cox and N. Sridhar, A traction law for inclined fiber tows bridging mixed-mode cracks. *Mechanics of Advanced Materials and Structures* 2002; 9(4): 299–331.

[84] B.N. Cox, Snubbing effects in the pullout of a fibrous rod from a laminate. *Mechanics of Advanced Materials and Structures* 2005; 12(2): 85–98.

[85] L. Tong and X. Sun, Bending effect of through-thickness reinforcement rods on mode I delamination toughness of DCB specimen. I. Linearly elastic and rigid-perfectly plastic models. *International Journal of Solids and Structures* 2004; 41(24-25): 6831–6852.

[86] L. Tong and X. Sun, Bending effect of through-thickness reinforcement rods on mode II delamination toughness of ENF specimen: Elastic and rigid-perfectly plastic analyses. *Composites Part A: Applied Science and Manufacturing* 2007; 38(2): 323–336.

[87] K.P. Plain and L. Tong, Traction law for inclined through-thickness reinforcement using a geometrical approach. *Composite Structures* 2009; 88(4): 558–569.

[88] H. Cui, Y. Li, S. Koussios, L. Zu and A. Beukers, Bridging micromechanisms of Z-pin in mixed mode delamination. *Composite Structures* 2011; 93(11): 2685–2695.

[89] L.W. Byrd and V. Birman, The estimate of the effect of z-pins on the strain release rate, fracture and fatigue in a composite co-cured z-pinned double cantilever beam. *Composite Structures* 2005; 68(1): 53–63.

[90] M. He and B.N. Cox, Crack bridging by through-thickness reinforcement in delaminating curved structures. *Composites Part A: Applied Science and Manufacturing* 1998; 29(4): 377–393.

[91] Ratcliffe J.G. and O'Brien T.K., Discrete spring model for predicting delamination growth in z-fibre reinforced DCB specimens. Technical Report NASA/TM-2004-213019, NASA, May 2004.

[92] M. Grassi, B. Cox and X. Zhang, Simulation of pin-reinforced single-lap composite joints. *Composites Science and Technology* 2006; 66(11-12): 1623–1638.

[93] J. Toral Vazquez, B. Castanié, J.-J. Barrau and N. Swiergiel, Multi-level analysis of low-cost Z-pinned composite joints: Part 2: Joint behaviour. *Composites Part A: Applied Science and Manufacturing* 2011; 42(12): 2082–2092.

[94] W. Yan, H.-Y. Liu and Y.-W. Mai, Numerical study on the mode I delamination toughness of z-pinned laminates. *Composites Science and Technology* 2003; 63(10): 1481–1493.

[95] A.L. Cohen, From rapid prototyping to the second industrial revolution. University of Dayton: Dayton, OH, 1992.

[96] S.S. Gill and M. Kaplas, Comparative study of 3D printing technologies for rapid casting of aluminium alloy. *Materials and Manufacturing Processes* 2009; 24(12): 1405–1411.

[97] W. Shambley, From RP to AM: A review of prototyping methods. *Metal Casting Design and Purchasing* 2010; 12(4): 34–37.

[98] F. Abe, K. Osakada, M. Shiomi, K. Uematsu and M. Matsumoto, The manufacturing of hard tools from metallic powders by selective laser melting. *Journal of Materials Processing Technology* 2001; 111(1-3): 210–213.

[99] E. Louvis, P. Fox and C.J. Sutcliffe, Selective laser melting of aluminium components. *Journal of Materials Processing Technology* 2011; 211(2): 275–284.

[100] Konrad Bartkowiak, Sven Ullrich, Thomas Frick and Michael Schmidt, New Developments of Laser Processing Aluminium Alloys via Additive Manufacturing Technique. *Physics Procedia* 2011; 12, Part A: 393–401.

[101] S.M. Gaytan, L.E. Murr, F. Medina, E. Martinez, M.I. Lopez and R.B. Wicker, Advanced metal powder based manufacturing of complex components by electron beam melting. *Materials Technology* 2009; 24(3): 180–190.

[102] M. Svensson and U. Ackelid, Titanium alloys manufactured with electron beam melting mechanical and chemical properties. *Medical Device Materials V - Proceedings of the Materials and Processes for Medical Devices Conference* 2010; pages 187–194.

[103] B. G. I. Dance and E. J. C. Kellar, Workpiece structure modification. Technical Report WO 2004028731 A1, International patent publication, 2004.

[104] P. A. Hilton, B. G. I. Dance and L. Nguyen, Laser beam induced surface modification using the Surfi-Sculpt process. Technical Report Technology Briefing 919, TWI, 2009.

[105] A. L. Buxton and Dance B. G. I., Surfi-Sculpt – Revolutionary surface processing with an electron beam. *Proceeding of ASM International, ISEC Congress* 2005; .

[106] Dance B. G. I. and A. L. Buxton, An introduction to Surfi-Sculpt technology - new opportunities, new challenges. *Proceeding of* 7^{th} *International Conference on Beam Technology* 2007; .

[107] Fronius, CMT: cold metal transfer, www.fronius.com. February 2012.

[108] J. Butler. Ph.D. thesis, Cranfield University, 2012.

[109] A. Joesbury, D. Ayre, I. K. Partridge, P. Colegrove and S. W. Williams, New approaches to metal-composite joining. *Proceedings of* 11^th *Triennial International Conference on the Science and Technology of Adhesion and Adhesives* 2011; 1: 206–213.

[110] K. H. Schwalbe, I. Schider and A. Cornec, The SIAM method for applying cohesive models to the damage behaviour of engineering materials and structures. Technical report, GKSS, Jan 2009.

[111] D.S. Dugdale, Yielding of steel sheets containing slits. *Journal of the Mechanics and Physics of Solids* 1960; 8(2): 100–104.

[112] G.I. Barenblatt, The Mathematical Theory of Equilibrium Cracks in Brittle Fracture. *Advances in Applied Mechanics* 1962; 7(C): 55–129.

[113] A. Hillerborg, M. Modéer and P.-E. Petersson, Analysis of crack formation and crack growth in concrete by means of fracture mechanics and finite elements. *Cement and Concrete Research* 1976; 6(6): 773–781.

[114] G. Alfano and M.A. Crisfield, Finite element interface models for the delamination analysis of laminated composites: Mechanical and computational issues. *International Journal for Numerical Methods in Engineering* 2001; 50(7): 1701–1736.

[115] P. P. Camanho and C. G. Dávila, Mixed-Mode Decohesion Finite Elements for the Simulation of Delamination in Composite Materials. *NASA* 2002; 1(TM-2002211737): 1–37.

[116] C.G. Dávila, P.P. Camanho and M.F. De Moura, Mixed-mode decohesion elements for analyses of progressive delamination. *Collection of Technical Papers - AIAA/ASME/ASCE/AHS/ASC Structures, Structural Dynamics and Materials Conference* 2001; 3: 2277–2288.

[117] C.G. Dávila, P.P. Camanho and A. Turon, Effective simulation of delamination in aeronautical structures using shells and cohesive elements. *Journal of Aircraft* 2008; 45(2): 663–672.

[118] R. Borg, L. Nilsson and K. Simonsson, Simulating DCB, ENF and MMB experiments using shell elements and a cohesive zone model. *Composites Science and Technology* 2004; 64(2): 269–278.

[119] M. Meo and E. Thieulot, Delamination modelling in a double cantilever beam. *Composite Structures* 2005; 71(3-4): 429–434.

[120] M. Alfano, F. Furgiuele, A. Leonardi, C. Maletta and G.H. Paulino, Mode I fracture of adhesive joints using tailored cohesive zone models. *International Journal of Fracture* 2009; 157(1-2): 193–204.

[121] M.A.L. Silva, M.F.S.F. de Moura and J.J.L. Morais, Numerical analysis of the ENF test for mode II wood fracture. *Composites Part A: Applied Science and Manufacturing* 2006; 37(9): 1334–1344.

[122] M.F.S.F. de Moura and A.B. de Morais, Equivalent crack based analyses of ENF and ELS tests. *Engineering Fracture Mechanics* 2008; 75(9): 2584–2596.

[123] M.F.S.F. De Moura, N. Dourado, J.J.L. Morais and F.A.M. Pereira, Numerical analysis of the ENF and ELS tests applied to mode II fracture characterization of cortical bone tissue. *Fatigue and Fracture of Engineering Materials and Structures* 2011; 34(3): 149–158.

[124] T. Diehl, On using a penalty-based cohesive-zone finite element approach, Part I: Elastic solution benchmarks. *International Journal of Adhesion and Adhesives* 2008; 28(4-5): 237–255.

[125] T. Diehl, On using a penalty-based cohesive-zone finite element approach, Part II: Inelastic peeling of an epoxy-bonded aluminum strip. *International Journal of Adhesion and Adhesives* 2008; 28(4-5): 256–265.

[126] K. Song, C. G. Dávila and C. A. Rose, Guidelines and parameter selection for the simulation of progressive delamination. *Proceedings of annual international Abaqus Users Conference* 2008; .

[127] C. Sun, M.D. Thouless, A.M. Waas, J.A. Schroeder and P.D. Zavattieri, Ductile-brittle transitions in the fracture of plastically deforming, adhesively bonded structures. Part II: Numerical studies. *International Journal of Solids and Structures* 2008; 45(17): 4725–4738.

[128] M.S. Kafkalidis and M.D. Thouless, The effects of geometry and material properties on the fracture of single lap-shear joints. *International Journal of Solids and Structures* 2002; 39(17): 4367–4383.

[129] Q.D. Yang, B.N. Cox, R.K. Nalla and R.O. Ritchie, Fracture length scales in human cortical bone: The necessity of nonlinear fracture models. *Biomaterials* 2006; 27(9): 2095–2113.

[130] C.T. Sun and Z.-H. Jin, Modeling of composite fracture using cohesive zone and bridging models. *Composites Science and Technology* 2006; 66(10): 1297–1302.

[131] T.M. Koh, S. Feih and A.P. Mouritz, Experimental determination of the structural properties and strengthening mechanisms of z-pinned composite T-joints. *Composite Structures* 2011; 93(9): 2222–2230.

[132] B.N. Cox and D.B. Marshall, The determination of crack bridging forces. *International Journal of Fracture* 1991; 49(3): 159–176.

[133] L.E. Asp, The effects of moisture and temperature on the interlaminar delamination toughness of a carbon/epoxy composite. *Composites Science and Technology* 1998; 58(6): 967–977.

[134] M. Troulis, Effect of Z-fiber pinning on the mechanical propertiesof carbon fibre/epoxy composites. Ph.D. thesis, Cranfield University, 2003.